1-13-2021

Corrosion Performance of Additively Manufactured Alloys and Hot Corrosion

Ali Hemmasian Ettefagh

CORROSION PERFORMANCE OF ADDITIVELY MANUFACTURED ALLOYS AND HOT CORROSION

A Dissertation

Submitted to the Graduate Faculty of the
Louisiana State University and
Agricultural and Mechanical College
in partial fulfillment of the
requirements for the degree of
Doctor of Philosophy

in

The Department of Mechanical & Industrial Engineering

by
Ali Hemmasian Ettefagh
BSc, Amirkabir University of Technology, 2006
MSc, University of Tehran, 2009
PhD, Louisiana State University
May 2021

Acknowledgments

All chapters of this dissertation were either supported by the NSF EPSCoR CIMM project under award #OIA-1541079, or by the U.S. Department of Energy, Office of Science, Office of Basic Energy Sciences, under Award Number DE-SC0019378.

Table of Contents

List of Tables

List of Figures

Abstract

Additive manufacturing (AM) has gained attentions in recent years due to its unique properties in the fabrication of complex parts. Same as any other new topics, in some areas, there are still lack of enough knowledge and there are the needs for further investigations to enable the applications of AM parts widely in industries. Chapter 2, and Chapter 5 to Chapter 8 of this report are focused on the corrosion properties of the parts and coatings fabricated using the laser powder bed fusion based AM method or laser surface processing method, including a comprehensive review. Laser powder bed fusion based AM was used to prepare copper alloy, titanium alloy and stainless steel AM parts and laser surface modification was performed on Fe-14Cr alloy.

The application of nickel superalloys is well known in various industries. Chapter 3, Chapter 9, Chapter 10 are a part of a DOE funded project which has the final goal of producing Inconel 939 based superalloy parts with additive manufacturing method. The first step was to modify its composition to reach a better fatigue behavior (Chapter 9) with the help of phase composition and antiphase boundary energy associated with each phase. Since the lack of information about the hot corrosion properties of the newly designed alloys, the last chapter has been dedicated to evaluate Inconel 939 corrosion performance at elevated temperatures.

Chapter 1. Introduction

Thanks to the distinguished properties of laser beams, such as high intensity and little divergence, laser based additive manufacturing and surface modification has gained increasing interests in recent years. Laser based manufacturing and surface modifications can be applied to produce unique and complex shaped parts or improve wear behaviors, biocompatibility, and corrosion performance. Years of technology advancements in this area have resulted in an ascending usage of the laser based technique, compared to other conventional manufacturing and surface modification processes.

Additive manufacturing (AM) has the ability to produce complex shaped parts. Small tolerances and automated process are the additional advantages of this technique, in comparison to other conventional manufacturing methods like machining, welding, forging, and casting (Manfredi, Calignano et al. 2014, Gao, Zhang et al. 2015). Laser-based powder bed fusion process is a laser AM method, which promises increased economy and speed when production volumes and batch sizes are small. Using fine metal/alloy powders (10 to 45 μm in diameter), laser-based powder bed fusion process can produce complex shaped components that cannot be easily produced by conventional methods. Employing a high power laser source, laser-based powder bed fusion process makes 3D metal/alloy parts layer by layer to form a 3D structure based on a computer aided design (CAD) design (Pham and Dimov 2001, Zhang, Liu et al. 2007, Akinlabi, Mahamood et al. 2016, Herzog, Seyda et al. 2016). This technique has been used to build physical models, prototypes, tooling components, and functional parts with complex shapes (Yasa and Kruth 2011, Zhong, Liu et al. 2016). Laser-powder-bed-fusion based additive manufacturing (LPBF-AM) is a popular metal additive manufacturing method, which uses a focused laser beam to melt and fuse metallic powders to form complex shaped parts with near full-density (Gu,

Meiners et al. 2012). Due to the small size of the laser melt pool and high cooling rate, LPBF-AM parts possess characteristic phases and/or microstructures that are different from those formed in traditional processes, such as wrought and cast (Gu, Meiners et al. 2012, Yap, Chua et al. 2015). Although LPBF-AM parts provide the mentioned advantages compared to the other methods, high residual stress due to the repeated heating and rapid solidification is one of the drawbacks of this method (Mercelis and Kruth 2006). As a remedy, annealing process is almost inevitable after the manufacturing step (Montero Sistiaga, Nardone et al. 2016).

One of the studied LPBF-AM parts in this dissertation is made with alloy Cu-Sn. Cu-Sn alloys (tin-bronze) are used in a wide range of technological applications. For example, Cu-Sn (0~2 wt. % Sn) alloys are better chip interconnects than their Al-Cu counterparts due to the high activation energy for electromigration (Lee, Hu et al. 1995); Cu-10Sn alloy is suited for making bearings due to its excellent mechanical properties, high thermal conductivity, as well as good wear and corrosion resistance (Ünlü and Atik 2010). Traditional methods for fabricating Cu-Sn alloy parts, such as casting and mechanical alloying, have been extensively studied (Canakci, Varol et al. 2014, Chen, Wang et al. 2015). However, the properties of Cu-Sn alloy parts made by additive manufacturing are less well known. LPBF-AM has been used successfully to fabricate Cu-Sn alloy parts using Cu-4Sn alloy (Mao, Zhang et al. 2017), Cu-4.3Sn alloy (Ventura, Wade et al. 2017), Cu-10Sn alloy (Bhat, Balla et al. 2011, Scudino, Unterdörfer et al. 2015, Deng, Kang et al. 2018), and Cu-15Sn alloy (Mao, Zhang et al. 2018) powders. However, these Cu-Sn alloy AM studies mainly focused on microstructure characterizations and mechanical property evaluations.

Mao et al. (Mao, Zhang et al. 2017) claimed the successful fabrication of Cu-4Sn parts by LPBF method. They found that the density and hardness of the samples are mainly controlled by

laser power which optimized to be 93% for the theoretical density and 118 HV for the hardness. They reported a tensile strength of 316–320 MPa for the samples prior to perform a pressure processing on them. Ventura et al. (Ventura, Wade et al. 2017) produced Cu-4.3Sn alloy by LPBF method and heat treated the samples at 600 °C and 900 °C for 1 hour. Their studies via tensile testing and microstructure characterization on as-printed and heat treated samples show that after heat treatment process, the yield strength was lower along with a notable increase of the ductility which are the result of a lower dislocation density and the recrystallization process. The geometry of the samples and their surface finish also affects the mechanical properties, however, not as important as the heat treatment process. Scudino et al. (Scudino, Unterdörfer et al. 2015) compared the mechanical properties of Cu-10Sn alloy prepared by LPBF and cast alloy. They reported that the room temperature tensile strength jumped from 120-180 MPa for the cast samples to 220-420 MPa for LPBF samples along with the improvement in ductility from 7 to 17% which can be ascribed to the high cooling rate during LPBF process which leads to a more refined microstructure. Mao et al. (Mao, Zhang et al. 2018) optimized the printing parameters of Cu-15Sn alloy and studied the effect of heat treatment (500-700 °C for 4h) on the strengthening mechanism of the samples. They claimed that the annealing process transforms the strengthening mechanism from fine-grain to solid solution strengthening.

For applications using Cu-Sn alloys, corrosion performances are as important as the mechanical properties. Corrosion behavior of traditional cast Cu-Sn alloys with varying tin contents have been extensively studied (Touloukian, Powell et al. 1970, Chiavari, Colledan et al. 2006, Ingo, De Caro et al. 2006, Sidot, Souissi et al. 2006, Souissi, Sidot et al. 2007, Robbiola, Tran et al. 2008, Šatović, Žulj et al. 2009). Corrosion behaviors of Cu-Sn alloy parts manufactured with conventional methods are also well studied for different environments and Sn contents (Sidot,

Souissi et al. 2006, Souissi, Sidot et al. 2007, Drach, Tsukrov et al. 2013, Zohdy, Sadawy et al. 2014). Two types of surface layers can be formed on Cu-Sn alloys after immersion in a corrosive environment. Type I is called noble patina, which is mainly formed by copper oxide on the surface as a protective layer. Type II is called vile patina, which involves the formation of a copper chloride layer (Robbiola, Tran et al. 2008, Šatović, Žulj et al. 2009).

From the corrosion behavior point of view, stainless steels (SS) are a key type of industrial alloys (Sedriks 1996, Henry, Takadoum et al. 2009). Therefore, stainless steels AM parts are examined in this dissertation. The corrosion resistance of stainless steels is mainly attributed to the presence of at least 11 wt% of chromium, which forms a protective layer of chromium oxide. The characteristic of the SS316L protective layer can be found in open literatures (Kim and Young 2013). Stainless steels also have many other alloying elements such as nickel, molybdenum, copper, and aluminum that could affect the electrochemical behavior of SS parts under a variety of working environments, along with the mechanical properties and phase stabilities (Davis 1994, Sedriks 1996). Among numerous types of SS, AISI316L is used extensively in different industries, such as pharmaceutical, petrochemical, offshore drilling, marine shipping, water desalination, etc. (Alves, Stenner et al. 2006). AISI316L SS is an austenitic stainless steel, which provides a good resistance to the chlorine attacks in marine environments (Jun, Zhang et al. 2014).

It has been reported (Barkia, Aubry et al. 2020) that AM AISI316L parts can be used as a structural material without any post treatment due to both higher ductility and yield strength compared to conventional AISI316L parts. On the other hand, Blinn et al. (Blinn, Krebs et al. 2020) believe that considering the highly inhomogeneous distribution of residual stresses in AM parts, a stress relieving post treatment is inevitable. They showed that a post heat treatment process can increase the fatigue life of AISI316L AM parts by an improved defect tolerance. The tensile

properties of AM AISI316L has been reported by Li et al (Li, Voisin et al. 2019). They could fabricate samples with the density up to 98.8% using optimized laser parameters, however, the microstructure were highly heterogeneous. They claimed that the large variation in mechanical properties of different samples is due to their sensitivity to sample geometry and built-in flaws. Ashouri et al. (Ashouri, Voshage et al. 2020) varied the processing parameter of LPBF AM process and reported their influence of the mechanical strength of the samples under Static bending and cyclic axial loading.

Despite the numerous works on determining the mechanical and corrosion behavior of AISI316L, the studies on the corrosion behaviors of laser AM parts are still limited. For laser-based powder bed fusion related corrosion studies, the effect of changing printing parameters to the resulting corrosion performance, the localized corrosion behaviors, and the passive layer formation are interesting research topics (Sun, Moroz et al. 2014, Ziętala, Durejko et al. 2016, Sander, Thomas et al. 2017). In addition, the evaluation of the effect of heat treatment is mainly focused on the mechanical properties in the previous works (Tolosa, Garciandía et al. 2010, Yasa and Kruth 2011, Montero Sistiaga, Nardone et al. 2016). The corrosion performance of additively manufactured stainless steel will be reviewed comprehensively in Chapter 2.

Titanium and its alloys have been widely employed in different industries such as aerospace, biomedical, marine, and automotive due to their excellent properties such as high strength, good fracture toughness, low density, and high corrosion resistance (Donachie 2000, Tamilselvi, Raman et al. 2006, Banerjee and Williams 2013, Dai, Zhang et al. 2016, Lin, Lv et al. 2017). The most commonly used titanium alloy, Ti-6Al-4V, has a low Young's modulus (~120 GPa) compared to its counterparts such as stainless steel (~200 GPa) and excellent corrosion resistance (Luo, Yang et al. 2013, Zhang, Wei et al. 2014). The formation of a protective dense

oxide surface layer being the primary reason for the outstanding corrosion behavior of titanium alloys (Marino, de Oliveira et al. 2001, Chen and Tsai 2011).

According to previous work (Huang, Hu et al. 2016, Barriobero-Vila, Gussone et al. 2017), the microstructure of Ti-6Al-4V alloy produced by the LPBF process method consists of a non-equilibrium phase called α′ in contrast with the equilibrium phases of α and β. In other words, the rapid solidification during the production of AM parts leads to the formation of an undesirable highly strained phase, as well as deteriorating mechanical characteristics of the parts (Yang, Yu et al. 2016). In order to overcome these issues, heat treatment is typically adopted before the final application of the manufactured parts. Several studies have been conducted to investigate the effect of post heat treatment through the examinations of kinetics (Malinov, Guo et al. 2001, Stefansson, Semiatin et al. 2002, Semiatin, Stefansson et al. 2005), phase morphology (Gil, Ginebra et al. 2001, Katzarov, Malinov et al. 2002, Semiatin, Knisley et al. 2003), microstructure, and mechanical properties (Wang, Wu et al. 2016, Yang, Yu et al. 2016, Bilgin, Esen et al. 2017). Bilgin et al. (Bilgin, Esen et al. 2017) studied the effect of post heat treatment of AM Ti-6Al-4V AM parts on the ductility and hardness of the parts. They found that a post heat treatment results the transformation of non-equilibrium α′-martensitic phase to equilibrium α and β-phases along with a relief of residual stress. This phase transformation is necessary to improve the ductility of AM parts without losing too much strength. Wang et al. also reported the formation of non-equilibrium phases during AM process due to the fast solidification rate and a heat treatment process is unavoidable to tailor the mechanical properties of the printed parts in a way to meet the industrial demand for Ti–6Al–4V alloy (Wang, Wu et al. 2016). Leuders et al. (Leuders, Thöne et al. 2013) heat treated the AM parts at 800 °C for 2 h and reported that the this post tratements reduced the

residual stress of the as-printed part from 200 MPa to about 5 MPa for heat treated samples and this decrease improves the fatigue behavior by a factor of four.

However, there is still a lack of studies focusing on the corrosion evaluation of Ti-6Al-4V parts made by AM methods. In this dissertation, I studied the corrosion behavior of AM Ti-6Al-4V alloy samples before and after heat treatment processes. It has been reported that annealing below 550°C or above 1000°C produces some negative effects such as age hardening and excessive grain growth (Pujadó 2012), hence, two temperatures, 600°C and 800°C, were selected as the post heat treatment temperature conditions. Polarization curves and Electrochemical Impedance Spectroscopy (EIS) were applied to compare the corrosion rate of the heat treated AM samples with wrought commercially available samples to evaluate the effect on the corrosion parameters. In addition, XRD, microstructure analysis and CALPHAD calculations were applied to evaluate the formed phases and describe the causal relationships after the heat treatment process.

Chapter 5 to Chapter 7, contain an evaluation on corrosion behavior of three different additively manufactured alloys, namely copper ally (Cu-10Sn), stainless steel (AISI316L), and titanium alloy (Ti-6Al-4V). Cu-10Sn (wt. %) alloy specimens were prepared by laser-based powder bed fusion additive manufacturing (LPBF-AM). The corrosion properties of LPBF-AM Cu-10Sn specimens were investigated under both as-fabricated (AF) and vacuum annealed (VA) conditions, at 600ºC and 800ºC. The corrosion rate of the AF specimens is found to be almost two times higher than that of the VA specimens due to the differences in passive layer, intergranular corrosion, and internal galvanic corrosion. For AISI316L, both LPBF-AM and conventional stainless steel 316L samples were examined in NaCl 3.5% solution before and after the annealing process using Tafel curves, Electrochemical Impedance Spectroscopy, and X-ray diffraction. The results indicate that the AM parts have an improved corrosion behavior than the conventional

wrought samples. Besides, the heat treatment process is found to further decrease the corrosion rate of the AM parts through the relieving of the residual stress. In contrast, the post annealing induced improvement to corrosion resistance for the wrought samples is due to the elimination of martensite phase which almost always exists after the plastic deformation during their production process. For Ti alloy, the corrosion behavior of Ti-6Al-4V alloy parts produced by LPBF-AM was evaluated. The effect of post annealing heat treatment on the corrosion resistance of AM parts is studied by comparing the heat treated samples with cold rolled commercial titanium alloy samples. The results obtained via corrosion tests show that the corrosion rate of as-fabricated AM parts is almost sixteen times worse than the commercial grade samples. The accelerated rate was due to the presence of non-equilibrium phases and can be ameliorated by a proper post heat treatment process at 800°C for 2 hours. The proposed heat treatment makes the corrosion behavior of AM parts comparable to the commercial grade samples, due to the stress relief of the martensitic phase and formation of BCC phase of β Ti-6Al-4V which has a higher corrosion resistance. CALculation of PHAse Diagrams (CALPHAD) method was used to identify the equilibrium phases.

Since the first introduction of Oxide Dispersion Strengthened (ODS) alloys several decades ago, ODS alloys have found applications in many industrial sections (Oksiuta, Hosemann et al. 2014, Chen 2018, Kim, Kim et al. 2019). To disperse nano-sized oxide particles into the alloy matrix, various fabrication methods can be used, including selective laser melting (Walker, Berggreen et al. 2009), mechanical alloying (MA) (Liu, Wang et al. 2015, Chen 2018), sol-immersion methods (Guo, Jia et al. 2010), and internal oxidation (Schneibel and Shim 2008). Among these techniques, MA, coupled with hot isostatic pressing (HIP) or hot extrusion based consolidation process (De Castro, Marquis et al. 2011, Frelek-Kozak, Kurpaska et al. 2018), is the most widely used method to produce bulk ODS alloys. Spark plasma sintering (SPS) is a

comparatively new technique which has been utilized recently for the consolidation of powder mixtures. In this method, rapid consolidation takes place under a very high heating rate with pulsed electrical current. The rapid process will not only maintain the basic properties/microstructures of the initial powders, but also improve the mechanical properties of the consolidated parts (Suárez, Fernández et al. 2013). Recently, SPS has been successfully applied to consolidate ODS steels (Li, Lu et al. 2016, Frelek-Kozak, Kurpaska et al. 2018). Typically, low voltage (<10 V) but high current (1000–5000 A) DC pulses are applied to alloy powders contained in a graphite mold, along with a uniaxial pressure (up to 100 MPa). After reaching the target temperature, the sample is typically held isothermally for 3 to 20 min; and then followed by rapid cooling (Auger, Huang et al. 2018).

Fe-14Cr ODS steel is a potential candidate for applications such as nuclear reactors, combustion parts for engines, and stirrers for the glass industry due to its unique properties at elevated temperatures and supercritical environments (Li, Chu et al. 2019, Vasquez, Giroux et al. 2019). Due to the moderate Cr content, the corrosion resistance of Fe-14Cr ODS is worse than high Cr content steels. Coatings are typically applied to improve the corrosion resistance (Kim, Kim et al. 2019, Li, Chu et al. 2019) of steels.

Thanks to the distinguished properties of laser beams, such as high intensity and little divergence, laser surface modification has gained increasing interests in recent years. Laser based surface modifications can be applied to improve wear behaviors, biocompatibility, and corrosion performance (Ettefagh and Guo 2018, Asl, Ganjali et al. 2019, Ettefagh, Zeng et al. 2019, Moradi, Ghorbani et al. 2019, Park, Sim et al. 2019). Common laser based alloy surface treatment techniques include laser alloying, laser cladding, laser peening, laser hardening, and surface laser scanning (Volovitch, Masse et al. 2008, Abedi, Salehi et al. 2010, Majumdar and Manna 2010,

Ma, Peng et al. 2018, Ardila-Rodríguez, Menezes et al. 2019, Moradi, Ghorbani et al. 2019), among others. In Chapter 8, the optimization of laser surface treatment on Fe-14Cr samples was performed, with the goal of improving the corrosion resistance of Fe-14Cr ODS steel. To speed up the laser optimization process, a two-stage searching process was adopted to effectively identify the optimum laser processing parameters, which can lead to the formation of a uniform surface oxide coating on Fe-14Cr ferritic alloy. Laser source parameters including laser power, scanning speed, and hatching space were manipulated to produce the most uniform protective layer on the alloy surface. In the first stage, the optimized laser energy density was identified; and in the second stage, the optimization of the laser power/speed combinations was performed. Optimum values were obtained based on the uniformity of the formed surface scale and corrosion behavior of the processed surfaces. Applying two best sets of these parameters, two samples were treated with a single pass of laser scanning and two others were treated with an additional pass of laser scan, with laser scanning tracks at 90 degrees of angle to the first layer of scan. The corrosion properties of these laser processed samples were compared with the sample without surface treatment. The protective nature of the formed surface layer was characterized using Raman spectroscopy and X-Ray diffraction (XRD) techniques. The optimum laser processing parameters were found to be 175 w of laser power, 200 mm/s of scanning speed, and 0.025 mm of hatching space. Corrosion behavior of laser-treated samples with the optimum laser parameters was found to be 5 and 13 times better respectively than the baseline sample in 3.5 wt% NaCl water solution, in term of corrosion rate. The formation of a uniform thin oxidation layer was the main reason for the improved corrosion performance.

Ni-base superalloys generally have excellent high-temperature strength, creep rupture resistance and corrosion resistance, and have been widely adopted in key components within the

mid to high temperature regions of gas-turbine engines. These alloys typically comprise a γ (FCC) matrix phase, strengthened by either γ′ (A_3B type of an ordered L12 structure, e.g. Ni_3Al) or γ″ (an ordered body-centered tetragonal) coherent precipitates. The γ-γ′-γ″ alloys generally offer better mechanical strengths over the γ-γ′ alloys due to the additional strengthening effects offered by the lattice distortions surrounding the coherent γ″ phase (a mismatch of ~3%) (Oblak, Duvall et al. 1974, Bowman 1988, Field, Pollockf et al. 1992). However, the γ″ phase is unstable under temperatures above 650 °C and decomposes to a δ (orthorhombic DO_a) phase, which deteriorates the overall strength of the three-phase alloys (Sundararaman, Mukhopadhyay et al. 1988, Slama and Abdellaoui 2000, Mignanelli, Jones et al. 2017). As a result, the γ-γ′ alloys are the focus of the present research.

CALPHAD Stands for CALculation of PHAse Diagrams and is a methodology introduced in the previous century by Larry Kaufman. Based on the results of this method, the regions where phases are stable, or regions where two or more of them coexist can be recognized on an equilibrium phase diagram with temperature and composition of a chemical system (Saunders and Miodownik 1998, Kaufman and Ågren 2014). The aim of this method is to predict the state of a system under different conditions and a graphical demonstration for the experimental information on states of equilibrium in complex systems. Several commercial products on the market can be applied for this purpose including FactSage, MTDATA, PANDAT, MatCalc, JMatPro, and Thermo-Calc. The later one was used in this project.

In Chapter 9, a short study on the alloy design of a nickel superalloy has been presented. Mechanical and fatigue performance of γ-γ′ Ni-base superalloys are strongly affected by the antiphase boundary energy (APBE) of the γ′ precipitates which, in turn, is dictated by the alloy's composition. Due to the multicomponent character of these alloys, establishing composition-

APBE relationships are challenging, even though the qualitative effect of individual solutes on the APBE may be known. The aim of this part of the study was to obtain the stability range of γ′ phase in Inconel 939 with CALPHAD software. The results were then fed to the other research team to calculate the APBE energy of this phase and its impact on the fatigue life.

Nickel-based superalloys have a wide application in a vast range of industries such as petrochemical, aerospace industries and gas turbines due to their reportedly excellent high-temperature corrosion, oxidation resistance and creep-rupture strength (McLean and Sciences 1995, Eliaz, Shemesh et al. 2002). Regarding the working environments and its oxygen, sulfur, carbon, and chlorine content, the surface of the parts is subjected to corrosive compounds like metallic chlorides and sulfates which results in a hot corrosion attack on the surface and reduction of the lifetime due to degradation of the critical properties. NaCl is usually present in the air and forms other salts such as Na_2SO_4 and $NaVO_3$ as a result of the reaction with fuel impurities (Yoshiba 1993, Zheng, Schmitz et al. 2012). Two types of hot corrosion have been identified based on the temperature of the environment. High-temperature hot corrosion (HTHC) occurs in the range of 800–950 ◦C and it is related to the interaction of the molten salts with the surface. Low-temperature hot corrosion (LTHC) is known as Type-II with the temperature range of 600–800 ◦C and LTHC pitting has been reported due to the reaction of the surface with molten eutectic salts (Eliaz, Shemesh et al. 2002, Mahobia, Paulose et al. 2013, Salehnasab, Poursaeidi et al. 2016).

Several studies have been dedicated to propose the hot corrosion mechanism of nickel-based superalloys (Gurrappa and technology 2003, Gonzalez-Rodriguez, Haro et al. 2006, Sidhu, Prakash et al. 2006, Babu, Kiruba et al. 2019). It is well known that chromium content is the critical factor for providing hot corrosion resistance by forming Cr_2O_3 at high temperature and other alloying elements such as aluminum, titanium, tungsten, and molybdenum which are added to

improve the mechanical properties may affect the mechanism (Pettit, Meier et al. 1984, Kamal, Jayaganthan et al. 2010). The corrosion rate is associated with the inward diffusion of oxygen along with the diffusion of substrate elements in the opposite direction (Liu, Ma et al. 2010). This concept will be elaborated in detail in Chapter 3.

Inconel 939 has γ solid-solution matrix with γ′ precipitates which are essential for the mechanical properties. Al and Ti are known to be γ′ formers whereas Mo, Nb, and W improve the mechanical properties over solid solution hardening (Jahangiri, Arabi et al. 2012, Zhu, Wise et al. 2013). This superalloy has gained a lot of attention for a wide range of applications in industrial gas turbines because of the limitations of other Inconel alloys at higher temperatures due to the coarsening of the γ" precipitation (Sjöberg, Imamovic et al. 2004). However, there is a lack of enough studies about hot corrosion mechanism of this alloy. Consequently, in the last chapter, the hot corrosion behavior of Inconel 939 superalloy is assessed. The weight gain versus time of this superalloy in the mixture of $75Na_2SO_4{-}25NaCl$ (wt.%) at temperatures of 700 °C and 800 °C to simulate the actual working condition in the marine environment. Moreover, a detailed and comprehensive microstructural characterization using XRD, SEM, and EDS of the corrosion products were conducted systematically. Based on the obtained results, the plausible mechanism of the corrosion scales formation was proposed. Results indicated severe hot corrosion attack with increasing the temperature. A duplex microstructure corrosion layer was identified including Cr-depletion zone close to the inner layer at 800°C. Main corrosion products have been identified based on the results of corrosion tests, XRD and microstructure analysis. At 700°C, considering the domination of diffusive reactions, the corrosion layer was a single protective one mainly consists of chromium oxide. Some spallation of the corrosion products was observed at 800°C.

Chapter 2. Corrosion Performance of Additively Manufactured Stainless Steel Parts: A Review

Stainless steel (SS) alloys have significant uses in many industrial applications like aerospace, medical device, pipeline, automotive, and die and tool industries, in the form of austenitic, martensitic, ferritic, or austenoferritic (duplex) (Sedriks 1996, Alam, Mehdi et al. 2020). These categories are based on the microstructures of SS which are dictated by the chemical composition of the alloy and the manufacturing process (Olsson and Landolt 2003, Sander, Thomas et al. 2017, Alam, Mehdi et al. 2020). The addition of elements such as chromium, nickel, carbon, molybdenum, copper, nitrogen, aluminum, sulfur, and selenium can modify the corrosion resistance, strength, ductility, machinability, and the stability of phases in SS alloys (Davis 1994, Sedriks 1996, Al-Amr 2005).

Different classes of SS such as precipitation hardening stainless steels (Murr, Martinez et al. 2012), tool steels (Mazumder, Choi et al. 1997), austenitic stainless steels (Carlton, Haboub et al. 2016), and maraging steels (Casalino, Campanelli et al. 2015) are frequently used in additive manufacturing (AM). Besides the general applications, SS can also be utilized for high hardness and strength purposes (Ngo, Kashani et al. 2018) due to its relatively high strength, low density, and outstanding corrosion performance. The main focus of this review chapter is the corrosion resistance of SS, which is primarily attributed to the formation of a protective Cr_2O_3 passive film on the surface. This is possible when the chromium content is about 11 wt% or more (Davis 1994, Sedriks 1996, Al-Amr 2005).

This chapter was previously published as Ali Hemmasian Ettefagh, Shengmin Guo, and Jonathan Raush, "Corrosion performance of additively manufactured stainless steel parts: A review" Additive Manufacturing, (2020): 101689. Reprinted by permission of Elsevier.

Many types of SS have been additively manufactured and their mechanical or corrosion behaviors have been studied, Figure 2-1-left. The chemical compositions of these alloys are presented in Table 2-1. The most studied SS alloy, 316L, is an austenitic alloy widely used in industrial applications due to its high corrosion resistance along with acceptable mechanical properties (Sedriks 1996, Cruz, Chao et al. 2020). Formation of a thin protective layer on the surface and the presence of molybdenum in its chemical composition are known to be the reason for its better performance against both general and localized corrosion attacks relative to other grades of austenitic SS such as 304 and 304 L (Sedriks 1996, Fredriksson, Petrini et al. 2013, Biehler, Hoche et al. 2014, Bevan, Ameri et al. 2017). In addition, the low carbon content of this alloy is beneficial for the welding process by decreasing carbide precipitation at grain boundaries (Washko and Aggen 1990). Hence, 316 L is one of the few choices for the marine, medical and food industries where excellent anti-corrosion properties are needed (Geenen, Röttger et al. 2017). AISI 420 is a martensitic SS, whose properties can be tailored by the heat treatment process (Isfahany, Saghafian et al. 2011, Alam, Mehdi et al. 2020). Considering its good tensile strength, high hardness, and reasonable corrosion resistance, AISI 420 is also commonly used in industry. The final properties of this alloy are a function of the processing parameters. An anisotropic 3D structure has been noted for AM AISI 420 parts due to repeated heating and solidification cycles in melting-based AM processes (Popovich, Sufiiarov et al. 2017, Kok, Tan et al. 2018). Under the pre-hardened and tempered condition, a tensile strength of 700–930 MPa is reported (Brnic, Turkalj et al. 2011). Precipitation hardening (PH) SSs such as 17-4 PH, have recently gained interest in aerospace, nuclear, and marine applications for AM due to their duplex microstructure of combined martensite and austenite (Hunt, Derguti et al. 2014, Yadollahi, Shamsaei et al. 2017). The tensile and impact strength, fracture toughness and corrosion resistance of those martensitic

precipitation hardened SSs have been studied for high service temperatures up to 300 °C (Wu and Lin 2002, Lin, Cao et al. 2012, Murr, Martinez et al. 2012). Another group of steels that has been evaluated for AM is High Strength Low Alloy Steels (HSLA) like AISI 4135 which, although often not categorized as SS, nevertheless has a wide range of applications despite their relatively poor corrosion performance (Craig 1982, Huang, Yu et al. 2017). However, it has been shown that adjusting the nickel content as an austenite forming element in the feedstock powder of the AM process can improve the corrosion resistance by affecting the microstructure of the alloy (Zhang, Zhang et al. 2018).

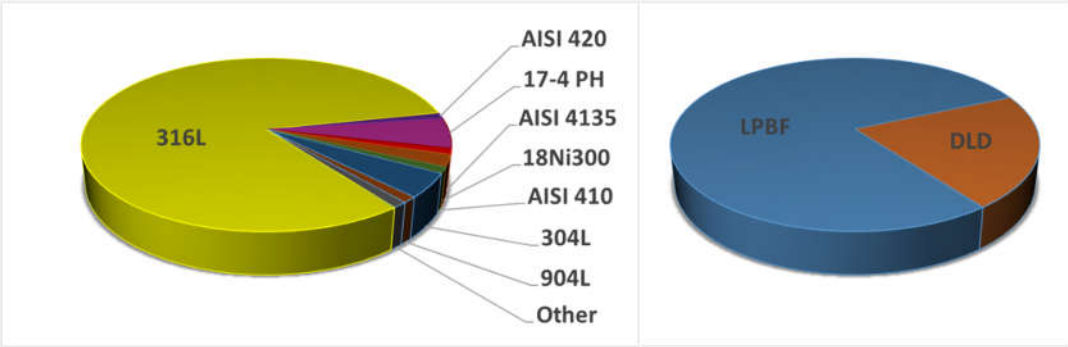

Figure 2-1. (left) Relative emphasis on types of AM SSs, (right) Relative emphasis on applied AM methods for SSs. The data were collected from over 300 research papers cited by this chapter.

2.1. Additive manufacturing process

With the capability of producing near net shape and complex parts, additive manufacturing, also known as 3D printing, has found a growing demand in a wide range of industries and research topics (Eyers and Potter 2017, Kocovic 2017, Zeng, Zhang et al. 2020). The minimum waste of raw materials and rapid production of unique parts in small quantities are major benefits of AM (Ziętala, Durejko et al. 2016, Sander, Tan et al. 2018). In terms of corrosion performance, traditional methods may cause intergranular corrosion in SSs (García, Martín et al. 2007) and this is another reason for the rapid development of advanced technologies like AM. Metal AM is

categorized into two main groups: the first group is known as powder bed fusion which itself includes two methods, laser powder bed fusion (LPBF) and electron beam melting (EBM). Direct laser deposition (DLD) is the second group of common metal AM processes (Lewandowski and Seifi 2016, Yusuf and Gao 2017). Among these methods, LPBF and DLD are widely used for SS AM (Figure 2-1-right) and will be discussed in detail.

Table 2-1. Chemical compositions of SSs (commonly processable by AM) in % wt

Alloy	Cr	Ni	Mo	Mn	Si	P	C	S	W
	16.13-18.74	10.0-13.6	2.0-2.8	<2.3	<1	<0.12	<0.03	<0.03	<0.04
316 L	**O**	**Nb**	**Ti**	**Al**	**Cu**	**N**	**V**	**Co**	**Fe**
	<0.05	<0.01	<0.01	<0.01	<0.20	<0.15	<0.05	<0.13	Bal.
	Cr	**Ni**	**Mo**	**Mn**	**Si**	**P**			
	12.26-12.30	<0.17	<0.03	1.1-1.2	0.11-0.50	0.015-0.023			
AISI 420	**C**	**S**	**V**	**Co**	**Fe**				
	0.23-0.26	0.009-0.108	<0.04	<0.02	Bal.				
	Cr	**Ni**	**Mo**	**Mn**	**Co**	**Nb**	**Si**		
	17.60-19.21	8.73-10.74	<0.042	1.06-1.60	<0.03	<0.05	<0.57		
304 L	**P**	**C**	**S**	**O**	**N**	**Fe**			
	0.005-0.010	<0.015	0.003-0.02	0.017-0.038	<0.011	Bal.			
	Cr	**Ni**	**Mo**	**Mn**	**Si**				
AISI	16.5	1.7	1	<0.5	1.15				
4136	**Si**	**C**	**B**	**Fe**					
	1.15	<0.18	1.25	Bal.					
	Cr	**Ni**	**Mo**	**Mn**	**Si**	**P**	**C**		
	15.19-16.02	4.12-4.54	0.025-0.230	0.22-0.53	0.17-0.33	0.013-0.022	0.017-0.047		
17-4 PH	**S**	**Ta**	**Nb**	**Cu**	**N**	**O**	**Fe**		
	<0.002	<0.001	0.23-0.29	3.21-3.95	0.023-0.036	0.014-0.068	Bal		

LPBF, also known as selective laser melting (SLM), is the most widely applied method for the production of SS via AM due to relatively wide raw powder availability, remarkable flexibility in design, as well as cost and time savings (Yusuf and Gao 2017). The final part is produced layer-by-layer with computer-aided design (CAD) based control (Ettefagh, Zeng et al. 2019, Yusuf, Chen et al. 2020). A focused laser beam (typically from a fiber laser doped with rare-earth elements) is utilized to selectively melt and fuse the successive layers until completing fabrication of a near-net-shape object, as shown schematically in Figure 2-2-left (Akinlabi, Mahamood et al. 2016, Herzog, Seyda et al. 2016). Compared to traditional manufacturing methods, extreme local heating (up to 2500°C), higher cooling rates (10^5–10^7 K/s), and re-melting of previous layers results in a novel microstructure of LPBF parts containing non-equilibrium phases with a large range of compositions, inclusions, and residual stress (Gu, Meiners et al. 2012, Sun, Tan et al. 2016, Sun, Brandt et al. 2017). This condition also induces un-melted powder, porosities, the formation of dislocation cells, micro-cracks, and rough surfaces (Santos, Shiomi et al. 2006, DebRoy, Wei et al. 2018, Kong, Dong et al. 2019). These metallurgical defects, along with the molten pool boundaries, can eventually lead to a sharp drop in plasticity and act as the preferred sites for localized corrosion (Ganesh, Giri et al. 2012, Shifeng, Shuai et al. 2014, Kong, Ni et al. 2018). Therefore, the quality of LPBF parts is the foremost challenge for using AM parts in various industries. It is acknowledged that process parameters including laser power, hatch spacing, scanning speed, layer thickness, and build direction dictate the final microstructure and service performance of the produced parts (Gu, Meiners et al. 2012, Li, Ramezani et al. 2018). Moreover, a post-heat treatment process may be applied to reduce the mentioned defects and improve the service performance of the part as a result (Kong, Ni et al. 2018).

DLD is another additive manufacturing technology that is used to fabricate SS parts by a simultaneous supply of raw materials and energy to the build surface (Figure 2-2-right) (Wang, Felicelli et al. 2008, Mahamood and Akinlabi 2017, Zhang, Zhang et al. 2017). It is also known by many other names such as laser engineered net shaping (LENS), direct laser fabrication (DLF), direct metal deposition (DMD), direct light fabrication (DLF), laser metal deposition (LMD), laser deposition welding (LDW), powder fusion welding (PFW), laser powder deposition (LPD), direct energy deposition (DED), direct laser metal deposition (DLMD), or in some cases, the general title of "laser cladding" (Wang, Felicelli et al. 2008, Gu, Meiners et al. 2012, Wong and Hernandez 2012, Ziętala, Durejko et al. 2016, Ghosal, Majumder et al. 2018, Alam, Mehdi et al. 2020). In this method, raw metal is fed to the device in the form of powder or wire and a laser source melts the feedstock and fabricates a near-net-shape part layer-by-layer based on a CAD design (Santos, Shiomi et al. 2006, Wang, Felicelli et al. 2008). There is a precise control of the powder feed, laser power and other parameters in this method, and therefore, DLD can use a broad spectrum of raw materials. Several research papers are available showing a huge improvement in tensile and fatigue strength of DLD SS compared to the parts produced by traditional methods (Keicher 2001, Yadollahi, Shamsaei et al. 2015). DLD can also be applied in surface engineering and additive repairing by tailoring the surface properties and/or composition based on their applications (Toyserkani, Khajepour et al. 2004, Pinkerton, Wang et al. 2008). Cooling rate is a function of processing parameters and, based on experimental measurements, is estimated to be in the range of 10^3–10^5 K/s in DLD processes, which, when compared to LPBF, results in a coarser microstructure along with the possibility of more residual ferrite and a higher porosity level in the as-fabricated parts. These are important factors in functional properties and specifically, the corrosion behavior of the part (Lewandowski and Seifi 2016, Ma, Wang et al. 2017, Yusuf, Nie et

al. 2018, Melia, Nguyen et al. 2019). Compared to LPBF, DLD employs a relatively higher energy density and for this reason and due to a larger melting pool, the cooling rate during DLD is significantly lower, but DLD solidification rates are still much faster than traditional casting methods (Suzuki, Yamaguchi et al. 2001, Kong, Dong et al. 2019, Shao, Yu et al. 2019).

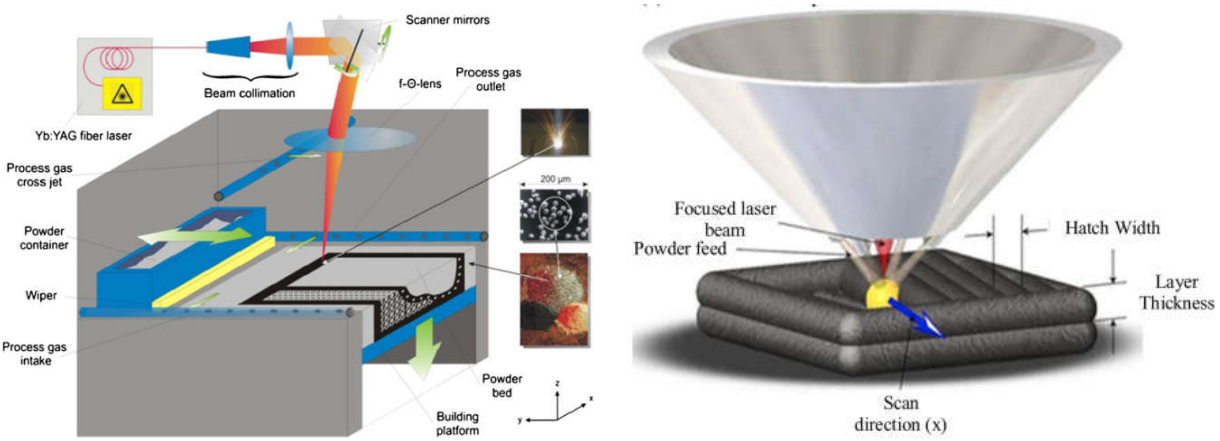

Figure 2-2. Schematic view of (left) LPBF (Tolosa, Garciandía et al. 2010), and (right) DLD AM methods (Melia, Nguyen et al. 2019).

2.2. Special applications of AM SS

The general application of AM SS parts is growing rapidly in industries such as aerospace, automotive, and marine based on the discussed advantages of this manufacturing method. For instance, many parts of a jet engine can be manufactured by AM in weeks as opposed to several months for traditional methods (Han 2017, Kellner 2017). AM SS parts have been progressively used for some special environments that will be elaborated upon in this section with the focus on their corrosion performance. For these applications, the solution used for corrosion tests is different from the general application where a mixture of various concentrations of NaCl and water is used to simulate the working environment of the part ((Sun, Moroz et al. 2014, Schaller, Taylor et al. 2017, Ni, Kong et al. 2018, Laleh, Hughes et al. 2020) to name a few). In all of these applications, AM is becoming increasingly popular by the day.

2.2.1. Bio Applications

Due to its possessing excellent corrosion resistance with good mechanical properties, availability and reasonable cost, the application of SS, and specifically 316 L SS, has grown greatly for medical implants (Roland, Retraint et al. 2006, Arifvianto, Mahardika et al. 2011, Trelewicz, Halada et al. 2016, Man, Dong et al. 2019). These applications include orthopedic bone fixation devices, orthodontic wires, plates and screws used in craniofacial applications, orthopedics for joint replacement and fracture repair, cardiovascular implants (stents, artificial valves), coronary and pulmonary stents, hip prosthesis, and artificial eardrums (Hermawan, Ramdan et al. 2011, Manam, Harun et al. 2017, Lodhi, Deen et al. 2019). Electrochemical reactions of these parts inside the human body cause corrosion of the part. Corrosion in bio applications is an important issue, as it not only affects the lifetime and structural stability of the part itself but also causes inflammatory and anaphylactic reactions (Kamachimudali, Sridhar et al. 2003, Asri, Harun et al. 2017, Wen, Zeng et al. 2019). For instance, the release of Mo, Cr, and Ni ions from stents that are made of SS 316 L can cause immune reactions and limited inflammation (Figure 2-3)(Manivasagam, Dhinasekaran et al. 2010). All of these may affect the implantee quality of life and any failure may lead to severe pain and probable post-surgical operations (Reclaru, Lerf et al. 2001, Li, Yin et al. 2014, Harun, Asri et al. 2018). For instance, Ni is one of the major alloying elements of 316 L SS. The release of Ni ions in the body results in severe inflammation in surrounding tissues and adverse cellular reactions due to its toxicity (Wataha, O'Dell et al. 2001, Li, Yin et al. 2014, Kong, Ni et al. 2018). It also has been reported that the use of wrought 316 L SS causes the formation of a cytotoxic constituent through a set of corrosion reactions (Shih, Shih et al. 2004). Generally, SSs are prone to localized corrosion that should be addressed in detail for bio applications. The

formation of MnS inclusions in SS creates some regions with depleted chromium and these sites act as the initiation point of localized corrosion as a consequence of the heterogeneous structure of the oxide film (Ryan, Williams et al. 2002, Williams, Kilburn et al. 2010). A statistical study showed that after fracture (42%), corrosion is the second leading root cause of implant failures by frequency (24%), and before a vicious cycle of releasing small metal particles along with the implants (14%) (Sailer, Philipp et al. 2009). Several approaches have been examined in order to increase the long-term stability of SS in the human body. Surface laser melting is proposed to selectively melt and dissolve MnS inclusions in the oxide surface followed by quenching to homogenize the protective layer (Carboni, Peyre et al. 2002, Zhang, Zou et al. 2006, Yao, Katona et al. 2018, Ettefagh, Wen et al. 2020, Zeng, Wen et al. 2020). Coating methods seem inefficient for this purpose considering the defective nature of coats and their mechanical instability (Eric Jones, Chen et al. 2014). Some researchers show that reinforcing the surface oxide by ion implantation can improve the corrosion resistance effectively, however, the high applied energy during this surface modification method worsens the surface topography which is also an important factor in implant failure (McCafferty 2001, Feng, Cai et al. 2012, Zhou, Zhang et al. 2014, Chaichi, Prasad et al. 2019). Although a study shows that the passive film formed on AM SSs for bio applications is more stable with better barrier characteristics and has an improved cell adherence ability compared to traditional counterparts (Lodhi, Deen et al. 2019), improving the corrosion performance of AM SS to be used in the bio environment is still challenging and needs more research.

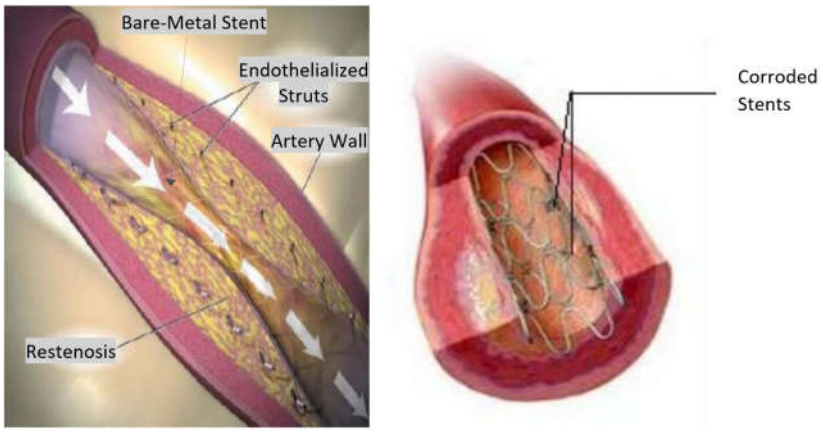

Figure 2-3. corrosion of stent made of SS 316 L (Manivasagam, Dhinasekaran et al. 2010).

2.2.2. Nuclear industries

SSs and in particular, 316 L, are extensively used in the nuclear industry to manufacture both inside and outside parts of reactor pressure vessels in a relatively reduced time, cost, and supply chain, even employed during the plant's planned refueling outage (Anderson 2015, Lou, Song et al. 2017, Ettefagh, Wen et al. 2018). The recent improvement in AM of 316 L SS results in the capability to produce near full density parts and this achievement has solved major concerns in using AM parts in nuclear facilities (Verlee, Dormal et al. 2012, Wu, Brown et al. 2014). In nuclear reactors, SS is in contact with high-temperature water with a temperature of roughly 290 °C (Lou, Andresen et al. 2018, Hanbury and Was 2019). At this critical condition, a duplex oxide layer can be formed on the surface (Stellwag 1998, Ehrnstén 2012). The outer layer mainly consists of either magnetite or hematite where the type of formed iron oxide depends on the electrochemical potential (Raiman, Bartels et al. 2017). The inner oxide layer is the chief protective layer that prevents further diffusion of cations from the bulk through the surface layer. This layer is made of spinel oxides of iron, nickel, and chromium where the higher the latter, the more protective the oxide layer (Terachi, Yamada et al. 2008). However, it is well known that stress corrosion cracking (SCC) is one of the major concerns of SSs in a nuclear plant, from their vulnerability to SCC while

in high-temperature water (Figure 2-4) (Han, Mei et al. 2016). The severity of SCC has been credited to the synergy of several parameters such as environmental chemistry, residual strain in the alloy, temperature, irradiation damage, surface condition, and electrochemical potential (Andresen and Briant 1989, Hong 2001, Andresen and Morra 2008, Andresen and Morra 2008, Turnbull, Mingard et al. 2011, Was, Ashida et al. 2011, Andresen 2013). Based on these factors, and due to its lower SCC properties, it is not recommended to use AM 316 L SS in critical conditions without performing a recrystallization process and/or hot isostatic pressing (HIP) to further increase the density of the AM part and modify the microstructure. A study shows that the crack growth rate of AM samples after HIP and recrystallization processes is one tenth of the as-received AM SS 316 L samples (Lou, Song et al. 2017). However, engineering judgment is required to find an optimized balance between time/cost savings and the quality of the product (Anderson 2015, Lou, Song et al. 2017). SCC of SSs in high-temperature water has gained more attention in recent decades after several incidents involving intergranular stress corrosion cracking in reactors (Stahle, Hochmann et al. 1979, Airey 1983). Two primary sources have been mentioned as the initiation sites for intergranular cracking: 1) the nucleation of chromium carbide in the grain boundaries along with the depletion of chromium in these regions as a result, and 2) increase in cracking susceptibility by the segregation of impurities such as nitrogen, sulfur, or phosphorus to the grain boundaries. Moreover, the presence of MnS inclusions are known to be responsible for transgranular cracking of SS in high-temperature water (Stahle, Hochmann et al. 1979, Andresen and Briant 1989). Additionally, extensive crack branching during SCC has been credited to the formation of Si-rich oxides along the grain boundaries. Therefore, controlling the amount of these elements either in the powder making process or AM build process is essential to reducing SCC susceptibility (Lou, Andresen et al. 2018).

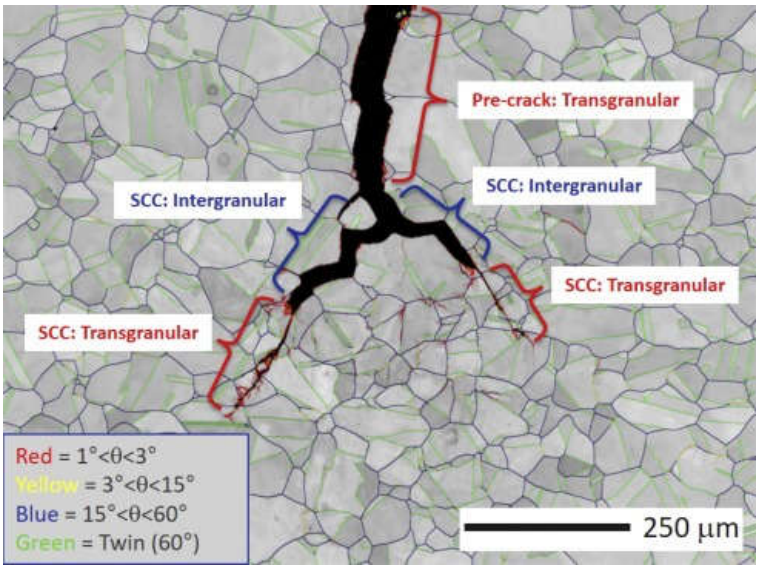

Figure 2-4. EBSD SCC map of AM SS 316 L tested in high temperature water (Lou, Song et al. 2017).

2.2.3. Bipolar plates in fuel cells

In a solid polymer fuel cell (SPFC) or a proton exchange membrane fuel cell (PEMFC), the bipolar plate serves several functions. The first role is to generate a flow field on the surface to provide reactant gases for the gas diffusion electrodes. Removing product water and making available a series electrical connection are other responsibilities of this multi-function component (Davies, Adcock et al. 2000). Currently, graphite is the most widely used material for this purpose despite its brittleness and lack of mechanical strength. Consequently, the plate needs to be thick enough to overcome these issues and this makes the cell bulky and heavy (Lee, Huang et al. 2004). To find an alternative material for this purpose, the minimum requirements should be addressed. An ideal bipolar material possesses excellent corrosion performance, high electrical and thermal conductivity, high manufacturability, is chemically inert, and is low density with high mechanical strength (Davies, Adcock et al. 2000, Lee, Huang et al. 2004, Karimi, Fraser et al. 2012). Austenitic stainless steels possess most of these requirements along with a lower cost and the possibility of mass production compared to graphite plate. In addition, the high strength of SS allows the

production of thin plates (Davies, Adcock et al. 2000, Kong, Ni et al. 2018). Therefore, SS are promising candidates for this application and several evaluations have been performed to assess their function as a bipolar plate.

From a corrosion point of view, it is stated that the degradation of bipolar plates is one of the key issues in the functionality of fuel cells that results in contamination of the system and decreases its conductivity. Two sources of corrosion attack have been mentioned in the literature: 1) the conducting membrane used in fuel cells is typically made from a perfluorinated sulfonic acid polymer which leaves the bipolar plate in a strong acid environment during its operation (Cho, Jeon et al. 2005), 2) the oxidation reaction on the anode anodizes hydrogen and generates protons ($2H2 \rightarrow 4H^{+}+4e^{-}$). Hydrogen ions react with the oxygen on the cathode to form water molecules after passing through the membrane and reaching the cathode ($O_2+4H^{+}+4e^{-} \rightarrow 2H_2O$). Due to the presence of hydrogen on the anode surface and the moisture of the membrane, severe acidic conditions occur around the bipolar plate (Lee, Huang et al. 2004). On the other hand, metal ions can poison the membrane of fuel cells (Lee, Huang et al. 2004, Cho, Jeon et al. 2005). All of these conditions show the importance of more corrosion-based research on using SS as an alternative material for bipolar plates, since the previous research does not provide satisfactory results (Bar-On, Kirchain et al. 2002, Wind, Späh et al. 2002, Cho, Jeon et al. 2005). The same path should be considered for AM SS for this application to assure the endurance of the part in service. For example, in the automotive industry, a fuel cell should last at least 3000-5000 hours in service without evidence of corrosion attack (Davies, Adcock et al. 2000).

2.2.4. Acidic media

Generally speaking, SSs are not recommended for highly acidic conditions, ascribed to the non-homogeneity (i.e. inclusions and chromium depleted zones) and instability of the passive film

layer in such media (Vignal, Krawiec et al. 2007, Wijesinghe and Blackwood 2007, Marcus, Maurice et al. 2008). These restraining parameters are more pronounced for AM parts and limit the application of AM SSs in acidic media. However, their performance in acidic conditions should be addressed since they might be exposed to low pH for some applications. For example, sulfur-oxidizing bacteria (SOB) may exist in the environment and produce sulfuric acid that causes microbial corrosion even in a non-acidic environment which is comparatively unpredictable and tremendously localized (Okabe, Odagiri et al. 2007). Breached pores and surface roughness of AM parts can increase such kinds of attacks by facilitating the metabolization of bacteria and consequently more by-produced sulfuric acid as a result. Another issue associated with AM SSs in a sulfuric acid environment is hydrogen embrittlement (HE) where hydrogen ions diffuse to the sample relatively easily to form brittle hydride and carbide participates (He, Han et al. 1997, Agyenim-Boateng, Huang et al. 2017, Miller, Martin et al. 2018). The severity of HE is known to be directly related to structural defects acting as trapping sites for hydrogen. Therefore, AM parts are more susceptible to HE than traditional parts due to a comparatively higher density of pores and dislocations, as well as residual stresses that facilitate the diffusion of hydrogen into the structure (Agyenim-Boateng, Huang et al. 2017, Silverstein and Eliezer 2018).

Several studies have been conducted on the corrosion performance of AM SSs in acidic media. In this research, the porosity of the part is the most prominent factor by serving as crevice zones and should be noted. It has been reported that the stagnation of electrolyte inside the pores changes its chemistry toward a lower pH by hydrogen evolution and de-passivation inside the pores (Itzhak and Aghion 1983, Otero, Pardo et al. 1995, Geenen, Röttger et al. 2017). In this condition, the outer areas act as cathodic sites along with severe anodic activities inside the pore, which leads to the initiation of corrosion attacks. Pores with all ranges of diameters expedite

corrosion attacks. However, smaller pores (<10 μm) have the capability of passive film formation, which lowers, but not eliminates, the risk of localized corrosion attacks (Otero, Pardo et al. 1998, Schaller, Taylor et al. 2017, Kong, Ni et al. 2018).

The grain size distribution of the AM part is another factor that is important in passive film formation and growth. To enhance the corrosion properties of AM SSs, grain refinement is one of the suggested processes to improve the growth of the passive layer in acidic media by decreasing the diffusion path length for chromium toward the surface to form a protective and homogeneous chromium oxide layer (Meng, Frankel et al. 2003, Lodhi, Deen et al. 2018). Severe plastic deformation (SPD), hydrostatic extrusion (HSE), and equal channel angular pressing (ECAP) are some of the reported methods to refine the grain size to sub-micrometer levels (Pisarek, Kędzierzawski et al. 2007, Zheng, Gao et al. 2012, Muley, Vidvans et al. 2016).

2.3. Passive film properties

Generally, the formation of a surface protective layer is known to be the reason for the extraordinary corrosion performance of SSs. Despite differences in reported compositions, several research papers confirm that the passive film of SSs consists of two layers of oxides and hydroxides of iron (III) and chromium (III) (Cheng, Zhao et al. 2013, Massoud, Maurice et al. 2013, Vignal, Krawiec et al. 2013). The majority of researchers believe that Fe can diffuse further outward since it has higher mobility compared to Cr, thus, the outer layer is mainly iron oxide and the inner layer is chromium oxide (Lorang, Belo et al. 1994, Freire, Carmezim et al. 2010). In some other papers, the duplex nature of the passive film is described as an outer layer of Cr hydroxide, and a mixture of Fe and Cr oxides as the inner layer enriched with Cr_2O_3 (Carmezim, Simoes et al. 2005, Fattah-Alhosseini, Golozar et al. 2010). Unlike chromium compounds, iron oxide is not considered as a protective layer and has a slight decreasing effect on surface corrosion reactions (Sun, Wu et al.

2009, Habib, Damra et al. 2011). Corrosion performance of SSs highly depends on the growth and stability of a passive film which is a function of several parameters such as corrosive media, alloy composition, microstructure, etc. (Fattah-Alhosseini, Golozar et al. 2010). For instance, in solutions with higher pH values, the formed passive layer is thicker and more stable due to the higher stability of iron oxide (outer layer) in alkaline solutions (Figure 2-5). Quite the opposite, the inner chromium oxide layer is more resistive in acidic solutions where the passive film might be just a monolayer of chromium compounds at very low pH, which is identical for both AM samples and their conventional counterparts (Carmezim, Simoes et al. 2005, Lodhi, Deen et al. 2018). On another note, defects and inclusions in the passive film trigger localized corrosion attacks through several mechanisms like depleting a region of Cr or decreasing the re-passivation ability of the alloy (Stewart and Williams 1992, Ryan, Williams et al. 2002, Meng, Frankel et al. 2003). The ability to recover the passive film after its removal is also important in erosion-corrosion studies (Lu, Luo et al. 2008).

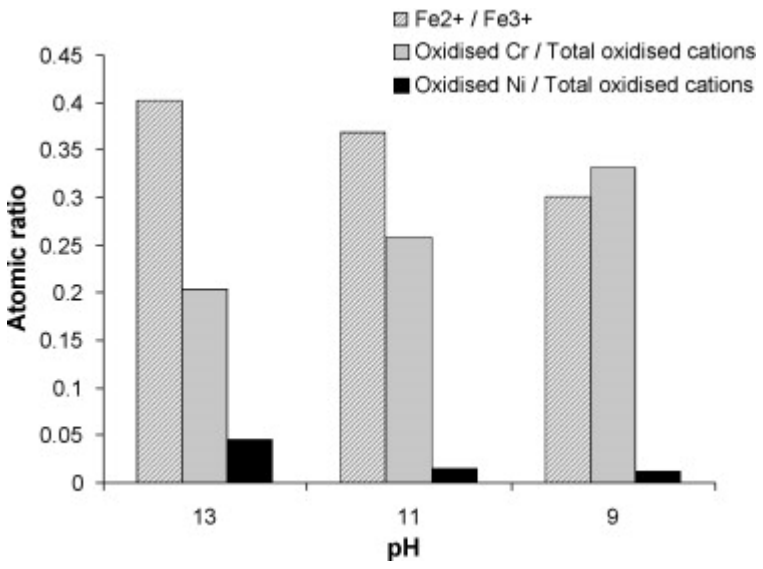

Figure 2-5- Ion ratios in the passive film of SS 316 at different pH values, calculated from XPS spectra (Freire, Carmezim et al. 2010).

In AM, considering the quite different production mechanism compared to traditional methods, process parameters play an important role in the passive film formation, stability, and self-repair capability. For example, in a study, the passive film of AM SS exhibited better barrier characteristics in extreme acidic media compared to traditionally made SS due to its finer grain structure, resulting in a lower corrosion rate as well as a higher breakdown potential (Lodhi, Deen et al. 2018). Other studies report a thicker passive layer on AM samples in different media with a higher ratio of hydroxide content which shows the thickening has taken place in the outer layer of the passive film (Habib, Damra et al. 2011, Man, Dong et al. 2019). The thicker passive film of AM samples compared to their conventional counterparts is attributed to the higher dislocation density of the former, which are the preferred sites for the growth of passive film due to the higher lattice distortion and activation energy. Based on this hypothesis, it has been observed that the corrosion potential and the thickness of passive film both decreased after a post-heat-treatment process on as-fabricated AM parts (Kong, Dong et al. 2019). Alternatively, using improper process parameters has a converse effect on the corrosion behavior due to the voids in the structure which worsens the stability of passive films (Čapek, Machová et al. 2016). Developing an unstable or thin passive film on the surface will eventually lead to the formation of steady state pits and decrease the pitting potential (Kong, Dong et al. 2019). It has also been demonstrated that the re-passivation ability of AM SS is relatively weaker than traditionally fabricated parts, attributed to the induced pores during the process. When the solution is trapped in these pores, chemistry changes of the solution inside the pore de-passivates and hinders the formation of the passive layer (Otero, Pardo et al. 1998, Burstein, Liu et al. 2004, Laleh, Hughes et al. 2019).

For bio applications, it is critically important to minimize the risk of AM SS implant corrosion by modifying and stabilizing the protective Cr_2O_3 layer on the metal substrate to

postpone the corrosion reactions (Kumar, Narayanan et al. 2009, Ibrahim, Sarhan et al. 2017, Harun, Asri et al. 2018). One of the suggested methods is thermal oxidation with optimum temperature and duration which accelerates the formation of iron and chromium oxides on the whole surface and even in protuberant areas of oxide film before contacting body tissues (Buscail, El Messki et al. 2008, Zhang, Shi et al. 2018). Too high temperatures or extended duration of soaking may lead to the breakdown of the chromium oxide layer and degrade the corrosion performance (Habib, Damra et al. 2011, Harun, Asri et al. 2018). A study shows improved corrosion performance, both generally and localized, for AM SS 316L in simulated body fluid (SBF) when processed at low power (Kong, Ni et al. 2018).

2.4. Metallurgical parameters affecting corrosion performance

In general, several metallurgical parameters such as phase distribution, microstructure, porosity, residual stress, surface roughness, etc. affect the corrosion performance as well as the mechanical behavior of metal parts (Gu, Meiners et al. 2012, Herzog and Seyda 2016, Sames, List et al. 2016, Ettefagh, Guo et al. 2020). In the AM process, these factors are determined by the printing process parameters including laser power, scanning speed, hatch spacing, layer thickness, and powder size (de Lima and Sankaré 2014, Miranda, Faria et al. 2016). On the other hand, localized heating and rapid solidification of metals during AM causes a different behavior compared to their traditionally manufactured counterparts, which emphasizes the necessity of broad studies on every aspect of AM to qualify these parts for industrial purposes (Cruz, Chao et al. 2020, Kavousi, Novak et al. 2020). SSs are exceptionally sensitive to process parameters (Murr, Martinez et al. 2012, Ngo, Kashani et al. 2018). For instance, there is evidence that lowering the formation of metallic droplets obstructs the preferred uniform spreading of the molten powder during laser melting (known as balling phenomena) in LPBF AM with non-optimized AM

processing parameters (Kruth, Froyen et al. 2004, Gu and Shen 2009, Ni, Kong et al. 2018, Kong, Dong et al. 2019). It has also been shown that the number of dislocations in an AM SS is much higher than wrought SS due to fast cooling in the AM process which reduces the yield strength of AM samples (Gorsse, Hutchinson et al. 2017). In other literature, samples produced through the LPBF method with a higher energy density as a function of process parameters mostly demonstrated better performance compared to samples produced with lower energy density projecting the importance of optimization of the parameters (Barile, Casavola et al. 2019). In other words, optimization of parameters can eliminate some of the weak points of AM, i.e. modified microstructure, increased density (Dai, Zhang et al. 2017, Suryawanshi, Prashanth et al. 2017).

In this section, seven key metallurgical characteristics that govern microstructure, passive film formation, re-passivation, and thus corrosion performance of AM SSs are described and the effects of process parameters on them are discussed in detail.

2.4.1. Porosity

Generally, pores are preferred sites for corrosion attack, especially pitting. AM as a powder-based manufacturing method is accompanied by the inevitable presence of pores in the produced parts, which can affect mechanical properties and corrosion performance (Otero, Pardo et al. 1995, Rahimi, Tabaian et al. 2012, Ziętala, Durejko et al. 2016, Laleh, Hughes et al. 2020). Typically, pores appear either around the un-melted powder particles or due to trapped gas in the powder or melt pool during its initial processing, such as gas atomization or laser melting process, respectively. Elemental mapping of voids has revealed the presence of oxide powder and non-melted silicon in the pores of AM parts as confirmation of these sources (Ni, Kong et al. 2018). Pores of AM parts can be categorized into two classes of regular (spherical) and irregular (non-spherical) pores (Figure 2-6) (Laquai, Müller et al. 2018, Maximenko and Olevsky 2018).

Spherical pores form as a result of trapped gas during powder production and/or in the melting pool. This type of pore is relatively smaller than irregular pores. The geometry of regular-shaped pores and their inherent presence in the part, regardless of the printing processing parameters, have made them less important as a focus of corrosion studies of AM SS parts (Sander, Thomas et al. 2017). On the other hand, non-spherical pores form due to the un-melted powder particles which are the direct outcome of improper processing parameters (Laleh, Hughes et al. 2020). As reported by many researchers, this class of pores, also called lack of fusion (LOF) pores, can considerably lower the density and play a significant role in facilitating both initiation (reaching the surface) and propagation (geometry and irregular shape) of pits, and the enrichment of aggressive ions at their corners due to their irregular shape (Schaller, Mishra et al. 2018, Suryawanshi, Baskaran et al. 2018, Kong, Dong et al. 2019, Melia, Nguyen et al. 2019, Laleh, Hughes et al. 2020). In related studies, the breakdown potential (E_b) of the passive film was typically employed as an indication for passive film properties against localized corrosion attacks in the presence of pores. A lower E_b demonstrated a higher susceptibility to pitting associated with the presence of LOF pores compared to denser parts and to samples produced by traditional manufacturing methods. The overall qualitative results are almost identical in every environment including sulfuric and phosphoric acid, ferric chloride, as well as NaCl contained aqueous solutions (Otero, Pardo et al. 1998, Prieto, Singer et al. 2019).

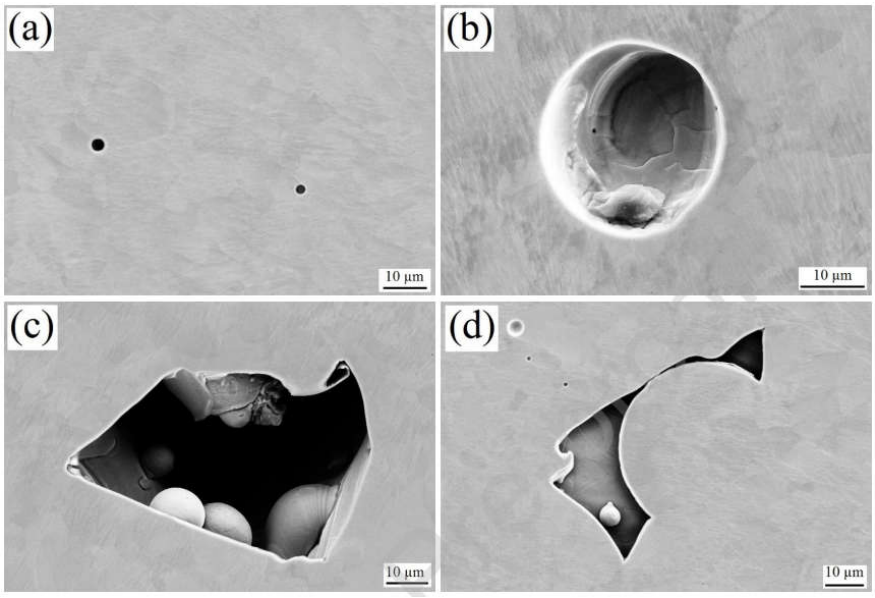

Figure 2-6- (a,b) spherical/regular-shaped, (c,d) non-spherical/irregular-shaped pores formed during additive manufacturing of SS 316 L by LPBF method (Laleh, Hughes et al. 2020).

Nevertheless, the level of porosity and the density of the part can be optimized to some extent by applying the right sets of printing parameters such as scanning speed and laser power, by affecting the heating and cooling rate of the melt pool (Kong, Dong et al. 2019, Man, Dong et al. 2019, Laleh, Hughes et al. 2020). For instance, too high a scanning speed (>1400 mm/s) or too low of laser power can dramatically accelerate the formation of LOF pores in AM SS caused by remaining un-melted powder. Too high of laser power, on the other hand, facilitates trapping of gasses in the printed part (Wolff, Lee et al. 2016, Sander, Thomas et al. 2017, Ni, Kong et al. 2018, Laleh, Hughes et al. 2020). Several quantitative studies are available as evidence for this result. A study shows that a porosity level of above 2% with pore size up to 50 µm is the reason for poor corrosion performance of AM SS 316 L and 17-4 PH samples (Geenen, Röttger et al. 2017, Schaller, Taylor et al. 2017). Similarly, a porosity level of 1.7% in AM SS leads to poor corrosion resistance compared to traditionally manufactured samples, even though the E_b values for both groups are in the same range (Sun, Moroz et al. 2014). Other studies report that samples with a

density of higher than 99.1% have the highest E_b value compared to lower density levels and these values are almost identical to the traditionally fabricated samples with almost no effect on pitting potential (Sun, Tan et al. 2016, Zhang, Liu et al. 2017, Laleh, Hughes et al. 2020, Zhou, Hu et al. 2020). Alternatively, a density level of lower than 99.1% results in unsatisfactory corrosion performance with an E_b value of 200 mV below traditional 316 L SS (Laleh, Hughes et al. 2020). To validate the effect of porosity on corrosion performance of AM SSs, a comparison was made and confirmed the higher pitting potential of non-porous areas compared to porous regions of AM SS 304L by greater than 200 mV. This finding endorses the role of pores in the pit initiation process (Schaller, Mishra et al. 2018). A study on the metastable pitting characteristic of LPBF 316 L shows that by keeping the porosity level of AM SS 316 L in the range of 0.04 %-0.5 %, pit initiation can be delayed remarkably compared to traditionally produced samples (Sander, Thomas et al. 2017). This behavior is claimed to be the result of the dissolution of MnS inclusions during rapid solidification in the AM process, which is known to be the main cause of pit initiation in SSs (Chao, Cruz et al. 2017). However, during polarization tests of AM and conventional SS 316L, several current spikes have been detected at the high anodic potential for AM samples which is an indication of metastable pit formation. In other words, there is a pre-existing passive layer on the sidewalls of pores, but this protective layer is not stable enough and collapses at higher anodic potentials causing fluctuations on the anodic branch of the polarization curve. These fluctuations are more pronounced for the specimens with higher porosity levels (Pistorius and Burstein 1992, Sun, Moroz et al. 2014, Sander, Thomas et al. 2017). Production processes and the quality of the feedstock can also affect the porosity level of the AM part (Sutton, Kriewall et al. 2017, Harun, Asri et al. 2018). Using powders with larger particles, irregular shapes, and higher contamination are all reported to increase the porosity level of AM SS parts (Sutton, Kriewall et al. 2017).

Moreover, a study compares the final density of LPBF parts using either gas or water atomized 316 L SS powders and found utilizing water atomized powder results in a lower density due to higher oxygen content and lower packing density (Li, Shi et al. 2010). All of these parameters should be considered for quality purposes.

A more systematic optimization method for AM processing parameters to attain the densest possible AM SS parts is via laser energy density (LED), also known as volumetric energy density (VED), calculated by dividing laser energy by the product of scanning rate, hatch spacing and layer thickness (Yusuf and Gao 2017, Kluczyński, Śnieżek et al. 2018, Yusuf, Chen et al. 2020). A low level of LED causes non-spherical pores but high amounts of this parameter lead to the formation of spherical pores during the AM process (Vilaro, Colin et al. 2011, Maskery, Aboulkhair et al. 2016). Reports indicate that the densest SS 316L samples with a porosity level of roughly 0.3% can be achieved by AM with a laser energy density of around 105 J/mm^3 (Cherry, Davies et al. 2015). However, despite this low level, porosities are not evenly distributed in the part. For instance, for 316 L SS produced by LPBF methods, the average porosity level was ~0.82% whereas the localized pore concentration in some regions were reported to be as high as 1.68% which may lead to anisotropic behavior of the AM part (Yusuf, Chen et al. 2017). Taking everything into account, an AM SS with optimized processing parameters can demonstrate a comparable or even improved corrosion behavior compared to conventionally made SSs by keeping the porosity level as minimal as possible (Ziętala, Durejko et al. 2016, Ettefagh and Guo 2018, Cruz, Chao et al. 2020).

2.4.2. Inclusions

Austenitic SSs such as 316 L and 304 L are typically vulnerable to pitting corrosion due to the presence of unwanted inclusions as the second phase in the austenite matrix. Manganese sulfide

(MnS) is the most prominent, and has a significant role in the corrosion performance of SSs depending on their density, composition, and size. The elimination or size control of MnS can be presumed as a corrosion inhibition method of SSs (Baker and Castle 1993, Ryan, Williams et al. 2002, Hemmasian-Ettefagh, Amiri et al. 2010, Williams, Kilburn et al. 2010, Jun, Holguin et al. 2014, Lillard, Kashfipour et al. 2016). During the steelmaking process, Mn is added to form MnS and neutralize the negative effect of FeS formation. In other words, MnS is thermodynamically more stable and has a higher melting point compared to FeS, and its formation eliminates the presence of low melt FeS along grain boundaries in the steel structure which is the leading cause of cracking problems during hot rolling (Reed 1983). However, it is theorized that there is a drop in chromium content of the alloy in the areas surrounding MnS inclusions, and this Cr depleted region together with the inclusion itself have a lower Cr content than the critical value for passive layer formation which leads to localized corrosion vulnerability (Ryan, Williams et al. 2002, Wijesinghe and Blackwood 2007, Jun, Holguin et al. 2014, Yusuf, Chen et al. 2020). During the pit initiation process, elemental and ionic sulfur (S, S^{2-}, HS^{-}, $S_2O_3^{2-}$) are formed as a result of MnS oxidation which provides an inappropriate environment for the re-passivation process and pits propagate as a result (Castle and Ke 1990, Ke and Alkire 1995, Ryan, Williams et al. 2002, Krawiec, Vignal et al. 2005, Chiba, Muto et al. 2013).

On this basis, considering the rapid solidification associated with the AM process, much research has reported that no, or at least much smaller, MnS inclusions and Cr depletion zones in the matrix form, which causes a substantial increase in the pitting potential of AM SSs -by roughly 300 mV in different corrosive media (Stewart and Williams 1992, Carboni, Peyre et al. 2002, Chao, Cruz et al. 2017, Sander, Thomas et al. 2017, Ni, Kong et al. 2018, Schaller, Mishra et al. 2018, Kong, Dong et al. 2019). However, in traditional manufacturing methods, the cooling rate

is relatively lower, providing enough time for Mn and S to diffuse and form deleterious MnS inclusions (Lou, Song et al. 2017, Lou, Andresen et al. 2018). The increase in pitting resistance of AM parts is also attributed to the change in chemistry, size, and shape of inclusions after the AM process. Several studies show the formation of nanoscale oxide inclusions enriched of Mn, Si, Al, Cr, N, and O (Figure 2-7) which have no negative effect or even improve corrosion performance (Stewart and Williams 1992, Zheng, Li et al. 2013, Saeidi, Gao et al. 2015, Chao, Cruz et al. 2017, Kurzynowski, Gruber et al. 2018, Schaller, Mishra et al. 2018, Man, Duan et al. 2019). The size of inclusions after the AM process is in the range of 5-200 nm as opposed to their conventional counterparts with inclusions in the size range of 2–4 μm which is 1-3 orders of magnitude larger (Chao, Cruz et al. 2017, Schaller, Mishra et al. 2018, Man, Dong et al. 2019). This range of nano-inclusion size is reported to exist in both LPBF and DLD methods of AM and are too small to initiate pitting corrosion in AM samples (Saeidi, Gao et al. 2015, Carlton, Haboub et al. 2016, Sander, Thomas et al. 2017, Kong, Dong et al. 2018). Also, the shape of the inclusions after the AM process is reported to be spherical versus irregular shapes in conventionally fabricated parts (Chao, Cruz et al. 2017).

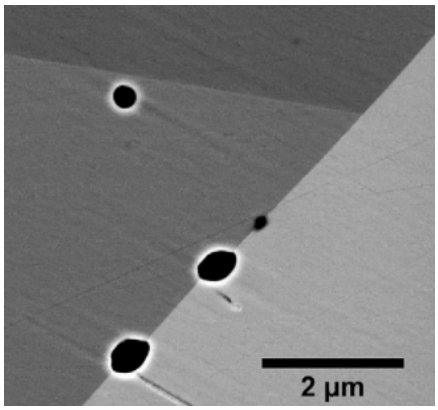

Figure 2-7- Back-scattered electron image showing the formation of oxide inclusions in recrystallized AM SS 316 L (Lou, Andresen et al. 2018).

Since post-heat-treatment is an inevitable process in many industrial applications of AM parts, it is important to understand the effect of heat treatment on the preformed inclusions during the AM process. After the post-heat-treatment process, the inclusions become smaller in size, and from the chemical composition point of view, the elements with lower melting points such as Al diffuse to the matrix and change to the composition of nano-inclusions (Kong, Ni et al. 2018, Kong, Dong et al. 2019). The lingering inclusions in a heat-treated AM part can be categorized into three classes: (1) Manganese silicate inclusions formed in the as-fabricated samples which still exist after a heat treatment process in the temperature range of 900-1000 °C with a duration of 15-60 min; (2) Heat treatment at temperatures of 1100-1200 °C will result in the formation of irregular manganese chromite inclusions from the manganese silicate inclusions; and (3) Harmful MnS inclusions (pitting initiators) which are formed in the same heat treatment condition as type (2) and should be acknowledged as the main reason for dramatic decreases of corrosion resistance after heat treatment processes on AM SS parts at temperatures above 1000 °C. At this high temperature, the non-equilibrium state of the as-fabricated structure has enough time to move toward the equilibrium state by forming MnS from saturated Mn and S in the matrix (Laleh, Hughes et al. 2020).

2.4.3. Residual stress

Heating and cooling regimes during melting of the top layer and re-melting of underlying layers in the AM process causes anisotropic residual stress in different regions of the produced part where in some places, it may exceed the yield strength of the material, distort the part, and affect both mechanical and corrosion performance (Shiomi, Osakada et al. 2004, Mercelis and Kruth 2006). Alternatively stated, rapid heating, fast solidification, and thermal expansion cause elastic strain and local distortion of the lattice which develops residual stress in either tensile or

compressive forms (Schajer 2013). The considerable thermal gradient (Figure 2-8-left) which enhances distortion within the AM part is one of the impelling parameters on the magnitude of residual stress along with several others such as build direction, yield strength, process parameters, and shape of the part. All of these parameters result in a more complicated behavior of residual stress in AM parts compared to parts that evolve through the traditional manufacturing methods (Mercelis and Kruth 2006, Yadroitsev and Yadroitsava 2015, Zhao, Iyer et al. 2017, Li, Liu et al. 2018, Bartlett and Li 2019).

Two models have been proposed to hypothesize the source of residual stress during AM. According to the temperature gradient mechanism (TGM) model, a laser source with high energy density heats a small area of the feedstock. This area tends to expand due to the input heat, but this thermal expansion has been restricted by the neighboring areas with lower temperatures, which induces a compressive stress during the heating stage. Conversely, during the cooling stage, the same area tends to shrink after the removal of the heat source, however, previously formed plastic strain limits the shrinkage and causes tensile stress in the location (Li, Liu et al. 2018). The cool-down phase model is another approach to explain the generation of residual stress in AM parts. Based on this model, which is founded on the layer-by-layer nature of fabrication, re-melting and re-solidification occur in underneath layers as well as the top layer, and each layer tends to shrink after cooling down. Because of this thermal cycle, and limited in shrinkage with its sublayer, tensile stress is developed in the layers (Mercelis and Kruth 2006).

Residual stress can be classified length scale-wise into three categories (Figure 2-8-right): Type I (macroscale), Type II (microscale, anisotropic properties on grain-scale), and Type III (nanoscale, dislocations or vacancies) (Withers and Bhadeshia 2001). Although almost all of the studies on the effects of residual stress on the properties of AM parts ignore the small effects of

types II and III on the overall residual stress in the structure, a few research papers demonstrate qualitatively that a post-heat-treatment on as-fabricated AM SS can reduce the dislocation density and type III of residual stress as a result (Tomus, Tian et al. 2016, Li, White et al. 2017). The measurement of local residual stress in a part is difficult and requires some advanced methods involving advanced sample preparation and data analysis with X-ray or neutron based techniques. However, some simpler optical-based measurement methods are now employed by industries to analyze residual stress distribution and structural integrity of AM parts. The hole-drilling method (HDM) accompanied by electronic speckle pattern interferometry (ESPI) is a common method for this purpose (Hauk 1997, Luo and Jones 2010, Schajer 2013, Barile, Casavola et al. 2016, Mukherjee, Zhang et al. 2017, Zhao, Iyer et al. 2017).

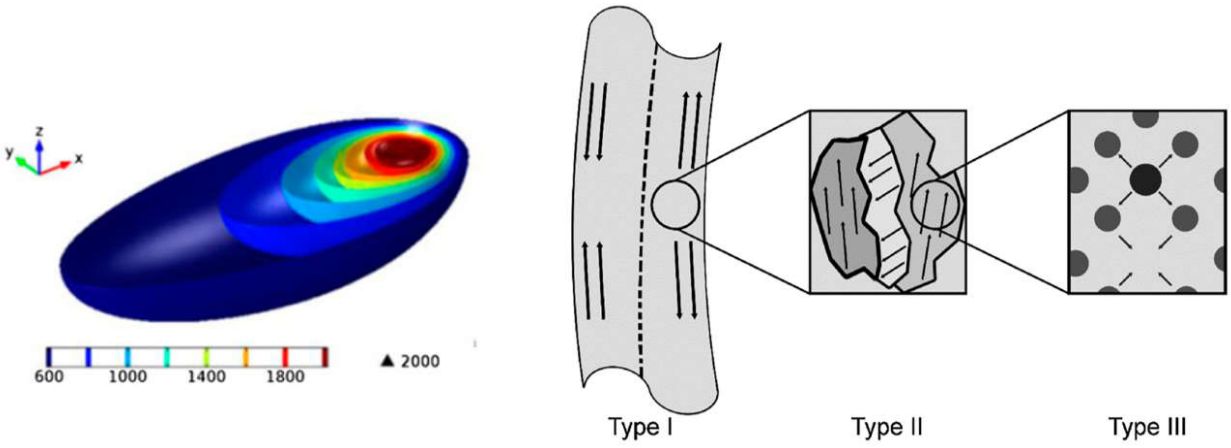

Figure 2-8- (left) Temperature contour during additive manufacturing of SS 316 L shows a temperature gradient of ~2000K on the surface (Yadroitsev and Yadroitsava 2015), (right) different classifications of residual stress based on the length scale, type I: macroscale, type II: microscale caused by misalignment of grains, and type III: nanoscale caused by substitutional atoms (Bartlett and Li 2019).

The nature of residual stress in AM SSs is quite complex and controversial in different studies. Some studies show that the compressive stress in the part induced during the manufacturing process may increase the corrosion resistance by lowering the passive current

density due to forming a denser passive film on AM SSs (Navai 1995). With this assumption, post-heat-treatment may be harmful to corrosion performance by eliminating the compressive residual stress (Chao, Cruz et al. 2017). Some studies even suggest introducing the compressive stress externally on the surface of the manufactured part to slightly enhance the corrosion performance (Peyre, Scherpereel et al. 2000, Peyre, Carboni et al. 2007, Takakuwa and Soyama 2014, Simson, Emmel et al. 2017). This hypothesis is based on the role of compressive stress on lowering the point defect concentration of the passive film which increases the resistance to pit initiation and decreases the passive film growth rate (Cruz, Chao et al. 2020).

Generally, including the role of residual stress in distortion of the AM part, which is more noticeable in thin-walled designs (Mukherjee, Zhang et al. 2017), residual stress is believed to accelerate both corrosion attack and stress corrosion cracking (SCC) (Örnek and Engelberg 2016, Örnek, Idris et al. 2016, Almuaili, McDonald et al. 2017, Jirandehi, Mehdizadeh et al. 2020). A study claims that the regions under tensile stress and compressive stress form a micro galvanic couple where the former acts as anode and the latter as the cathode. This galvanic couple region has been mentioned as the primary pit initiation sites of the part (Chen, Van Boven et al. 2007, Van Boven, Chen et al. 2007). In addition, delamination of the layers and initiation and growth of cracks have been mentioned as a direct result of residual stress, which is specifically important to the study of SCC of AM SSs (Geenen, Röttger et al. 2017, Lou, Song et al. 2017). However, countless stress/strain conditions on the surface of AM parts makes it very difficult to evaluate the SCC of these parts using modeling of residual stress formation (Örnek 2018). In addition, it has been shown that the change of residual stress grows with depth of the printed part and this means the underneath layers are favored for the initiation of SCC (Zhao, Iyer et al. 2017).

As mentioned before, there are several distinct compressive/tensile sites on the AM surface, which makes this topic more complicated (Örnek 2018). Taking into account the complex impact of residual stress on the properties of the materials, it is almost inevitable to seek a remedy for decreasing this parameter in AM parts for industrial applications. Some methods are applied to reduce the residual stress in AM SSs. The most common is to preheat the feedstock and substrate material to decrease the thermal gradient within the part (Zaeh and Branner 2010, Kruth, Deckers et al. 2012, Buchbinder, Meiners et al. 2014). Moreover, applying severe plastic deformation (SPD) on as-fabricated parts as a post processing procedure is presented to be an effective method for improving material properties by producing an ultra-fine grained microstructure (Yusuf, Chen et al. 2020). Post annealing is another typical remedy to decrease the residual stress of printed parts (Montero Sistiaga, Nardone et al. 2016, Ettefagh and Guo 2018). However, in all of these methods, the formation of a secondary phase may act as a new source of residual stress which should be addressed (Örnek 2018).

2.4.4. Surface roughness

Surface roughness as an inherent characteristic of AM parts is one of the key parameters in determining their corrosion behavior since a rougher surface accelerates electrochemical reactions between the surface and environment leading to both general and localized corrosion (Zuo, Wang et al. 2002, Shahryari, Kamal et al. 2008). The surface roughness of AM parts is quite higher than other traditional manufacturing methods and highly depends on the laser energy density (Figure 2-9). For example, research shows a roughness of 10-30 μm for AM LPBF parts as opposed to ~1 μm for parts produced by milling (Wang, Liu et al. 2016). Four main reasons have been mentioned as the sources of a rough surface on as-fabricated parts (Jamshidinia and Kovacevic 2015, Fox, Moylan et al. 2016, Gockel, Sheridan et al. 2019, Kong, Dong et al. 2019):

1) Evaporation: an unstable and irregular melt pool during the AM process is attributed to the produced gasses during the powder melting along with the Marangoni force which destabilizes the melt flow and increases both surface roughness and porosity (Strano, Hao et al. 2013, Chen, Gu et al. 2017, Tian, Tomus et al. 2017). Less gas expansion is reported for thinner powder layers. However, choosing a smaller powder layer thickness extends the production time which should be taken into account (Qiu, Panwisawas et al. 2015, Aqilah, Farazila et al. 2018).

2) Balling phenomena: low laser power cannot deliver sufficient energy to melt the powder particles completely. Consequently, the adhesion of solid particles to the surface increases the surface roughness (Gu and Shen 2009, Aboulkhair, Maskery et al. 2016). Increasing the heat input by using higher laser power can be assumed as a remedy for this issue. In addition, higher heat input increases the wettability of the melt via the keyhole effect and enhances the interlayer connection by flattening the melt pool. This phenomenon also relieves the surface tension of the melt and reduces the balling phenomena and the eventual surface roughness as a result (Kruth, Froyen et al. 2004, Calignano, Manfredi et al. 2013). However, an optimized heat input should be applied since too high a heat input can be harmful to surface roughness by agitating the melt pool and growing recoil pressure (Jamshidinia and Kovacevic 2015). Another reason for balling phenomena is the size of the initial powders. As the laser spot diameter is usually 50-100 μm, it is difficult to melt powder particles with a diameter of more than 100 μm which leaves a negative effect on the surface roughness (Yadroitsev, Bertrand et al. 2007, Yadroitsev, Thivillon et al. 2007). Another study shows that the accumulated heat during AM of a thin-walled object increases the adhesion of partially melted particles to the surface and deteriorates the final surface finish (Jamshidinia and Kovacevic 2015).

3) Staircase effect: an additively manufactured part is created by stacking several 2D layers on top of each other to form a 3D object. However, a geometric difference is expected between theory (CAD design) and the actual printed part (Thomsen, Malmström et al. 2009). This difference is attributed to the layer-by-layer build up during AM and is known as the staircase or stair-stepping effect, which is more pronounced for inclined surfaces (Barari, Kishawy et al. 2017). Using initial powders with a smaller diameter is proposed to diminish the staircase effect along with a decreasing layer thickness (Santos, Shiomi et al. 2006, Thomsen, Malmström et al. 2009).

4) Facing orientation: several pieces of research literature express a difference in the surface roughness for upward and downward facing surfaces with different angles of inclination. Results show that upward-facing surfaces have a lower surface roughness. This is likely from filling of the gaps by the particles during the manufacturing of upward-facing surfaces (Bacchewar, Singhal et al. 2007, Strano, Hao et al. 2013, Triantaphyllou, Giusca et al. 2015).

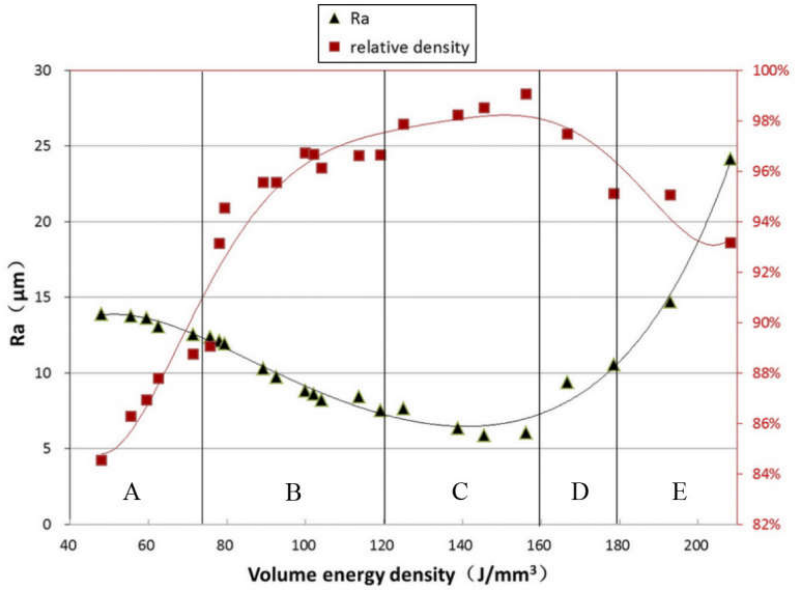

Figure 2-9- dependence of surface roughness to laser energy density for as-fabricated SS 316 L (Wang, Liu et al. 2016).

2.4.5. Alloying elements and elemental segregation

It is well known that the outstanding corrosion performance of SSs is principally attributed to the presence of at least 11 wt. % Cr as an alloying element that forms a protective layer of chromium oxide on the surface (Gil, Brühl et al. 2006, Abedi, Salehi et al. 2010). However, the role of other elements is not negligible in both mechanical and corrosion properties of AM SSs. Ni is generally known as an austenite stabilizer element by lowering the austenite/ferrite or martensite transformation temperature to sub-zero temperatures (Yang and Ren 2010). It also affects AM SS properties such as cracking susceptibility, wear resistance, microhardness, microstructure, and corrosion and oxidation resistance. For some types of SSs like 35CrMO, poor corrosion resistance limits its application in industry. It has been reported that by optimization of nickel content in such alloys, it is possible to improve corrosion properties while maintaining its significant mechanical behavior. This enhancement is ascribed to the formation of austenite instead of ferrite as the constituent phase due to the change of the solidification model as a result of increasing Ni content. Quantitatively, adding roughly 10 wt.% of Ni to the initial composition of 35CrMo SS suppresses the anodic dissolution of SS by dropping the corrosion rate by an order of magnitude along with an increase of ~220 mV in corrosion potential for the as-fabricated sample (Zhang, Zhang et al. 2018).There are, however, some limitations associated with nickel such as its high cost and allergic reactions in the case of bio-applications (Yang and Ren 2010). For this reason, developing low-nickel or nickel-free SS powders for AM is a new subject of interest. Nitrogen, as an interstitial element of SSs, causes a more homogenous distribution of other alloying elements and decreases the tendency of forming Cr clusters in the structure. Therefore, by strengthening the solid solution and improving short-range order, nitrogen is recognized as a strong austenite former in SSs (Gavriljuk, Shanina et al. 2000). With the presence of nitrogen in

the alloy composition, the development of Cr clusters is prevented, creating a more efficient passive layer of Cr_2O_3 on the top layer, and improving intercrystalline, pitting, and crevice corrosion resistance as a result (Levey and Van Bennekom 1995, Jargelius-Pettersson 1999, Baba, Kodama et al. 2002). The common method for adding nitrogen to the initial powder of the AM process with a higher amount than its solubility range is to first add manganese to increase the solubility of nitrogen and lower the nickel content. The next step is to melt SS under a nitrogen atmosphere where nitrogen atoms are absorbed into the melt (Pridantsev and Levin 1966, Feichtinger and Stein 1999). However, it should be noted that excessive nitrogen causes the formation of CrN and gas pores during the AM process. Research demonstrates that adding 0.3 wt.% of N with this method can improve the stability of austenite in modified AM SS 316L (Cui, Uhlenwinkel et al. 2020).

Oxygen may be introduced to the feedstock powder in the powder making process. This preexisting oxygen transforms to surface oxides on powder particle surfaces during the AM process and considerably lowers the pitting potential of AM SSs (Schaller, Taylor et al. 2017). C and Mo are also important alloying elements in the composition of SSs from a corrosion point of view. The formation of carbides and their precipitation at grain boundaries causes intergranular corrosion. Hence, the amount of this element should be kept low (~0.03 wt.%) (Gubicza, El-Tahawy et al. 2016, Yusuf, Nie et al. 2018). The presence of Mo in the alloy composition is essential for the formation of the passive film and improves pitting resistance (Sedriks 1996, Bevan, Ameri et al. 2017). Studies show that Mo forms some oxyanions such as molybdate in the passive film and these anions act as corrosion inhibitors (Clayton, Halada et al. 1995, Trelewicz, Halada et al. 2016). Moreover, an intermetallic layer of Mo-Ni is formed beneath the top passive

layer which increases the protection and blocks the inward diffusion of aggressive ions like Cl (Halada and Clayton 1993).

The high energy associated with the AM process causes the vaporization of some powder particles or coverts them into soot, and also cause microsegregation in the elemental distribution of the printed part (He, DebRoy et al. 2003, Yakout, Cadamuro et al. 2017). A study shows that in an AM SS 316L, Cr and Ni contents vary in the range of 9-15% and 5-10%, respectively, while some regions with no Mo content have been detected which confirms the existence of areas with the subcritical amount of key alloying elements (Yakout, Elbestawi et al. 2018). Considering the mentioned role of each element in the corrosion performance of AM SSs, this segregation leads to the spatially heterogeneous composition of SSs and impacts their corrosion behavior (Trelewicz, Halada et al. 2016). For instance, lower nickel and chromium contents are reported at the center of the AM part due to its relatively higher built-up energy during the process. Furthermore, the regions with lower Mo content have a different passive formation mechanism, which makes it less protective locally and increases the passive current density. This increase is as high as an order of magnitude in acid solutions compared to traditionally fabricated SSs (Trelewicz, Halada et al. 2016). Therefore, applying any redistribution process such as heat treatment on AM parts might considerably influence their corrosion behavior.

2.4.6. Grain size and shape

Generally, depending on the corrosive media, grain size affects the corrosion performance of SSs. For instance, in acid media, grain size below 2 μm is reported to increase the general corrosion rate of SS 304 due to an unstable passive film at the grain boundaries (Di Schino and Kenny 2002). In contrast, the nano-scale grain size range purportedly improves corrosion performance (Li, Wang et al. 2004). However, some reports show the loss of passive layer

protection on the surface of nano-crystallized SS 316 due to the increasing number of active sites for corrosion attack (Hao, Deng et al. 2009). The effect of grain size on the corrosion performance of AM SSs is also controversial considering quite contradictory results reported in the literature. EBSD analysis shows that AM SS grains are more irregular and elongated perpendicular to the scanning direction with a large size range versus regular polygonal grains of traditionally fabricated samples with a narrow range of size, which is attributed to the much lower cooling rate of conventional manufacturing methods. Specifically for AM processes, some of the researchers demonstrate the existence of sub-grains with sizes of 0.5–1 μm inside each grain in the as-fabricated structure (Figure 2-10) with an elevated concentration of Mo and dislocation density at sub-grain boundaries, which increases the reactivity of the surface as well as the risk of intergranular corrosion (Saeidi, Gao et al. 2015, Trelewicz, Halada et al. 2016, Kong, Ni et al. 2018, Kong, Ni et al. 2018, Man, Duan et al. 2019). Moreover, unlike LPBF with complete austenite phases, for the DLD method, sub-grain boundaries were found to be enriched of Cr and Mo and almost depleted of Ni. There is an indication of the formation of intercellular delta ferrite on the sub-grain boundaries of AM SS 316 L which is one of the downsides of DLD over LPBF considering its lower cooling rate during the process (Ziętala, Durejko et al. 2016, Alsalla, Smith et al. 2018, Lei, Xie et al. 2019, Ni, Kong et al. 2019). It is stated that the effect of AM processing parameters on the average grain size is relatively insignificant (Trelewicz, Halada et al. 2016, Ni, Kong et al. 2018), however, a strong relation between laser energy density and scanning strategy with resulting sub-grain structure has been reported (Kurzynowski, Gruber et al. 2018, Alam, Mehdi et al. 2020). A comparison between the corrosion rate of AM samples and their conventional counterparts shows that the degradation of corrosion performance after the AM process not only is the outcome of sample porosity but also because of the grain structure of as-

fabricated samples (Kamath, El-Dasher et al. 2014, Trelewicz, Halada et al. 2016). On the contrary, others believe that this super high density of sub-grain boundaries of as-fabricated SSs acts as the preferred sites for passive film nucleation, resulting in a more protective surface layer (Kong, Dong et al. 2019, Man, Dong et al. 2019, Kong, Dong et al. 2020).

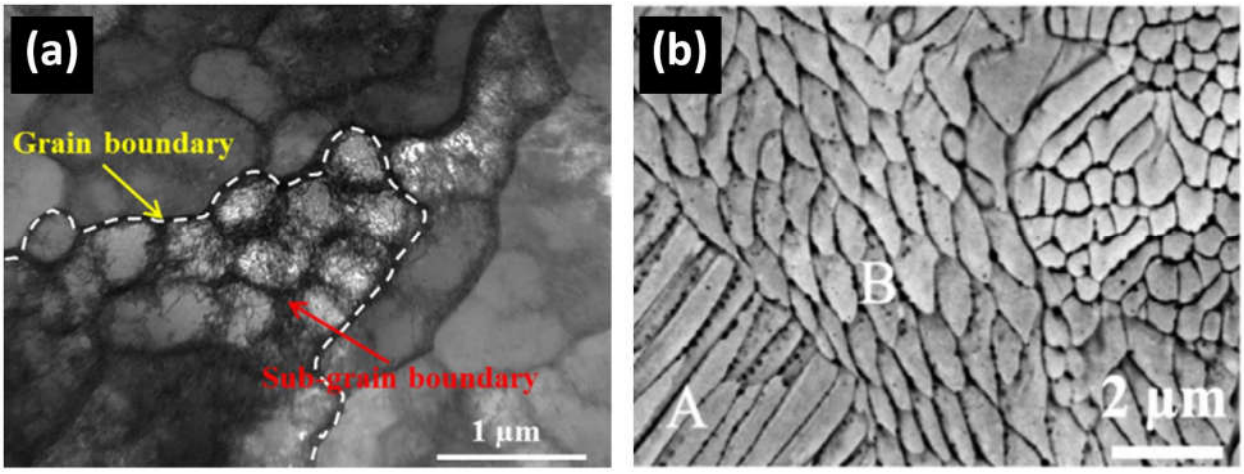

Figure 2-10- (a) TEM image (Man, Dong et al. 2019) (b) SEM image (Wang, Liu et al. 2020) of AM SS 316 L showing grain and sub-grain boundaries inside them. A and B represent two different grains.

The shape of grains is especially important in the SCC performance of AM SSs where the elongated grains cause an anisotropic behavior against crack growth. Considering grain elongation in the build direction, a crack faces more grain boundaries perpendicular to the build direction, resulting in a slower propagation rate (Strondl, Lyckfeldt et al. 2015, Galati, Iuliano et al. 2017, Jirandehi and Chakherlou 2019, Valente, Christiansen et al. 2019, Zhang, Dodaran et al. 2019). Alternatively, elongated grains have been known as a source of localized corrosion attacks (Trelewicz, Halada et al. 2016).

Grain refinement processes reportedly improve the corrosion and mechanical performance of stainless steel (Zhang, Shi et al. 2007, Misra, Nune et al. 2013, Mohan, Prabhath et al. 2015, Khajouei-Nezhad, Paydar et al. 2017). Modifying the surface texture to nano-scaled grains or ultra-

fine grains decreases the chromium diffusion path to the surface and thickens the formed protective film in a corrosive media by promoting passive film formation (Balusamy, Kumar et al. 2010). Commonly, severe plastic deformation (SPD) methods have been applied as a post-treatment on as-received AM SSs to decrease the grain size to the ultrafine (0.1-1 μm) or even nano-scale range (Valiev, Estrin et al. 2006, Langdon 2013). Several SPD techniques such as accumulated roll bonding (ARB) and equal channel angular processing (ECAP) are being tested on AM SSs to achieve this goal. However, high-pressure torsion (HPT) is the most popular method, refining the grain structure uniformly down to below the 50 nm range and eliminating scan tracks by imposing an extreme torsional strain on a sample (Zhu and Langdon 2004, Xu, Horita et al. 2007, Tikhonova, Enikeev et al. 2016, El-Tahawy, Gubicza et al. 2017, El-Tahawy, Huang et al. 2017). Among several advantages of HPT over other post-treatment SPD methods, the most important to achieve higher corrosion resistance in AM SSs are obtaining much smaller grains, higher efficiency, and producing grain boundaries with higher misorientation angles (Zhilyaev, Nurislamova et al. 2003, Yusuf, Nie et al. 2018). Recrystallization heat treatment is another method for refining grains by removing melt pool boundaries, sub-grain boundaries, and dislocations of as-fabricated SSs to improve their corrosion performance (Kong, Ni et al. 2018, Zhou, Hu et al. 2020). It is reported that holding samples fabricated from SS 316L and SS 304L at 1060 °C for 30 min followed by furnace cooling partially recrystallizes the as-fabricated structure and generates more grains along the closed packed direction (110) which is known to have higher pitting resistance (Krishnan, Dumbre et al. 2013, Kong, Ni et al. 2018). Additionally, recrystallization decreases the crack growth rate and lowers the risk of SCC as a result of the elimination of the microstructural anisotropy (Lou, Othon et al. 2017). However, a post-heat-treatment process should be performed cautiously at temperatures above 1000 °C since some research suggests lower corrosion resistance

of recrystallized samples compared to as-fabricated ones due to the elimination of sub-grain boundaries and the precipitation of inclusions. In other words, sub-grain boundaries act as nucleation sites for passive film and their elimination leads to a thinner protective layer on the surface (Liu, Li et al. 2010, Ralston, Birbilis et al. 2010, Kong, Dong et al. 2020, Zhou, Hu et al. 2020). On the other hand, heat-treatment at temperatures below 1000 °C not only retains sub-grain boundaries but also transforms the dislocation walls to sub-grain boundaries, which along with stress-relieving and eliminating melt pool boundaries (instead of recrystallization), are believed to be beneficial for corrosion performance (Ettefagh and Guo 2018, Zhou, Hu et al. 2020).

2.4.7. Phases

Generally speaking, despite the presence of "austenite" in the title of austenitic SSs, according to the Fe–Cr–Ni phase diagram, equilibrium phases at room temperature are listed as σ, δ-ferrite and carbides (Lippold and Savage 1982). This means that applying an improperly designed thermal regime during either manufacturing or post-processing causes the formation of the mentioned unwanted phases, which are in contrast to the better corrosion performance of a fully austenitic microstructure. Among the mentioned unwanted phases, σ has the most detrimental effect on the corrosion behavior of SS by significantly decreasing the Cr amount on its interface and reducing pitting resistance and ductility of SSs as an intermetallic phase with tetragonal crystal structure (Chastell and Flewitt 1979, Kington and Noble 1991, Chen, Li et al. 2018). In all AM manufacturing methods, phases are vastly different from the equilibrium phases considering the non-equilibrium nature of the process. However, as-fabricated phases may be different for LPBF and DLD methods. For LPBF, while the cooling rate is much faster than equilibrium conditions, the formation of unwanted phases is unlikely and a fully austenitic microstructure with cellular-dendritic substructures can be achieved by selecting the proper printing parameters (Jerrard, Hao

et al. 2009, Man, Dong et al. 2019). The core of these austenite dendrites contains a lower amount of Cr and Ni compared to the initial composition which can act as initiation sites for corrosion attacks in some solutions such as ferric chloride (Cui and Lundin 2007). However, a general evaluation of the sole effect of the microstructure of AM SSs by the LPBF method shows a minor role of unwanted phases in corrosion performance so that it can be neglected (Schaller, Mishra et al. 2018). For the DLD method, taking into account its comparatively lower cooling rate than LPBF, the formation of unwanted phases along the sub-grain boundaries is more probable during manufacturing. Intracellular δ-ferrite has been reported to be formed considerably for different types of AM SSs through the DLD method (Zheng, Zhou et al. 2008, Ziętala, Durejko et al. 2016, Guo, Zou et al. 2017, Ma, Wang et al. 2017, Suresh, Dasgupta et al. 2017). For this reason, performing a proper post-heat-treatment is unavoidable in the case of a high content of unwanted phases to ensure a fully austenitic microstructure. It is claimed that solution annealing in the temperature range of 1040-1120 °C followed by water quenching can dissolve unwanted phases into the austenite matrix (Padilha, Plaut et al. 2006, Chen, Li et al. 2018). However, despite some reports about the effect of solution annealing on the improvement of SCC resistance and mechanical properties of AM SSs for high-temperature applications (Gibson, Rosen et al. 2014, Lou, Song et al. 2017, Salman, Gammer et al. 2019, Dodaran, Ettefagh et al. 2020), heat-treatment might have some negative effects on the corrosion behavior as described in the last section.

2.5. Knowledge gaps and prospects

Although there have been many studies about the corrosion behavior of AM SSs, there still exists a lack of conclusive information in some cases, which indicates the necessity for future work in this area. Below are some of the important gaps that the current efforts have not addressed or for which there are controversies regarding their outcomes.

- The studies focused on AM processes involving several variables such as process parameters, alloy composition, test method, electrolyte, pH, and temperature, which makes a general cross-paper study and comparison difficult. A standard test method for corrosion performance of AM alloys can be provided by related organizations which facilitates the application of AM components in industry.
- The main source of different metallurgical properties of AM parts is printing processing parameters. An optimized set of parameters significantly affect the corrosion performance in different media. However, there is a lack of systematic analysis to introduce the optimum set for each alloy in a certain environment.
- There is not a general agreement on the source of residual stress and its effect on corrosion performance. The same controversy exists relative to the passive film formation mechanism on AM SSs parts and the role of microstructure, grain size and structure on the passive layer.
- There is also needed clarity on the best use of heat treatment since there can be both positive (densification, grain refinement) and negative (reduction of dislocation density, elimination of sub-grain boundaries, precipitation of inclusions) effects on the corrosion performance.
- Currently, all of the research on AM SS is limited to the alloys available on the commercial market. However, considering the distinct conditions during AM processes like high energy, rapid cooling rates, and micro-segregation, designing new SSs tailored especially for AM is an interesting topic.
- There is a lack of information about the long term exposure of AM SSs in industrial applications.

2.6. Conclusion

This review chapter summarized the assessments on additively manufactured stainless steel parts with the focus on corrosion performance in a vast range of applications including biomedical, nuclear, and fuel cell industries, which require a higher degree of consideration regarding corrosion. Pros and cons of LPBF and DLD as the leading AM methods to manufacture SS parts were discussed and compared with conventionally manufactured counterparts. The main difference between the two methods is the relatively faster cooling rate during LPBF which results in fewer inclusions and unwanted phases. Moreover, passive film properties and its formation mechanism were elaborated in detail with the effect of process parameters on its quality. The core part of the chapter is a systematic review of the microstructural features of AM SS parts such as porosity level, precipitation of inclusions, residual stress, surface roughness, chemical composition, and elemental segregation, grain size, and phases. In each section, the source of each feature and the effect of AM processing parameters were discussed and its role in the corrosion performance was evaluated.

- The level of porosity and the density of the part can be optimized by applying the right sets of printing parameters. AM SS parts with porosity levels below 1% showed almost identical, or in some cases better, corrosion properties compared to the traditionally made samples. However, current spikes in the anodic branch of polarization curves confirm metastable pit formation due to the presence of pores in the structure.
- Due to the rapid solidification during AM, MnS inclusions and Cr depletion zone sizes are much smaller than in traditionally made samples (nano-scale vs. micro-scale) regardless of the process parameters, resulting in a higher pitting resistance of AM SS parts. A post-heat-

treatment at temperatures above 1000 °C provides enough time for diffusion and the formation of more inclusions, hence, lowering the corrosion resistance.

- The residual stress of AM SSs is a function of build direction, yield strength, process parameters, and shape of the part. The effect of residual stress on corrosion performance is quite complex. Compressive residual stress makes the passive film slightly denser by lowering point defect concentration. However, along with the distortion in the part, residual stress causes micro galvanic couples between regions under tensile stress and compressive stress which are the main pit initiation sites of the part.
- The surface roughness of AM parts is quite higher than other traditional manufacturing methods due to evaporation, balling phenomena, staircase effect, and facing orientation which all can be optimized by controlling the processing parameters. Decreasing the roughness of the surface diminishes the electrochemical reactions between the surface and environment leading to both general and localized corrosion reduction.
- Among alloying elements, Cr and Ni have a positive effect on the corrosion performance whether by forming the passive layer or stabilizing the austenite matrix. O is known to lower the pitting potential of AM SSs. C forms carbides and their precipitation at grain boundaries cause intergranular corrosion. The presence of Mo in the alloy composition is essential for the formation of the passive film and improves the pitting resistance. The high energy associated with the AM process causes spatially heterogeneous composition of SSs and affects the corrosion behavior based on the role of each element.
- The effect of grain size and formation of sub-structure on the corrosion performance of AM SSs is controversial in the literature. The dominant hypothesis is that super high density of sub-grain boundaries of as-fabricated SSs acts as the preferred sites for passive

film nucleation resulting in a more protective surface layer. The shape of grains is important in the SCC performance of AM SSs where the elongated grains cause an anisotropic behavior against crack growth. Grain refinement processes such as heat-treatment and SPD reportedly improves the corrosion performance of stainless steels.

- AM parts produced through LPBF have almost fully austenitic microstructures by selecting proper sets of processing parameters. On the other hand, considering the slower cooling rate during the DLD method, some unwanted phases such as Intracellular δ-ferrite might be formed, which have a lower corrosion resistance compared to the austenite phase. A post-treatment might be needed to achieve a completely austenitic matrix.

Chapter 3. Hot Corrosion Behavior of Nickel-Based Superalloys: A Review

Hot corrosion and oxidation are considered as a major issue in both coal-fired power plants and gas turbines which reduce the lifetime of hot section components as well as increase downtimes and operating costs (Hidalgo, Varela et al. 2001, Prashar and Vasudev 2020). Gas turbine hot section components are subjected to hot corrosion attacks and the intensity of damage is a function of several parameters such as cyclic loading conditions, fuel impurities like Sulphur, sodium, vanadium, potassium, lead, and molybdenum, alloying elements, temperature, and regional atmospheric condition (Stringer 1987, Khajavi and Shariat 2004). The first evidence of hot corrosion was observed in the 1940s in boiler tubes in a coal-fired steam generating plant. However, public awareness was not achieved until the late 1960s after a series of incidents for rescue helicopters and planes during the Vietnam conflict (Rapp 1986, Singh, Puri et al. 2007). Since then, the same problem has been noticed in other industries like internal combustion engines, gas turbines, boilers, industrial waste incinerators, and fluidized bed combustion. In these systems, air to fuel ratio is much more than the stoichiometric values of combustion reactions which results in the presence of hot oxygen-rich gas in the system (Stringer 1987). This excessive oxygen along with the deposited fuel and atmospheric contaminations (such as Na, V, S, and Cl in the form of Na_2SO_4, NaCl, and or V_2O_5) results in a series of reactions lead to the degradation of metallic parts in such environments at elevated temperatures (Lai 2007, Khan, Sundarrajan et al. 2015). A statistical evaluation shows that hot corrosion-related issues are the reason for over 30% of failures in power plants. This percentage is over 55% in the coal-fired boiler (Becker, Shipley et al. 2002, Singh, Puri et al. 2007). For all these reasons, in-service inspections are necessary with non-destructive testing (NDT) methods to reveal anomalies and detect vulnerable sites for hot corrosion attacks. NDT methods such as visual examination, ultrasonic testing, magnetic flux leakage

methods, tomography, liquid penetration testing, gamma and x-radiography, leak testing, interferometry, vibration monitoring, magnetic particle inspection, infrared thermography, eddy current testing, acoustic emission, and laser holograph are reported to be applied successfully in monitoring hot corrosion damages in their early stages and predicting the required maintenance services (Christl, Rahmel et al. 1987, Raj, Jayakumar et al. 1995, Jaykumar, Palanichamy et al. 2001, Mudgal, Singh et al. 2014). On the other hand, it is crucial to evaluate the performance of different alloys in simulated conditions to predict the mechanism of hot corrosion reactions, calculate their expected lifetime, and enable proper material selection. In this chapter, the hot corrosion of different types of nickel-based superalloys, commonly used for turbine blade manufacturing, is reviewed thoroughly including the types of hot corrosion in different environments, mechanisms, the role of alloying elements, and a summary of corrosion control methods.

3.1. Nickel-based superalloys

Nickel Superalloys are mainly developed for applications associated with severe mechanical stress at elevated service temperatures (up to 1000°C) such as gas turbines, nuclear industries, ultra-super-critical power plants, aerospace structures, and pressurized water reactors (PWR) (Pottlacher, Hosaeus et al. 2002, Singh, Puri et al. 2007, El-Awadi, Abdel-Samad et al. 2016, Ramkumar, Abraham et al. 2017). For instance, over 50% of a typical gas turbine is made from superalloys for high temperature and harsh environment application (Wang, Mukherji et al. 1995, Kamal, Jayaganthan et al. 2010). In a coal-fired power generation system, the temperature of the components reaches over 800°C and hot corrosion is a major issue for superheater and reheater materials which can be considerably overcome by using nickel superalloys (Viswanathan, Henry et al. 2005, Aung and Liu 2014). Because of the unique structure of nickel superalloys and

their alloying elements, they can maintain their mechanical properties (strength, creep, and fatigue resistance) at temperature ranges up to 80% of their melting point which is a much higher fraction than any other classes of alloys (Prashar and Vasudev 2020). However, oxidation, sulfidation and hot corrosion attacked are inevitable due to the extreme environment, and the presence of molten salts as a byproduct of fuel combustion results in the degradation of the alloy (Zheng, Schmitz et al. 2012, Mannava, Sambasivarao et al. 2019) and for this reason, it is almost impossible for them to possess both mechanical strength and corrosion resistance at high-temperature ranges simultaneously (Sidhu, Prakash et al. 2006).

Nickel superalloys usually contain different combinations of more than 10 alloying elements including chromium, aluminum, cobalt, molybdenum, iron, titanium, tungsten, etc. (Stoloff 1990, Rahman, Priyadarshan et al. 2009). The high-temperature strength is achieved by solid solution strengthening of the matrix which is the γ phase (FCC) with a secondary participate phase enriched of aluminum, titanium, molybdenum, etc. (Pollock and Tin 2006, Tan, Ren et al. 2008, Khan, Sundarrajan et al. 2014). Among the mentioned alloying elements, chromium and aluminum are well known for the formation of a protective dense oxide layer on the surface that secures the high-temperature corrosion resistance (Singh, Puri et al. 2005, Asala, Andersson et al. 2019). Thus, the hot corrosion rate is controlled by the inward diffusion of oxygen through this protective layer or outward diffusion of alloying elements from the matrix (Liu, Ma et al. 2010). Other alloying elements are mainly added to improve the mechanical properties at elevated temperature by whether solid solution hardening (Mo and W) or the formation of γ' phase at grain boundaries (Al and Ta) (El-Awadi, Abdel-Samad et al. 2016). Although outstanding mechanical properties is the number one priority in materials selection and alloy designing process based on their application, the enhancement of high-temperature corrosion performance should be carefully

considered as well to prevent catastrophic incidents and develop new alloys capable of enduring harsher environments (Das 2013, Fesharaki, Shoja-Razavi et al. 2019). The rest of this chapter is a summary of some nickel superalloys which are widely used in industries involving environments with hot corrosion reactions.

3.1.1. Inconel 617

This nickel-based superalloy is a solid solution strengthened superalloy by precipitation of $M_{23}C_6$ carbides and contains nickel, chromium, cobalt, aluminum, and molybdenum as the main alloying elements. Among these elements, cobalt and molybdenum are responsible for improving mechanical properties by solid solution strengthening and providing promising creep resistance compared to other alloys of this class (Yeh, Chang et al. 2014, Hari, Arivazhagan et al. 2020). High chromium and aluminum contents secure the outstanding hot corrosion performance and superior oxidation resistance of the alloy in different pressurized environments for temperature ranges above 800°C (Homaeian and Alizadeh 2016). However, using low-grade fuels makes it susceptible to hot corrosion attacks which should be addressed (Bhuyan, Pradhan et al. 2019).

3.1.2. Inconel 625

Inconel 625 is known as a high chromium and molybdenum nickel-based superalloy. In this alloy, molybdenum, and niobium are distributed in the nickel-chromium FCC matrix and provide a decent combination of creep, yield, and fatigue strength without any precipitation heat-treatment process (Sims, Stoloff et al. 1987, Kashaev, Horstmann et al. 2013). Moreover, the formation of MC and M_6C carbides enriched of Ni, Nb, and Mo might further improve the mechanical properties (Ramkumar, Abraham et al. 2017). From a corrosion point of view, chromium improves the corrosion performance at elevated temperatures and Molybdenum contributes to decreasing the pitting corrosion. For these reasons, this alloy is a good candidate to

be used in harsh industrial environments with the presence of chloride ions along with the high pressure and temperature (Wang, Li et al. 2017, Khorsand, Sheikhi et al. 2018). To further improve the hardness and wear resistance of Inconel 625, some methods such as adding ceramic particles (TiC and CrC) to the structure have been proposed (Nurminen, Näkki et al. 2009, Wilson and Shin 2012). However, this process might deteriorate the corrosion performance due to the formation of galvanic coupling, the formation of an interfacial phase, process contamination, and microstructural change (Bakkar and Ataya 2014, Bakkar, Ahmed et al. 2019).

3.1.3. Inconel 718

Inconel 718 is the most widely utilized precipitation hardened nickel-based superalloys for manufacturing hot section components in critical applications because of its mechanical strength, high-temperature creep, excellent weldability, and high-temperature corrosion resistance. This alloy consists of γ phase matrix and precipitate phases such as γ′-Ni_3(Al, Ti) and γ″- Ni_3(Nb, Ta) which are coherent to the γ matrix. The presence of Nb leads to the formation of the γ″ phase which is sluggish in precipitation and improves hot cracking by delaying age-hardening (Eliaz, Shemesh et al. 2002, Ramkumar, Abraham et al. 2017, Ramkumar, Bhalodi et al. 2017, Pradhan, Mahobia et al. 2018, Nabavi, Goodarzi et al. 2019). γ″ phase also provides better weldability due to the lower level of Al and Ti compared to other superalloys strengthened by γ′ phase. However, considering the transformation of body-centered tetragonal γ″ phase to orthorhombic δ phase above 650°C and substantial deterioration of weldability and corrosion performance, this temperature is assumed as a restriction for Inconel 718 applications. Despite several research projects that have been performed to improve the stability range of the γ″ phase, limited success has been achieved (Sjöberg, Imamovic et al. 2004, Valle, Santana et al. 2019). Furthermore, like most of the superalloys, high-temperature corrosion resistance of Inconel 718 is attributed to the

formation of protective chromium oxide on the surface as a result of selective oxidation of chromium. However, this layer becomes unstable over 1000°C which is a threshold for the application of any alloy with the mentioned protection mechanism (Pérez, Hierro et al. 2001, Wang and Chen 2006). The presence of sodium chloride in the service environment of this alloy (i.e. coastal areas) leads to the hot corrosion attacks in the form of pits formation, depletion from alloying elements, and internal sulfidation or oxidation (Kumar, Satapathy et al. 2019).

3.1.4. Inconel 738

Inconel 738 can withstand up to 980°C of service temperature due to its modified microstructure. It is a precipitation hardening superalloy which is mainly hardened by ordered γ′ phase in the disordered γ matrix. In parallel, the hardening of this alloy is also achieved by grain boundary strengthening (carbides and γ′) and solid solution strengthening (Cr, Co, W, and Mo) (Fahrmann and Metzler 2016, Ramakrishnan and Dinda 2019). Depends on the manufacturing and heat treatment process, several precipitates such as $M_{23}C_6$ and MC carbides and γ′ with different shapes might be formed and affect the final properties of the alloy. The reason for the outstanding mechanical behavior of this alloy at extremely high temperature is the formation of up to 30-80% volume fraction of the γ′ phase in the matrix (SUN, ZHONG et al. 2005, Sidhu, Ojo et al. 2007, Ramakrishnan and Dinda 2019). Despite the relatively high percentage of Al and Ti in this alloy which makes the repairing of damaged surface challenging, Inconel 738 is widely used in hot sections of gas turbines due to its excellent hot corrosion performance and exceptional elevated temperature strength (Ojo, Richards et al. 2004, Egbewande, Buckson et al. 2010).

3.1.5. Inconel 740

Inconel 740 is the modified version of the Nimonic 263 superalloy for increased corrosion resistance by increasing Cr and decreasing Mo contents. Reports show that this modification has

also led to the higher strength of the alloy (Zhao, Xie et al. 2004, Jin-tao, Yan et al. 2018). The microstructure of this superalloy consists of several phases such as γ matrix, γ′ precipitate, γ–γ′ eutectic, and some others such as carbides. At high temperatures, undesirable phase transformation of γ′ to η, coarsening of γ′ and the formations of G phase cause its failure to fulfill the requirements. However, these adverse structural changes do not occur below 750°C which is considered as the safe temperature for Inconel 740 applications (Zhao, Xie et al. 2006, Xie, Zhao et al. 2008, Aung and Liu 2014). A study shows that a higher mechanical strength and structural stability can be achieved by increasing the Nb content of this alloy and adjust Al, Ti, and Si simultaneously to maintain excellent corrosion performance. Increasing Cr content is not an option since it facilitates the formation of the harmful σ phase (Zhao, Xie et al. 2006).

3.1.6. Inconel 783

A low coefficient of thermal expansion (CTE) is essential for some applications of superalloys to keep the tight clearance between the blade tip and case at a high service temperature of gas turbines (Kang, Liu et al. 2003). The low CTE of the first generation superalloys such as alloys 907 and 909 was achieved by the sole decrease of chromium content which deteriorated the corrosion resistance at high temperature (Smith and Heck 1996). Inconel 783 has been newly designed specifically for this purpose by keeping the Cr content at low levels and increase Al content of the alloy that results in the formation of Aluminide phase along with γ' in the austenitic γ matrix to improve high-temperature performance as well as about 5% of reduction in the density compared to Inconel 718. It is discovered that low CTE, oxidation resistance, and mechanical properties of this alloy is associated with the described structure and Al/Cr content (Heck, Smith et al. 1998).

3.1.7. Inconel 825

Also known as Incoloy 825, is a nickel-based superalloy stabilized by Ti to improve corrosion attacks in the form of intergranular corrosion or pitting (Arivarasu, Roshith et al. 2017). Due to its resistance to Sulfuric and phosphoric acids as well as crevice corrosion and stress corrosion cracking, a broad spectrum of applications both in low and elevated temperatures have been recognized for this alloy (Muthu, Arivarasu et al. 2019).

3.1.8. Inconel 939

As a γ' hardening alloy, Inconel 939 (also known as Nimocast 739) can be used for turbine blades up to service temperature of 850°C (Durand-Charre 1998, Zhu, Wise et al. 2013). A higher volume fraction γ' phase is essential to assure the mechanical properties of the alloy and can be formed by a proper heat treatment design. The composition of this nickel-based superalloy is in a way to improve its weldability compared to other alloys with a reduced risk of heat affected zone cracking during welding (Sjöberg, Imamovic et al. 2004). Stable σ-phase microstructure, fair corrosion resistance, appropriate impact properties, maintaining tensile and creep properties after long service time, and decent castability also makes of this alloy one of the few candidates for some high-temperature applications. At high service temperature, a surface oxide layer can be formed at the expense of leaving a depletion zone behind with a unique Ni matrix and other unknown phases that are still under study (Gibbons and Stickler 1982, Zhu, Wise et al. 2013, Shaikh 2018, Dodaran, Ettefagh et al. 2020).

3.1.9. TMS-138

This alloy is developed as the fourth generation of nickel-based superalloys which has outstanding mechanical properties compared to previous generations and makes it a good fit for manufacturing high-temperature turbine blades for jet engines (AOKI 2003). Re and Ru content

of TMS-138, as well as a large negative lattice misfit between γ and γ' phases, are the main reasons for drastic improvement in phase stability and remarkable creep and fatigue properties at elevated temperature (Zhang, Murakumo et al. 2002, Zhang, Murakumo et al. 2003, Zhou, Ro et al. 2004). However, due to insufficient amount of Cr and Al in the alloy composition, a post-treatment such as aluminide coating is necessary to make the hot corrosion performance comparable to other nickel-based superalloys (Kawagishi, Sato et al. 2009, Montero, Ishida et al. 2020).

3.1.10. Ni−20Cr−18W

In this alloy, both carbide precipitation and solid solution mechanisms are responsible for strengthening of the alloy. Cr and W are added to provide solid solution the strengthening. Studies show acceptable oxidation resistance due to the Cr content as well as high-temperature plasticity and strength in different conditions (Hu, Bai et al. 2012, Zhang, Dong et al. 2015).

3.2. Hot corrosion

Two classes of damages have been recognized for nickel-based superalloy turbine blades at severe operating conditions. First, damages due to mechanical and thermal stresses as a result of the thermal gradient, centrifugal force, aerodynamic force, etc. For this type, research topics are focused on the mechanical properties of superalloys namely low cycle and thermal fatigue and creep (Kargarnejad and Djavanroodi 2012, Yang, Li et al. 2015). The Second class of damages is those associated with the environmental attacks to the blades because of some factors like high temperature, air and fuel contamination, solid particles, etc. which result in hot corrosion and erosion attacks independently or simultaneously (Błachnio 2011, Kosieniak, Biesiada et al. 2012, Zeng, Zhang et al. 2020). Nickel-based superalloys suffer from accelerated oxidation at elevated temperature in an oxidizing atmosphere. This phenomenon is known as hot corrosion of the alloy where the formation of a porous non-protective layer of oxide on the surface and internal

sulfidation do not involve any aqueous electrolytes (Rapp and Zhang 1994). Unlike oxidation, the rate of this type of damage is unpredictably fast and leads to catastrophic failures due to de-alloying, loss of surface strength, and crack initiation in case of not addressing (Zheng, Maicang et al. 2011). Hot corrosion damages have been reported since the 1940s, however, it became a hot topic in the 60s after some alleged failures in military aircrafts (Sidhu, Agrawal et al. 2005). Several parameters affect the severity of hot corrosion attacks, namely operating temperature, flux velocity of the salt, SO_2 content of the gas, and history of alloy (Aung and Liu 2013, Nabavi, Goodarzi et al. 2019). Hot corrosion attack is mainly due to the formation of some contamination and salts in the working environment of superalloys attributed to some elements like Na, V, S, and Cl and their reactions in the combustion system. These elements have different sources, for instance, Na and S (~0.4%) present in the fuel or intake air. Moreover, NaCl (~1%) comes from the marine atmosphere, brings Cl ions to the system, and accelerates the formation of Na_2SO_4 (Luthra and Spacil 1982, Deb, Iyer et al. 1996, Khan, Sundarrajan et al. 2014, Saladi, Menghani et al. 2015). It is reported that a minimum amount of 0.008 ppm of Na is needed in the service environment to initiate the corrosion attack (Eliaz, Shemesh et al. 2002). NaCl can also dissolve surface Cr_2O_3 to form $Na_2Cr_2O_7$ and chromium chloride (Equation 3-1 and Equation 3-2) which can be easily evaporated and make some pits in the alloy (Kameswari 1986, Gurrappa 1999, Mannava, Rao et al. 2016). The damaging effect of Cl in the system is either by the formation of volatile chlorides or its synergism with sulfates which both accelerate the metal loss rate (Reid 1971). Furthermore, low-grade fuels, which are extensively used to reduce the operation costs, contain V (<500 ppm) and the presence of this element in the form of vanadium porphyrin (which then transforms to V_2O_5 during the operation) is almost inevitable in turbine environment (Barbooti, Al-Madfai et al. 1988, Kamal, Jayaganthan et al. 2010, Salehnasab, Poursaeidi et al.

2016). Depends on the V content of the deposits on the surface, eutectic salts with the melting point as low as 530°C can be formed, and therefore a broader temperature range for hot corrosion attack is expected. Moreover, the mixture of V compounds with Na_2SO_4, i.e. sodium metavanadate (Equation 3-3) has a low temperature (610°C) and a high solubility for protective oxides according to Equation 3-4 which markedly accelerate hot corrosion rate. It has been claimed that increasing the V content to 5 wt% exacerbates the corrosion kinetics values by 300% (Hancock 1987, Swaminathan, Raghavan et al. 1993, Rapp and Zhang 1994, Khan, Sundarrajan et al. 2015).

$$Cr_2O_3 + Na_2O + {}^3/_2\, O_2 \rightarrow Na_2Cr_2O_7 \qquad \text{Equation 3-1}$$

$$2Cr_2O_3 + 6Cl_2 \rightarrow 4CrCl_3 + 2O_2 \qquad \text{Equation 3-2}$$

$$Na_2SO_4 + V_2O_5 \rightarrow 2NaVO_3 + SO_3 \qquad \text{Equation 3-3}$$

$$Cr_2O_3 + 4NaVO_3 + {}^3/_2\, O_2 \rightarrow 2Na_2CrO_4 + 2V_2O_5 \qquad \text{Equation 3-4}$$

The deposited salt, also known as ash, damages the protective oxide layer via a series of chemical or electrochemical reactions. The main source of the salts is via the intake air and can be deposited on the part based on two mechanisms. The first mechanism is known as vapor deposition where salt spices are introduced to the combustion process after being vaporized and then condensed on the surface of the superalloy. A salt layer may also build up on the surface after the sticking of solid-state salt particles. The dominant mechanism is determined by the ambient condition in a certain spot as well as the part shape and can be a combination of two mentioned mechanisms (Santoro, Gokoglu et al. 1984, Tomeczek, Palugniok et al. 2004, Birello, Borello et al. 2013). The salt composition is related to the application and working environment of superalloy and can be a combination of one or more of Na_2SO_4 (melting point 884°C), V_2O_5 (melting point 670°C), and NaCl salts in the majority of cases (Reid 1971, Yang, Li et al. 2015). However,

Na_2SO_4 is considered as the prerequisite of hot corrosion attacks which can be promoted at the presence of other mentioned salts; namely, a combination of Na_2SO_4 and NaCl is much corrosive than each individual of these salts (Singh, Puri et al. 2007, Saladi, Menghani et al. 2014, Mannava, Sambasivarao et al. 2019). Various concentrations of Na_2SO_4 have been considered in corrosion studies of superalloys. For instance, it is more than 75% for turbine engines in the marine environment as opposed to less than 40% for aircraft and other land-based applications (Khan, Sundarrajan et al. 2015, Ramkumar, Bhalodi et al. 2017).

At working temperature range of superalloys (500-1000°C), the salt layer melts and starts degradation of the sublayer by acting as an ionic electrolyte to diffuse oxidizing compounds into the substrate and cause pitting and/or intergranular corrosion attacks (Fernández, Lasanta et al. 2012, Dorcheh, Durham et al. 2016). Although the service temperature might be lower than the melting point of each individual salt, a low melting point eutectic mixture is formed which increases the risk of attack even at temperatures as low as 550°C (Hejwowski 2006, Kamal, Jayaganthan et al. 2010). This thin film of molten salt may either combine with the protective oxide layer and forms onions, which is known as basic fluxing or decompose the protective layer into oxygen ion and cations which are known as acidic fluxing in this case (Rapp 2002, Sidhu, Agrawal et al. 2005). For instance, the acidic flux of protective Cr_2O_3 is in the form of $Cr_2(SO_4)_3$, while its basic flux form is Na_2CrO_4 (Pettit, Meier et al. 1984). Although both of these compounds are known as non-protective layers, acidic fluxing is more severe since its self-sustaining nature and occurrence at lower oxygen activities in the molten salt. Basic fluxing typically occurs at a lower partial pressure of SO_3 through the reaction of surface oxides with O^{2-} or Na_2O (Mannava, Rao et al. 2016, Prashar and Vasudev 2020).

Hot corrosion degradation proceeds through three distinct stages. The first step is incubation where the metal oxide starts forming on the surface in the absence of molten salts. As long as these protective oxides line Cr_2O_3 and Al_2O_3 are stable, the alloy will remain in this stage. In the second stage (initiation), the oxide growth develops internal stress and causes spalling or cracking of the surface oxide layer and exposure of the fresh substrate to the molten salt which increases the corrosion rate. Finally, during the propagation stage, the basic or acidic flux of the oxide takes place depends on the partial pressure of oxygen (Rapp and Zhang 1994, Pettit 2011). Cl content of the salt forms chloride compounds in the pore with a high tendency to react with alloying elements such as Cr and Al and diffuse them out of the alloy structure in the form of metal chlorides which then transform to non-protective oxides on the surface. Due to the de-alloying reactions and formation of a porous oxide on the surface, the degradation rate in the propagation stage is much larger than the initiation stage and the part should be removed immediately from service by the start of this stage. However, to decrease failure costs of the system, the main focus should be on the initiation stage from a technical point of view (Stringer 1987, Aung and Liu 2013).

3.2.1. Types of hot corrosions

Depends on many factors like the temperature of corrosive media, thermodynamic conditions, alloy type, and corrosion products, two types of hot corrosion may occur. High temperature hot corrosion (HTHC) is titled as type-I and takes place at a temperature range where Na_2SO_4 can be present in a molten state (~750-950°C) (Pradhan, Mahobia et al. 2018). Na comes from either the marine environment or the fuel and directly reacts with the existing sulfur of the fuel. Moreover, in presence of a small amount of sulfur, NaCl becomes unstable and which can

easily lead to the formation of Na_2SO_4 via several oxidizing reactions like Equation 3-5 and Equation 3-6 (Salehnasab, Poursaeidi et al. 2016):

$$2NaCl + SO_2 + O_2 \rightarrow Na_2SO_4 + Cl_2 \qquad \text{Equation 3-5}$$

$$2NaCl + SO_3 + H_2O \rightarrow Na_2SO_4 + 2HCl \qquad \text{Equation 3-6}$$

Besides, NaCl eliminates the incubation stage in the progress of hot corrosion reactions (Stringer 1987). The existence of other impurities like V, P, Cl, etc. lowers the melting point of the salt and broadens the temperature range of Type-I hot corrosion. A series of chemical reactions between the molten salt and base metal gives rise to the formation of a porous non-protective outer layer prone to spalling off and leaves a Cr depleted zone in the base metal which increases the oxidation rate of the region. There might be other alloying elements oxides and sulfides underneath the outer porous layer (Eliaz, Shemesh et al. 2002, Rapp 2002). It is stated that crystal orientation and surface finish of the base alloy can impact this type of hot corrosion. Additionally, K_2SO_4 is reported to have the same impact on HTHC as Na_2SO_4 and should be addressed in the calculation of the effective impurities of air or fuel (Eliaz, Shemesh et al. 2002, Montero, Ishida et al. 2020). At the first stage of HTHC, the surface roughness increases due to the growth and partial breakdown of the oxide layer. However, mechanical properties are still not affected since the Cr depletion zone has not been formed yet. By continuing the breakdown and a further increase in surface roughness, the Cr depletion zone starts to form. The escalation in depth of this zone sacrifices the mechanical properties and removal of the part from service should be considered rigorously. Otherwise, a catastrophic failure is highly probable due to the loss of mechanical integrity (Eliaz, Shemesh et al. 2002). Generally, type-I of hot corrosion is characterized by a porous non-protective surface layer and a Cr depletion area beneath that (Rapp 1987). Due to its

importance for nickel-superalloys, the mechanism of HTHC will be elaborated with more details in the next section.

Type-II is low-temperature hot corrosion (LTHC) in which Na_2SO_4 reacts with the base metal sulfates such as (Ni, Fe, Co)SO_4 to form a low melting point eutectic like Na_2SO_4-$NiSO_4$, causing degradation of nickel-based superalloys at the temperature range of ~550–750°C by preventing a protective layer to be formed. The high partial pressure of SO_3 in the environment is required in the case of LTHC for the formation of eutectic compounds and sustaining the hot corrosion reactions at a moderate temperature range. The source of sulfur is either air or fuel contaminations (Luthra 1982, Yang, Li et al. 2015, Brooking, Gray et al. 2018). Unlike HTHC where sulfidation is improbable due to instability of sulfate compounds, in LTHC, the failure is typically due to the formation of pits at high-stress sites as an outcome of internal sulfidation and neither the incubation stage nor Cr depletion zone is reported in this type (Stringer 1987, Lu 2011, Salehnasab, Poursaeidi et al. 2016, Kumar, Satapathy et al. 2019). Counter migration of SO_3 and alloying elements of the substrate is the essential stage for the propagation of LTHC attacks on nickel-based superalloys (Shih, Zhang et al. 1989, Aung and Liu 2013). It is necessary to mention that both types of hot corrosion may be detected in a single system. for instance, the leading edge and high-pressure side of the turbine blade are the frontlines to be exposed to sulfur and other contaminations with high temperature and suffer from type-I, while the colder regions experience type-II of hot corrosion (Montero, Ishida et al. 2020).

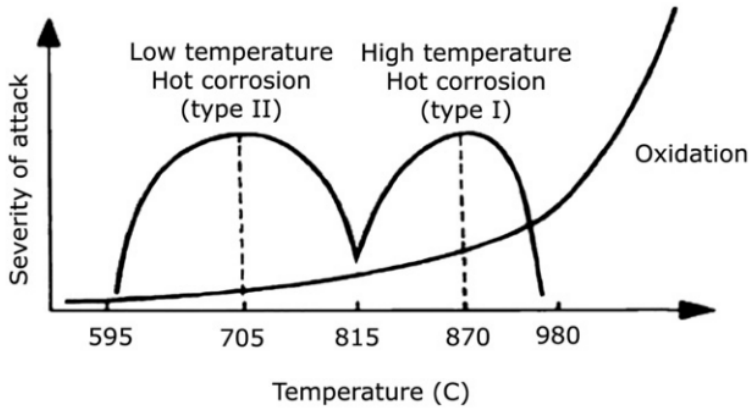

Figure 3-1- Schematic diagram for Type I and Type II hot corrosions (Salehnasab, Poursaeidi et al. 2016).

3.2.2. HTHC Mechanism

The rate of hot corrosion is a function of several factors i.e. fabrication condition, alloy composition, the velocity of gas and its composition, deposit rate of the salt and its composition, temperature, erosion, and sample geometry (Singh, Puri et al. 2007). In the absence of salt deposit, oxygen reacts selectively with alloying elements namely Cr to form a protective oxide layer on the surface. Inward diffusion of oxygen and outward diffusion of Cr is essential after the formation of the very first layer of oxide. The formed Cr_2O_3 layer protects the substrate and decreases the oxidation rate significantly after growing to a certain thickness by blocking the further diffusion of oxygen and alloying elements. Cr_2O_3 is the most thermodynamically stable oxide and progress of oxidation is negligible after its formation. Some other protective compounds such as $NiCr_2O_4$ spinel might be formed as well during this process according to Equation 3-7 (Stott 1987). While the diffusion coefficient of anions and cations is relatively lower in the spinel phase than the oxide phases, further protection is expected if spinel phases exist (Mahesh, Jayaganthan et al. 2008, Kamal, Jayaganthan et al. 2011). The main reported damages in the initiation stage are attributed to the loss of the protective layer as a result of erosion, thermal stress, chemical reactions, etc.

which lead to the direct contact of a corrosive environment with the bare alloy (Eliaz, Shemesh et al. 2002). This mechanism is more or less the same for the first stage of hot corrosion reactions (initiation) at the presence of molten salts (Birks, Meier et al. 2006). However, the presence of molten salts leads to the flux of the oxide layer and loss of its protective properties in the propagation stage. The oxide layer fluxing mechanism was first introduced in the early 70s and can occur either in the form of basic or acidic (Goebel and Pettit 1970, Goebel and Pettit 1970). Based on this model, there is a solubility gradient of the oxide in the salt layer which is higher at the interface of salt/oxide. Hence, the oxide layer dissolves in the molten salt and re-precipitates in the form of non-protective oxide film on its way toward the salt/gas interface where the solubility is minimum. The main driving force for this set of reactions is the variation of oxygen activity in the molten salt which justifies the self-sustaining nature of hot corrosion attacks (Stringer 1987, Zhang, Hu et al. 1993). Studies show that the main fluxing mechanism for superalloys with a high content of Cr and Al is basic where surface oxides combine with oxygen ion to form anions. These reactions increase sulfur ion activity locally which facilitates the formation of FeS and $NaCrS_2$ as well as vanadates (Davis 1997, Kumar, Satapathy et al. 2019). Acidic fluxing takes place in lower oxygen activity in the molten salt and leads to the decomposition of oxides to oxygen anion and cations. Although acid fluxing is self-sustained and results in a much more severe oxidation damages, it is unlikely to occur in nickel-based superalloys unless V presents in the salt mixture. According to the literature, V forms V_2O_5 which is a very strong acidic oxide and causes the acidic flux of the protective layer. Moreover, the presence of vanadates in the molten salt increases the solubility of oxides dramatically (Sims and Hagel 1972, Goebel, Pettit et al. 1973, Zhang and Rapp 1987). Generally, it is reported that alloys with a high content of V, Mo, and W follow acidic fluxing in the propagation stage. These elements react with

Na_2SO_4 to form oxides which decrease the oxygen ion activity in the molten salt. This decrease turns the molten salt to an appropriate media for acidic fluxing of the oxide layer (Stringer 1987, Eliaz, Shemesh et al. 2002, Sidhu, Agrawal et al. 2005, Singh, Puri et al. 2007).

$$NiO + Cr_2O_3 \rightarrow NiCr_2O_4 \qquad \text{Equation 3-7}$$

$$FeO + (Cr,Al)_2O_3 \rightarrow Fe(Cr,Al)_2O_4 \qquad \text{Equation 3-8}$$

Continuing the fluxing, protective properties of surface oxide layer losses, and molten salt reaches the substrate. Cr from the substrate diffuses outward to react with the molten salt and leaves a Cr-depletion region behind which is highly prone to suffer from corrosion attacks. Furthermore, the formed oxides on the surface are non-protective and porous that facilitates the inward diffusion of S and formation of low melting point eutectic sulfides underneath the surface layer (El-Awadi, Abdel-Samad et al. 2016). In general, layers such as an outer oxide, inner oxide, Cr-depletion region, and internal sulfides can be detected after hot corrosion attacks. The inner oxide layer is thinner, contains less amount of cracks and inclusions, and is considered relatively more protective than the outer layer (Zhang, Dong et al. 2015). As the process proceeds, other alloying elements also diffuse outward to be oxidized and make the non-protective surface layer thicker which eventually spalled off (Lai 2007). However, the composition of the protective layer and the following corrosion products depends on the type of alloy. It is reported that for alloys containing a small amount of Al, the inner oxide layer is Al_2O_3 underneath a top layer of Cr_2O_3 (Knutsson, Lai et al. 2013). For instance, in the propagation stage of Inconel 740, SO_3 diffuses inward through the previously formed oxide layers to react with Co of the base alloy. After this stage, the outer porous layer mainly consists of some spinels such as $Ni_2Cr_2O_4$ and $Fe(Cr,Al)_2O_4$ according to Equation 3-7 and Equation 3-8 on top of loose flakes of Cr_2O_3, Al_2O_3, and TiO_2 with some content of nickel, cobalt, potassium and sulfur elements. Internal sulfidation also occurs in

Cr depletion region (Zhao, Xie et al. 2004, Zhao, Xie et al. 2005, Aung and Liu 2013). Another study indicates the initial oxidation of Cr, Fe, and Ni to form a protective layer on Inconel 718, however, the formation of these heavy oxides increases the risk of scale spallation. Although at the very first stage, Nb diffuses rapidly along the grain boundaries and form $CrNbO_4$ on the surface, Cr_2O_3 is formed at a faster pace which prevents the further diffusion of Nb. The enrichment of Nb in the oxide/substrate interface leads to the formation of the Ni_3Nb intermetallic phase which is believed to act as a diffusion barrier (DelaunayRID, Berthier et al. 2000). By increasing the time of exposure, Cl penetrates toward the substrate and forms some pits after the evaporation metal chlorides. Accordingly, sulfides are formed as a result of S reaction with Fe, Cr, and Ni which depletes Cr from the substrate (Ramkumar, Abraham et al. 2017, Pradhan, Mahobia et al. 2018, Pradhan, Mahobia et al. 2018). According to a study, the formed oxide on Inconel 738 shows a double-layer structure. The thicker outer layer is mainly Cr_2O_3 with a small amount of (Ni, Co)Cr_20_4 spinel while the inner one is a thin layer of TiO_2. Beneath these two layers, internal oxidation of Al takes place causes a depletion region of the γ′ phase and deterioration of mechanical properties (Pieraggi 1987). For GH4169 nickel-based superalloy, sulfidation of nickel substrate is evident. During the hot corrosion process, Cr and Fe diffuse outward to the surface and the oxidation of these alloying elements causes a depletion region in the substrate as well as decreasing the oxygen pressure on the surface. Lack of Cr and Fe in the depletion zone triggers the sulfidation of Ni and the formation of sulfides such as $NiSO_4$ and Ni_3S_2 with a very high thermal expansion coefficient. The progress in sulfidation leads to some cracks and cavities in the oxide layer. On the other hand, the protective oxide layer is dissolved by the molten salt and the newly formed layer is more porous. Hence, the deterioration of this alloy is reported to be a combination of oxidation and sulfidation at elevated temperatures (He, Lin et al. 2019, Yu, Liu et

al. 2019). The presence of some protective oxides such as NiO and NbO along with Cr_2O_3 in the formed protective layer of Inconel 625 which reduces the susceptibility to hot corrosion at high service temperature (Ramkumar, Abraham et al. 2017). For Nomonic263 alloy, initially, the protective surface oxide consists of NiO, Cr_2O_3, TiO_2, Co_3O_4, and Al_2O_3. However, V_2O_5 dissolve these oxides either through basic fluxing (in case of NiO, Cr_2O_3, and Al_2O_3) or by acidic fluxing (for Co_3O_4 and TiO_2) which accelerated the penetration of Cl toward the substrate to form volatile chlorides with Ni and Cl. The remained pits after the evaporation of chlorides act as crack initiators in the process (Gurrappa 1999, Mannava, Sambasivarao et al. 2019).

The progress of corrosion damages to the substrate is a function of several factors such as crystal orientation and characteristics, grain boundaries, and atomic structure (Randle 2010, Yanqiu, Zhixun et al. 2020). The importance of atomic density on type-I of hot corrosion has been confirmed. For instance, it has been shown that the corrosion rate of DD6 nickel-based superalloy on (001) plane is the lowest due to its high atomic packing density and more compact formed oxides. With the same rationalization, (111) and (011) planes are the next orientations with the lowest hot corrosion rate (Montero, Ishida et al. 2020, Yanqiu, Zhixun et al. 2020). Some other studies show that interconnected random high angle grain boundaries (RHAGB) help to propagate the corrosion damages to the core by facilitating the diffusion of S, O, and other oxidants such as N and C. The formation of carbides, sulfides, and oxides along the grain boundaries increases the hot corrosion depth of damage as a result of RHAGHBs network (Young, Nguyen et al. 2014, Pradhan, Bhuyan et al. 2018, Bhuyan, Pradhan et al. 2019). Surface finish is another important factor in the hot corrosion performance of nickel-based superalloys. It has been shown that generated dislocations during the surface grinding of fine polishing accelerate the diffusion of Al toward the surface and formation of protective Al_2O_3. Nonetheless, the sample with a mirror

surface after the electro-polishing process formed Al_2O_3 under a thick external NiO layer (Sudbrack, Beckett et al. 2015).

Typically, the hot corrosion performance of nickel-based superalloys follows a parabolic behavior which can be represented by Equation 3-9 and can be used to calculate K_p through experimental measurements. A higher calculated K_p shows lower resistance of superalloy to hot corrosion attacks.

$$\Delta W^2 = K_p t + A \qquad \text{Equation 3-9}$$

In this equation, t is the exposure time and M is the weight gain per surface area of the specimen. K_p is called the parabolic rate constant which is a temperature-dependent value and can be expressed using the Arrhenius equation (Equation 3-10).

$$K_p = K_o \exp(-\frac{Q}{RT}) \qquad \text{Equation 3-10}$$

In this equation, K_o is a constant, R is the gas constant, T is the temperature, and Q is the activation energy for hot corrosion reaction. One can calculate Q by plotting $\ln K_P$ vs. 1/T from the collected weight gain values from experimental data and calculated K_P from Equation 3-9. Both K_P and Q parameters can be applied to compare the hot corrosion performance of two samples. A larger value of K_P is an indication of a higher rate of corrosion kinetic. Besides, the lower value of Q shows a higher tendency to corrosion reactions from a thermodynamics point of view (Deb, Iyer et al. 1996, Garip and Ozdemir 2019).

3.3. Effect of alloying elements

The outstanding properties of nickel-based superalloys such as strength, toughness, and hot corrosion resistance are a direct outcome of numerous alloying elements in the chemical composition and the thermochemical history. Mn, Si, B, and Zr are mainly added to the alloy for mechanical purposes like grain boundary refining and there is no solid evidence for their impact

on hot corrosion properties (Gurrappa 2003, Shaikh 2018). A small amount of Al in the alloy can improve the hot corrosion and oxidation performance by promoting the protective scale adhesion, minimizing fluxing, and forming protective Al_2O_3 instead of fast-growing spinels (Stringer 1977, Darolia 2019, Ettefagh, Zeng et al. 2019). However, some elements such as W, V, and Mo have a detrimental impact on the corrosion resistance at elevated temperatures. Thus, a compromise should be considered in alloy design procedure in case of using bare alloy in the harsh environment (Otsuka and Rapp 1990, Eliaz, Shemesh et al. 2002). In this section, the effects of some of the major alloying elements on the hot corrosion performance of nickel-based superalloys are discussed.

Chromium is the main alloying element that is added to improve the hot corrosion performance of nickel-based superalloys. Studies show that at least 15 wt% of Cr is needed in the alloy composition to achieve a decent resistance against hot corrosion attacks, especially HTHC. Some literature even reports a higher minimum for these criteria (Stringer 1987, Gagliano, Hack et al. 2009). The positive impact of Cr on hot corrosion performance is attributed to the initial formation of a continuous and adherent layer of Cr_2O_3 and its reaction with the molten salt to stabilize the melt chemistry. Stable compounds such as Na_2CrO_4 have been formed as a result of Cr_2O_3 dissolution in molten Na_2SO_4 and keep the acidity/basicity of the salt in an optimum range which is not enough neither for basic nor acidic fluxing. This chemistry stabilization prevents further dissolution of the protective oxide layer (Goebel, Pettit et al. 1973, Chang, Wang et al. 2017). Other positive impacts like the self-healing ability of Cr_2O_3 and suppressing the formation of deleterious sulfides (i.e. nickel sulfide and aluminum sulfide) have been mentioned for the Cr role in improving hot corrosion properties (Murata, Hashizume et al. 2000, Bürgel, Grossmann et al. 2004, Ettefagh and Guo 2018). However, TCP phases might be formed at high Cr content which

deteriorates the strength and ductility of the superalloy at high temperature. Adding refractory elements like Mo, W, Re, and Ta with limited Cr content is claimed to eliminate this risk and maintain the hot corrosion resistance (Bürgel, Grossmann et al. 2004, Reed 2008). Other than improving high-temperature oxidation and sulfidation of nickel-based superalloys, Cr is known as a solid solution strengthener and carbide former (Cr_7C_3 and $Cr_{23}C_6$) form mechanical properties point of view (Donachie and Donachie 2002, Shaikh 2018, Prashar and Vasudev 2020).

Cobalt is mainly added to nickel-based superalloys to improve their high-temperature creep, tensile strength, and other mechanical properties as well as welding performance through solid solution strengthening and raising solvus temperature of γ′ phase (Donachie and Donachie 2002, Shaikh 2018). However, the effect of Co on hot corrosion performance is not as important as other alloying elements. A few studies have been performed to validate the minute changes in hot corrosion resistance caused by adding Co. It has been claimed that Co facilitates the formation of protective Cr_2O_3 and Al_2O_3 in some superalloys (Task, Gleeson et al. 2011, Qiao and Zhou 2012, Lu, Huang et al. 2018). Besides, the diffusion coefficient of S in Co is half of the same value for Ni which shows the possibility of increasing Co content to decrease internal sulfidation. This is especially important to develop corrosion resistive coatings (Beltran, Lindblad et al. 1975).

Molybdenum is typically added to nickel-based superalloys as a solid solution strengthener and carbide former (MoC, $Mo_{23}C_6$, and Mo_6C) (Shaikh 2018). It is reported that Mo forms acidic salt enriched of SO_2 after the reaction of MoO_2 with Na_2SO_4 which significantly increases the hot corrosion rate of the alloy and ultimately leads to catastrophic failure of the component due to acidic fluxing. Other compounds such as Na_2MoO_4, $Na_2MoO_4.2MoO_4$, and $Na_2MoO_4.MoO_3$ are produced from MoO_3 (Equation 3-11 as an example) also have a high solubility for the protective oxide layer (i.e. Cr_2O_3 and Al_2O_3 according to Equation 3-12 and Equation 3-13) (Peters, Whittle

et al. 1976, Fryburg, Kohl et al. 1984, Misra 1986). Contrarily, the case of inward diffusion of sulfur toward the matrix, Mo shows a beneficial impact like Cr to combine with sulfur and hinder its diffusion (Goebel, Pettit et al. 1973). However, the negative impact of Mo on hot corrosion performance is more pronounced and alloys with a high level of Mo (> 3 wt%) should be avoided to be used in harsh environments.

$$Na_2SO_3 + MoO_3 \rightarrow Na_2MoO_4 + SO_3$$ Equation 3-11

$$Cr_2O_3 + 3MoO_3 \rightarrow 2Cr^{3+} + 3{MoO_4}^{2-}$$ Equation 3-12

$$Al_2O_3 + 3MoO_3 \rightarrow 2Al^{3+} + 3{MoO_4}^{2-}$$ Equation 3-13

The deleterious impact of W and V are more or less through the same mechanism as Mo. W, as carbide former element (WC, $W_{23}C_6$, and W_6C) facilitates acidic fluxing of the protective oxide layer by decreasing the oxygen ion activity in the environment by forming acidic WO_3. Continuous formation of this oxide on the surface self-sustains acidic fluxing and causes severe failure (Gurrappa 2003). Nb is also added to the alloy as carbide and intermetallic former. However, its negative effect on hot corrosion performance should be carefully considered in designing the heat treatment process in a way to deplete the Nb content from the matrix and precipitate it with other phases such as δ and γ″ phases. Remained Nb in the matrix may form $NaNbO_3$ which assists the dissolution of the protective oxide layer (He, Lin et al. 2019). In case of welding, adjustment of N content in the welding environment can diminish the negative effects of Nb. On the other hand, too high amount of N may promote micro-segregation and the formation of lave phases which are prone to hot corrosion attacks (Nabavi, Goodarzi et al. 2019).

Other than some positive impacts on mechanical properties such as forming hardening participated and intermetallic and improves creep properties, Tantalum is also reported to be

beneficial on hot corrosion resistance of nickel-based superalloys by forming solid phase of $NaTaO_3$, promoting the formation of $(Cr,Ti)TaO_4$ as an ion diffusion barrier layer, along with restraining the development of liquid $Na_2(Mo,W)O_4$ (Fryburg, Stearns et al. 1977, Fryburg, Kohl et al. 1984, Chang, Wang et al. 2015, Han, Chang et al. 2015). Besides, at the presence of Ta, sulfidation of Ta is preferred rather than chromium sulfidation and this preference saves more Cr to form a protective layer of Cr_2O_3. The presence of Ta can also neutralize the negative effect of Mo and W if Ta/(Mo + W) compositional ratio is about one (Chang, Wang et al. 2015). It is noted that the Ta/Cr ration in the chemical composition of the nickel-based superalloy determines the protection mechanism due to the presence of Ta. If this ration is between 0.5 and 1, both Ta_2O_5 and Cr_2O_3 can be formed competitively, however, neither of them is considered as a dense and continuous layer in this condition and an increase in hot corrosion rate is expected. For Ta/Cr=0.5, the formation of Ta containing spinels suppresses the ion diffusion rate and improve the hot corrosion performance. Finally, in the case of Ta/Cr equals to less than 0.5, Ta promotes the oxidation of Cr on the surface through a doping mechanism which decreases the hot corrosion rate (Chang, Wang et al. 2017). Few studies about the role of other alloying elements like Ce, La, Y, Sc, and Hf show their beneficial effect on hot corrosion resistance by improving the adhesion of the protective layer to the substrate (Otsuka and Rapp 1990, Eliaz, Shemesh et al. 2002).

3.4. Corrosion control methods

Several methods are recommended for controlling the degradation rate of nickel-based superalloys and remaining the corrosion level in the initiation stage by preventing the propagation stage as long as possible. Hot corrosion protection methods are mainly focused on three areas: 1) alloy design, 2) reduce the corrosivity of the service environment, and 3) block the surface contact

with the aggressive environment by applying protective barriers (Aung and Liu 2013, Bhuyan, Pradhan et al. 2019). These approaches are discussed in this section with more details.

3.4.1. Alloy design

The role of each alloying element was elaborated in the previous section. Although adding some elements such as Al, Cr, Y, Zr, etc along with decreasing harmful elements like Mo and W can improve the corrosion resistance of nickel-based superalloy, precautions are necessary while they may exacerbate the mechanical properties (Fryburg, Kohl et al. 1984). For this reason, the modification range is quite limited through this approach and other methods should be applied simultaneously for lowering the corrosion rate. Using more corrosion resistive alloys is another option in this tactic. The existence of secondary phases, especially coarse refractory metal carbides in the microstructure is generally assumed to be detrimental on hot corrosion properties due to the localized attacks on one phase or along phase boundaries (Stringer 1977). Considering the importance of microstructure in determining the high temperature of alloys, grain boundary engineering (GBE) has been demonstrated to positively affect hot corrosion resistance by producing diffusion-resistant special boundaries through a thermo-mechanical process instead of random high angle grain boundaries (RHAGBs) which are the preferred path for the diffusion of S and O. GBE also limits the outward diffusion of Cr and the depletion of this element at grain boundaries (Deepak, Mandal et al. 2016, Bhuyan, Pradhan et al. 2019).

3.4.2. Environmental modification

Washing the hot components with plain water is a simple maintenance method to remove deposited salts and other contaminations from the surface of the alloy to prevent the initiation of hot corrosion. Washing frequency should be stated in the maintenance manual of the component and modified routinely according to the inspection results (Stringer 1987, Eliaz, Shemesh et al.

2002, Hemmasian-Ettefagh, Amiri et al. 2010). Fuel cleanness is another important parameter that should be addressed for both initiation and propagation stages. The level of Vanadium, alkali metal, and sulfur are supposed to be controlled and maintained in a certain range depending on the service environment and other protection methods. However, the maximum content of 0.5 ppm of V, 0.2-0.6 ppm for Na and K content, and 1% of S are generally accepted without any other protecting approach (Viswanathan 1987, Eliaz, Shemesh et al. 2002). Using fuel additives is another traditional tool since realizing the harmful effect of V content in the fuel. Oxides of some elements like Mg, Ca, Cr, Ba can be added to the fuel for this purpose. These compounds react with the V and form high melting point vanadates that do not stick to the surface of the component (Equation 3-14) (Stringer 1977, Hancock 1987). Moreover, there are some studies for the application of fuel additives whether to increase the melting point of Na_2SO_4 or depleting the environment from this harmful salt by forming stable Na compounds (Stringer 1977).

$$3MgO + V_2O_5 \rightarrow Mg_3V_2O_8 \qquad \text{Equation 3-14}$$

Adding Zn through anodes in the fuel tank is also reported to reduce Type-II hot corrosion by decreasing the solubility of surface oxides. Moreover, Zn reacts with Cl and prevents its reaction with the protective layer of the alloy by evacuating it to the salt/gas interface (Hancock, Hancock et al. 1989).

3.4.3. Surface Treatment

In recent years, surface treatment is the dominant process to improve the hot corrosion properties of nickel-based superalloys by blocking the access of molten salt to the surface oxide by applying a more protective coating. This process aims to develop in a thin layer with outstanding corrosion resistance on top of the component that also helps the component to withstand the thermal loads in service. Several methods have been introduced for this purpose.

However, regardless of the nature of the layer or coating approach, the layer should have good adhesion to the substrate, low diffusion coefficient, low solubility in molten salt, and proper stability at elevated temperature. Various high-temperature coating methods are qualified for this condition and can be categorized into three main types of diffusion, overlay, and thermal barrier coatings that are elaborated in detail in this section (Grünling and Bauer 1982, Sitek, Kwaśniak et al. 2016, Fesharaki, Shoja-Razavi et al. 2019).

Several thermal spray techniques such as low-pressure plasma spraying, Physical vapor deposition (PVD), high-velocity oxygen fuel spraying (HVOF), vacuum plasma spraying, atmospheric plasma spraying, flame spray, cold spray, detonation gun spray, and high-frequency pulse detonation are applied to perform surface treatment process and improve the hot corrosion resistance of superalloys (Abedi, Salehi et al. 2010, Adam Khan, Sundarrajan et al. 2014, Muthu, Arivarasu et al. 2019). TIG cladding and laser cladding are also becoming popular in coating industries due to a higher control over cracks and porosity of the coat (Poza, Múnez et al. 2014, Saroj, Sahoo et al. 2017, Wen, Zeng et al. 2019, Ettefagh, Wen et al. 2020). Detonation-gun (D-gun) spraying method has been widely used in industries due to its capability to provide a coating with acceptable adhesion to the substrate, high hardness, fine grain microstructure, and low porosity level which prevents the diffusion of corrosive particles (Saladi, Menghani et al. 2014, Saladi, Menghani et al. 2015). HVOF is also a relatively new technique to apply high-quality protective coatings with high hardness, high yield stress, and low porosity (Sidhu, Agrawal et al. 2005, Sidhu, Prakash et al. 2006). Ultrasonic shot peening (USSP) can be also utilized as the post-treatment of coated nickel-based superalloys. In this method, a thin nanostructure layer is formed as a result of shooting the surface with hard steel balls for a very short time which leads to the

improvement of hot corrosion resistance (Pradhan, Mahobia et al. 2018, Kumar, Satapathy et al. 2019).

Diffusion coating

In this method, the top surface of the alloy is enriched with mainly Al and in some cases Cr or Si for a better corrosion resistance along with maintaining the creep properties and mechanical strength of the bulk material. Coated samples with Cr_3C_2–NiCr coating show lower hot corrosion rate as well as improved wear and erosion resistance compared to bare samples in a molten salt environment which is due to the formation of a dense layer of protective Cr_2O_3, $NiCr_2O_4$, and their spinels to act as a diffusion barrier (Kamal, Jayaganthan et al. 2009, Saladi, Menghani et al. 2014). Despite a few applications for applying enriched chromium coat, the diffusive aluminide layer is widely applied on nickel-based superalloys due to its relatively low cost and convenient operation and numerous studies on its optimization. Nickel aluminide coating is one of the most applied inter-metallic coats for this purpose. The basic protection mechanism of this coating is to form an adherent, dense and continuous layer of aluminum oxide to significantly reduce the hot corrosion rate by separating the substrate from the surrounded harsh environment (Hearley, Little et al. 1999, Donachie and Donachie 2002, Ren, Wang et al. 2005, Rahimi, Tabaian et al. 2012, Kumar, Satapathy et al. 2019). β-NiAl with an ordered BCC or B2 structure acts as a reservoir to supply Al to the surface layer and sustain the formation of the Al_2O_3 scale during the high-temperature exposure (Das 2013).

Despite of the mentioned benefits, some drawbacks are also associated with Al diffusive coatings. Al_2O_3 protective layer may react with O_2^- and form AlO_2^- through a basic fluxing mechanism (Equation 3-15 and Equation 3-16). Subsequent reactions lead to the transformation of NiAl to the Ni_3Al phase which has lower hot corrosion resistance (Warnes and Punola 1997,

Magdziarz and Kalicka 2007). Modifying the aluminide coatings by adding some elements such as Co, Cr, Zr, Si, Pt, Cr, Hf, and Pd have been studies as a remedy for this problem (Angenete and Stiller 2001, Haynes, Pint et al. 2002, Task, Gleeson et al. 2011). Co improves the corrosion performance of the aluminized layer above 1000°C by forming the β-CoAl phase which has a high melting point (1640°C) (Rahman, Chawla et al. 2011). Co also has a higher tendency to react with Cl and makes the formation of nickel chloride more difficult. Moreover, it forms eutectic compounds like Na_2SO_4–$CoSO_4$ with the molten salt which is more stable than Na_2SO_4 (Fan, Jiang et al. 2014). Pt enhances the formation and adhesion of the α-Al_2O_3 layer to the substrate by restricting void growth beneath the surface layer and delays the formation of corrosion products during exposure. Moreover, it reduces the stress level in the oxide scale and facilitates the diffusion of Al in the coating along with restraining the diffusion of other alloying elements (Goward 1998, Zhang, Lee et al. 1999, Dahotre 2000, Liu, Jiang et al. 2017). For this purpose, a pre-deposit of Pt is needed on the surface with a thickness of ~5–8 μm. However, there are some limitations associated with this method. The high price of Pt limits the wide application of Pt modified aluminide layers for high-temperature applications. Besides, some reports show the deterioration of high cycle fatigue resistance due to the formation $PtAl_2$ phase (Tawancy, Abbas et al. 1992, Tawancy, Sridhar et al. 1992). For these reasons, the use of Pd instead of Pt has been proposed to eliminate these limitations since the price of Pd is roughly one-fourth of Pt and there is no harmful phase like $PtAl_2$ in the Al-Pd phase diagram (Lamesle and Steinmetz 1995, He, Guan et al. 2000). The aluminizing process can be also modified by adding Zr. It has been reported that Zr decreases the inward diffusion of Al to the substrate and improve the oxidation resistance of β-NiAl (Barrett 1988, Prescott, Mitchell et al. 1993).

$$Na_2SO_4 \rightarrow Na_2O + SO_2 + 1/2O_2$$ Equation 3-15

$$Al_2O_3 + Na_2O \rightarrow 2AlO_2^- + 2Na^+$$ Equation 3-16

Aluminizing can be performed via several techniques. Pack cementation is the most popular method due to its simplicity and low cost. In this approach, the component is submerged in a powder mixture including Al powder, Al_2O_3 powder as inert filler to prevent Al powder particles to be sintered, and NH_4Cl as a halide activator. At high temperature, the vapor of metal halide compounds such as AlCl, $AlCl_2$, $AlCl_3$ is formed and metal is deposited on the surface after some reduction reactions of this vapor (Das, Joshi et al. 2000, Xiang, Burnell-Gray et al. 2001). Chemical vapor deposition (CVD) is another aluminizing method that can be classified into two categories of low and high activity depending on the activity of Al. In low activity process, a conducting gas like hydrogen or argon provides $AlCl_3$ to the chamber from an external generator through hot ducts. The process temperature is about 1000°C and β-NiAl is the dominant surface phase (Sudhangshu 2007). In the high activity process, the vapor generator is located in the same chamber with Al-rich granulate. The process temperature is ~750-950°C and a post-heat treatment is essential to transfer the brittle Ni_2Al_3 phase into β-NiAl (Sudhangshu 2007, Sitek, Kwaśniak et al. 2016). Hot-dip aluminizing, slurry coating, and thermal spray coating are alternative aluminizing methods that are applied in industries (Wang and Chen 2006, Kumar, Satapathy et al. 2019).

Overlay Coating

MCrAlY coating is the generic terminology that is used for the family of overlay coatings. In this definition, M is the alloy base metal (Ni in case of nickel-based superalloys) or a combination of Ni and Co. Cr and Al content can be tailored over a range of composition. High-Cr low-Al serves better to protect base alloy against Type II hot corrosion while Low-Cr High-Al

is typically needed for protection against HTHC. The protection mechanism of MCrAly coatings is attributed to the formation of a dense, adherent, and uniform layer of Al_2O_3 and/or Cr_2O_3 on the surface of the alloy (Sun, Jiang et al. 2018). An ideal overlay coating is expected to have three main properties: 1) close chemical composition and microstructure with the substrate to provide compatibility with the substrate from a thermal expansion point of view and decrease thermal stress during service; 2) sustaining in the supply of Al and Cr to form a protective coating and prolong the service life; and 3) higher resistance to both types of hot corrosion compared to the bulk material (Bao, Wang et al. 2009). Different coating methods including air plasma spray (APS), magnetron sputtering (MS), vacuum plasma spray (VPS), electron-beam physical vapor deposition (EB-PVD), and arc ion plating (AIP) are now being used to apply overlay coatings on the nickel-based superalloys (Gurrappa 2000, Wang, Huang et al. 2000, Wang, Gong et al. 2002, Li, Zhang et al. 2003).

It is reported that in some aggressive environments, overlay coatings have a better performance compared to the diffusion coatings (Mévrel 1989, Sidhu, Agrawal et al. 2005). However, this type of coating is super sensitive to the amount of Al and its depletion as a result of spallation or inward diffusion during service determines the overall lifetime of the component (Bao, Wang et al. 2009). On the other hand, increasing the Al content of the coating will result in the loss of mechanical properties and causes brittleness of the surface (Tang, Ajdelsztajn et al. 2004, Bao, Wang et al. 2009). To solve this issue, MCrAlY coating with the gradient content of Al has been proposed to provide a balance between mechanical properties and hot corrosion performance. For this type of coatings, the outer layer and internal layers are Al-rich and Cr-rich, respectively. Several studies show an enhanced hot corrosion performance of this type of gradient Al distribution coatings compared to routine MCrAlY (Suresh 2001, Tang, Ajdelsztajn et al. 2004,

Bao, Wang et al. 2009, Jiang, Li et al. 2010). The microstructure and elemental composition of the inner layer are very similar to the base alloy to reduce the mismatch between substrate and coating. Moreover, high Cr content of the inner layer helps to battle against LTHC. At the same time, the Al_2O_3 layer can be formed from the outer Al-rich layer and protects Type-I hot corrosion and high-temperature oxidation. The gradient distribution of Al and Cr in the coat provides sustainability in protection over a long time (Bao, Wang et al. 2009). Another method to improve the resistance of overlay coatings is by adding some elements like Cr, Si, Hf, and Pt to the system. The coating is known as MCrAlYX in this case which X represents the added element. The impact of adding these elements in enhancing the hot corrosion performance of overlay coatings on top of nickel-based superalloys have been studied in several papers (Nakamori, Kayano et al. 1997, Nicholls 2000, Montero, Galetz et al. 2013, Boulesteix, Pedraza et al. 2017).

Thermal barrier coating

The aim of applying thermal barrier coatings (TBC) on nickel-based superalloys is to insulate the substrate from the aggressive environment and increase the safe operating temperature of the component. TBC typically consists of an outer layer of ceramic coating for thermal insulation (usually yttria stabilized zirconia, YSZ), and a diffusion or overlay coating as the inner layer (bond coat) which provides hot corrosion resistance with the above discussed mechanisms (Nicholls 2000, Sreedhar, Alam et al. 2009). One of the limitations of the TBC coatings is the poor durability under the marine atmosphere and with low-grade diesel fuel. This is because S, Na, V, and CaO in such environments react with the coating stabilizers. To overcome this issue, laser post-surface treatment has been offered (Longa-Nava, Zhang et al. 1996, Gurrappa 1998, Ettefagh, Wen et al. 2018, Zeng, Wen et al. 2020). The nano-size YSZ has also been studied and shows an improvement in the hardness, toughness, wear resistance, and thermal expansion coefficient, along

with a lower thermal diffusivity (Di Girolamo, Blasi et al. 2015, Han, Huang et al. 2015, Pakseresht, Javadi et al. 2016, Chaichi, Prasad et al. 2019). Air plasma spraying is the most practical method of applying TBC on different alloys. However, since nano-sized particles have a poor flowability, this method is challenging to apply nano-size YSZ powders. Recent studies in this area are focused on the application of spark plasma sintering (SPS) to fabricate nano-structured coatings (Khoddami, Sabour et al. 2007, Boidot, Selezneff et al. 2010, Song, Ma et al. 2010, Pakseresht, Javadi et al. 2016).

Applying TBC on a nickel-based substrate can increase the service temperature of the component thus improve the efficiency of gas turbines and power generators significantly. However, the interest in developing new materials/coatings for superior hot corrosion resistance at even higher temperatures still exists. There are some studies to replace the nickel-based superalloys with silicon-based ceramic matrix composites (CMC) such as silicon carbide, silicon nitride, and carbon fiber (Cf)-reinforced silicon carbide composites coupled with environmental barrier coatings (EBC) as a possible strategy to increase the service temperature of turbines. Rare earth silicates and polymer-derived ceramic (PDC) matrix composite coatings are shown to be a good candidate to serve as EBC for this purpose (Wang, Günthner et al. 2011, Chen, Zhang et al. 2020).

3.5. Conclusions

In this review chapter, hot corrosion related issues for several important nickel-based superalloys are presented. Studies on different types of nickel-based superalloys show that they can be used without further protection by relying on the natural formation of a protective oxide such as chromium oxide and aluminum oxide on the surface during their exposure to the corrosive

environment at high temperature. However, protection methods are necessary to enhance the lifetime of the components.

- Atmosphere and fuel contaminations cause the formation of Na_2SO_4 salt which it's melt deposits on the surface of the alloy at elevated temperature and causes degradation of the nickel-based superalloys. The presence of NaCl in the atmosphere and V in the fuel reduces the salt melting point by forming eutectic compounds and makes the damage more severe.
- Depending on the temperature, hot corrosion is classified into two categories. Type-I is known as high-temperature hot corrosion (HTHC) in which the loss of the protective surface layer takes place due to the basic or acidic fluxing of the surface oxide. Low-temperature hot corrosion (LTHC) is the second type in which the failure is typically due to the formation of pits at high-stress sites as an outcome of internal sulfidation and neither the incubation stage nor Cr depletion zone is reported in this type.
- Typically, mechanical properties are prioritized in the alloy designing process. Among alloying elements, Al, Cr, and Ta have a positive effect on hot corrosion performance. In contrast, Mo, W, V, and Nb deteriorate the resistance of the alloy against the corrosive environment. There is no solid evidence about the effect of other elements such as Co, Mn, Si, B, and Zr on the hot corrosion behavior of nickel-based superalloys.
- Environmental modification methods such as frequent cleaning of the surface or purifying fuel as well as adding some fuel additives can decrease the hot corrosion damages of the components.
- Diffusion, overlay, or barrier coatings are extensively applied to improve the corrosion resistance of nickel-based superalloys. Thermal spraying techniques are the main method for applying such coats.

Chapter 4. Methodology

4.1. LPBF-AM process

Spherical Cu-10Sn, SS316, and Ti64 alloy powders from Concept-Laser GmbH are used in a LPBF-AM system (Concept-Laser Mlab cusing R) under the protection of Ar gas to fabricate the AM specimens. This machine (Figure 4-1) utilizes a laser source to melt powder and fabricate parts with complex shapes from a CAD file with the capability to print both reactive and non-reactive powders with a proper surface finish and final density (GE Additive 2020). The term Cusing refers to the direct melting of metal powders process in a layer by layer manner based on a three dimentional CAD data. High energy laser source melts metal powder locally and the scanner redirects the focus area to the next powder particle while the former melted one solidifies. This process continues until covering the whole surface. The next layer identically starts by lowering the chamber base by the thickness of one layer. Eventually, the 3D object is fabricated layer by layer from bottom to top (GE Additive 2020).

Figure 4-1. (left) Concept-Laser Mlab cusing R, (right) Concept-laser laserCusing process (GE Additive 2020).

4.1.1. Cu-10Sn Alloy

Figure 4-2(a) shows that the typical diameters of the powders used are in the range of 10 to 30 μm. The LPBF-AM processing parameters are as follows: laser power 95W, scanning speed 1200mm/s, hatch space 50μm, and powder layer thickness 15μm. Laser "islands scanning strategy" is applied with a square island size of 5×5 mm2 as shown in Figure 4-2.(b), where Axis Z represents the building direction.

In order to evaluate the influence of building direction on the corrosion properties, two groups of cylindrical rod specimens are prepared, with the central axis oriented in either Vertical or Horizontal direction (Figure 4-2.(c)). Figure 4-2.(d) demonstrates the sectioning procedures for microstructural characterizations, and corrosion evaluation of as-printed and annealed specimens. To investigate the effect of heat treatment on microstructural evolution and properties of LPBF-AM specimens, vacuum annealing is applied at ~10^{-7} torr and temperatures of either 600℃ or 800℃ for 1 hour. The programmed heating and cooling rates are both 10℃/min. In this research, specimens are denoted by the combination of heat treatment conditions and the building orientations, i.e., AF-Horizontal, AF-Vertical, 600-Horizontal, 600-Vertical, 800-Horizontal, and 800-Vertical.

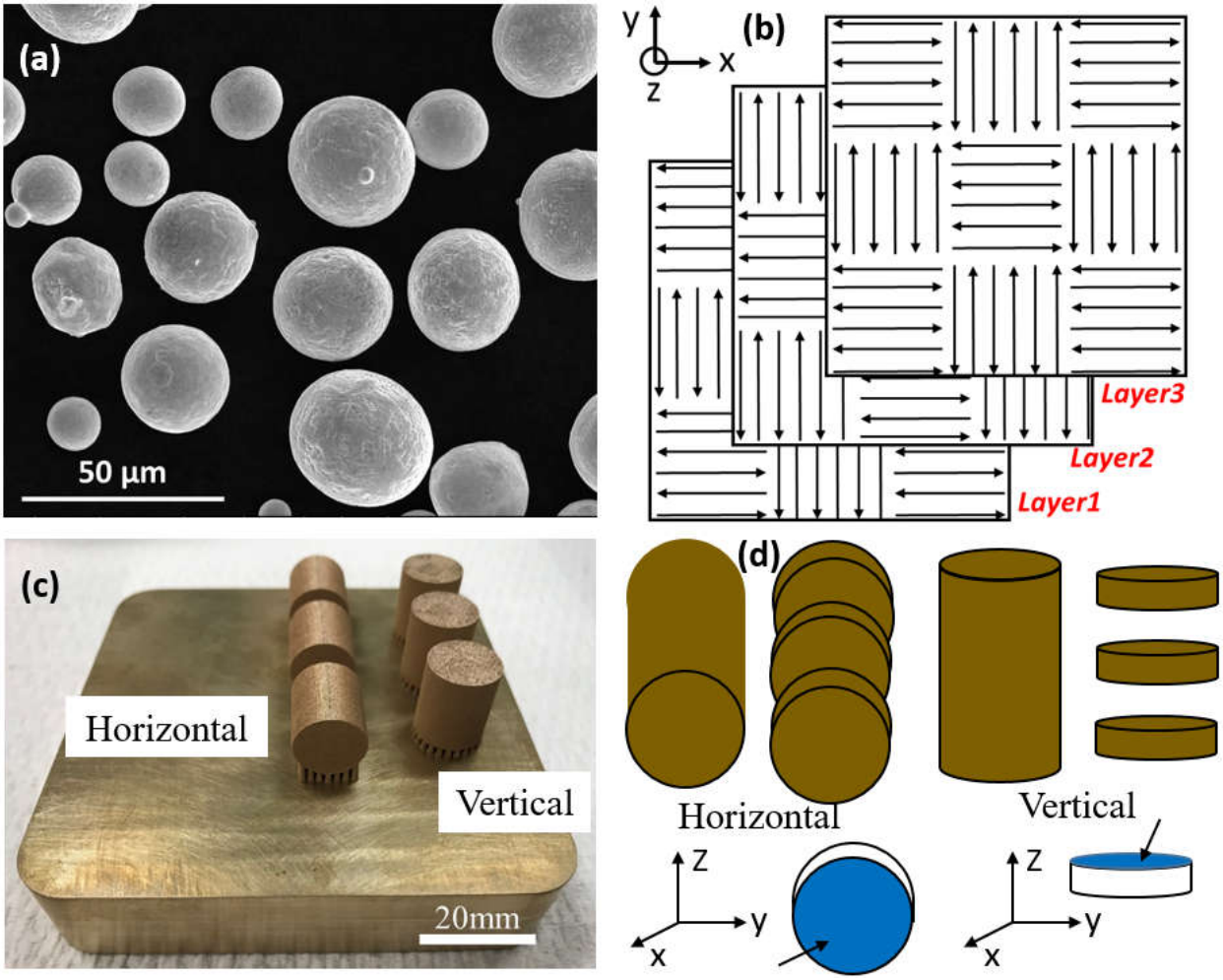

Figure 4-2. (a) A SEM image of Cu-10Sn powders. (b) A schematic illustration of the laser "islands scanning strategy". (c) As-fabricated cylindrical rod specimens, Vertical and Horizontal building orientations. (d) A schematic illustration of Vertical and Horizontal specimens with shaded surfaces subject to following microstructural characterization.

4.1.2. AISI316L Alloy

Austenitic stainless steel 316L powders from Concept-Laser (CL 20ES) were used, together with the Concept-Laser's "Speed-cusing" processing parameters. The process profile "Speed-cusing" is optimized by Concept-Laser for CL 20ES SS316L powders. Being a proprietary file, general users are not allowed to view and modify the settings. The chemical compositions of AISI316L are listed in Table 4-1 (particle size: 10-45 µm). Upon creation of a CAD model of the desired geometry, two-dimensional slicing and support structure information are created using the

AutoFab software for input into the Mlab system. Before the building process, the Mlab system is purged with argon (Ar) down to an oxygen level less than 0.7%. This oxygen level is maintained throughout the AM process. For each layer, after lower the building platform by 25 microns, a re-coater blade moves across the build platform and deposits an even layer of SS 316L powders onto the build platform. After the rectangular shaped plates were built, a Mitsubishi wire EDM machine (MV series) was used to cut out a small section for corrosion study.

Table 4-1. Chemical composition (wt%)of AISI316L stainless steel

	Cr	Ni	Mo	Mn	Si	P	C	S	Fe
Min	16.5	10.0	2.0	0.0	0.0	0.0	0.0	0.0	Balance
Max	18.5	13.0	2.5	2.0	1.0	0.045	0.030	0.030	Balance

Wrought samples with the same chemical compositions were bought from a commercial source, in order to perform a comparative study. Annealing process was performed on both AM and wrought samples in a Nabertherm GmbH N 7/H Furnace under argon atmosphere. Samples were annealed in 800 °C for 2 hours and then cooled down in the furnace atmosphere.

4.1.3. Ti-6Al-4V Alloy

Titanium alloy Ti-6Al-4V powders (CL 41TI ELI) were supplied by Concept-Laser. The processing parameters were set by Concept-Laser's "Speed-cusing" profile (package name: CL 41_cusing_100_with Islands_V1). The optimized laser process parameters are proprietary by the manufacturer, however, a number of researchers have reported optimized processing parameters for this system (Milton, Morandeau et al. 2016, Prashanth, Damodaram et al. 2017, Soro, Attar et al. 2019, Tan, Song et al. 2019). Those values are summarized in Table 4-2. The chemical compositions of the supplied Ti-6Al-4V powders and of the purchased wrought samples are listed in Table 4-3 based on the supplier data sheets. As can be seen, the chemical compositions of the sample sets are nearly equivalent, enabling an accurate comparison. In the AM process, a computer

aided design (CAD) model with the desired geometry was generated in the STL file format (Solidworks, 2015 ×64 Edition, Dassault Systèmes, France). AutoFab software (64 Bit, version 2.0, Concept-Laser GmbH, Germany) was used to generate two-dimensional slicing, including support structures. AutoFab created the input files, with the slicing information, for the Mlab system. Because titanium alloys are reactive, before the initiation of the AM process, argon was used to purge the processing chamber of the Mlab system. The chamber oxygen level was reduced to 0.5% before the fabrication process began. With continued argon gas purging, the oxygen level in the chamber during the AM process is typically lowered to less than 0.1%. In the layer-by-layer process, the building platform was lowered by 25 microns before applying a re-coater blade over the building platform to deposit a new layer of Ti-6Al-4V powders. For testing purposes, rectangular shaped plates with the size of 10cm×1.5cm×0.3cm were built with a 5mm×5mm island scanning strategy. To cut the samples to size, a wire electric discharge machining (EDM) machine (MV series, Mitsubishi, Japan) was used to prepare the sample final geometries.

Table 4-2. Processing parameters ranges used in literature for the fabrication of Ti-6Al-4V samples using the Concept-Laser GmbH Mlab-cusing-R system (Milton, Morandeau et al. 2016, Prashanth, Damodaram et al. 2017, Soro, Attar et al. 2019, Tan, Song et al. 2019)

Process parameters	
Laser Power (W)	95-100
Scanning Speed (mm/sec)	900-1000
Hatch spacing (μm)	100-110
Diameter of Laser (μm)	40-50

Wrought (cold rolled) Ti-6Al-4V specimens with the same chemical compositions were acquired from a commercial supplier to compare their behavior with the AM samples. For the annealing step, an argon atmosphere was provided in a GmbH N 7/H furnace (Nabertherm, Germany) in which the samples were annealed for 2 hours at either 600°C or 800°C followed by

a cooling stage in the furnace environment. These sample types were labeled as HT600 and HT800, respectively.

Table 4-3. Chemical composition (wt%) of Titanium alloy Ti-6Al-4V powders and wrought samples (based on the suppliers data sheet)

		Al	V	Fe	C	O	N	H	Ti
Powder	Min	5.50	3.50	0.00	0.00	0.00	0.00	0.000	Balance
	Max	6.50	4.50	0.25	0.08	0.13	0.05	0.012	Balance
Wrought	Min	5.50	3.50	0.00	0.00	0.00	0.00	0.000	Balance
	Max	6.75	4.50	0.40	0.08	0.20	0.05	0.015	Balance

4.2. Fe-14Cr alloy specimens preparation

Fe-14Cr-2W-0.3Ti-0.3Y_2O_3 (wt.%) powder mixture was prepared using commercial pure powders of Fe, Cr, W, Ti and Y_2O_3 purchased from a commercial source (>99.9 wt.%, Alfa Aesar). Mechanical alloying was performed on the powder mixture for 10 hours in a high energy ball mill (SPEXSamplePrep Mixer/Mill) with a stainless-steel ball to powder ratio of 10:1 under an argon environment. A typical SEM image of the powders and the size distribution after 10 hours of ball milling measured by laser diffraction spectrometry (Malvern MASTERSIZER 3000) can be seen in Figure 4-3.

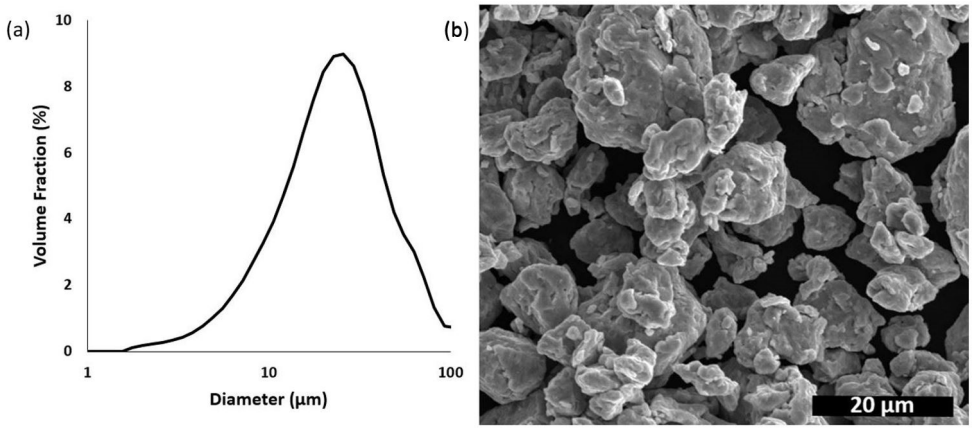

Figure 4-3. (a) Powder size distribution after 10 hours of ball milling, (b) SEM micrograph of Fe-14Cr-2W-0.3Ti-0.3Y_2O_3 powders.

The SPEX SamplePrep Mixer/Mills (Figure 4-4 left) is known as high-energy ball mills, which shakes containers back and forth roughly 1080 cycles per minute. This device is a decent candidate for mechanical alloying purposes considering the presence of steel balls in the powder chamber and the swing range of about 2 inches (SPEX Sampleprep 2010). Malvern MASTERSIZER (Figure 4-4 right) is a laser diffraction measurement device. The laser beam goes through powder sample, which can be both wet and dry dispersions, and then the intensity of the scattered light is measured. The smaller the particle size, the larger the scattered angle. The obtained date are then analyzed and presents powder size distribution as its output (Malvern Panalytical Ltd 2019).

Figure 4-4. (left) SPEX SamplePrep Mixer/Mills (SPEX Sampleprep 2010), (right) Malvern MASTERSIZER 3000 (Malvern Panalytical Ltd 2019).

Consolidation of Fe-14Cr-2W-0.3Ti-0.3Y_2O_3 powders was conducted using a Spark Plasma Sintering (SPS) system (FUJI-SPS DR. SINTER LAB) with a ϕ15mm graphite die at an axial pressure of 45 MPa (Figure 4-5 left). During the SPS process, the temperature was raised from room temperature to 700 °C at a rate of 100 °C/min, and then to 850 °C at a rate of 50 °C/min. The samples were kept at 850 °C for 4 minutes before cooled down to room temperature (Figure 4-5 right). In this system, a graphite die is packed with powder mixture and placed between two

electrodes in the chamber. A pulsed DC current along with a uniaxial pressure facilitate the sintering of the mixture in a few minutes. Typically, full densification takes place in a much shorter time and lower temperature in SPS compared to other conventional pressure-free or hot-pressing methods (Calnano 2014).

Figure 4-5. (left) Spark Plasma Sintering (SPS) system (FUJI-SPS DR. SINTER LAB) (Calnano 2014), (right) Thermal profile of consolidation process via SPS in a graphite die.

After SPS process, surface treatment was applied on the Fe-14Cr-2W-0.3Ti-0.3Y_2O_3 SPS samples using a custom laser system composing a 200W IPG ytterbium fiber laser and a laser scan head (ProSeries II). A 58 μm laser spot size was achieved using a JENar F-Theta lens at the focal plane which was 403.8 mm below the lens surface. The test was performed in an inert argon environment by vacuum the chamber from the initial atmosphere pressure to 150 Pascal and then refill the chamber with argon gas back to the atmosphere pressure. The residual oxygen in the chamber is one of the sources of oxygen for the formation of oxides. It is well known that the protective nature of an oxide layer highly depends on the oxygen partial pressure. Simply using air can lead to the formation of a non-protective layer on the alloy surface (Baer 1980). In addition, for a working condition with relatively high vapor pressure, the oxide layer is less protective due to the loss of Cr through $CrO_2(OH)_2$ evaporation (Asteman, Svensson et al. 2002, Liu, Tang et al.

2006). To provide a suitable condition for forming a protective layer, the tests were performed in a controlled atmosphere with an oxygen concentration about 0.03%. The laser was in continuous wave mode and the wavelength is 1064 nm. Figure 4-6 demonstrates a schematic design of the custom laser system (Wen, Zeng et al. 2019, Ettefagh, Wen et al. 2020) and the used scanning pattern to achieve full surface coverage of the disk shaped samples with a diameter of 15 mm.

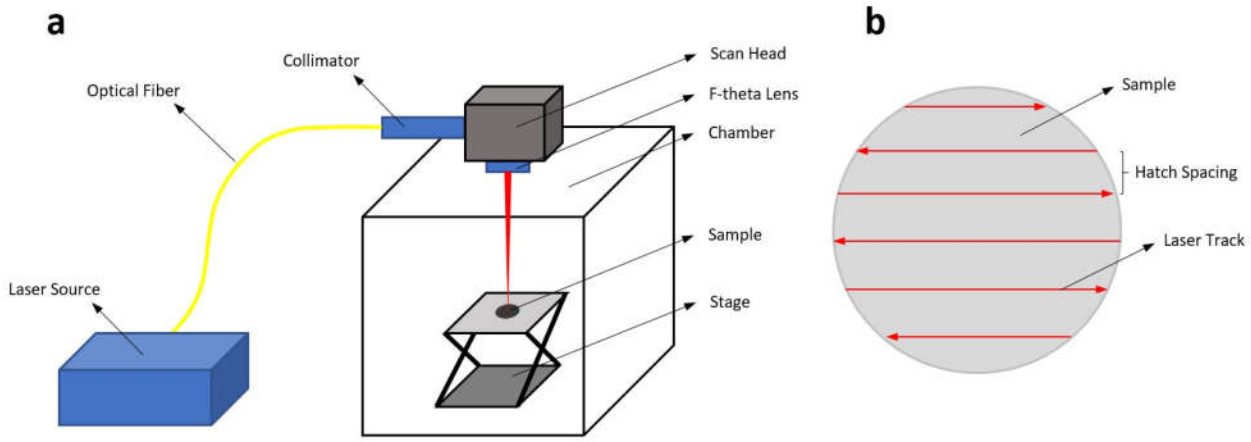

Figure 4-6. (a) Schematic drawing of the custom laser system used for surface laser processing [31, 32], (b) Laser pattern used for scanning the surface of the samples.

For laser processing, surface energy density (E') is calculated with the unit of J/mm^2 as a fraction with the numerator of laser power (P in W) over the product of laser scanning speed (v in mm/s) and hatching space (H in mm) as the denominator.

4.3. Inconel 939 specimen preparation

Inconel 939 powders were purchased from LPW Technology Inc, USA, which were gas atomized with particle size to be 15-45 µm. The elemental composition of the powders is listed in Table 4-4. Mini Arc Melter MAM-1 (Edmund Bühler GmbH Lab Tec) was used for the preparation of samples, which was equipped with a water-cooled copper crucible plate and a nonconsumable tungsten electrode. Prior to the arc melting process, 10g of the as-received Ni939 raw powders were measured. After putting the powders in the crucible, the chamber was depressurized and then

refilled using pure Ar (ultra high purity 5.0 grade, Airgas) for five cycles to minimize the oxygen content, with the final Ar pressure in the chamber set to be 30 kPa. The powders were first melted and cast to a button-shape sample, then the obtained sample was flipped and re-melted for three more times to ensure homogeneity. All of the samples were ground using SiC sandpaper up to 1200 grit size, then washed ultrasonically with acetone, denatured ethanol and distilled water in sequence prior to corrosion tests.

Table 4-4. Composition information of Inconel 939 alloy powders

Concentration of elements (wt. %)									
Al	B	Bi	C	Co	Cr	Fe	Mg	N	Nb
1.9	0.010	< 0.001	0.15	19.2	22.3	0.1	< 0.1	0.01	1.0
Zr	Pb	S	Si	Ta	Ti	Tl	W	Ni	
0.11	< 0.001	< 0.001	0.1	1.5	3.6	< 0.001	2.0	Bal	

4.4. Corrosion tests

4.4.1. At ambient temperature

To evaluate the corrosion performance at ambient temperature, a 3-electrode standard corrosion cell was utilized to perform the electrochemical tests, using a saturated calomel electrode (SCE) as the reference electrode, a platinum counter electrode, and the specimens as the working electrode with an exposed area of 1cm^2. Corrosion tests were conducted in 3.5 wt.% NaCl water solution at room temperature with naturally dissolved oxygen using a CHI-604C corrosion tester (CH Instruments, Inc). This device is designed for a wide range of electrochemical measurements along with the simulation and fitting software which can be helpful for electrochemical processes and corrosion mechanism studies.

Open circuit potential (OCP) was recorded for a duration of ~60 hours for Cu-10Sn and ~30 hours for Ti-6v-4Al and Tafel curves were obtained within the potential ranges stated in Table 4-5 depends on the tested material at a scan rate of 1.67 mV/s. Prior to the corrosion tests, the

specimens surfaces were prepared by polishing with SiC paper (grit sizes 320, 600, 800 and 1000 in sequence), rinsing, and soaking in the test environment for 1 hour. To assure the reproducibility of the tests, all of the corrosion tests were performed at least three times. For weight loss test, all the polished specimens were washed by deionized water, ethanol, and acetone, and weighed after drying. Cu-10Sn specimens were then hung in the solution for 11 days and the weight of corroded specimens was tracked every 24 hours. Prior to weighing, specimens were cleaned and dried.

Table 4-5. Potential ranges applied for corrosion tests of the samples

	Potential Range (V_{SCE})
Cu-10Sn (Chapter 5)	-1.5 to 0
AISI316L (Chapter 6)	-0.75 to +0.5
Ti-6Al-4V (Chapter 7)	-1 to +1.5
Fe-14Cr (Chapter 8)	-1 to -0.2

For EIS measurements, the frequency range was 0.01 Hz to 100 kHz at $E=E_{(Open\ Circuit)}$. After gathering EIS curves, the experimental data were analyzed with the electrochemical software of the CHI-604C to generate the equivalent circuits.

4.4.2. Hot Corrosion test

To mimic the real application condition of Inconel 939 in a marine gas turbine engine chamber, a salt mixture consisting of 75% Na_2SO_4 + 25% NaCl (Wt.%) was prepared and samples were immersed completely in this mixture in a porcelain crucible. Before that, the weight of the samples was measured using a digital balance with an accuracy of 0.1 mg and crucibles were preheated for 1 h at the test temperature to remove any moisture. The crucibles containing samples and salt mixture were exposed to high temperatures (700°C and 800°C) in a benchtop furnace (Neytech Vulcan Model 3-550) for 1, 3, 5, 10, 20, 50, and 100 h. After each interval, one sample was taken out and cooled in the air. To remove the remained salts on the surface and loose corrosion products, specimens were washed ultrasonically with distilled boiling water and

hydrochloric acid, respectively. Finally, samples were checked for their weight change with the same digital balance.

4.5. Materials characterization

Phase identifications were carried out using a PANalytical Empyrean XRD (Malvern Panalytical, UK) by CuKα radiation at room temperature on specimens. θ-2θ scans were conducted in the angular range of 20°-120° 2θ with a scanning step size of 0.026°. An FEI Quanta3D FEG Dual-Beam scanning electron microscope/focused ion beam (SEM/FIB) instrument, with an electron backscatter diffraction (EBSD) attachment and an energy dispersive spectroscopy (EDX) attachment, was used for elemental analysis and microstructural examination of specimens. Prior to EBSD examinations, specimens were mechanically ground using SiC papers of different grit sizes (320, 600, 800, 1000 and 1200 grits, in sequence), polished with the MetaDi^{TM} Supereme polycrystalline diamond suspension (6 μm, 3 μm, 1 μm, in sequence), followed by a final vibratory polishing with 50 nm silica suspension on a Pace Technologies GIGA 0900 Vibratory Polisher for 12 hours. EBSD mapping was performed at 30 kV and 23 nA. Raw EBSD data are then analyzed with the TSL OIM software. After polishing, both AF and VA specimens were etched (5g $FeCl_3$, 10 ml HCl, and 100 ml deionized water) at room temperature before SEM examination. In addition, Raman spectroscopy (Renishaw inVia Reflex Raman Microscope) was conducted on the laser modified samples of Fe-14Cr to identify the formed oxide layer. For Raman mapping, a 532 nm laser was used with magnification of 100X and step size of 500 nm. The surface micro-hardness was measured using a Vickers microhardness tester (FM-110, Future-tech corp., Tokyo, Japan) where necessary. Moreover, CALculation of PHAse Diagrams (CALPHAD) calculations were performed using the Thermo-Calc software (version 2019, Thermo-Calc Software Inc. Sweden) and TCTI1 and TCNI8 databases thermodynamic database.

Chapter 5. Corrosion Properties of Cu-10Sn Alloy Prepared by Laser-Powder-Bed-Fusion Additive Manufacturing

5.1. Microstructure characterization

Figure 5-1 shows XRD θ-2θ scans obtained from Cu-10Sn pre-alloyed powders, AF specimens, and VA specimens. The raw Cu-10Sn powders contained two phases which can be identified as the α-Cu(Sn) phase (a Cu-rich phase) and the intermetallic compound δ-$Cu_{40.5}Sn_{11}$ phase (a Sn-rich phase). After LPBF-AM processing, the phase compositions of both AF-Horizontal and AF-Vertical specimens are similar to those of the raw powders, i.e., both α and δ phases can be identified, consistent with other studies (Scudino, Unterdörfer et al. 2015, Mao, Zhang et al. 2018). However, a closer examination reveals that the α phase diffraction peaks in AF specimens shift towards smaller angles as compared to those in the pre-alloyed powders. For example, as shown in Figure 5-1.(b), the (111) peak of α phase in AF-Horizontal specimen is 42.87º, slightly smaller than that of raw powders (43.01º). This shift of α phase peak to a lower angle suggests Sn diffusion into the α phase during the LPBF-AM process. After annealing, all the specimens contain only the α phase (Figure 5-1.(a) and (b)), indicating that Cu and Sn are mixed homogeneously after annealing at 600℃/800℃ for 1 hour. It is also clear that the diffraction peaks from the annealed specimens became narrower than those corresponding to the AF specimens, implying compositional homogenization as well as grain growth. To determine the phase constituents of AF specimens, Rietveld refinement analysis of the XRD data obtained from AF-Vertical specimen was carried out, and shown in Figure 5-1.(c). The refinement results confirm

This chapter was previously published as Congyuan Zeng, Bin Zhang, Ali Hemmasian Ettefagh, Hao Wen, Hong Yao, W. J. Meng, and Shengmin Guo, " Mechanical, Thermal, and Corrosion Properties of Cu-10Sn Alloy Prepared by Laser-Powder-Bed-Fusion Additive Manufacturing" Additive Manufacturing, 35 (2020): 101411. Reprinted by permission of Elsevier.

that the XRD pattern of AF-Vertical Cu-10Sn specimen is fitted well when the phase constituents are assumed to be the face-centered cubic (FCC) α-Cu phase and the δ-$Cu_{40.5}Sn_{11}$ phase (weighted profile reliability factor, R_{wp}=9.02%), indicating a coexistence of the $Fm\bar{3}m$ α-Cu (Sn) phase and the $F\bar{4}3m$ δ-$Cu_{40.5}Sn_{11}$ phase at room temperature. The content of the δ-$Cu_{40.5}Sn_{11}$ phase is estimated to be 25.9 wt.%.

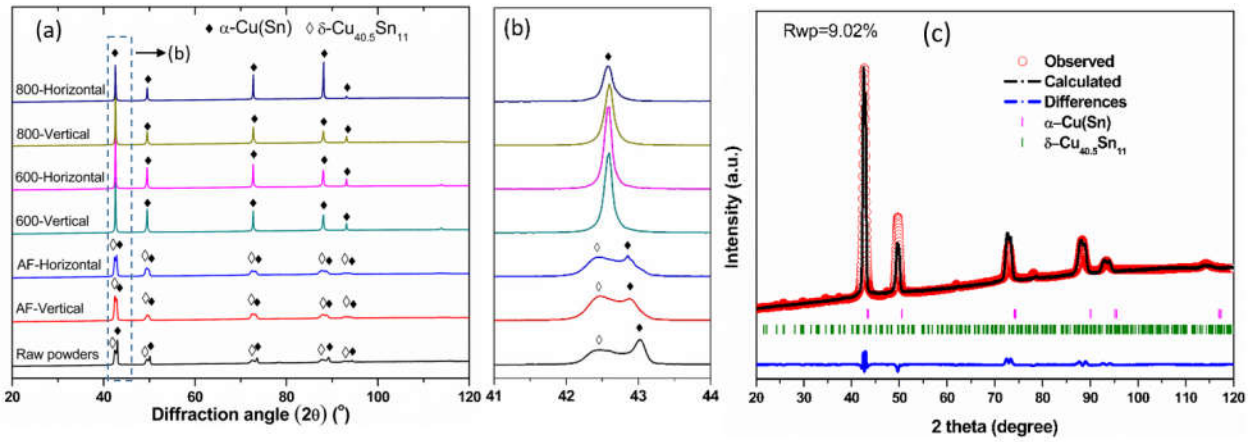

Figure 5-1. XRD and Rietveld refinement analysis results: (a) θ-2θ scans over the 2θ angle range of 20° - 120° from raw Cu-10Sn powders, AF and VA specimens; (b) θ-2θ scans over a narrow 2θ angle range of 41° - 44°; (c) Rietveld refinement analysis of the θ-2θ scan obtained from the AF specimen.

Figure 5-2 summarizes the SEM images obtained from the AF specimens after etching. Figure 5-2(a) shows a typical melt pool profile, marked with dash lines, resulting from the LPBF-AM process. A closer examination reveals that the specimen microstructure is not uniform, and three different regions with distinct microstructures can be discerned, as marked with squares 1, 2, and 3 in Figure 5-2(a). The region marked by square 1 is located at the intersection region of two adjacent melt tracks, and Figure 5-2(b) shows the corresponding microstructure at higher magnification. Cellular structures can be observed, and these cellular structures consist of α phase (grey regions) and (α+δ) eutectoid phase (bright rings). The widths of the bright rings are ~100 nm. Figure 3(c) depicts the microstructure of region 2 in Figure 5-2(a), in the center of a melt track.

Again, the α phase matrix and the (α+δ) phase white rings can be observed. The average size of the structures in region 2 is much larger than that in region 1. Region 3 is located across the melt pool border line, and columnar structures can be identified. These columnar structures grow towards the center of the melt track along the temperature gradient direction. The spacing between columnar features is less than 1 μm. Similar microstructural morphologies were observed in LPBF-AM processed Cu-10Sn alloy (Scudino, Unterdörfer et al. 2015) and Cu-15Sn alloy (Mao, Zhang et al. 2018). Figure 5-2(e) and (f) illustrate the microstructures of an AF-Vertical specimen within the laser scanning plane, where laser tracks are evident and micron-sized pores can also be observed. The width of each laser track is ~50 μm, consistent with the hatch space used in this work.

Figure 5-3 shows EBSD inverse pole figure (IPF) orientation maps of AF and VA specimens. Again, the mapped surfaces of the Horizontal specimens are parallel to the building direction (BD) (Figure 5-3(a), (c) and (e)), while the mapped surfaces of the Vertical specimens are perpendicular to the building direction (Figure 5-3(b), (d) and (f)). Figure 5-3(a) shows the complex grain morphology for an AF-Horizontal specimen, with both elongated and equiaxed grains observed. Similar to the aforementioned columnar structures, the elongated grains are not aligned strictly along the building direction. This can be ascribed to the complex thermal gradients caused by the zigzag laser scanning directions and island laser scanning strategy employed in this work, and similar results can be found in LPBF-AM AlSi10Mg parts (Sidot, Souissi et al. 2006). The elongated grains can be tens of micron in length and grow across several layers. Comparing Figure 5-3(a) with Figure 5-2(a) to (d), it is evident that the microstructures revealed by etching are not necessarily grains because of the apparent size difference between the etched structures and the mapped grains.

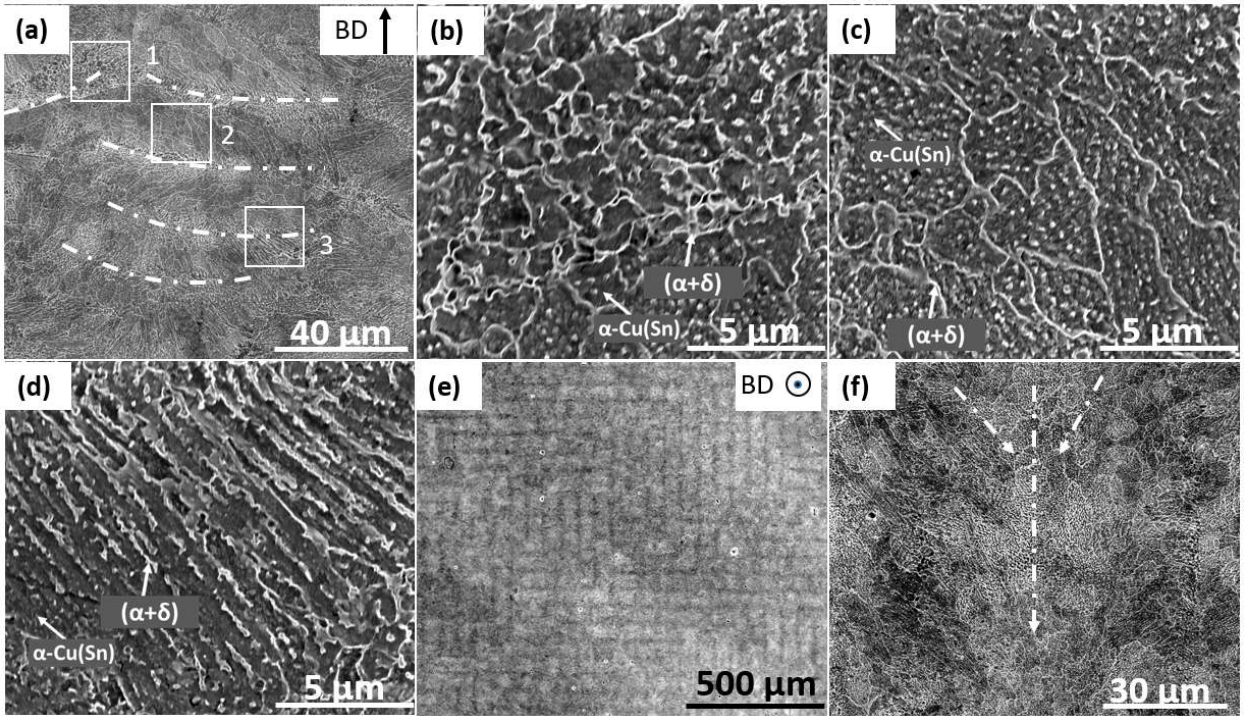

Figure 5-2. SEM imaging of etched AF specimens: (a) SEM image from one AF-Horizontal specimen; (b)/(c)/(d) magnified SEM images from areas 1, 2, and 3, respectively, as marked by the white squares in (a); (e)/(f) SEM images from one AF-Vertical specimen, showing laser tracks with varying magnifications.

The average grain size, *d*, is estimated by the linear interception method using the TSL OIM software, and the value of *d* is ~2.1 µm for AF-Horizontal specimen. The small grain size is attributed to the high cooling rate associated with the LPBF-AM process. Figure 5-3(b) presents the EBSD orientation map of an AF-Vertical specimen. The laser scanning tracks, as shown by the black dashed arrows, can be easily distinguished due to the fact that grains tend to grow towards the melt pool center. In addition, grains with different shapes can also be observed. The average grain size, *d*, of the AF-Vertical specimen is measured to be ~1.9 µm, close to its AF-Horizontal counterpart.

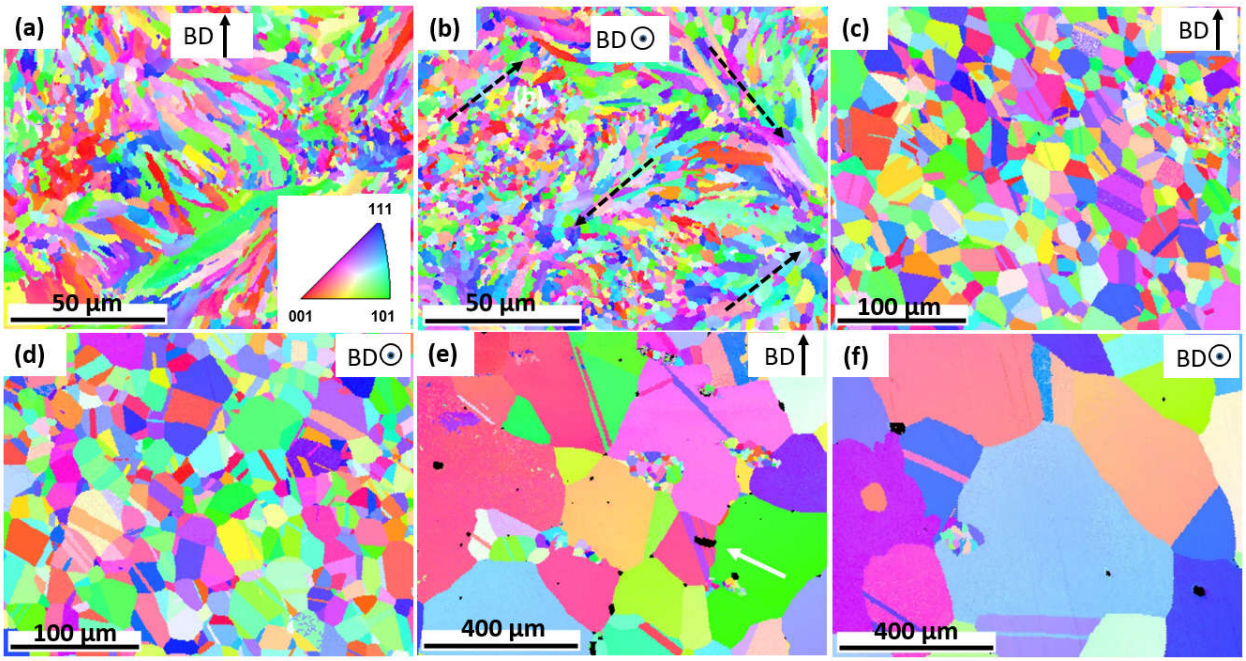

Figure 5-3. Microstructural characterization by EBSD: inverse pole figure (IPF) maps of (a) one AF- Horizontal specimen; (b) one AF- Vertical specimen; (c) one 600-Horizontal specimen; (d) one 600-Vertical specimen; (e) one 800-Horizontal specimen; and (f) one 800-Vertical specimen.

Figure 5-3(c) to (f) summarize the EBSD IPF orientation maps of VA specimens. Clearly, grain morphologies have changed significantly after annealing, as compared to the AF specimens. After annealing, the grains are predominantly equiaxed, and an ample amount of twining can be observed within Cu-10Sn grains. Figure 5-3(c) shows the grain morphology of a 600-Horizontal specimen. The presence of a small cluster of grains with sizes significantly smaller than the other grains may be a result of insufficiently long holding time at 600°C. The average grain size, *d*, is determined to be ~6 µm, including that portion of abnormally fine grains and intersection with twins. The average grain size of the 600-Vertical specimen, as shown in Figure 5-3(d), is measured to be ~8 µm. After annealing at 800°C for 1 hour, dramatic grain growth was observed, as depicted in Figure 5-3(e) and (f). Small clusters of finer grains are also observed, implying abnormal grain growth occurring in the annealing process. The average grain size, *d*, is calculated to be ~66 µm and ~120 µm for the 800-Horizontal and 800-Vertical specimens, respectively, again including the

finer grains and twin intersections. The huge difference between the calculated average grain sizes of the 800-Horizontal and 800-Vertical specimens can be attributed to the existence of many more clusters of extremely fine grains in the former than in the latter. Pores also grew significantly in VA specimens. As shown in Figure 5-3(e) and (f), the largest pore can be ~50 μm in length and ~20 μm in width. It is also interesting to note that the pores after annealing are not uniformly distributed throughout the entire specimen volume, and most of the pores are located at grain boundaries or regions close to grain boundaries. The polished surface of an 800-Horizontal specimen shows numerous pores with varying sizes, from sub-micron to tens of microns, Figure 5-3(e), while the mapping surface of an 800-Vertical specimen only presents several pores, as displayed in Figure 5-3(f).

5.2. Corrosion property

The weight changes of AF-Horizontal, 600-Horizontal, and 800-Horizontal specimens in a 3.5 wt. % NaCl water solution were recorded daily for 11 days (Figure 5-4(a) and Table 5-1), which gave a measure of the relative corrosion rates. It is obvious that the corrosion rate of AF specimen is higher than that for the heat treated ones. According to data shown in Figure 5-4(a), the same corrosion performance was observed for vacuum annealed specimens at 600℃ and 800℃. Figure 5-4(b) presents θ-2θ XRD patterns obtained from AF and VA specimens after weight loss test. The presence of a Cu_2O phase can be identified on all three specimen surfaces. The remaining peaks arise from the α phase and δ phase, as shown in Figure 5-1. The absence of chloride compounds on the surface after the immersion test confirms the low aggressive corrosive environment and formation of noble patina (type I) on the surface.

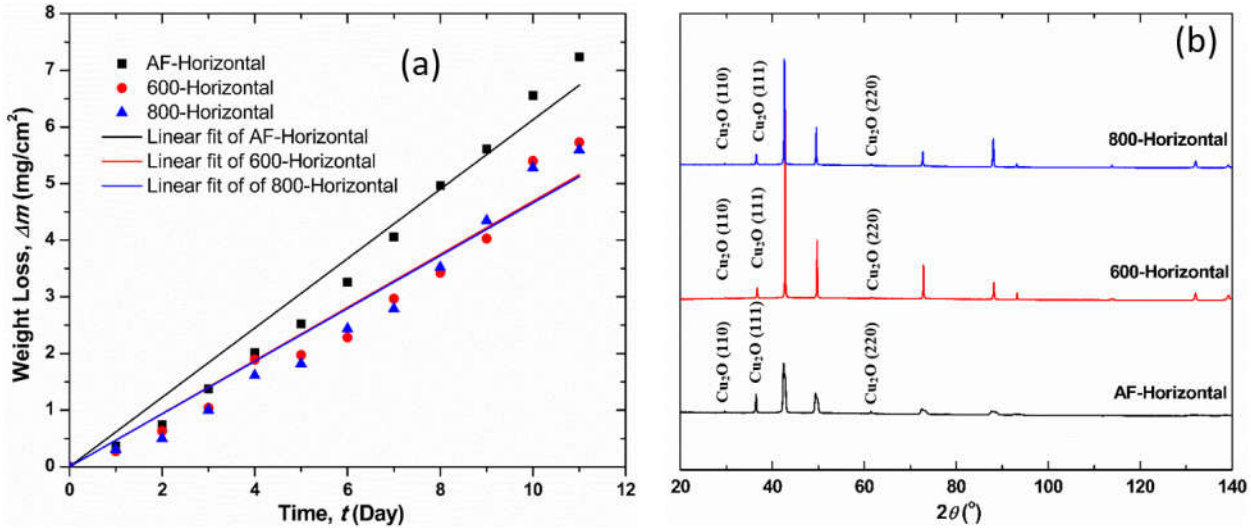

Figure 5-4. (a) Weight loss test results of AF-Horizontal, 600-Horizontal and 800-Horizontal specimens in 3.5 wt% NaCl water solution during 11 days. (b) XRD patterns of the surfaces of AF-Horizontal, 600-Horizontal and 800-Horizontal specimens after weight loss test, revealing the formation of Cu_2O phase.

Table 5-1. Slopes describing the weight loss rate of the AF-Horizontal, 600-Horizontal and 800-Horizontal samples immersing in the solution for 11 days

Sample	Slope ($mg/cm^2.day$)	R^2
AF-Horizontal	0.612	0.98
600-Horizontal	0.469	0.96
800-Horizontal	0.466	0.96

Figure 5-5(a) shows the change of specimens surface potential with time in an open circuit potential (OCP) test. It is clear that the curves are qualitatively similar for all three specimens, i.e., the potential decreases for the first couple of hours due to dissolution of pre-formed compounds on the surfaces, then the potential increases due to the formation of a protective layer (Cu_2O), and finally the potential reaches a steady state known as OCP. Minute fluctuations on the curves are a sign of precipitation and dissolution of the compounds during the reaction process between the specimens surfaces and the solution. Same as weight loss results, almost the same curves are

obtained for the two VA specimens. However, the AF specimen has a more negative OCP value (~ -0.17V) and needed a much longer time (30 hours) for the surface to achieve the steady state as compared to the VA cases (~ -0.155V and 8 hours). It appears that the heat treatment process has a stabilizing effect on the formed passive layer by improving the passive layer quality and/or thickness.

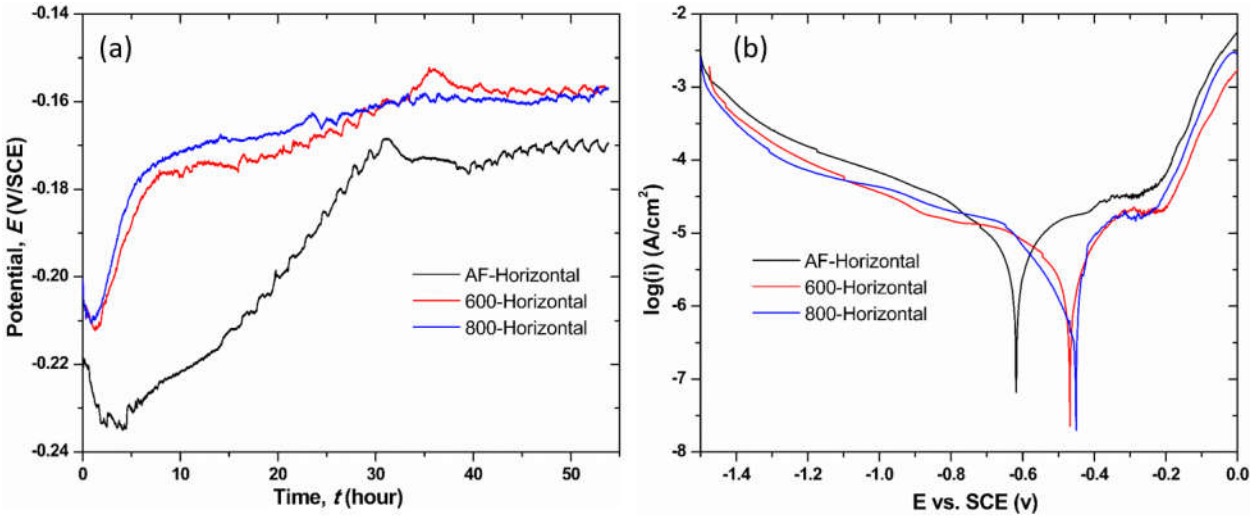

Figure 5-5. (a) Open circuit potential vs. time curves of specimens in 3.5 wt.% NaCl water solution; (b): The potentiodynamic polarization test results obtained after 1 h open-circuit immersion for AF-Horizontal, 600-Horizontal and 800-Horizontal specimens in 3.5 wt.% NaCl water solution.

Table 5-2. Corrosion test results obtained from potentiodynamic polarization measurements

Sample	E_{corr} (v)	i_{corr} ($\mu A/cm^2$)	i_p ($\mu A/cm^2$)	E_p (v)
AF-Horizontal	-0.620±0.024	7.586±0.288	31.623±1.265	-0.262±0.009
600-Horizontal	-0.468±0.015	3.388±0.108	21.380±0.663	-0.204±0.008
800-Horizontal	-0.451±0.014	3.236±0.113	16.218±0.584	-0.223±0.008

Figure 5-5(b) and Table 5-2 summarize the results of potentiodynamic polarization tests. As shown in Figure 5-5(b), little difference is observed for both VA specimens, while it is evident that the curve of AF specimen shifts to higher current densities and lower potentials compared to

the VA specimens, indicating a more active surface and higher corrosion rate for the AF specimen. Specifically, as listed in Table 5-2, the corrosion current density of AF specimen is 7.586 $\mu A/cm^2$, over two times of the corrosion current density of the 800-Horizontal specimen, 3.236 $\mu A/cm^2$. The corrosion rate for both VA specimens are similar, consistent with the results from weight loss and OCP tests. In addition, all potentiodynamic curves have a region in the anodic branch where the current density is almost constant in the potential range of -0.2 ~ -0.35V. This observation confirms the formation of a passive layer, which mainly consists of Cu_2O, as suggested by the XRD results shown in Figure 5-4(b).

Intergranular corrosion is a localized form of corrosion, attacking along grain boundaries (GBs) due to the higher energy state of GBs as compared to the remaining parts of the surface. It is well known that an alloy with finer grains can have a higher rate of intergranular corrosion due to higher GBs density (Ralston, Birbilis et al. 2010, Gollapudi 2012). In addition, it has been reported that due to the possible intervention of GBs in passive layer formation, this passive layer can be less protective for specimens with finer grains, which in turn results in a higher corrosion rates (Barbucci, Farne et al. 1998, Li, Jiang et al. 2007). Figure 5-6(a) shows the surface of 800-Horizontal specimen after weight loss test. It is evident that intergranular corrosion attack occurred along grain boundaries, as indicated by the white arrows. In addition to intergranular corrosion, galvanic corrosion is another reason for the higher corrosion rate for the AF specimen. It's well known that a surface consisting of two phases can suffer from galvanic corrosion in a corrosive media where the more resistive phase serves as cathode and causes the corrosion of the other phase (Fu, Tang et al. 2015). As mentioned before, AF specimens contain both α and δ phases, while VA specimens only contain the α phase. Studies have revealed that the δ phase exhibits a better corrosion resistance as compared to the α phase (Souissi, Sidot et al. 2007, Šatović, Žulj et al.

2009). Consequently, the δ phase can work as a cathode and lead to preferred corrosion attacks on the α phase. Figure 5-6(b) shows the surface morphology of AF specimen after corrosion test. Melt pool profiles are clearly observed, and the white structures are mainly distributed on regions close to melt pool borders, Figure 5-6(c). It is clear that these white microstructures protrude out of the specimen surface, similar to etched microstructures shown in Figure 5-2(d). Therefore, the observation of the white structures and dark regions can be ascribed to galvanic corrosion caused by the co-existence of α and δ phases.

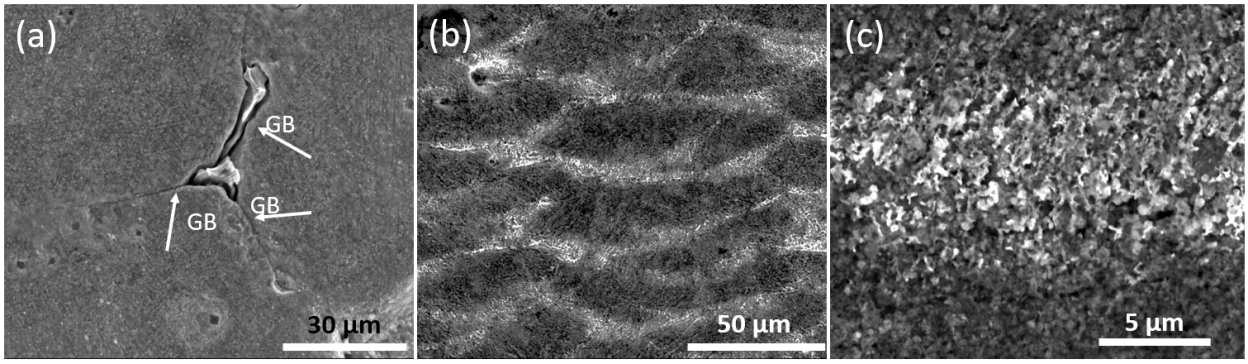

Figure 5-6. SEM images of surface morphologies after weight loss test. (a) 800-Horizontal specimen, (b) (c) AF-Horizontal specimen.

5.3. Conclusions

Cu-10Sn alloy specimens have been successfully prepared with LPBF-AM. The effects of buliding direction and heat treatment on corrosion properties of Cu-10Sn alloy samples are studied. The following conclusions can be reached.

(1) The AF specimens under two different building orientations are found to have similar corrosion properties.

(2) The AF specimens have fine grains with average grain size ~2 µm, and consist of a Cu-rich α phase and a Sn-rich δ phase due to the rapid cooling during the LPBF-AM. Vacuum-

annealed specimens possess equiaxed grains, and grain sizes increase significantly. Only α phase can be detected in VA specimens.

(3) Heat treatment results in a significant improvemnet in corrosion performance by decreasing the corrosion rate by almost 50% due to the modification of passive layer morphology as well as the decrease of the susceptibility to intergranular corrosion and internal galvanic corrosion.

Chapter 6. Corrosion Behavior of Additively Manufactured AISI316L Parts and the Effect of Post Annealing Process

6.1. Results and discussion

Tafel curves for the wrought and AM samples before and after the annealing process are presented in Figure 6-1. It clearly indicates that the corrosion rate of the AM sample is less than that of the wrought one before the post heat treatment process and the trend is the same after annealing with a lower intensity. In other words, as shown in Figure 6-1, the AM parts' curve is shifted to lower values of current density compared to the wrought sample. On the other hand, although the curves for both samples are shifted to lower values of current density after the annealing process, the changes are more pronounced for the wrought sample. The related key parameters measured from these polarization curves can be found in Table 6-1. Those results are attained by Tafel extrapolation. As can be seen in Table 6-1, i_{corr}, which represents the corrosion rate of the samples, decreased for both wrought and the AM samples after heat treatment and the best result belongs to the heat treated AM sample. In addition, the corrosion potential (E_{corr}) is more positive after heat treatment process for both wrought and printed samples compared to the as-received ones, which indicates the less tendency to form metal ions and corrosion process.

On the other hand, for the Tafel curves for all four cases, a wide range of potential with almost constant values in current density can be detected, which represents an active-passive behavior. The constant current density suggests the same corrosion mechanism on the surfaces of all samples, even though the stability range can be different. The mentioned range is identified on Figure 6-1 as ΔE on the heat-treated AM sample as an example and the related values are reflected

---

This chapter was previously published as Ali Hemmasian Ettefagh, Shengmin Guo, "Electrochemical behavior of AISI316L stainless steel parts produced by laser-based powder bed fusion process and the effect of post annealing process" Additive Manufacturing, 22 (2018): 153-156.. Reprinted by permission of Elsevier.

in Table 6-1. In addition, it can be seen that there exists a sudden increase of the current density just out of the ΔE range (passive layer break down point). This occurs on a more positive value of potential for the heat-treated samples compared to the as received ones, and for the AM samples compared to the wrought ones. These results suggest a more stable passive film for the AM samples, which has become more stable after the annealing process.

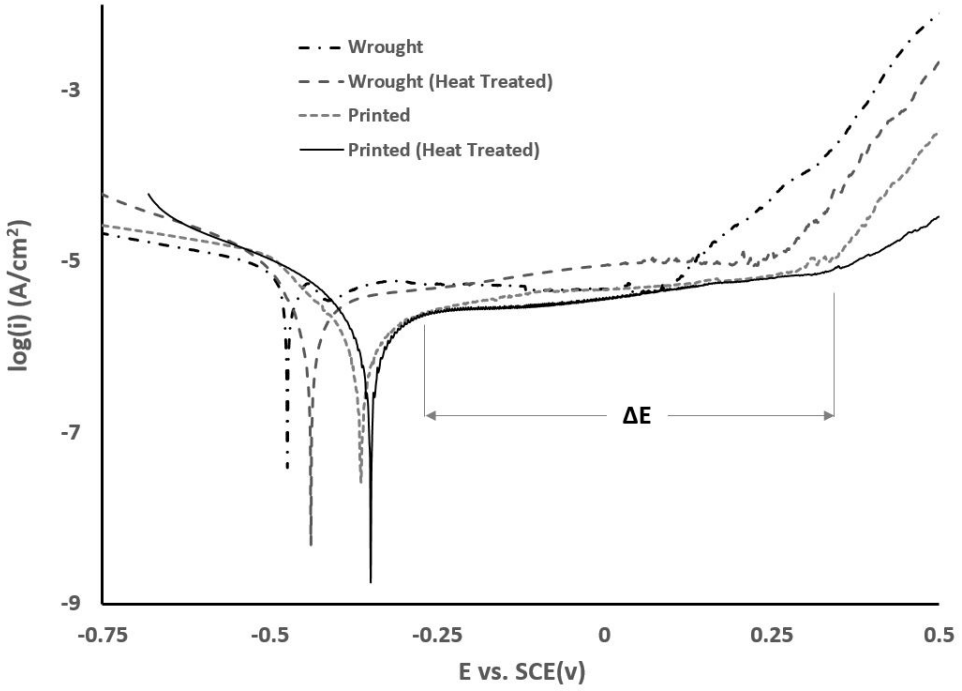

Figure 6-1. Tafel curves obtained in 3.5% NaCl Solution. The indicated ΔE range refers to the passive layer stability potential range for the annealed AM (printed) sample.

Table 6-1. Corrosion parameters attained from polarization curves and Tafel extrapolation

Sample	E_{corr} (v)	i_{corr} ($\mu A/cm^2$)	ΔE (v)
Wrought	-0.471±0.017	4.16±0.146	0.463±0.015
Wrought (Heat-Treated)	-0.434±0.013	2.69±0.078	0.564±0.020
Printed	-0.362±0.014	1.29±0.053	0.609±0.019
Printed (Heat-Treated)	-0.347±0.010	1.14±0.039	0.613±0.025

EIS measurements were subsequently performed in order to confirm this finding. The Nyquist plots of the samples are depicted in Figure 6-2. According to these plots, typical capacitive semi-loop shapes are similar for all samples but with different diameters. The trend of these curves is caused by a combined effect of electric double layer capacitance and the charge transfer resistance. To find the values of these parameters, it is necessary to fit these curves with the equivalent circuit. Figure 6-2 also shows the proposed circuit for this situation, which best fits the results and consists of R_{Ω} (electrolyte resistance), R_P (passive layer resistance), C_P (capacitive properties of passive layer), R_{CT} (charge transfer resistance of electrochemical double layer), and C_{DL} (capacitive properties of electrochemical double layer). This type of equivalent circuit represents an electrode with a protective coating layer. The parameters for such an equivalent circuit can be found in Table 6-2 and their trend will be discussed in the next paragraph. Based on the Nyquist plots, it is confirmed that the mechanism of corrosion reaction for all samples are the same and mainly controlled by the charge transfer phenomena through the protective layer.

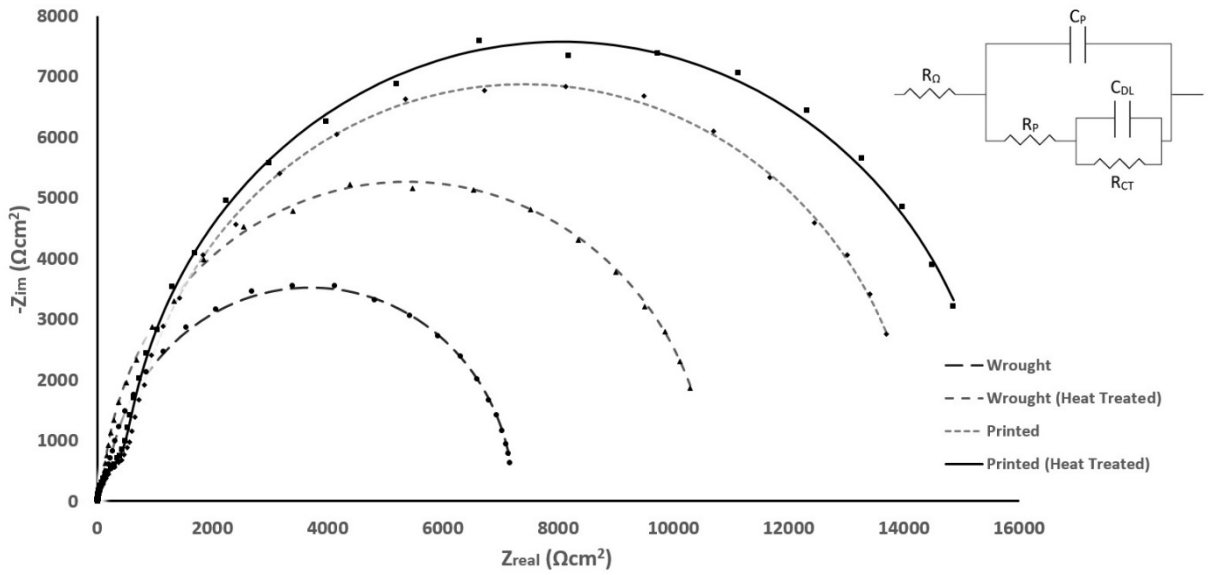

Figure 6-2. Nyquist plots of wrought and AM (printed) AISI316L samples before and after the annealing process in 3.5 wt% NaCl and the electric equivalent circuit used to fit the curves.

Table 6-2. Measured parameters from the simulation of Nyquist plots with an electric equivalent circuit shown in Figure 6-2

Sample	R_Ω (Ωcm^2)	R_P (Ωcm^2)	C_P ($\mu F/cm^2$)	R_{CT} (Ωcm^2)	C_{DL} ($\mu F/cm^2$)
Wrought	7.92	710	86.3	6514	93.9
Wrought (Heat-Treated)	8.34	1002	56.2	9636	31.4
Printed	8.83	1239	84.3	13038	177.0
Printed (Heat-Treated)	10.71	1326	42.9	14285	70.2

The results indicate that R_Ω is low and almost identical for all testing cases, which is consistent with the observed reproducibility of the test setup. The fact that C_P has decreased for the AM annealed sample refers to a better protection of the passive layer. Both R_P and R_{CT} are higher for the as received and annealed AM parts, which also indicate more resistance for the mass transfer in the diffusion and double layer (passive film) respectively. Specifically, the higher value of R_{CT} for the AM samples compared to the wrought ones suggests a better quality of passive film. This protective layer is formed on the AM parts' surface. This finding agrees with the Tafel curves where the passivation ranges of the AM samples are wider (ΔE in Table 6-1). Similar to the Tafel curves, the differences between the parameters of annealed and as received AM parts are relatively small. This suggests that the mechanism associated with the corrosion rate decrease after the heat treatment process is not dominated by the quality of passive layer or phase change. In contrast, the as received and the heat-treated wrought samples show a large difference.

Figure 6-3 depicts the XRD profiles of the wrought and AM samples before and after the annealing process. It is observable that the wrought sample contains two phases, which are γ (Austenite) and α' (martensite), whereas the AM samples have no martensite phase. The formation of martensite phase can be attributed to the plastic deformation during the manufacturing process of the wrought sample. It is well known that plastic deformation can induce the martensite phase

and the martensite phase can deteriorate the corrosion behavior along with the passivation capability of the surface as a result of the formed dislocations and internal stress (Jinlong, Meng et al. 2017). After the heat treatment of the wrought sample, the intensity of the (111) martensite phase decreased and (201) and (211) peaks disappeared, suggesting the reduction of non-equilibrium phase quantity in the structure, which can be considered as an explanation for a better corrosion behavior of heat-treated wrought sample compared to the as received one. But in case of AM samples, the detected phases for both annealed and as received specimens are the same.

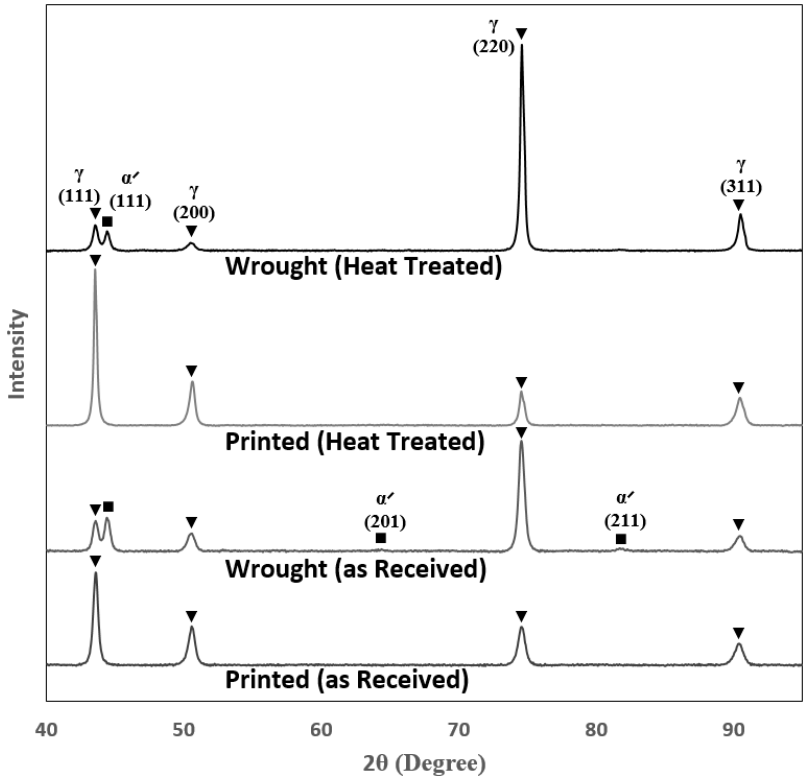

Figure 6-3. XRD profile of the AISI316L AM (printed) and wrought samples, before and after the annealing process. ■ bullets indicate α′ (martensite) phase while ▼ bullets represent the γ (Austenite) phase.

Based on the information obtained in the XRD patterns, the Tafel curves can be reinterpreted from the corrosion potential aspect. Figure 6-1 clearly shows that the corrosion potential of the AM samples are in the range of more positive values compared to wrought samples

and this is more obvious for the heat-treated AM sample. This increase in corrosion potential can be credited to the lack of martensite phase in the AM sample. As the corrosion potential is dominated by the fastest reaction, in the case of commercial wrought AISI316L testing, the anodic reaction is governed by the corrosion of a less resistant phase, which is martensite in the wrought sample. This phase has decreased after the annealing process but still exists in the wrought sample and deteriorates the corrosion behavior despite its improvement compared to as received wrought sample. In contrast, the absence of this martensite phase in the AM sample led to a more positive corrosion potential, along with a decrease in the corrosion rate. After annealing for 2 hours in 800°C, the residual stresses associated with the fast heat up and rapid solidification during the AM process are relieved and this is the main reason of the slight improvement of the corrosion behavior after the heat treatment of AM parts. In other words, the presence of this stress leads to the formation of corrosion cells within the structure with the stressed zones acting as the anodic regions. Despite this mechanism not being the controlling regime of the corrosion of AISI316 AM parts, the elimination of the residual stress can lead to a less susceptible passive film in a non-stressed situation and a slight decrease of corrosion rate as a result. This finding is in agreement with the previous researches on the characteristic of passive film of austenitic stainless steels (Takakuwa and Soyama 2014, Nazarov, Vivier et al. 2017).

6.2. Conclusions

The corrosion behavior of AISI316L samples produced via laser-based powder bed fusion AM method was investigated before and after the annealing process and compared to the conventional wrought samples of the same alloy and heat treatment cycle. Results of electrochemical tests, including Tafel curves and EIS measurements, showed a decrease in the corrosion rate for the AM samples due to the ability to form a thicker and more stable protective

layer on the surface despite the same corrosion mechanism of both types of samples. The corrosion behavior of heat-treated AM sample is slightly better due to the elimination of residual stress after the annealing process. Post heat treatment results in a lower corrosion rate in the wrought sample mainly due to the reduction of non-equilibrium martensite phase in the structure. Coupling Tafel curves, Electrochemical Impedance Spectroscopy, and XRD results, it's confirmed that, for both wrought and AM samples, heat treatment is a positive factor on the corrosion behavior with two different mentioned mechanisms.

Chapter 7. Corrosion Behavior of Additively Manufactured Ti-6Al-4V Parts and the Effect of Post Annealing

7.1. Results and discussion

Figure 7-1 (left) shows the variation of open circuit potential for all of the samples. According to these results, the open circuit potential of the samples move, with increasing time, toward more positive values (anodic direction) which indicates the formation of a passive film on the surface of all samples. Furthermore, the surface potentials become stabilized after about 20 h for wrought, as-fabricated AM and heat treated AM samples and the final stabilized potential for the as-fabricated AM sample is slightly higher than the others.

Figure 7-1 (right) depicts the Tafel curves for wrought, as-fabricated AM, HT600, and HT800 samples. From these curves, it is clear that the general corrosion behavior of the as-printed sample has deteriorated compared to the wrought samples, based on the shift of the related curve to a higher current density. After the heat treatment process, it can be seen that HT600 and HT800 curves have shifted towards lower current densities and this shift is more noticeable for the HT800 case, indicating the lowest corrosion rate among the AM samples. The potential at which the direction of current reverses for each sample is its corrosion potential (E_{corr}). Then by extrapolation of the cathodic branch of each curve to E_{corr}, corrosion current density (i_{corr}) can be obtained. These results (average values and standard deviations) are gathered in Table 7-1.

This chapter was previously published as Ali Hemmasian Ettefagh, Congyuan Zeng, Shengmin Guo, and Jonathan Raush" Corrosion behavior of additively manufactured Ti-6Al-4V parts and the effect of post annealing" Additive Manufacturing, 28 (2019): 252-258. Reprinted by permission of Elsevier.

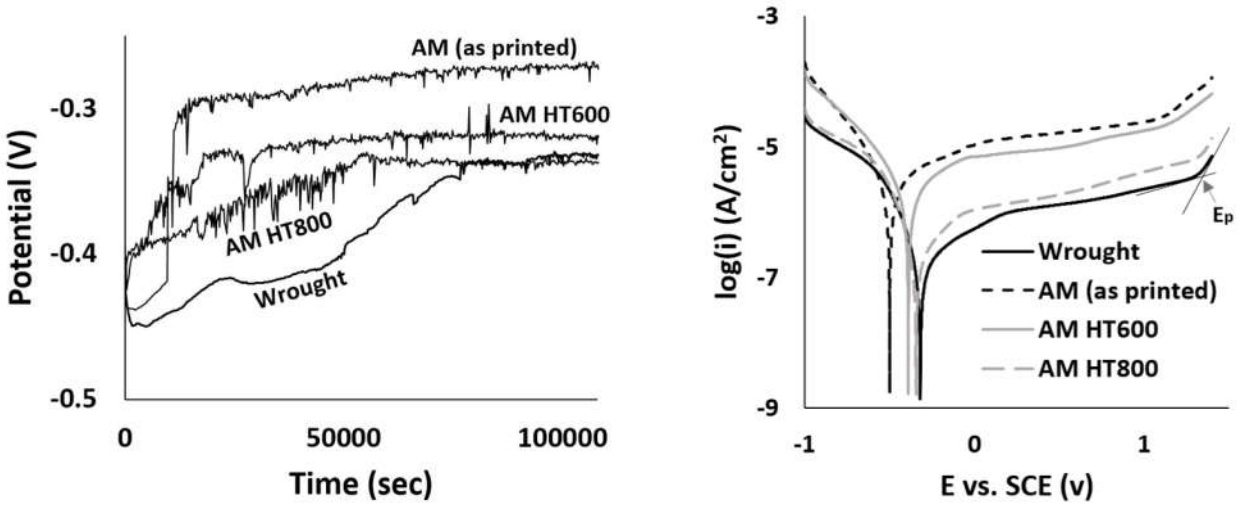

Figure 7-1. (left) Open circuit potential as a function of time, and (right) Tafel curves of the tested samples. All tests were performed in 3.5wt% NaCl water solution.

Table 7-1. Corrosion parameters obtained from polarization curves

Sample	E_{corr} (v)	i_{corr} ($\mu A/cm^2$)	i_p ($\mu A/cm^2$)	E_p (v)
Wrought	-0.318±0.010	0.115±0.004	1.514±0.048	1.345±0.043
AM (as-printed)	-0.494±0.016	1.820±0.059	18.621±0.601	1.131±0.037
AM HT600	-0.390±0.013	1.480±0.048	12.589±0.417	1.186±0.038
AM HT800	-0.337±0.011	0.151±0.006	1.995±0.065	1.318±0.044

Based on the Tafel curves of the tested samples, the passive region can be clearly seen. This region has an almost constant current density value over a certain range of potential. This observation suggests an active-passive behavior of all samples with a similar corrosion mechanism in accordance with OCP test results. The breakdown of the passive layer can be recognized on the Tafel curves by the existence of a sudden increase of the current density. Average current density of the passivation area and the potential at the breakdown point are labeled by i_P and E_P respectively. E_P is considered the end point of the near constant current density range. For the annealed samples, i_P is lower than for as-fabricated and the passive layer breaks in a more positive E_P. The values for the HT800 samples are nearly equivalent to those of the wrought samples.

According to Table 7-1, the passive layer current density for the as-fabricated AM sample is almost sixteen times higher than that of the wrought samples. However, after the heat treatment process for 2 hours at 800°C, the current density is comparable to that of the wrought sample.

The general corrosion rates of the samples were obtained by the Tafel extrapolation method as E_{corr} and i_{corr} in Table 7-1. The corrosion rate is dominated by the passive layer behavior for this alloy. These results suggest a less stable passive film and a higher corrosion rate for the as-fabricated AM sample. The corrosion rate of the as-fabricated AM parts is almost sixteen times higher than the wrought samples whereas values for the HT800 sample improve significantly and are within about 30 percent of the wrought case.

It should be mentioned that the increase in the current density just out of the relatively stable range of potential could also be attributed to other phenomena such as oxygen evolution. To evaluate this potential mechanism, the surfaces of the samples were observed under SEM to observe any pit initiation after the corrosion tests. These images are presented in Figure 7-2. As can be seen here, the as-fabricated AM sample experienced significant pitting phenomenon. However, this localized corrosion becomes less severe after heat treatment at 600°C and pits have almost been eliminated by the heat treatment process at 800°C. Severe pitting phenomena in the as-fabricated AM samples demonstrate that the additively manufactured Ti-6Al-4V parts require a proper heat treatment process to have a comparable corrosion behavior to wrought parts. HT800 appears to be a suitable process to eliminate the pitting. The HT800 sample corrodes almost uniformly according to visual examination (Figure 7-2), and results in a surface quality more or less the same as the wrought sample. This conclusion is in agreement with the Tafel diagram results and similar investigations (FERDINANDOV, GOSPODINOV et al. , Gurrappa 2003).

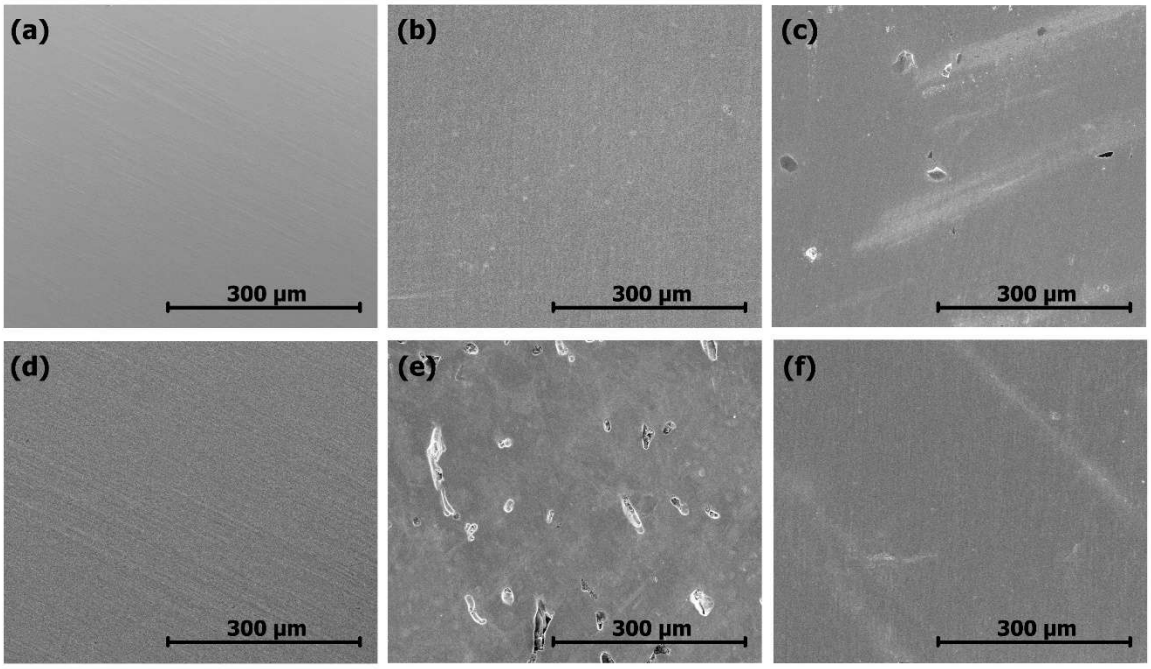

Figure 7-2. SEM images of the sample surfaces. (a) Wrought before corrosion tests, (b) AM as-printed before corrosion tests, (c) AM HT600 after corrosion tests, (d) Wrought after corrosion tests, (e) AM as-printed after corrosion tests and (f) AM HT800 after corrosion tests. All images are taken at the magnification of ×250.

In order to further confirm the above findings, EIS measurements were performed to evaluate the corrosion mechanism by obtaining the Bode and Nyquist plots and their associated equivalent circuits. It is well known that a greater arc radius of the curves of a Nyquist plot indicates a better corrosion resistance ability (Pujadó 2012). Figure 7-3-d describes this trend with the wrought sample having the highest arc radius followed by the AM HT800 sample. In addition, according to the Bode plots (Figure 7-3-b,c), at high frequencies, the log |Z| metric trends towards constant values while the phase angle values drop to zero at high frequencies. In the range of medium to low frequencies, the phase angle values approach 90° suggesting that a protective film (i.e. passive layer) has been formed on all of the samples in the solution. A result which is supported by the attained Tafel curves. Furthermore, the higher values of phase angle in the wrought sample indicate a more protective passive film compared to the as-printed sample. As

indicated by Figure 7-1 and Figure 7-3 (Tafel, Nyquist, and Bode plot results), the 2 hour, 800°C heat treatment process generates a protective layer comparable to the wrought sample. The proposed equivalent circuit in Figure 7-3-d is the best fit based on the above characterizations and the Nyquist plots. The related parameters for the equivalent circuits can be found in Table 7-2. In this circuit, R_Ω represents the electrolyte resistance; R_P is the resistance of the passive layer; CPE1 indicates the capacitive property of the passive layer; R_{CT} is related to the electrochemical double layer and its charge transfer resistance; and CPE2 shows the capacitive properties of the electrochemical double layer. Constant phase elements (CPEs) were used in this equivalent circuit to match the rough surface feature of the electrodes. According to these data, the same mechanism, which is chiefly governed by the charge transfer through the passive layer, is suggested for all of the samples. These outcomes are in agreement with the published literature (de Assis, Wolynec et al. 2006, Dai, Zhang et al. 2016).

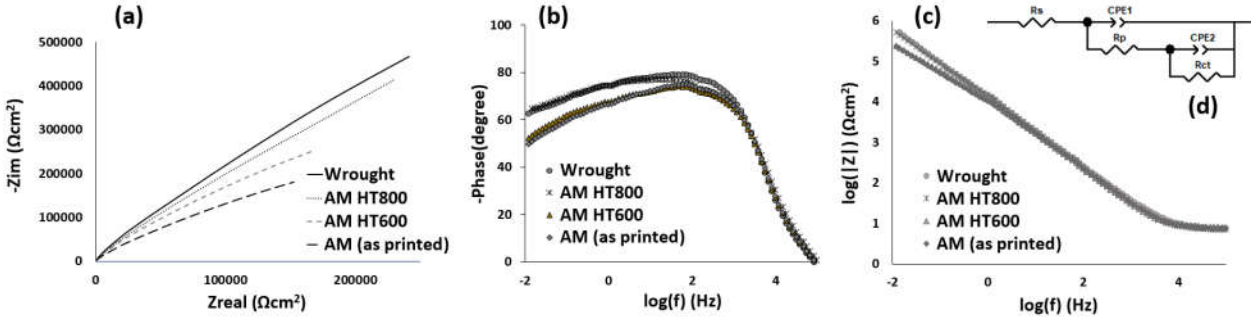

Figure 7-3. (a) Nyquist plots and (b),(c) Bode plots of all samples accompanied with (d) the electric equivalent circuit. All tests were performed in 3.5wt% NaCl water solution.

A consistent reading of the electrolyte resistance (R_S) value, regardless of the sample types and test setup in Table 7-2, indicates a good reproducibility of the tests. In addition, R_P and R_{CT} values represent the mass transfer resistance in the diffusion and passive film (double layer), respectively. These two parameters for the AM samples are significantly less than the values for the wrought samples indicating the deterioration of corrosion behavior of the AM samples

compared to the wrought ones. Results for HT600 and HT800 cases show a gradual improvement after the annealing process, where the corrosion behavior and the quality of the passive layer of the AM HT800 samples are comparable to the wrought samples. These findings are also in accordance with the results obtained from Tafel curves.

Table 7-2. Electrochemical impedance parameters obtained by equivalent circuit shown in Figure 7-3

Sample	R_S ($\Omega.cm^2$)	R_P ($M\Omega.cm^2$)	R_{CT} ($M\Omega.cm^2$)	Error (%)
Wrought	6.907	0.61	4.220	2.45
AM (as-printed)	7.124	0.20	0.899	2.23
AM HT600	7.240	0.39	2.050	3.14
AM HT800	6.852	0.59	3.908	2.51

XRD profiles of all samples can be seen in Figure 7-4. It is clear that the same phases are present at the same angles of diffraction (2θ), but with different intensities, for the tested samples. Both wrought and AM samples consist of mainly hexagonal Ti (α) with the preferred crystal direction of (101) and a BCC phase (β) which is more obvious in the wrought sample. It is noticeable that α peaks in the AM samples are broader relative to the same peaks of wrought samples suggesting a non-equilibrium phase structure (α′). The existence of a non-equilibrium phase structure is due to the rapid solidification during the LPBF process. This thermal regime prevents the diffusion of vanadium and as a result, α′ has a higher content of vanadium compared to α phase. Sallica-Leva et al. suggested that the broader peaks of non-equilibrium phases were associated with this higher solute content of this phase in a fast cooling rate where the vanadium element was trapped in the atomic structure and the supersaturation of vanadium resulted in a deformation of the crystal and broadening of the related peaks (Dai, Zhang et al. 2016).

Additionally, two peaks of β phase at 2θ=39.5° and 2θ=57°are less pronounced in the as-fabricated AM samples.

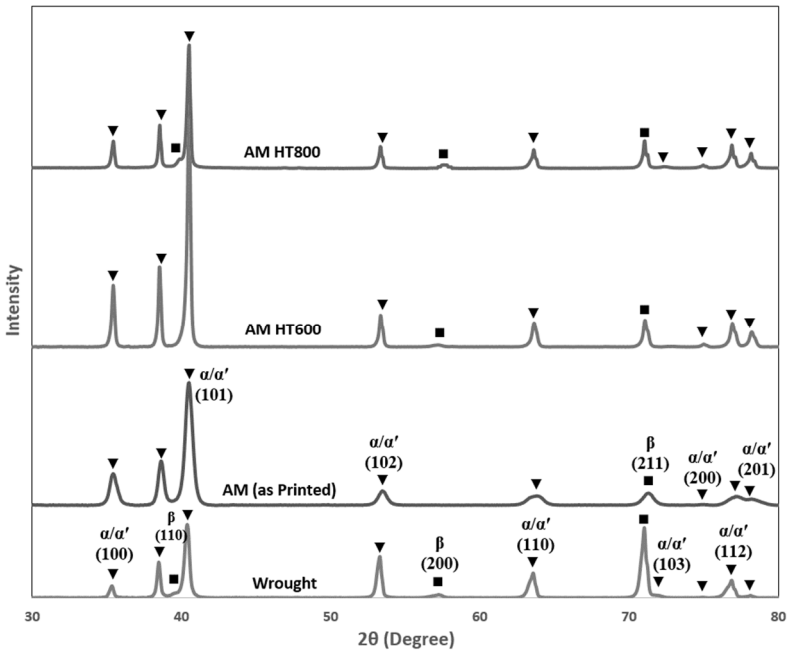

Figure 7-4. X-ray diffraction pattern of the AM and wrought samples of Titanium alloy Ti-6Al-4V. Both as-printed AM samples and samples undergone heat treatment are shown. ■ bullets represent β phase and ▼ bullets indicate the α or α′ phase.

After annealing of the AM samples, hexagonal Ti peaks become narrower and the two less pronounced β peaks reappear. These β peaks are more noticeable in the HT800 sample which suggests the reduction of the non-equilibrium phase quantity in the structure. Considering the supersaturated content of vanadium in α′, the heat treatment process leads to the diffusion of this element to β phase which can dissolve more vanadium compared to α and α′ phases. Hence, the gradual convergence of α′ to α phase and increasing levels of β phase will occur. This claim is in agreement with previous work in this field (Vrancken, Thijs et al. 2012, Sallica-Leva, Caram et al. 2016, Xu, Lui et al. 2017). Accordingly, it is expected that the microstructure of the HT800 sample should be more or less the same as the wrought sample containing equilibrium phases of α and β as opposed to a needle shaped martensitic structure.

Figure 7-5 presents the SEM images showing the microstructure of the samples. As can be seen, the wrought sample primarily consists of equilibrium α and β phases (dark and light areas respectively). Unlike the wrought sample, the as-fabricated AM sample only exhibits the martensitic needle-shaped structure of α′ phase. As mentioned before, the formation of this structure is due to the nature of the LPBF process which involves rapid heating and solidification and results in the strain in the structure, degrading the corrosion resistance due to its higher energy. Similar microstructures for wrought and AM samples have been reported previously (Sallica-Leva, Caram et al. 2016). The microstructure of the HT600 sample is visually quite similar to the as-fabricated AM samples and a martensitic structure is still dominant. By increasing the heat treatment temperature to 800°C, the needle-shaped non-equilibrium phase transforms to α and β phases and the structure is comparable to the wrought sample. These findings are in accordance with XRD results and corrosion behavior of the samples reported in this research and in work previously reported (Vrancken, Thijs et al. 2012). It has been claimed that by a heat treatment process, β phase is formed on the boundaries of the original α′ phase due to the diffusion of vanadium (Sallica-Leva, Caram et al. 2016). This vanadium transfer process leads to the transformation of α′ martensitic structure to equilibrium α phase. Due to the sluggish diffusion of vanadium, heat treatment at 600°C for 2 hours is not adequate to provide the proper condition for this transformation to occur and as a result, the AM HT600 structure remains needle-shaped, similar to the as-printed sample. On the other hand, formed β phases can be clearly seen as the white areas in the HT800 sample microstructure (Figure 7-5-d), comparable to the wrought sample (Figure 7-5-a). The less protective passive layer and higher corrosion rate obtained in corrosion tests can be attributed to this non-equilibrium phase; and by its transformation to α and β equilibrium phases in the HT800 sample, the microstructure and corrosion behavior are both

similar to the results of the wrought sample. As the anodic reaction is controlled by the corrosion of a less resistant phase (needle-shaped phase), the elimination of this phase (according to the SEM images) is the main reason for the improved corrosion performance for the HT800 sample.

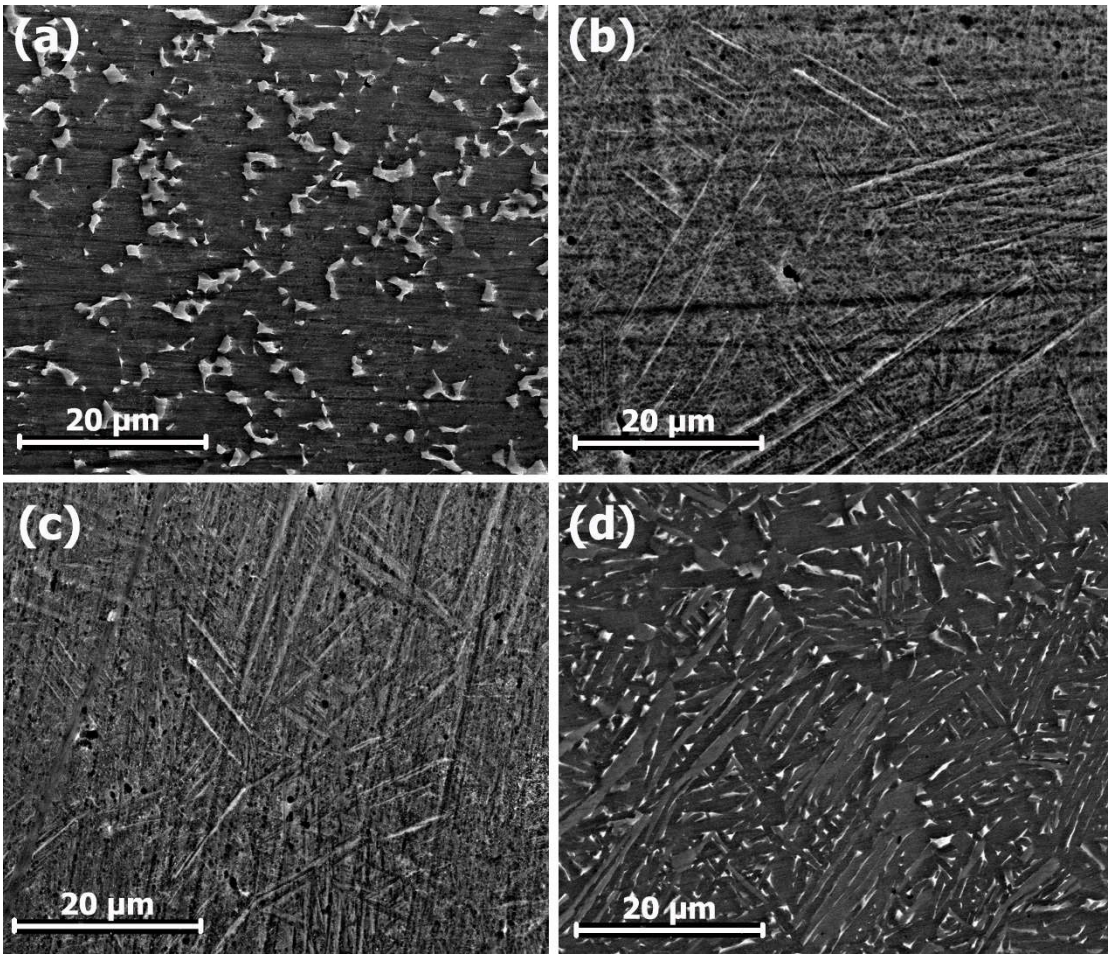

Figure 7-5. Microstructure of Ti6Al4V: wrought or AM and heat treated at different temperatures for 2 hr , a) Wrought, (b) AM (as-printed), (c) AM HT600, and d) AM HT800. Lighter zones in wrought and HT800 samples are β phase, and the dark phase is α phase. All images are taken at the magnification of ×2500.

In order to provide a more systematic evaluation of equilibrium phases of this alloy, the CALPHAD method was applied. For this purpose Thermo-Calc software and the TCTI1 thermodynamic database were used to obtain the phase diagram of the alloy at different temperatures under equilibrium conditions along with the chemical compositions of each phase at

500°C. These results are presented in Figure 7-6 and Table 7-3, respectively. In agreement with Figure 7-4 and Figure 7-5, at lower temperatures, BCC phase (β) is one of the equilibrium phases which has been suppressed under the fast cooling rate during the AM process which explains the degraded corrosion resistance of the AM sample compared to the wrought one. It is well known that β phase Ti-6Al-4V has a better corrosion resistance compared to α phase Ti-6Al-4V. It is claimed that this behavior is due to the more stable oxide film formed on β titanium (Chen and Tsai 2011). This is in accordance with the results of Tafel curves and the stability trend of the passive layers on different samples (Table 7-1). Nonetheless, according to CALPHAD calculations (Table 7-3), β phase contains a higher value of vanadium and lower value of aluminum whereas the former improves the resistance of the phase to dissolution and the latter is known as an α stabilizer (Safdar, Wei et al. 2012). As a result, the formation of β as one of the equilibrium phases decreases the dissolving rate of the alloy and improves the corrosion resistance.

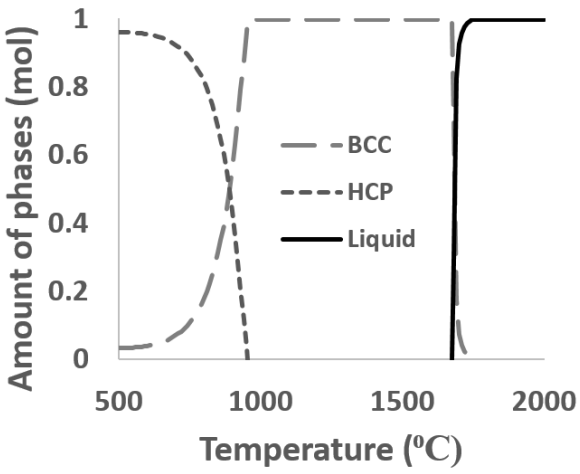

Figure 7-6. Stable phases at different temperatures under equilibrium solidification condition based on CALPHAD calculations by Thermo-Calc software.

During AM process, due to its rapid melt and solidification, equilibrium phases are unlikely to be produced and instead, non-equilibrium HCP titanium known as α′ predominates. As described before, needle-shaped microstructure and broadened XRD peaks of α phase and a lack

of β phase in the as-fabricated AM samples confirm the non-equilibrium composition of the alloy after the AM process. The as-printed samples also naturally have a higher energy state from a corrosion point of view. Corrosion cells can(Chen and Tsai 2011) be formed due to this higher energy whereby stressed zones are considered as the anodic regions and dissolve easier as a result. Post heat treatment processes enable thermally activated diffusion phenomena, including the formation of equilibrium phases of α and β, and the elimination of the strained non-equilibrium martensitic phase. This homogenization process under heat treatment is the primary reason for decreasing the corrosion rate and increasing the corrosion potential.

Table 7-3. Chemical composition of stable phases at 500°C based on CALPHAD calculations

	Mole Fraction (%)				
Phase	Ti	V	Al	Fe	Other
BCC (β)	42	51	4	3	0.001
HCP (α)	87	2	10	0.007	0.204

7.2. Conclusions

The corrosion behavior of Ti-6Al-4V alloy samples manufactured by the laser-based powder bed fusion additive manufacturing method were evaluated by focusing on the role of the heat treatment process with comparison to the wrought alloy of the same chemical composition.

(1) Results of polarization Tafel curves showed that due to the rapid solidification during the AM process and the lack of the more stable β phase, the corrosion behavior of the as-fabricated AM samples was deteriorated. These results were further confirmed by EIS tests which indicated a less protective passive layer for the as-printed samples than for wrought, but which could be improved after heat treatment processes.

(2) Post heat treatment of the AM sample results in the stress relief of the martensitic phase and formation of BCC β phase which has a higher corrosion resistance. Both of these

changes lead to an improvement of corrosion behavior of AM samples and result in performance comparable to that of wrought samples.

(3) XRD, microstructure analysis, and CALPHAD calculations all confirmed that for the AM specimens, the annealing process could improve the corrosion behavior based on the two explained mechanisms (stress relief of the martensitic phase and formation of BCC β phase).

(4) Results indicate that the laser-based powder bed fusion AM method accompanied with the post heat treatment processes can be used to produce Ti-6Al-4V AM parts with a negligible negative effect on the corrosion behavior in comparison to wrought material.

Chapter 8. Laser Surface Modifications of Fe-14Cr Ferritic Alloy for Improved Corrosion Performance

8.1. Towards laser parameter optimization

Laser processing parameters include laser power (P), scanning speed (v), and hatching space (H). In this research, the criterion for laser parameter optimization is to achieve a uniform surface coating, with the hypothesis that a uniform surface coating should lead to an improved corrosion performance. To optimize the laser parameters, a two-stage process is adopted with stage-one for identifying the suitable laser energy level while stage-two for identifying the best laser power-scanning speed combination.

Table 8-1. Identify the best laser energy density

Sample No.	Laser Power P (W)	Scanning Speed v (mm/s)	Hatching Space H (mm)	Energy Density E' (J/mm^2)
SPS	N/A	N/A	N/A	N/A
Y01	125	180	0.080	8.68
Y02	125	180	0.020	34.72
Y03	125	180	0.012	57.87

This chapter was previously published as Ali Hemmasian Ettefagh, Hao Wen, Ardalan Chaichi, Md Imdadul Islam, Fengyuan Lu, Manas Gartia, and Shengmin Guo, " Laser surface modifications of Fe-14Cr ferritic alloy for improved corrosion performance" Surface and Coatings Technology 381 (2020): 125194. Reprinted by permission of Elsevier.

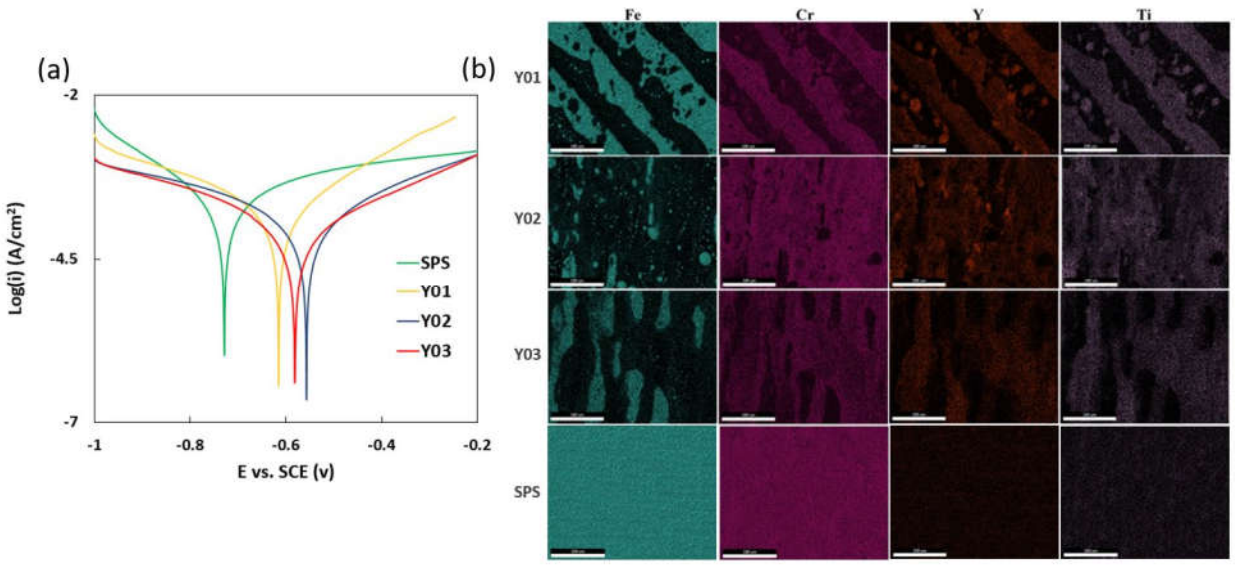

Figure 8-1. (a) Polarization curves in 3.5% NaCl Solution, and (b) Elemental map for Fe, Cr, Y, and Ti using EDS on SEM for samples Y01 to Y03 along with the SPS sample. The scale bars are all indicating 100 μm.

For stage-one, the attempted three sets of laser parameters and the calculated energy density (E') can be found in Table 8-1. In these sets, laser power and scanning speed were kept constant while hatching space was altered for three different energy densities (samples Y01, Y02 and Y03). Besides, to evaluate the role of the laser scanning process, one sample was prepared without laser scanning process and was tagged SPS. Visual inspection reveals a high surface roughness on the Y03 sample, which indicates excess laser power density. And in case of Y01, a visible stripe surface pattern suggests an uneven molten track coverage on the surface. Figure 8-1 (a) demonstrates the polarization test results of samples with the stage-one laser processing parameters together with the results of SPS sample. Based on these curves, corrosion current density (i_{corr}) and corrosion potential (E_{corr}) were calculated by Tafel extrapolation method and the results are shown in Table 8-2. It can be seen that Y02 exhibits the best corrosion performance by offering the lowest corrosion current density and the most positive corrosion potential. In addition, all three laser treated samples show a better corrosion performance compared to the SPS sample. It has been

argued that the formation of the surface layer containing chromium, titanium, and yttrium oxides protects the surface and improves the corrosion resistance of samples (Cho and Kimura 2007). To check the uniformity of surface coatings, elemental distributions on the surface of Y01 to Y03 samples were performed by EDS. The results of these measurements are presented in Figure 8-1 (b). From these maps, it is clear that iron is concentrated in regions with low levels of chromium, yttrium, and titanium. In other words, the later three elements seem to form regions that cover the iron base but these iron-depleted regions are not uniform over the entire sample surfaces. From the measurements, it is obvious that the formed layers on Y01 and Y03 are not uniform, with the molten track marks clearly shown. For case Y02, the non-uniformity has decreased in some levels qualitatively. On the other hand, unlike surface treated samples, the map for SPS sample shows a uniform distribution of all elements confirming the uniform chemical composition of samples after ball milling. Based on visual inspection and the results of corrosion test and elemental distribution, the energy density of Y02 was judged the best.

Table 8-2. Corrosion potential and current density obtained from Tafel curves in Figure 8-1 (a)

Sample No.	E_{corr} (v)	i_{corr} ($\mu A/cm^2$)
SPS	-0.728±0.025	97.7±4.0
Y01	-0.615±0.024	72.4±2.3
Y02	-0.557±0.017	25.7±0.7
Y03	-0.581±0.023	33.9±1.4

Table 8-3. Identify the best laser power-speed combinations

Sample No.	Laser Power P (W)	Scanning Speed v (mm/s)	Hatching Space H (mm)	Energy Density E' (J/mm^2)
SPS	N/A	N/A	N/A	N/A
Y02	125	180	0.020	34.72
Y04	44	50	0.025	35.20
Y05	75	86	0.025	34.89
Y06	175	200	0.025	35.00

For stage-two, the energy density of Y02 was selected and fixed while three different laser power/speed combinations, Y04-Y06 in Table 8-3, were evaluated. To establish the link between surface coating uniformity and the corrosion performance, corrosion tests and elemental distribution were performed on Y04 to Y06 samples. The results of these tests can be seen in Figure 8-2 and Table 8-4 along with the previous results for Y02 and SPS samples. From the elemental map, it is clear that Y06 exhibits the best uniformity. The same deduction can be extracted from corrosion results and the trend of the corrosion rates is more or less proportional to the uniformity of the surface layer. In addition, the corrosion rate of SPS sample is the worst compared to any of the laser-treated samples. Based on the obtained results from all the 6 sets, Y02 and Y06 laser parameters were identified to be the best ones.

8.2. Laser double scan and corrosion performance

To further improve the coating surface uniformity, Y02 and Y06 laser parameters were selected for an additional surface scan with 90 degrees of angle to the first pass of laser scanning. The samples with double passes of laser processing are named YY02 and YY06. To demonstrate the effectiveness of the additional pass of laser scanning, polarization curves and surface elemental distributions were obtained for these samples, Figure 8-3, and the associated corrosion parameters are summarized in Table 8-5. After applying two passes of surface laser scanning, the corrosion performance improved even more, suggesting the formation of a more protective layer on the surface. According to Table 8-5, the corrosion rate of YY06 sample has been decreased about 13 times compared to the same sample without any surface laser scanning. This value for Y06 with a single pass of laser scanning is almost 5 times, indicating the role of laser scanning in forming the protective layer. Besides, according to Figure 8-3 (b), the elemental distribution of Cr, Y and Ti

elements have been improved after two passes of surface treatment, suggesting a uniform layer on the surface, possibly consist of oxides of the mentioned elements.

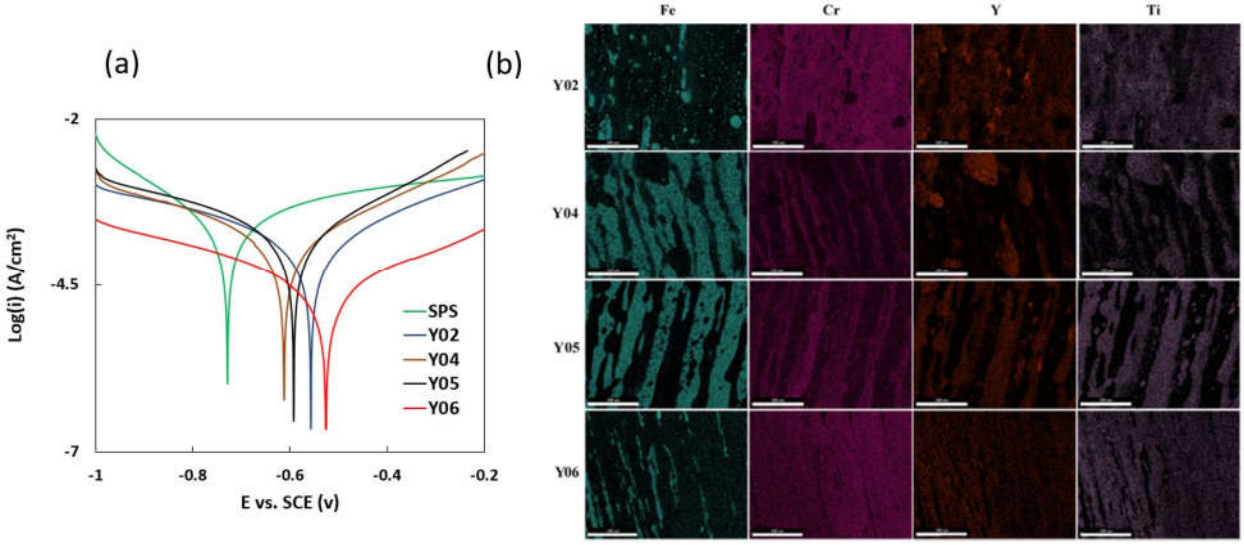

Figure 8-2. (a) Polarization curves in 3.5% NaCl Solution, and (b) Elemental map for Fe, Cr, Y and Ti using EDS on SEM for samples Y04 to Y06. The scale bars are all indicating 100 µm.

Table 8-4. Corrosion potential and current density obtained from Tafel curves in Figure 8-2 (a)

Sample No.	E_{corr} (v)	i_{corr} (µA/cm2)
SPS	-0.728±0.025	97.7±4.0
Y02	-0.557±0.017	25.7±0.7
Y04	-0.612±0.019	71.1±2.5
Y05	-0.592±0.022	58.9±2.3
Y06	-0.526±0.021	18.2±0.6

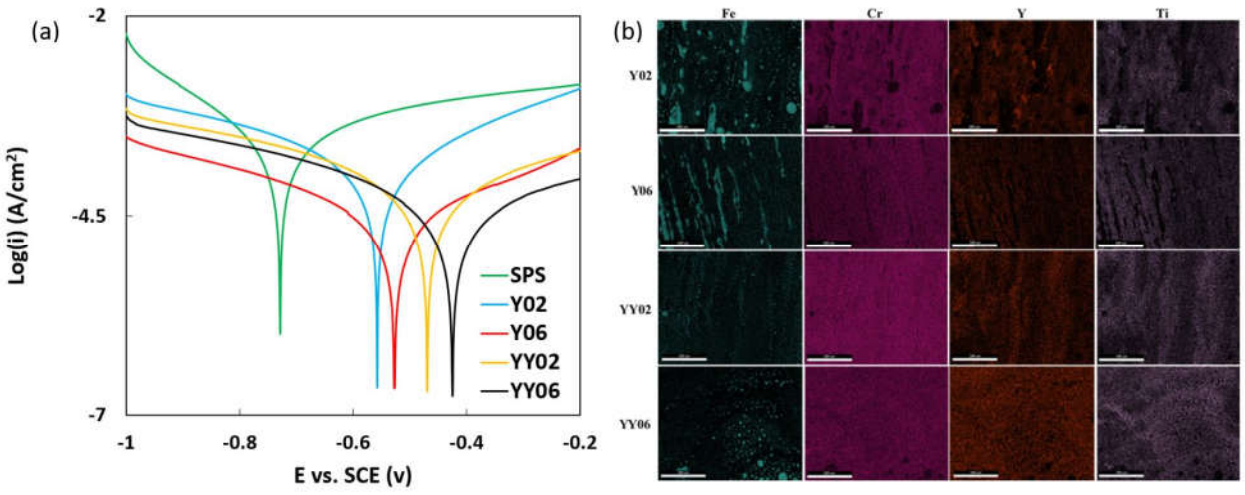

Figure 8-3. (a) Polarization curves in 3.5% NaCl Solution, and (b) Elemental map for Fe, Cr, Y and Ti using EDS on SEM for optimum sets of parameters with single or double passes of surface treatment. The scale bars are all indicating 100 μm.

Table 8-5- Corrosion potential and current density obtained from Tafel curves in Figure 8-3 (a)

Sample No.	E_{corr} (v)	i_{corr} ($\mu A/cm^2$)
SPS	-0.728±0.025	97.7±4.0
Y02	-0.557±0.017	25.7±0.7
Y06	-0.526±0.021	18.2±0.6
YY02	-0.469±0.018	11.7±0.4
YY06	-0.427±0.013	7.4±0.2

8.3. Coating characterizations

To understand the mechanisms for improved corrosion performance, additional surface characterizations including X-ray diffraction, Raman spectroscopy, and microhardness were performed on the samples. Figure 8-4 (a) shows the XRD patterns of SPS, Y02, Y06, YY02, and YY06 samples. After laser surface processing, the formation of Cr_2O_3 is apparent, with a relatively high intensity for the relevant XRD peaks. Small amounts of other oxides such as $Y_2Ti_2O_7$ and Fe_2CrO_4 are also detected on the laser processed samples, which are all known to be protective oxides. Main detected peaks in SPS sample are associated with chiefly iron and chromium elements which were applied to make this alloy. These peaks are much less pronounced in Y02

and Y06 samples and completely disappeared after two passes of laser scanning on YY02 and YY06 samples. Dominant peaks of chromium oxide in laser-scanned samples prove that by providing enough energy, Cr_2O_3 will form on the top layer of the laser processed samples. Although the chamber was purged with Argon before the laser processing, residual oxygen is still expected in the laser processing chamber. Y06 and YY06 samples were recognized for the uniform elemental distributions and good corrosion performance. Figure 8-4 (b) and (c) show the cross-sectional Raman maps of Y06 and YY06 samples. The green color illustrates the formation of a primary Cr_2O_3 layer on the surface, which is mostly responsible for the improvement of corrosion behavior. Pink color shows the substrate right beneath the Cr_2O_3 coating. As can be seen, the thickness of the Cr_2O_3 coating increases from ~3 µm to ~5 µm after performing the second pass of laser treatment.

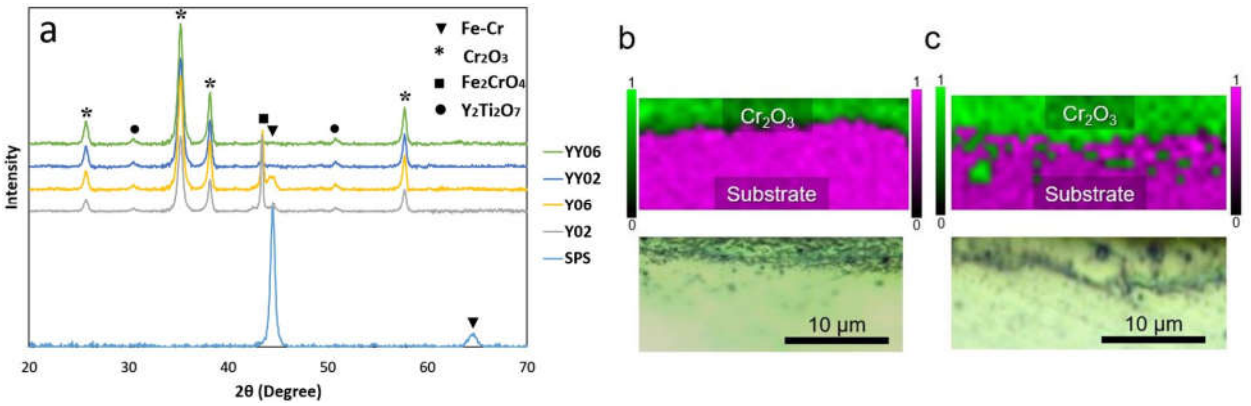

Figure 8-4. (a) XRD plots of SPS only and Laser surface treated samples of Fe-14Cr alloy, (b) Cross-sectional Raman spectroscopy and microscopy of Y06, (c) Cross-sectional Raman spectroscopy and microscopy of YY06.

The results of XRD and Raman spectroscopy can justify the noted improvement of corrosion resistance in Y06 and YY06 samples. XRD results of the laser-scanned samples confirm the elemental map presented in Figure 8-3 (b), which imply that the major elements on the surface of Y2, Y6, YY02, and YY06 are Cr, Y, and Ti. XRD results proof that the formed phases are mainly

Cr_2O_3 (confirmed by Raman spectroscopy) and a tiny amount of $Y_2Ti_2O_7$ (Figure 8-4). These results endorse the corrosion trend of the modified samples presented in Figure 8-3 (a). The development of Cr_2O_3 is well-known to be the protection mechanism of chromium contained steels and expected to improve the corrosion performance of Fe-14Cr. The formation of Cr_2O_3 and a tiny amount of Fe_2CrO_4 in laser processed samples suggests that due to the high temperature during the laser melting process, a uniform oxide layer can be formed under optimized laser processing parameters. The formation of a titanium-yttrium oxide in the shape of Y-Ti-O nanoclusters (Lu, Lu et al. 2017) or $Y_2Ti_2O_7$ and/or Y_2TiO_5 (Liu, Wang et al. 2015) is claimed to be the consequence of adding Y_2O_3 to the initial powder mixture during the mechanical milling step. Besides, it has been stated that despite the protective role of chromium oxide scale on the surface, the stability of small yttrium oxide particles results in finer grains of the matrix and finer grains enhance the diffusion of Cr to the surface and accelerate the formation of protective layer along with providing oxygen (Hoelzer, Pint et al. 2000, Hu, Zhou et al. 2013). Thus, optimized laser surface treatment provided a proper situation for the formation of protective oxides on the surface of Fe-14Cr-2W-0.3Ti-$0.3Y_2O_3$ alloy. In contrast, the SPS process, with a relatively low processing temperature, cannot provide the suitable condition for the formation of a uniform protective layer. Higher corrosion rate of SPS sample is the outcome of lacking a protective layer on the surface.

With the aim of comparing the formed phases after the non-equilibrium process of surface treatment with the equilibrium phases, the property phase diagram and stable phases at 500 °C of Fe-14Cr steel with 0.3wt% Y_2O_3 were calculated using ThermoCalc software (TCNI8 thermodynamic database) based on CALculation of PHAse Diagrams (CALPHAD) methods and can be seen in Figure 8-5 and Table 8-6 According to these results, under an equilibrium condition, the thermodynamically stable phases are mainly the elemental BCC structure of Fe-Cr, and yttrium

oxide within the whole range of temperature which is very similar to the XRD results of 0-SPS sample and a small amount of Fe-W rich lave phase is formed at lower temperatures. However, unlike the almost equilibrium composition of samples after SPS process, the non-equilibrium nature of laser surface treatment leads to the formation of protective oxides on the surface.

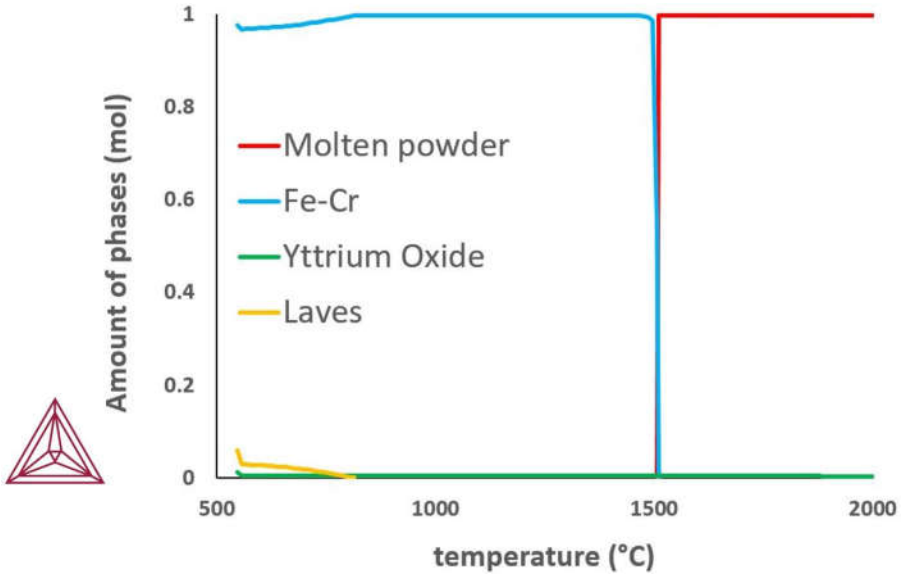

Figure 8-5. Property phase diagram of Fe-14Cr and the stable phases under equilibrium solidification from 2000 °C to 500°C based on ThermoCalc software.

Table 8-6. Stable phases and their chemical composition at 500 °C based on ThermoCalc software

		Mole Fraction (%)					
Phase	(%)	Fe	Cr	W	Ti	Y	O
BCC (Fe-Cr)	96.46	84.47	15.31	0.06	0.16	0	0
Y_2O_3	0.37	0	0	0	0	40	60
Laves	3.17	54	13	27	6	0	0

The results of microhardness tests on the selected samples along with the error bar (one-standard-deviation measure of the data scatter) are presented in Figure 8-6. As can be seen, the hardness of the SPS sample (without any surface laser processing) is the minimum one. After one pass of surface laser treatment, the hardness value dramatically increases due to the formation of

the mentioned oxide phases on the surface layer along with the microstructural changes of the substrate. To quantify laser surface treatment, two parameters are commonly considered, which are 1. Laser interaction time (laser spot size divided by the scanning speed), and 2. Beam density (laser power divided by the spot size). Laser interaction time is 0.322 ms and 0.290 ms for Y02 and Y06 respectively, and the beam density is 4.73×10^4 W/mm^2 and 6.62×10^4 W/mm^2 for Y02 and Y06 respectively. It is well known that by increasing these laser parameters, the average surface hardness would increase (Moradi and KaramiMoghadam 2019). In Y02 and Y06 cases, the combination of laser interaction time and beam density values made the almost equal surface hardness results understandable. The microhardness values for YY02 and YY06 samples are slightly higher than the values for the Y02 and Y06 samples, indicating a slightly thickened coating layer, in agreement with Figure 6 results. More detailed assessment on hardness results will be reflected in future publications.

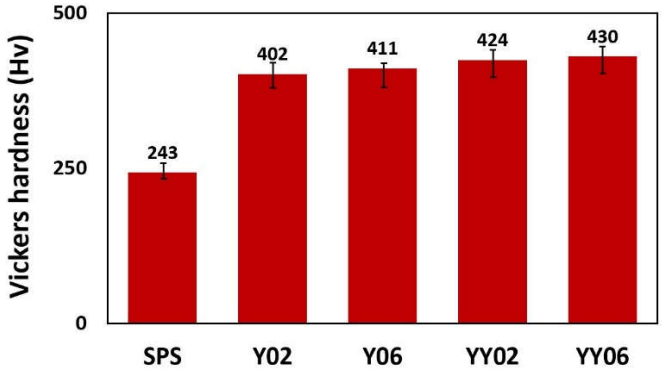

Figure 8-6. Micro-hardness measurements for the 3-SPS sample (without surface scanning), Y02 and Y06 with one round of surface laser scanning and YY02 and YY06 with two passes of laser surface treatment.

8.4. Conclusions

The optimum laser processing parameters were obtained in a two-stage searching process for improved corrosion performance of Fe-14Cr ferritic alloy. Laser parameters including laser

power, scanning speed, and hatching space were manipulated to produce a uniform protective layer on the alloy surface.

(1) The two-stage searching strategy, where the laser energy density was optimized first, followed by the optimization of the laser power/speed combinations, was an effective method to optimize laser processing parameters.

(2) Improved corrosion performance and the uniformity of elemental map distribution lead to the identification of two sets of optimized laser processing parameters. The best sample was scanned using a laser power of 175 W, a scanning speed of 200 mm, and a hatching space of 0.025 mm. The corrosion resistance of the laser processed sample was 5 times higher in a simulated marine condition than the bare sample due to the formation of the protective coatings on the surface.

(3) A second pass of laser scanning with 90 degrees of angle to the first layer of laser scan decreased the corrosion rate by almost 90% compared to the bare sample.

(4) The formation of Cr_2O_3 on the surface was identified with Raman Spectroscopy as well as XRD and can be recognized as the main reason for the improved corrosion performance of laser-scanned samples.

Chapter 9. Inconel 939 Alloy Modification and the Effect of Chemical Composition on Phase Stability

9.1. Phase diagram

Inconel 939 is a γ′-hardening superalloy with good strength at elevated temperatures. Structure is characterized by γ solid-solution matrix and the γ′ precipitates that are critical for the mechanical properties. High volume fraction of γ′ precipitates can be achieved through heat treatments and at the same time, it is important to avoid certain embrittling phases such as Sigma (Bowman 1988, Field, Pollockf et al. 1992). Figure 9-1 shows the equilibrium phase diagram of this alloy. As can be seen, by decreasing the temperature from the melting point, γ phase is formed at the temperature around 1300°C, then by further decrease of the temperature, at 1100°C γ′ starts to form as the second dominant phase. By reaching to 900°C, unwanted Sigma phase appears. For this reason, the selected temperature for all of the CALPHAD calculations in this study were 900°C. Table 9-1 shows the base composition of Inconel 939 that was utilized in this research.

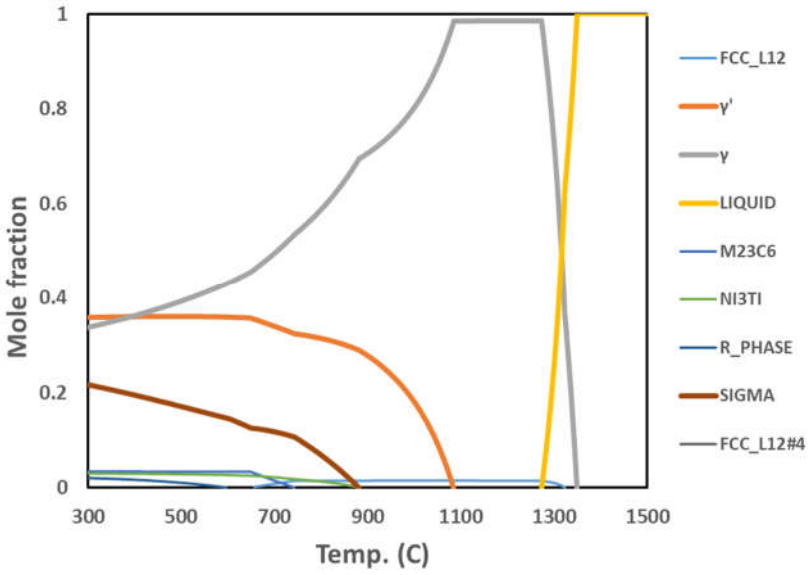

Figure 9-1. Equilibrium phase diagram of Inconel 939.

Table 9-1. Base composition in wt%, of Inconel 939 (Sjöberg, Imamovic et al. 2004)

Element	C	Co	Cr	Mo	W	Ta	Nb	Al	Ti	Ni
Mol%	0.71	18.22	24.35	0.006	0.62	0.45	0.64	4.19	4.38	Bal.

9.2. Composition effects on the stability of ternary γ′ phase

For the ternary cases, the mixture of excessive third elements into the base Ni_3Al can result in the decomposition of the γ′ phase. The stability of the γ′ phase due to the introduction of solutes is first investigated using Thermo-Calc software with the TCNI8 database (Andersson, Helander et al. 2002). Figure 9-2 shows the mole fraction of γ′ phase as a function of composition, which is given by the mole fraction of Al and the solute element. These solutes are all of the substitutional type (Sluiter and Kawazoe 1995). It can be observed from Figure 9-2 that the solutes prefer to form substitutes on certain atomic sites over others. As a guide to the eye, the red dashed lines correspond to the compositions in which the solute atoms only replace the Al atoms. Compositions above the diagonal lines correspond to substitutions of both Al and Ni by the solutes. The horizontal line of 25% of Al correspond to the substitution of Ni atoms. Compositions below the diagonal lines correspond to Al% + Solute% below 25% and suggest replacement of Al sites by Ni atoms. In the case of Ti (Figure 9-2-a), the coincidence (or near-coincidence) between the field of 100% γ′ and the dashed line suggests that the solute atoms prefer to replace aluminum atoms, which is in agreement with the literature (Sluiter and Kawazoe 1995, Gorbatov, Lomaev et al. 2016). In the cases of Cr and Mo, similar preferences can be observed (Figure 9-2‑b and d). However, in the literature, the agreement on such preferences has not been well established (Machlin and Shao 1977, Ochial, Oya et al. 1984, Wolverton and De Fontaine 1994, Sluiter and Kawazoe 1995). In the case of Co, Figure 9-2‑c suggests that the solute atoms simultaneously replace Al and Ni at an approximate ratio of 1:7 (green dashed line), giving strong preference to

Ni sites. This is in qualitative agreement with the literature, although the latter suggests an exclusive preference of Co replacing Ni in γ′ phase (Sluiter and Kawazoe 1995).

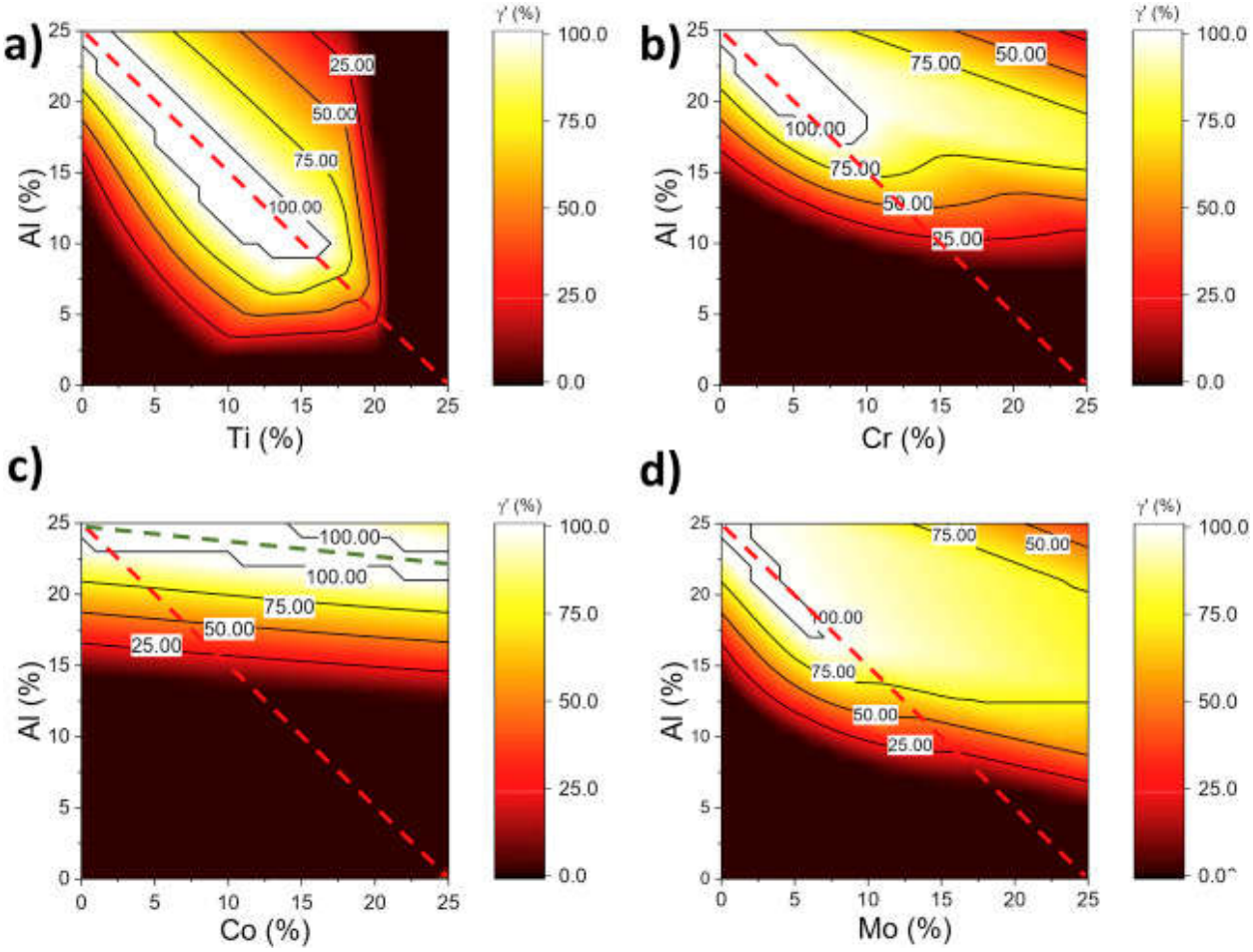

Figure 9-2. Phase fractions of γ′ as functions of compositional adjustment in a ternary alloy Ni-Al-M. (a) M = Ti (b) M = Cr (c) M = Co (d) M = Mo. Elemental fractions are given in mole fractions.

9.3. Elemental boundary condition for Inconel 939

In order to calculate the Anti-Phase Boundary Energy in nickel superalloy by Cluster Expansion method and Monte Carlo simulations, we need to know the possible range of each alloying element in which no unwanted phases has been formed and there are γ and γ′ phases only in the structure the same as original Inconel 939. There were two different approaches to reach to this goal: a) changing one element at the expense of just nickel (labeled as “Sacrificial Nickel”);

and b) keep the ratio of all other elements constant (same as base Inconel 939) and just change one alloying element percentage (labeled as "Constant Ratio"). The criteria for stopping the calculations was the formation of more than 5 wt% of any unwanted phase (rather than γ and γ′) in the system. The following phased were detected during calculations:

- γ: FCC contains solid solution elements.
- γ′: Ni_3(Al, Ti) with a cubic crystal structure that is an ordered variation of face centered cubic structure. Increase in this phase volume fraction at the operating temperature improves the long-term strength of the alloy.
- Sigma: Cr rich intermetallic phase, formed by two transition elements. Hard and brittle behavior results in loss of mechanical resistance at elevated temperatures. Sigma is usually tetragonal. $Co_{13}Cr_{17}$ is an example composition of this phase.
- γ″: Ni_3Nb or Ni_3V with a cubic crystal structure that is a variation of body-centered tetragonal DO22 structure.
- $M_{23}C_6$: Cr-rich, toughness decreased sharply due to the carbides precipitation at grain boundaries. Provides resistance to grain boundary sliding but also a risk of brittleness.
- BCC/B2: High Entropy phase consists of Co, Ni, Al, Cr, Ti.
- MU (ε): Rhombohedral, $(Ni,Co)_7(Mo,W)_6$. Usually found in superalloys containing relatively large amounts of the heavy elements such as molybdenum and tungsten. Coarse, irregular Widmanstatten platelets.

Left and right columns of Table 9-2 show the possible ranges of each element with "Sacrificial Nickel" and "Constant Ratio" approaches respectively. The red bolded values are the reasons for stopping the calculations due to the formation of more than 5 Mol% of an unwanted phase.

Table 9-2. The possible range of each alloying element by changing its mole percentage, (left column) at the expense of nickel content ("Sacrificial Nickel" approach), (right column) keeping the ration of all other elements constant ("Constant Ratio" approach), and all of the formed phases in that range. Red bolded values indicate the reasons for stopping the calculations

Ti	Sacrificial Nickel			
	Start	End	Max	At Ti%
Ti (Mol%)	**1.80**	**5.26**	5.26	5.26
Gamma	87.96	60.49	87.96	1.80
Gamma P	**10.61**	32.82	32.82	5.26
L12	1.43	1.46	1.46	5.26
Sigma	0.00	**5.05**	5.26	5.26
Ni3Ti	0.00	0.18	0.18	5.26

Ti	Constant Ratio			
	Start	End	Max	At Ti%
Ti (Mol%)	**1.65**	**5.50**	5.50	5.50
Gamma	88.28	59.55	88.27	1.65
Gamma P	**10.24**	33.53	33.53	5.50
L12	1.48	1.44	1.48	1.65
Sigma	0.00	**5.03**	5.03	5.50
Ni3Ti	0.00	0.0045	0.0045	5.50

Co	Sacrificial Nickel			
	Start	End	Max	At Co%
Co (Mol%)	**0.00**	**44.88**	44.88	44.88
Gamma	65.03	80.29	80.29	44.88
Gamma P	31.62	15.54	31.97	5.00
L12	0.00	1.50	1.50	44.88
Sigma	0.00	0.00	2.71	43.00
BCC	0.00	**6.94**	6.94	44.89
MC	3.34	0.00	3.36	5.00

Co	Constant Ratio			
	Start	End	Max	At Co%
Co (Mol%)	**14.20**	**36.00**	36.00	36.00
Gamma	62.03	87.96	87.96	36.00
Gamma P	31.39	**10.88**	31.39	14.20
L12	1.51	1.15	1.51	14.20
Sigma	**5.06**	0.00	5.06	14.20

Al	Sacrificial Nickel			
	Start	End	Max	At Al%
Al (Mol%)	**2.48**	**5.25**	5.25	5.25
Gamma	78.83	60.47	78.83	2.48
Gamma P	14.68	33.01	33.01	5.25
L12	1.45	1.46	1.46	5.25
Sigma	0.00	**5.06**	5.06	5.25
Ni3Ti	**5.04**	0.00	5.04	2.48

Al	Constant Ratio			
	Start	End	Max	At Al%
Al (Mol%)	**2.56**	**5.60**	5.60	5.60
Gamma	77.79	59.40	77.79	2.56
Gamma P	15.67	34.16	34.16	5.60
L12	1.48	1.43	1.48	2.56
Sigma	0.00	**5.00**	5.00	5.60
Ni3Ti	**5.06**	0.00	5.06	2.56

Cr	Sacrificial Nickel			
	Start	End	Max	At Cr%
Cr (Mol%)	**5.90**	**25.94**	25.94	25.94
Gamma	88.51	64.83	88.51	5.90
Gamma P	**10.08**	28.68	28.68	25.94
L12	1.41	1.46	1.46	25.94
Sigma	0.00	**5.03**	5.03	25.94

Cr	Constant Ratio			
	Start	End	Max	At Cr%
Cr(Mol%)	**0.00**	**26.47**	26.47	26.47
Gamma	76.20	65.85	76.20	0.00
Gamma P	21.91	27.70	28.61	17.00
L12	1.89	1.41	1.89	0.00
Sigma	0.00	**5.04**	5.04	26.47

Mo	Sacrificial Nickel			
	Start	End	Max	At Mo%
Mo (Mol%)	**0.006**	**2.32**	2.32	2.32
Gamma	70.68	60.93	70.73	0.170
Gamma P	27.86	28.33	28.33	2.32
L12	1.46	1.46	1.46	all
Sigma	0.00	**5.00**	5.00	2.32
MU	0.00	4.28	4.28	2.32

Mo	Constant Ratio			
	Start	End	Max	At Mo%
Mo(Mol%)	**0.006**	**2.90**	2.90	2.90
Gamma	70.68	63.15	70.82	0.170
Gamma P	27.86	26.81	27.86	0.006
L12	1.46	1.41	1.46	0.006
Sigma	0.00	3.57	3.57	2.90
MU	0.00	5.06	**5.06**	2.90

9.4. Effect of composition

In order to evaluate the effect of compositional change on the mechanical behavior of alloy 939, three different compositions were selected. These compositions are in a way that all of them contain the same amount of γ′ phase, but different APB energy based on the obtained formula in the literature (Dodaran, Ettefagh et al. 2020). Based on the proposed APB energy formula, increase in the amount of Ti will cause an increase in APB energy. For Cr, Co and Al, this impact is vice versa. Table 9-3 shows the chemical compositions of the three suggested samples along with their calculated APB energy and γ′ amount.

Table 9-3. Chemical composition in wt%, of Inconel 939, and three other samples with the same amount of γ′ phase

Sample	C	Co	Cr	Mo	W	Ta	Nb	Al	Ti	Ni	γ′ (%)	γ_{APB} (mj/m2)
Sample 1	0.15	22.08	23.37	0.01	2.04	1.46	1.06	3.16	2.34	Bal.	27.86	207.21
Sample 2	0.15	17.65	21.04	0.01	2.01	1.44	1.05	1.70	4.76	Bal.	27.86	322.68
Sample 3	0.15	20.47	22.90	0.01	2.03	1.45	1.06	2.55	3.02	Bal.	27.86	261.34
Inconel 939	0.15	19.00	22.40	0.01	2.02	1.44	1.05	2.00	3.71	Bal.	27.86	298.99

Mini Arc Melter MAM-1 (Edmund Bühler GmbH Lab Tec) was used for the preparation of samples, which was equipped with a water-cooled copper crucible plate and a nonconsumable tungsten electrode. Prior to the arc melting process, 10 g raw powders were measured. After putting the powders in the crucible, the chamber was depressurized and then refilled using pure Ar (ultra-high purity 5.0 grade, Airgas) for five cycles to minimize the oxygen content, with the final Ar pressure in the chamber set to be 30 kPa. The powders were first melted and cast to a button-shaped sample, then the obtained sample was flipped and re-melted for three more times to assure homogeneity.

Before heat treatment process, the phases of the samples were measured using XRD. The results are presented in Figure 9-3. Based on these results, it is obvious that even before heat

treatment, all of the samples contain just γ and γ′ which may be due to the fast cooling pace during the arc melting process. Despite this finding, a two-step heat treatment is inevitable to grow the γ′ grains in the structure (Mišković, Jovanović et al. 1992). The first step is a solution treatment at 1150°C for 4h followed by fast air cooling. Aging process is the second step of heat treatment which is keeping the sample at 850°C for 6h and then cool it down to the room temperature in the air. This part of project is still on going.

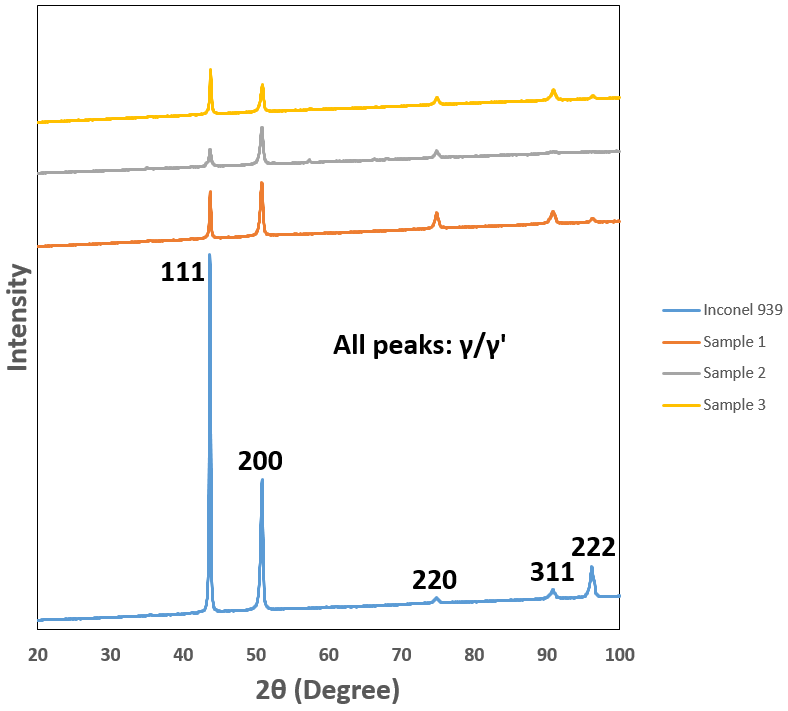

Figure 9-3. X-ray diffraction pattern of the prepared samples along with Inconel 939.

Chapter 10. Hot Corrosion Characteristics of Inconel 939 Superalloy in Molten Salt

10.1. Corrosion kinetics

Figure 10-1.a shows weight gain curves as a function of exposure time of Inconel 939 samples. This figure shows a weight gain up to around 20h and then the rate of weight gain dramatically decrease up to 100 h at both temperatures. Visual inspection revealed spallation of the surface layer only for the sample which was exposed to corrosive environment for 100h at 800°C. To calculate the parabolic rate constant (Kp), the second power of weight gain values of the first 20 h were plotted as a function of time, so kp would be the slope of the curve fitting in Figure 10-1.b which can be seen on this figure. From Figure 10-1, it is obvious that the hot corrosion behavior of this alloy is close to parabolic rates which indicates that a thermal diffusion process determines the corrosion rate (Yuan and Wang 2010) and this fact can justify the higher corrosion rate of samples at 800°C than 700°C. It is known that the lower values of Kp results in a higher oxidation resistance and vice versa. For a better judgment, calculated Kp of this alloy have been collected in Table 10-1 along with the same parameter of Inconel 617 and Inconel 738 from other sources. According to these results, the values of Kp for Inconel 939 at 700°C were found to be in between of the values for other two alloys which implies that the corrosion resistance of Inconel 939 is better than Inconel 617, but worse than Inconel 718 at 700°C. On the other hand, at 800°C, Inconel 939 is the worst among others from hot corrosion resistance point of view.

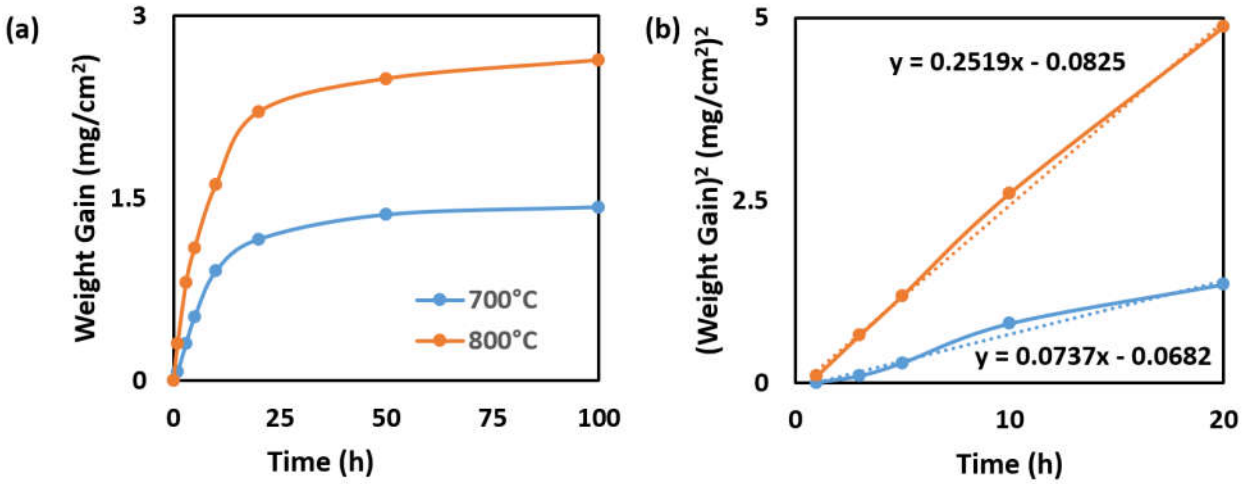

Figure 10-1. (a) Weight gain (mg/cm^2) versus time curve for Inconel 939 subjected to hot corrosion for 100 h at 700°C and 800°C. (b) (Weight gain)^2 versus time to calculate the parabolic rate constant (kp) on the basis of the first 20h exposure time.

Table 10-1. Values of parabolic rate constant (Kp)(10^{-10}g^{2}cm^{-4}s^{-1})

Alloy	700C	800C
Inconel 939	0.205	0.700
Inconel 617 (El-Awadi, Abdel-Samad et al. 2016)	0.214	0.556
Inconel 738 (El-Awadi, Abdel-Samad et al. 2016)	0.091	0.110

10.2. XRD analysis

Corrosion products on the top surface of the hot corroded Inconel 939 samples were identified using XRD after 100h of exposure to the molten salts mixture at 700°C and 800°C. The results along with the XRD pattern of the bare sample before corrosion tests are presented in Figure 10-2. All samples show the presence of FCC peaks of γ/γ' phase. For the temperature test of 700°C, other peaks are attributed to Cr_2O_3, TiO_2 and some small peaks of $(Cr,Ti)_2O_3$. By increasing the temperature to 800°C, most of $(Cr,Ti)_2O_3$ phase has disappeared and the dominant corrosion products are Cr_2O_3 and TiO_2. During this high-temperature process, Cr and Ti diffuse outward to interact with oxygen and form oxide phases. In addition, it seems that a slight amount of sulfide (CrS) has been formed at 800°C. Weight gain curves (Figure 10-1) proves that at least some part of the formed oxides are protective layer which has hindered the scale formation by decreasing the

weight gain of the samples. The formation of chromium oxide has been noticed in other types of nickel superalloy, but to the best of our knowledge, there is no evidence of titanium oxide formation for other Inconel superalloys (Zhao, Xie et al. 2005, Cho, Hur et al. 2009, Knutsson, Lai et al. 2013, El-Awadi, Abdel-Samad et al. 2016, Mannava, Rao et al. 2016).

As can be seen, the main peaks of the bare samples are associated with γ/γ' phase of Inconel 939 which is an FCC structure. The same peaks are available in the corroded samples results with a lower intensity and slight shift to the higher angles. Stronger peaks of bare sample and the minimum intensity of the sample corroded at 800°C point to the formation of the surface layer after the hot corrosion process and this layer is thicker for the sample corroded at higher temperature. Furthermore, the peak shifts of γ/γ' phase can be an indication for the depletion of FCC structure from elements with higher atomic radius such as chromium and titanium due to their outward diffusion to the surface. This assessment will be evaluated more detailed in the next sections.

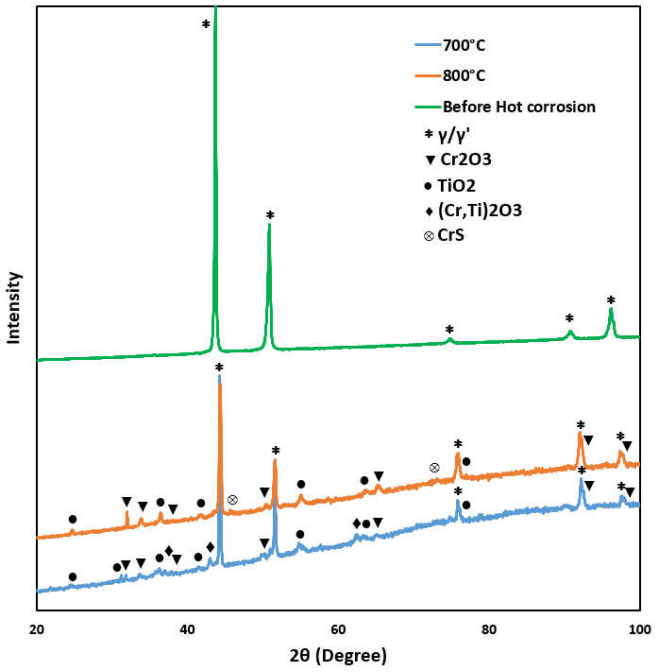

Figure 10-2. XRD pattern of Inconel 939 before and after hot corrosion for 100h at 700°C and 800°C.

10.3. Top surface and cross-sectional characterization

The morphology of the top surface and cross section of the samples hot corroded at 700°C and 800C after 100h and corresponding elemental distribution were evaluated by SEM and EDS and results are demonstrated in Figure 10-3 to Figure 10-6, and Table 10-3, respectively. Different features can be recognized for the samples corroded at 700°C and 800°C. For the sample corroded at 700°C, it can be seen in the microscopic image that a flat and compact layer has formed on the surface which contains mainly Cr and O according to the corresponding elemental distribution (Figure 10-3). Based on XRD results and point A in Table 10-2, it can be stated that this layer is the formed Cr_2O_3 on the top surface. A small trace of other elements such as Ni, Co and Ti can be detected which are due to the electron penetration depth during electron microscopy. Higher values of Ti compared to other elements of base alloy suggests that Ti should be closer to the surface underneath the chromium oxide layer or a mixed oxide of Cr and Ti such as $(Cr,Ti)_2O_3$ has formed.

Some peaks associated with this type of oxide can be seen in XRD results (Figure 10-2). Moreover, On the bottom left of the SEM image in Figure 10-3, some cracks are visible which can be as a result of the surface layer thickening of the chromium oxide layer and its transformation from protective to non-protective oxide layer despite that there was no sign of spallation after the experiment. Higher Na concentration at point B of Figure 10-3 and Table 10-2 shows that the salt may be trapped in the porosities of the non-protective chromium oxide layer. The composition of point C in Figure 10-3 was measured and results in Table 10-2 show that this small area is the residual salt on the surface which has not been removed after the dissolution step. The distribution of Na, S, and Cl was measured to see the formation of chlorine or sulfide compounds or probable residual salt on other parts of the surface. However, the results show the presence of these elements is practically ignorable on the surface. In other words, an oxide layer consists of mostly chromium and lower amount of titanium is the main formed layer on the top surface.

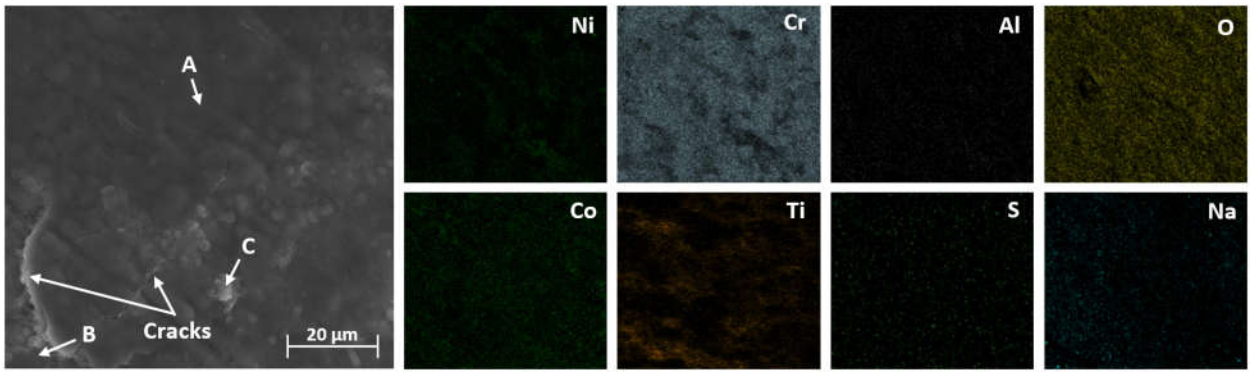

Figure 10-3. Microscopic image of the surface and the elemental distribution of the sample hot corroded at 700°C for 100h.

Table 10-2. EDS analysis of the sample corroded at 700°C for 100h

Point in Figure 10-3	Mass fraction (%)				
	Cr	Ti	O	Na	Others
A	42.83	3.39	50.25	-	3.53
B	38.21	5.08	49.76	1.39	5.56
C	19.81	1.97	46.19	14.62	17.41

Figure 10-4 shows the cross-sectional microstructure and elemental distribution of the sample corroded at 700°C for 100h. It is obvious that the cross section consists of two distinguished layers, top oxide layer and the substrate. Elemental distribution confirms that the top oxide layer has been formed mainly by Cr and a relatively small amount of Ti and the presence of other elements is not evident in this layer. In addition, although the concentration of Cr is a bit higher in the oxide layer compared to the substrate, this element still exists in the matrix and there is no sign of Cr depletion zone. The thin formed oxide layer (~10μm) approves the insufficient temperature for the migration of Cr to the surface or inward diffusion of oxygen and forming a thicker oxide layer along with leaving a Cr depletion zone behind. The same story is true for Ti while its concentration is visually almost the same in the substrate and oxide layer based on the related image in Figure 10-4.

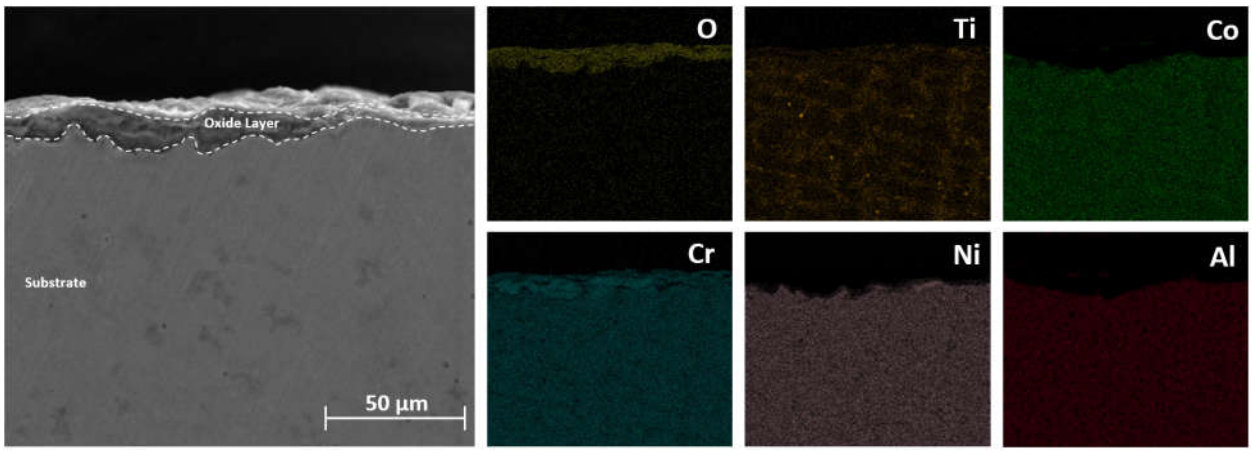

Figure 10-4. Microscopic image of the cross section of sample hot corroded at 700°C for 100h along with the elemental distribution.

For the samples corroded at 800°C, the microscopic image confirms the spallation after the corrosion test which is consistent with the visual inspection of samples after the hot corrosion test. This spallation is probably as a result of the formation of a thick corrosion scale on the surface. From Figure 10-5, it is observed that the surface of the sample consists of two distinctly different

regions, a rough uneven area (points A and B), and a uniform compact layer (area of the point C) which their compositions are presented in Table 10-3. Point A mainly consists of Cr and S which can represent the sulfidation on the surface. The absence of Na on this point eliminate the possibility of this area to be residual salt. For point B, Cr and O are the main elements, so it can be deduced that this area is chromium oxide. However, the morphology indicates that this layer is a porous non-protective oxide formed on the surface. Around point C, the occurrence of spallation is more evident. EDS results reveal a higher weight percentage of Ti and O along with the lower weight percentage of Cr suggesting the formation of titanium oxide underneath the not-detached protective chromium oxide layer which is now closer to the surface after the spallation of non-protective Cr_2O_3. This argument will be more elaborated in the cross-sectional analysis. No chlorine was detected neither in the sample corroded at 700°C nor in 800°C.

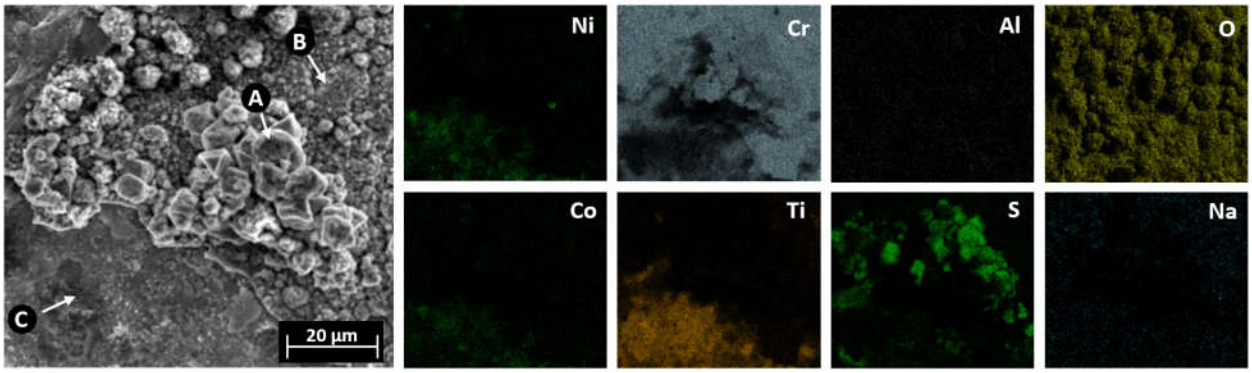

Figure 10-5. Microscopic image of the surface and the elemental distribution of the sample hot corroded at 800°C for 100h.

Table 10-3. EDS analysis of the sample corroded at 800°C for 100h

Point in Figure 10-5	Mass fraction (%)				
	Cr	Ti	O	S	Others
A	62.39	-	6.56	28.92	2.13
B	44.21	0.81	51.83	-	3.15
C	28.31	16.95	43.84	-	10.90

Figure 10-6 shows that the formed scale at 800°C is much thicker than the one formed at 700°C. This layer mainly formed by Cr and O and other elements appear to be absent in that. In addition, unlike the sample corroded at 700°C, internal oxidation after 100h of exposure took place which is clear in Figure 10-6. The inner oxide layer is thinner than the outer one and mainly consists of Ti and O. Besides, there is no trace of sulfur in the elemental map of the cross section which indicates that the sulfidation is limited to some porous parts of the surface (Figure 10-5) which is probably spalled with the non-protective oxide layer during the sample preparation for cross sectional analysis. Beneath the oxide layers in Figure 10-6, a relatively thick region labeled as Cr Depletion layer can be detected with apparent lower Cr and Ti content and accumulated Ni and Co, which confirms the outward diffusion of former two elements to the top surface to form oxide layers and their participation in corrosion reactions during hot corrosion. None of the salt elements were detected in the cross section which eliminate the possibility of the penetration of the melted salt to substrate. Based on these results it appears that Cr and Ti play the main role during hot corrosion.

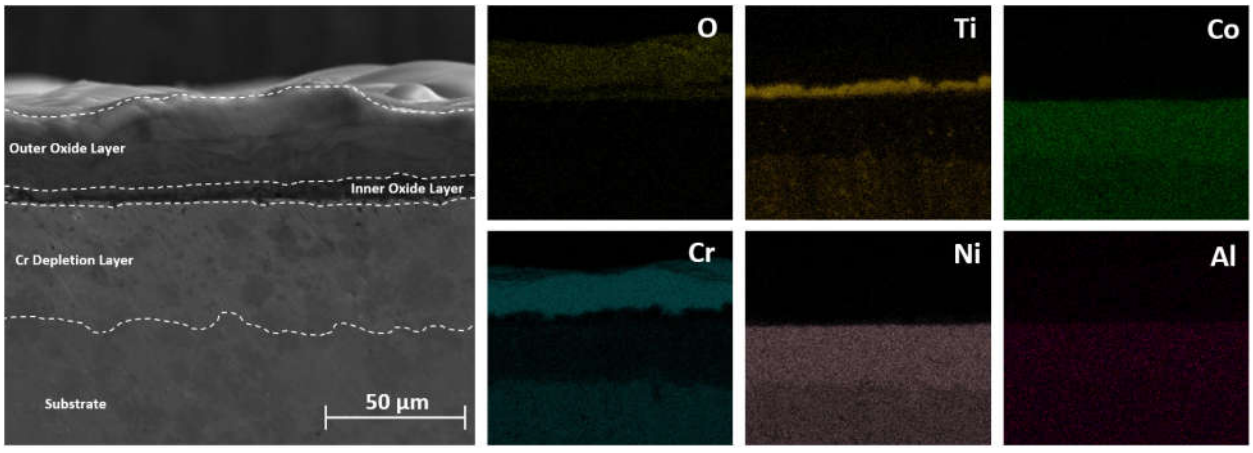

Figure 10-6. Microscopic image of the cross section of sample hot corroded at 800°C for 100h along with the elemental distribution.

This research is still on going and further discussion will be made based on the future test results on the samples. It is expected that with a set of microscopic images for the exposure times between 1 to 50h, a proper mechanism of hot corrosion can be proposed on this alloy for the first time.

10.4. Conclusion

For this part of the research, the hot corrosion behavior of Inconel 939 was evaluated at 700 and 800 for up to 100h. Results showed that corrosion is more severe at 800C due to the easier diffusion of the elements to the surface. The corrosion layer had a duplex nature for which the top layer was mainly chromium oxide and the inner one was titanium oxide. Some spallation was recognized for this sample which is believed to be non-protective chromium oxide. The oxide layer of the sample corroded at 700C was almost 5 times thinner than that of 800C. Moreover, the single layered oxide was detected to be chromium oxide with no Cr depletion region underneath.

Appendix. Reprint Permissions

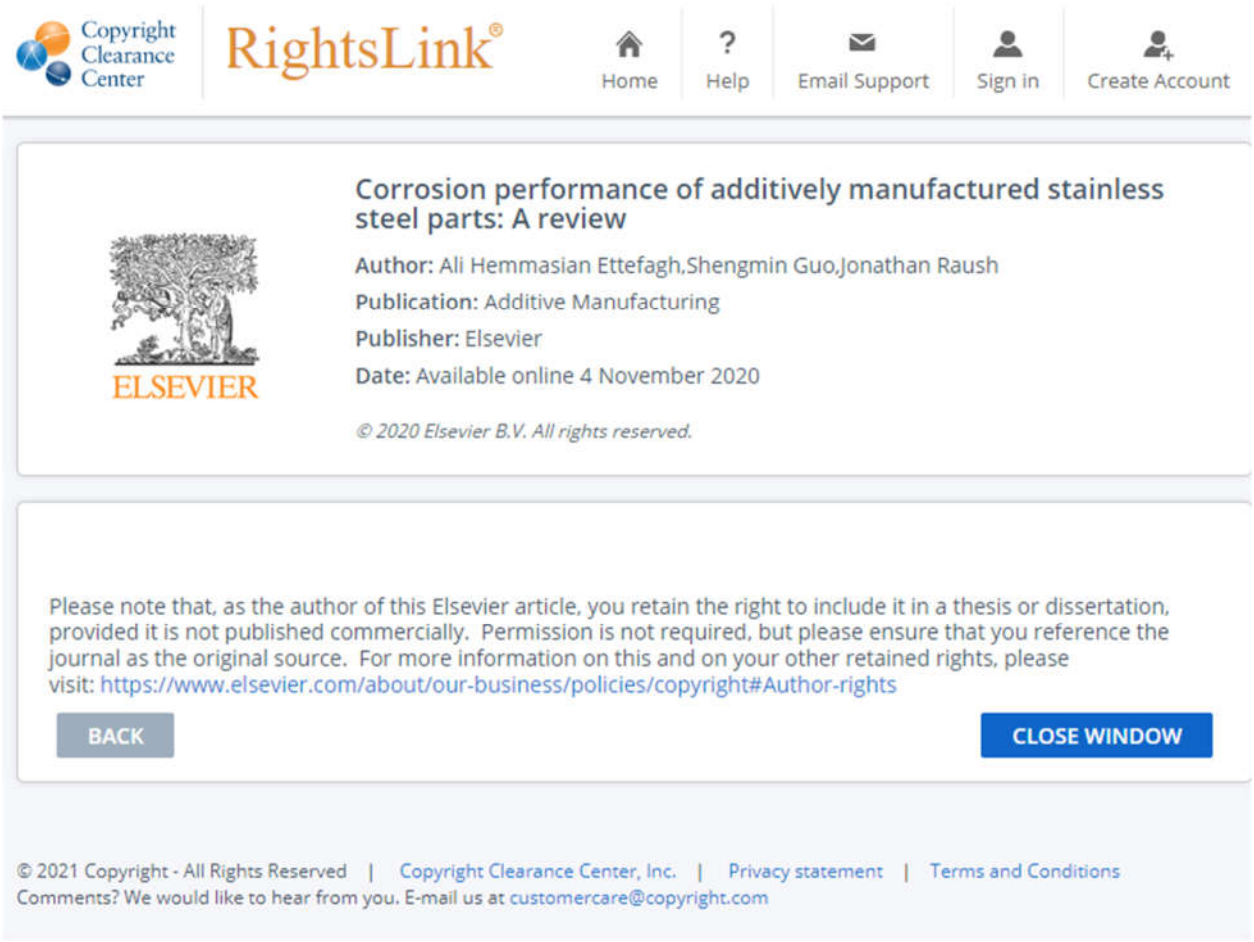

A.1. Reprint permission from the publisher for Chapter 2.

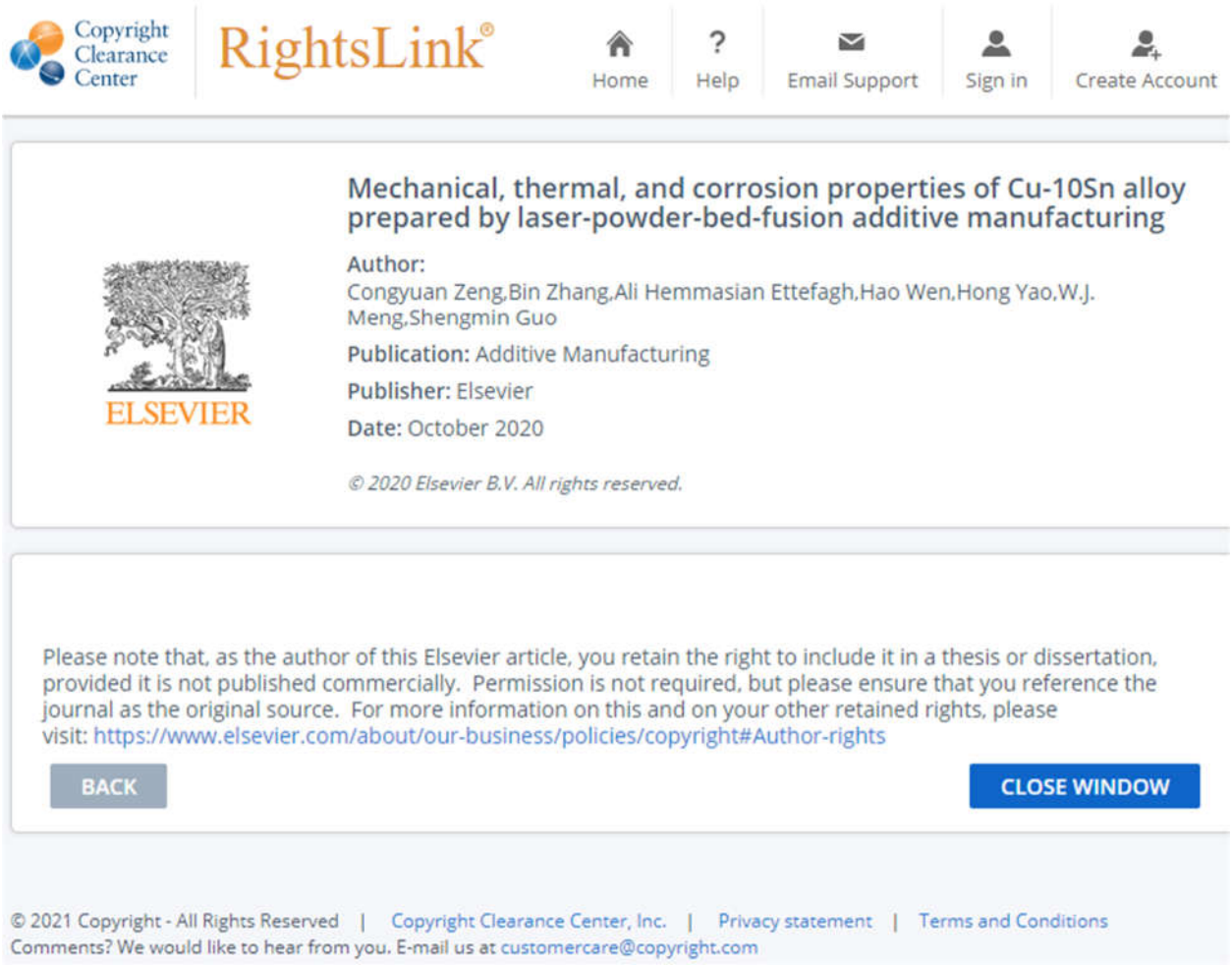

A.2. Reprint permission from the publisher for Chapter 5.

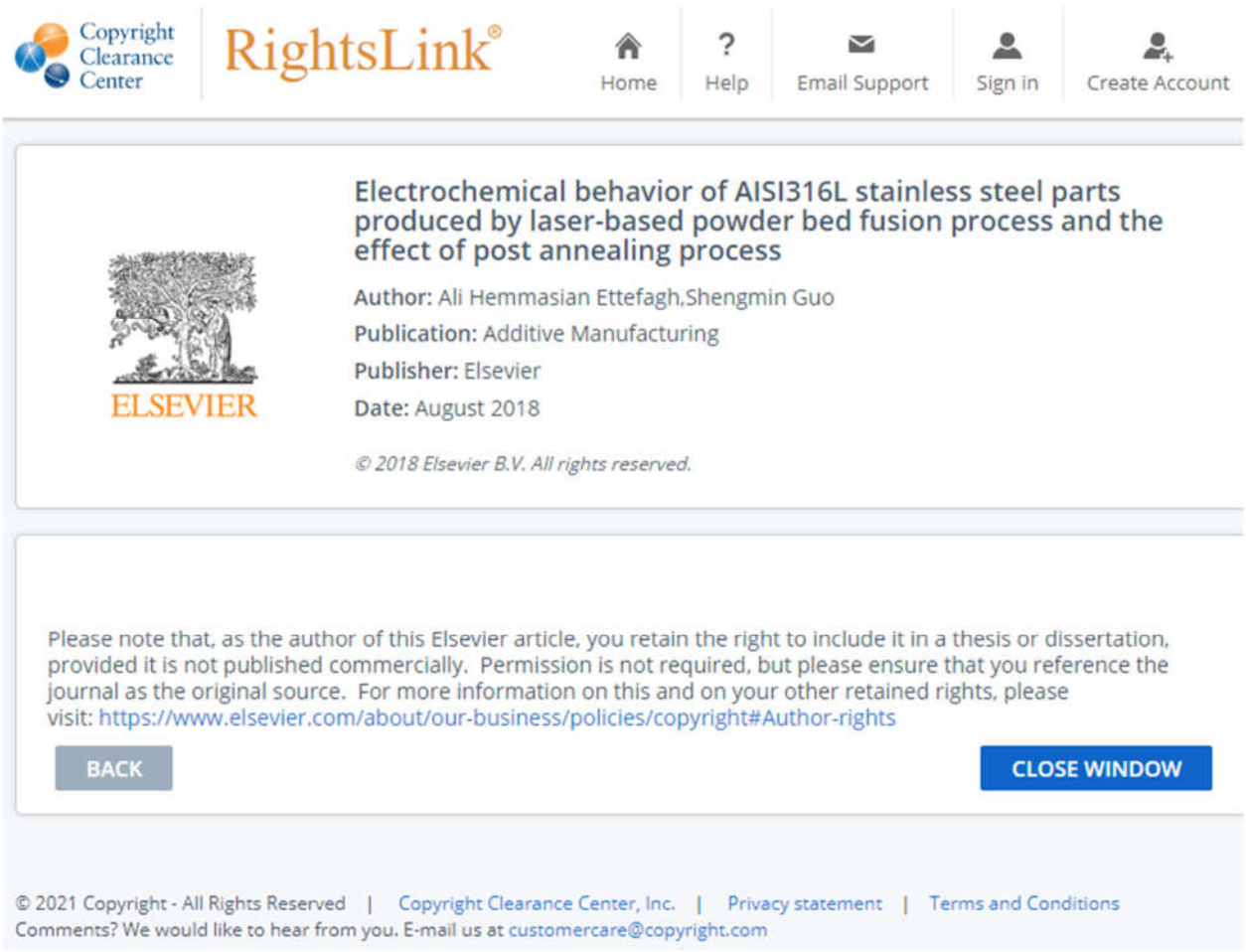

A.3. Reprint permission from the publisher for Chapter 6.

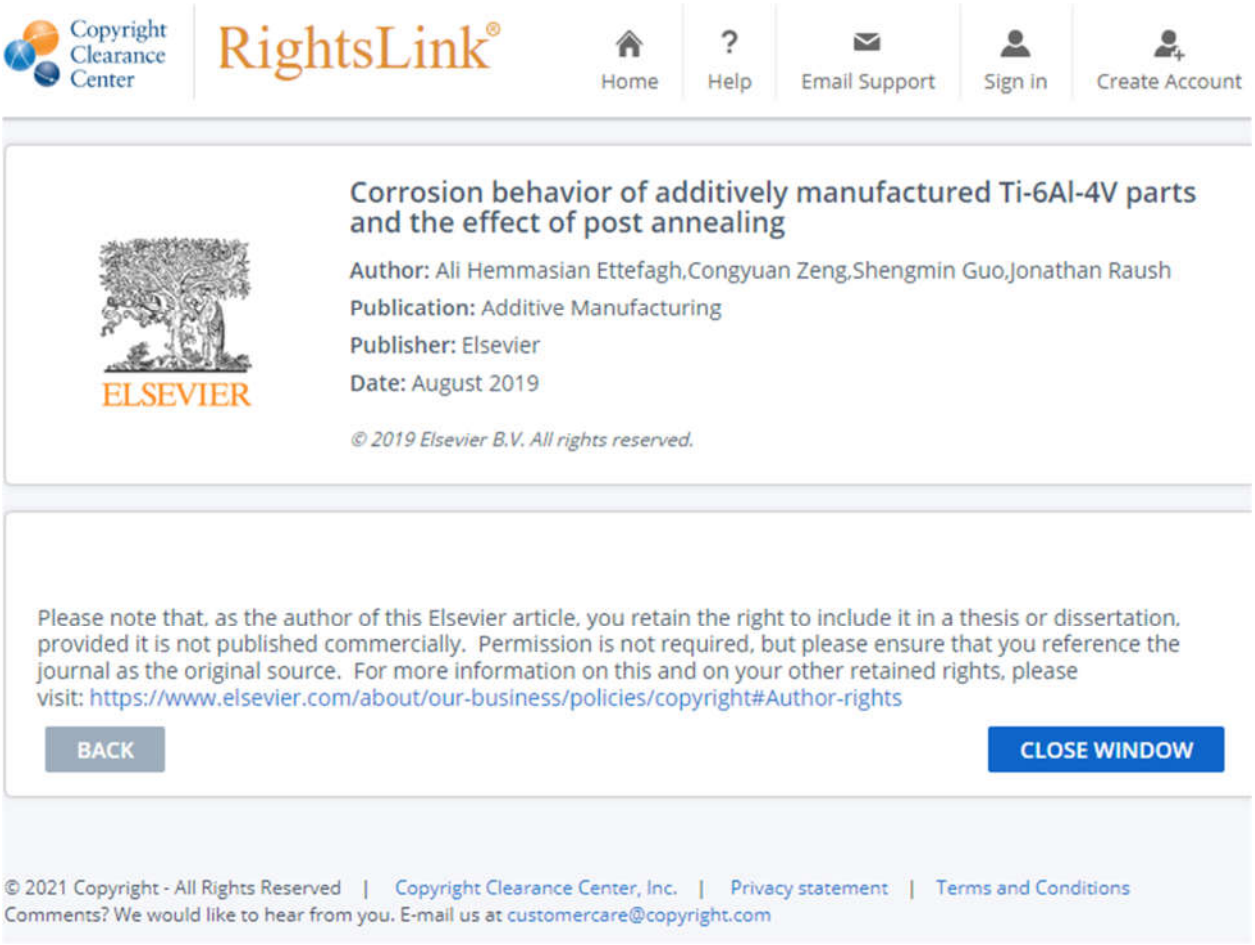

A.4. Reprint permission from the publisher for Chapter 7.

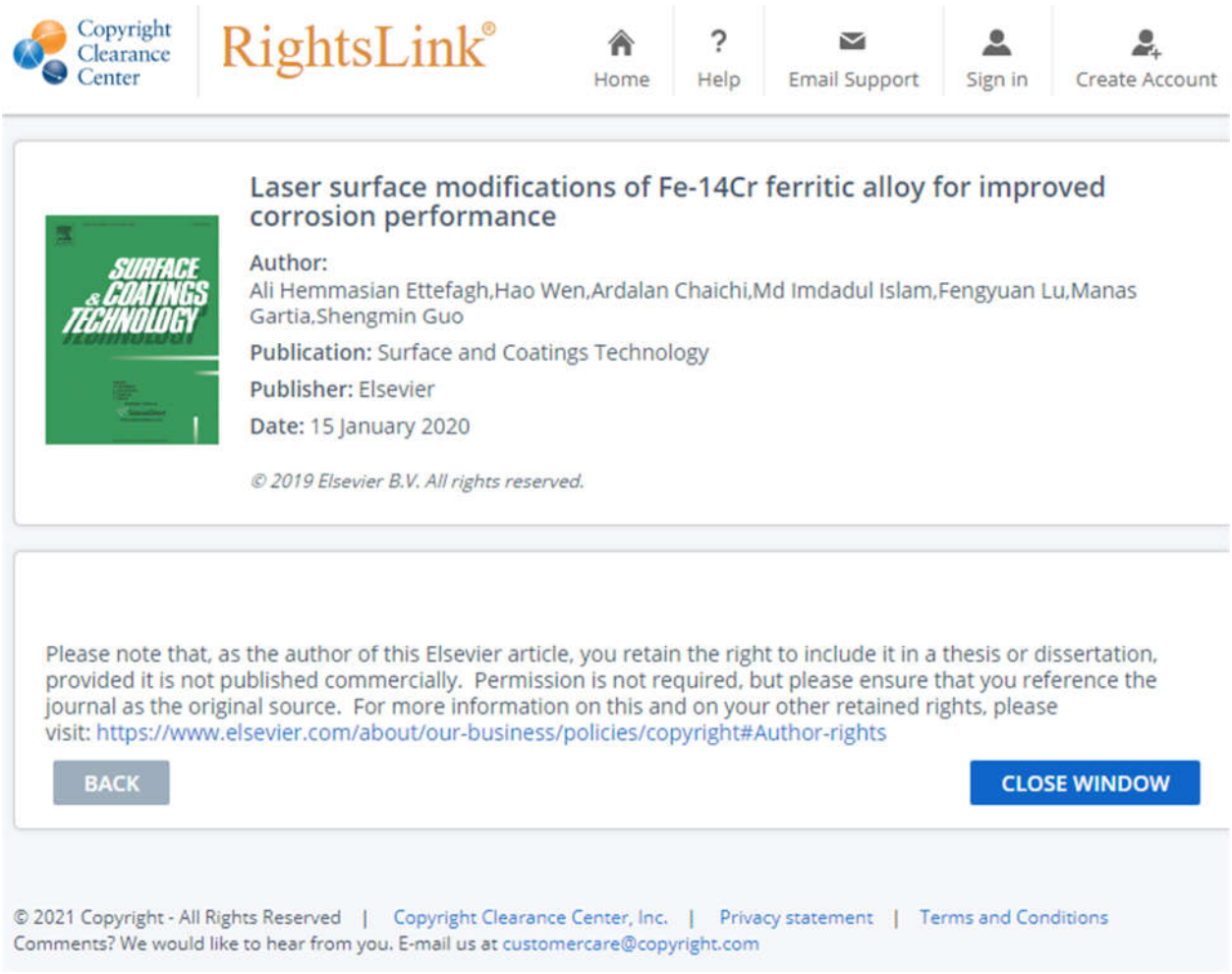

A.5. Reprint permission from the publisher for Chapter 8.

References

Abedi, H., et al. (2010). "Effect of high temperature post-oxidizing on tribological and corrosion behavior of plasma nitrided AISI 316 austenitic stainless steel." Vacuum 85(3): 443-447.

Aboulkhair, N. T., et al. (2016). "On the formation of AlSi10Mg single tracks and layers in selective laser melting: Microstructure and nano-mechanical properties." Journal of Materials Processing Technology 230: 88-98.

Adam Khan, M., et al. (2014). "Influence of plasma coatings on Inconel 617 for gas turbine applications." Surface engineering 30(9): 656-661.

Agyenim-Boateng, E., et al. (2017). "Influence of laser peening on the hydrogen embrittlement resistance of 316L stainless steel." Surface and Coatings Technology 328: 44-53.

Airey, G. (1983). Environmental degradation of materials in nuclear power systems-water reactors. Proc. Int. Symp.

Akinlabi, E. T., et al. (2016). Advanced Manufacturing Techniques Using Laser Material Processing, IGI Global.

Al-Amr, A. (2005). "Mechanical behavior and structure of passive films on austenitic stainless steels."

Alam, M. K., et al. (2020). "Mechanical behavior of additive manufactured AISI 420 martensitic stainless steel." Materials Science and Engineering: A 773: 138815.

Almuaili, F., et al. (2017). "Strain-induced reactivation of corrosion pits in austenitic stainless steel." Corrosion Science 125: 12-19.

Alsalla, H. H., et al. (2018). "Effect of build orientation on the surface quality, microstructure and mechanical properties of selective laser melting 316L stainless steel." Rapid prototyping journal.

Alves, H., et al. (2006). Alloys Suitable for Phosphoric Acid Applications. CORROSION 2006, NACE International.

Anderson, S. (2015). "Final Technical Report on Laser Direct Manufacturing (LDM) for Nuclear Power Components, DOE-NE0000542."

Andersson, J.-O., et al. (2002). "Thermo-Calc & DICTRA, computational tools for materials science." Calphad 26(2): 273-312.

Andresen, P. and C. Briant (1989). "Environmentally assisted cracking of types 304L/316L/316NG stainless steel in 288 C water." Corrosion 45(6): 448-463.

Andresen, P. and M. Morra (2008). "Stress corrosion cracking of stainless steels and nickel alloys in high-temperature water." Corrosion 64(1): 15-29.

Andresen, P. L. (2013). "Stress corrosion cracking of current structural materials in commercial nuclear power plants." Corrosion 69(10): 1024-1038.

Andresen, P. L. and M. M. Morra (2008). "IGSCC of non-sensitized stainless steels in high temperature water." Journal of Nuclear Materials 383(1-2): 97-111.

Angenete, J. and K. Stiller (2001). "A comparative study of two inward grown Pt modified Al diffusion coatings on a single crystal Ni base superalloy." Materials Science and Engineering: A 316(1-2): 182-194.

AOKI, Y. (2003). "Mechanical Properties and Castability of a 4th Generation Ni-base Single Crystal Superalloy TMS-138." Proceedings of IGTC2003, Tokyo.

Aqilah, D. N., et al. (2018). "Effects of process parameters on the surface roughness of stainless steel 316L parts produced by selective laser melting." Journal of Testing and Evaluation 46(4): 1673-1683.

Ardila-Rodríguez, L., et al. (2019). "Surface modification of aluminum alloys with carbon nanotubes by laser surface melting." Surface and Coatings Technology 377: 124930.

Arifvianto, B., et al. (2011). "Effect of surface mechanical attrition treatment (SMAT) on microhardness, surface roughness and wettability of AISI 316L." Materials Chemistry and Physics 125(3): 418-426.

Arivarasu, M., et al. (2017). "Investigations on metallurgical and mechanical properties of CO2 laser beam welded Alloy 825." Canadian Metallurgical Quarterly 56(2): 232-244.

Asala, G., et al. (2019). "Hot corrosion behaviour of wire-arc additive manufactured Ni-based superalloy ATI 718Plus®." Corrosion Science 158: 108086.

Ashouri, D., et al. (2020). "Mechanical behaviour of additive manufactured 316L f2ccz lattice structure under static and cyclic loading." International Journal of Fatigue 134: 105503.

Asl, S. M., et al. (2019). "Surface modification of 316L stainless steel by laser-treated HA-PLA nanocomposite films toward enhanced biocompatibility and corrosion-resistance in vitro." Surface and Coatings Technology 363: 236-243.

Asri, R., et al. (2017). "Corrosion and surface modification on biocompatible metals: A review." Materials Science and Engineering: C 77: 1261-1274.

Asteman, H., et al. (2002). "Oxidation of 310 steel in H2O/O2 mixtures at 600 C: the effect of water-vapour-enhanced chromium evaporation." Corrosion Science 44(11): 2635-2649.

Auger, M. A., et al. (2018). "Microstructural and mechanical characterisation of Fe-14Cr-0.22 Hf alloy fabricated by spark plasma sintering." Journal of Alloys and Compounds 762: 678-687.

Aung, N. N. and X. Liu (2013). "Effect of SO2 in flue gas on coal ash hot corrosion of Inconel 740 alloy–A high temperature electrochemical sensor study." Corrosion Science 76: 390-402.

Aung, N. N. and X. Liu (2014). "Effect of temperature on coal ash hot corrosion resistance of Inconel 740 superalloy." Corrosion Science 82: 227-238.

Baba, H., et al. (2002). "Role of nitrogen on the corrosion behavior of austenitic stainless steels." Corrosion Science 44(10): 2393-2407.

Babu, M. S., et al. (2019). "High-temperature oxidation and hot corrosion behavior of Er2Sn2O7+ Inconel 625 composite." Ceramics International.

Bacchewar, P., et al. (2007). "Statistical modelling and optimization of surface roughness in the selective laser sintering process." Proceedings of the Institution of Mechanical Engineers, Part B: Journal of Engineering Manufacture 221(1): 35-52.

Baer, D. (1980). Protective and non-protective oxide formation on 304 stainless steel, Battelle Pacific Northwest Labs., Richland, WA (USA).

Baker, M. and J. Castle (1993). "The initiation of pitting corrosion at MnS inclusions." Corrosion Science 34(4): 667-682.

Bakkar, A., et al. (2019). "Microstructure, wear, and corrosion characterization of high TiC content Inconel 625 matrix composites." Journal of Materials Research and Technology 8(1): 1102-1110.

Bakkar, A. and S. Ataya (2014). "Corrosion behaviour of stainless steel fibre-reinforced copper metal matrix composite with reference to electrochemical response of its constituents." Corrosion Science 85: 343-351.

Balusamy, T., et al. (2010). "Effect of surface nanocrystallization on the corrosion behaviour of AISI 409 stainless steel." Corrosion Science 52(11): 3826-3834.

Banerjee, D. and J. Williams (2013). "Perspectives on titanium science and technology." Acta Materialia 61(3): 844-879.

Bao, Z., et al. (2009). "Preparation and hot corrosion behaviour of an Al-gradient NiCoCrAlYSiB coating on a Ni-base superalloy." Corrosion Science 51(4): 860-867.

Bar-On, I., et al. (2002). "Technical cost analysis for PEM fuel cells." Journal of Power Sources 109(1): 71-75.

Barari, A., et al. (2017). "On the surface quality of additive manufactured parts." The International Journal of Advanced Manufacturing Technology 89(5-8): 1969-1974.

Barbooti, M. M., et al. (1988). "Thermochemical studies on hot ash corrosion of stainless steel 304 and inhibition by magnesium sulphate." Thermochimica acta 126: 43-49.

Barbucci, A., et al. (1998). "Corrosion behaviour of nanocrystalline Cu90Ni10 alloy in neutral solution containing chlorides." Corrosion Science 41(3): 463-475.

Barile, C., et al. (2019). "Analysis of corrosion on sintered stainless steel: Mechanical and physical aspects." Engineering failure analysis 95: 273-282.

Barile, C., et al. (2016). Overview of the effects of process parameters on the accuracy in residual stress measurements by using HD and ESPI. Residual Stress, Thermomechanics & Infrared Imaging, Hybrid Techniques and Inverse Problems, Volume 9, Springer: 113-118.

Barkia, B., et al. (2020). "On the origin of the high tensile strength and ductility of additively manufactured 316L stainless steel: Multiscale investigation." Journal of Materials Science & Technology 41: 209-218.

Barrett, C. A. (1988). "Effect of 0.1 at.% zirconium on the cyclic oxidation resistance ofβ-NiAl." Oxidation of Metals 30(5-6): 361-390.

Barriobero-Vila, P., et al. (2017). "Inducing stable α+ β microstructures during selective laser melting of Ti-6Al-4V using intensified intrinsic heat treatments." Materials 10(3): 268.

Bartlett, J. L. and X. Li (2019). "An overview of residual stresses in metal powder bed fusion." Additive Manufacturing 27: 131-149.

Becker, W. T., et al. (2002). "ASM handbook." Failure analysis and prevention 11: 1072.

Beltran, A. M., et al. (1975). Corrosion-resistant coating for superalloys, Google Patents.

Bevan, M. A., et al. (2017). Mechanical Properties and Behavior of Additive Manufactured Stainless Steel 316L. Characterization of Minerals, Metals, and Materials 2017, Springer: 577-583.

Bhat, A., et al. (2011). "Carbon nanotube reinforced Cu–10Sn alloy composites: mechanical and thermal properties." Materials Science and Engineering: A 528(22-23): 6727-6732.

Bhuyan, P., et al. (2019). "Evaluating the efficiency of grain boundary serrations in attenuating high-temperature hot corrosion degradation in Alloy 617." Corrosion Science 149: 164-177.

Biehler, J., et al. (2014). "Influence of the microstructure on the corrosion resistance of plasma-nitrided austenitic stainless steel 304L and 316L: Einfluss des Mikrogefüges auf die Korrosionsbeständigkeit von plasmanitriertem austenitischem Stahl 1.4307 und 1.4404." Materialwissenschaft und Werkstofftechnik 45(10): 930-946.

Bilgin, G. M., et al. (2017). "Optimization of the mechanical properties of Ti-6Al-4V alloy fabricated by selective laser melting using thermohydrogen processes." Materials Science and Engineering: A 700: 574-582.

Birello, F., et al. (2013). Modelling of deposit mechanisms around the stator of a gas turbine. Turbo Expo: Power for Land, Sea, and Air, American Society of Mechanical Engineers.

Birks, N., et al. (2006). Introduction to the high temperature oxidation of metals, Cambridge University Press.

Błachnio, J. (2011). "Analysis of causes of decohesion of a gas turbine blade made of EI 867-WD alloy." Aircraft Engineering and Aerospace Technology.

Blinn, B., et al. (2020). "Determination of the influence of a stress-relief heat treatment and additively manufactured surface on the fatigue behavior of selectively laser melted AISI 316L by using efficient short-time procedures." International Journal of Fatigue 131: 105301.

Boidot, M., et al. (2010). "Proto-TGO formation in TBC systems fabricated by spark plasma sintering." Surface and Coatings Technology 205(5): 1245-1249.

Boulesteix, C., et al. (2017). "Steam oxidation resistance of slurry aluminum and aluminum/silicon coatings on steel for ultrasupercritical steam turbines." Oxidation of Metals 87(3-4): 469-479.

Bowman, R. R. (1988). Effect of microstructure on the fatigue crack growth resistance of nickel-base super alloys, Georgia Institute of Technology.

Brnic, J., et al. (2011). "Martensitic stainless steel AISI 420—mechanical properties, creep and fracture toughness." Mechanics of time-dependent materials 15(4): 341-352.

Brooking, L., et al. (2018). "Interaction of hot corrosion fatigue and load dwell periods on a nickel-base single crystal superalloy." International Journal of Fatigue 117: 13-20.

Buchbinder, D., et al. (2014). "Investigation on reducing distortion by preheating during manufacture of aluminum components using selective laser melting." Journal of Laser Applications 26(1): 012004.

Bürgel, R., et al. (2004). "Development of a new alloy for directional solidification of large industrial gas turbine blades." Superalloys 25.

Burstein, G., et al. (2004). "Origins of pitting corrosion." Corrosion Engineering, Science and Technology 39(1): 25-30.

Buscail, H., et al. (2008). "Characterization of the oxides formed at 1000° C on the AISI 316L stainless steel—Role of molybdenum." Materials Chemistry and Physics 111(2-3): 491-496.

Calignano, F., et al. (2013). "Influence of process parameters on surface roughness of aluminum parts produced by DMLS." The International Journal of Advanced Manufacturing Technology 67(9-12): 2743-2751.

Calnano (2014). FUJI-SPS DR. SINTER LAB: 2.

Canakci, A., et al. (2014). "Synthesis of novel CuSn10-graphite nanocomposite powders by mechanical alloying." Micro & Nano Letters 9(2): 109-112.

Čapek, J., et al. (2016). "Highly porous, low elastic modulus 316L stainless steel scaffold prepared by selective laser melting." Materials Science and Engineering: C 69: 631-639.

Carboni, C., et al. (2002). "Influence of high power diode laser surface melting on the pitting corrosion resistance of type 316L stainless steel." Journal of materials science 37(17): 3715-3723.

Carlton, H. D., et al. (2016). "Damage evolution and failure mechanisms in additively manufactured stainless steel." Materials Science and Engineering: A 651: 406-414.

Carmezim, M., et al. (2005). "Capacitance behaviour of passive films on ferritic and austenitic stainless steel." Corrosion Science 47(3): 581-591.

Casalino, G., et al. (2015). "Experimental investigation and statistical optimisation of the selective laser melting process of a maraging steel." Optics & Laser Technology 65: 151-158.

Castle, J. and R. Ke (1990). "Studies by auger spectroscopy of pit initiation at the site of inclusions in stainless steel." Corrosion Science 30(4-5): 409-428.

Chaichi, A., et al. (2019). "Improvement of Tribological and Biocompatibility Properties of Orthopedic Materials Using Piezoelectric Direct Discharge Plasma Surface Modification." ACS Biomaterials Science & Engineering 5(5): 2147-2159.

Chang, J., et al. (2015). "Role of tantalum in the hot corrosion of a Ni-base single crystal superalloy." Corrosion Science 98: 585-591.

Chang, J., et al. (2017). "Interaction of Ta and Cr on Type-I hot corrosion resistance of single crystal Ni-base superalloys." Corrosion Science 117: 35-42.

Chao, Q., et al. (2017). "On the enhanced corrosion resistance of a selective laser melted austenitic stainless steel." Scripta Materialia 141: 94-98.

Chastell, D. and P. Flewitt (1979). "The formation of the σ phase during long term high temperature creep of type 316 austenitic stainless steel." Materials Science and Engineering 38(2): 153-162.

Chen, C.-L. (2018). "Investigation of W-Ti ODS coating on SUS304 steel fabricated by mechanical alloying technique." Surface Coatings Technology 350: 1105-1111.

Chen, C.-L. (2018). "Study of W-Co ODS coating on stainless steels by mechanical alloying." Surface Coatings Technology 350: 954-961.

Chen, H.-F., et al. (2020). "Recent progress in thermal/environmental barrier coatings and their corrosion resistance." Rare Metals 39(5): 498-512.

Chen, H., et al. (2017). "Improving additive manufacturing processability of hard-to-process overhanging structure by selective laser melting." Journal of Materials Processing Technology 250: 99-108.

Chen, J.-R. and W.-T. Tsai (2011). "In situ corrosion monitoring of Ti–6Al–4V alloy in H2SO4/HCl mixed solution using electrochemical AFM." Electrochimica Acta 56(4): 1746-1751.

Chen, W., et al. (2007). "The role of residual stress in neutral pH stress corrosion cracking of pipeline steels–Part II: Crack dormancy." Acta Materialia 55(1): 43-53.

Chen, X., et al. (2018). "Effect of heat treatment on microstructure, mechanical and corrosion properties of austenitic stainless steel 316L using arc additive manufacturing." Materials Science and Engineering: A 715: 307-314.

Chen, X., et al. (2015). "Strengthening and toughening strategies for tin bronze alloy through fabricating in-situ nanostructured grains." Materials & Design (1980-2015) 66: 60-66.

Cheng, C. Q., et al. (2013). "Facile chromaticity approach for the inspection of passive films on austenitic stainless steel." Corrosion Science 70: 235-242.

Cherry, J., et al. (2015). "Investigation into the effect of process parameters on microstructural and physical properties of 316L stainless steel parts by selective laser melting." The International Journal of Advanced Manufacturing Technology 76(5-8): 869-879.

Chiavari, C., et al. (2006). "Corrosion evaluation of traditional and new bronzes for artistic castings." Materials Chemistry and Physics 95(2-3): 252-259.

Chiba, A., et al. (2013). "Pit initiation mechanism at MnS inclusions in stainless steel: synergistic effect of elemental sulfur and chloride ions." Journal of the electrochemical society 160(10): C511.

Cho, E., et al. (2005). "Performance of a 1 kW-class PEMFC stack using TiN-coated 316 stainless steel bipolar plates." Journal of Power Sources 142(1-2): 177-183.

Cho, H. and A. Kimura (2007). "Corrosion resistance of high-Cr oxide dispersion strengthened ferritic steels in super-critical pressurized water." Journal of Nuclear Materials 367: 1180-1184.

Cho, S.-H., et al. (2009). "Hot corrosion behavior of Ni-base alloys in a molten salt under an oxidizing atmosphere." Journal of alloys 468(1-2): 263-269.

Christl, W., et al. (1987). "Application of the acoustic emission technique for the detection of oxide scale cracking during thermal cycling." Materials Science and Engineering 87: 289-293.

Clayton, C. R., et al. (1995). "Passivity of high-nitrogen stainless alloys: the role of metal oxyanions and salt films." Materials science & engineering. A, Structural materials: properties, microstructure and processing 198(1-2): 135-144.

Craig, B. D. (1982). "The effect of nickel on hydrogen cracking resistance in low alloy steels—A review." Corrosion 38(9): 457-463.

Cruz, V., et al. (2020). "Electrochemical studies on the effect of residual stress on the corrosion of 316L manufactured by selective laser melting." Corrosion Science 164: 108314.

Cui, C., et al. (2020). "Austenitic stainless steel powders with increased nitrogen content for laser additive manufacturing." Metals 10(1): 61.

Cui, Y. and C. D. Lundin (2007). "Austenite-preferential corrosion attack in 316 austenitic stainless steel weld metals." Materials & Design 28(1): 324-328.

Dahotre, N. (2000). "Functional coatings and their applications: a web perspective." Jom 52(1): 14-14.

Dai, N., et al. (2017). "Heat treatment degrading the corrosion resistance of selective laser melted Ti-6Al-4V alloy." Journal of the electrochemical society 164(7): C428-C434.

Dai, N., et al. (2016). "Corrosion behavior of selective laser melted Ti-6Al-4 V alloy in NaCl solution." Corrosion Science 102: 484-489.

Dai, N., et al. (2016). "Distinction in corrosion resistance of selective laser melted Ti-6Al-4V alloy on different planes." Corrosion Science 111: 703-710.

Darolia, R. (2019). "Development of strong, oxidation and corrosion resistant nickel-based superalloys: critical review of challenges, progress and prospects." International materials reviews 64(6): 355-380.

Das, D. (2013). "Microstructure and high temperature oxidation behavior of Pt-modified aluminide bond coats on Ni-base superalloys." Progress in Materials Science 58(2): 151-182.

Das, D., et al. (2000). "Effect of prealuminizing diffusion treatment on microstructural evolution of high-activity Pt-aluminide coatings." Metallurgical and Materials Transactions A 31(8): 2037-2047.

Davies, D., et al. (2000). "Stainless steel as a bipolar plate material for solid polymer fuel cells." Journal of Power Sources 86(1-2): 237-242.

Davis, J. R. (1994). Stainless steels, ASM international.

Davis, J. R. (1997). ASM specialty handbook: heat-resistant materials, Asm International.

de Assis, S. L., et al. (2006). "Corrosion characterization of titanium alloys by electrochemical techniques." Electrochimica Acta 51(8-9): 1815-1819.

De Castro, V., et al. (2011). "Stability of nanoscale secondary phases in an oxide dispersion strengthened Fe–12Cr alloy." Acta Materialia 59(10): 3927-3936.

de Lima, M. S. F. and S. Sankaré (2014). "Microstructure and mechanical behavior of laser additive manufactured AISI 316 stainless steel stringers." Materials & Design 55: 526-532.

Deb, D., et al. (1996). "A comparative study of oxidation and hot corrosion of a cast nickel base superalloy in different corrosive environments." Materials Letters 29(1-3): 19-23.

DebRoy, T., et al. (2018). "Additive manufacturing of metallic components–process, structure and properties." Progress in Materials Science 92: 112-224.

Deepak, K., et al. (2016). "Implication of grain boundary engineering on high temperature hot corrosion of alloy 617." Corrosion Science 106: 293-297.

DelaunayRID, F., et al. (2000). "SEM-EDS and XPS studies of the high temperature oxidation behaviour of Inconel 718." Microchimica Acta 132(2-4): 337-343.

Deng, C., et al. (2018). "Study on the selective laser melting of CuSn10 powder." Materials 11(4): 614.

Di Girolamo, G., et al. (2015). "Microstructural, mechanical and thermal characteristics of zirconia-based thermal barrier coatings deposited by plasma spraying." Ceramics International 41(9): 11776-11785.

Di Schino, A. and J. Kenny (2002). "Effects of the grain size on the corrosion behavior of refined AISI 304 austenitic stainless steels." Journal of materials science letters 21(20): 1631-1634.

Dodaran, M., et al. (2020). "Effect of alloying elements on the γ'antiphase boundary energy in Ni-base superalloys." Intermetallics 117: 106670.

Donachie, M. and S. Donachie (2002). "Understanding superalloy metallurgy." Superalloys A Tech. Guid: 25-39.

Donachie, M. J. (2000). Titanium: a technical guide, ASM international.

Donachie, M. J. and S. J. Donachie (2002). Superalloys: a technical guide, ASM international.

Dorcheh, A. S., et al. (2016). "Corrosion behavior of stainless and low-chromium steels and IN625 in molten nitrate salts at 600 C." Solar Energy Materials and Solar Cells 144: 109-116.

Drach, A., et al. (2013). "Field studies of corrosion behaviour of copper alloys in natural seawater." Corrosion Science 76: 453-464.

Durand-Charre, M. (1998). The microstructure of superalloys, CRC press.

Egbewande, A., et al. (2010). "Analysis of laser beam weldability of Inconel 738 superalloy." Materials Characterization 61(5): 569-574.

Ehrnstén, U. (2012). Corrosion and stress corrosion cracking of austenitic stainless steels. Comprehensive nuclear materials, Elsevier: 93-104.

El-Awadi, G., et al. (2016). "Hot corrosion behavior of Ni based Inconel 617 and Inconel 738 superalloys." Applied Surface Science 378: 224-230.

El-Tahawy, M., et al. (2017). The influence of plastic deformation on lattice defect structure and mechanical properties of 316L austenitic stainless steel. Materials Science Forum, Trans Tech Publ.

El-Tahawy, M., et al. (2017). "Stored energy in ultrafine-grained 316L stainless steel processed by high-pressure torsion." Journal of Materials Research and Technology 6(4): 339-347.

Eliaz, N., et al. (2002). "Hot corrosion in gas turbine components." Engineering failure analysis 9(1): 31-43.

Eric Jones, J., et al. (2014). "Corrosion resistance improvement for 316L stainless steel coronary artery stents by trimethylsilane plasma nanocoatings." Journal of Biomedical Materials Research Part B: Applied Biomaterials 102(7): 1363-1374.

Ettefagh, A. H. and S. Guo (2018). "Electrochemical behavior of AISI316L stainless steel parts produced by laser-based powder bed fusion process and the effect of post annealing process." Additive Manufacturing 22: 153-156.

Ettefagh, A. H., et al. (2020). "Corrosion performance of additively manufactured stainless steel parts: A review." Additive Manufacturing: 101689.

Ettefagh, A. H., et al. (2020). "Laser surface modifications of Fe-14Cr ferritic alloy for improved corrosion performance." Surface and Coatings Technology 381: 125194.

Ettefagh, A. H., et al. (2018). Phase Evolution and Corrosion Performance of Laser Processed Oxide Dispersion Strengthened Ferritic Alloys. ASME International Mechanical Engineering Congress and Exposition, American Society of Mechanical Engineers.

Ettefagh, A. H., et al. (2019). "Corrosion behavior of additively manufactured Ti-6Al-4V parts and the effect of post annealing." Additive Manufacturing 28: 252-258.

Eyers, D. R. and A. T. Potter (2017). "Industrial Additive Manufacturing: A manufacturing systems perspective." Computers in industry 92: 208-218.

Fahrmann, M. and D. Metzler (2016). "Simulation of γ′ precipitation kinetics in a commercial Ni-base superalloy." Jom 68(11): 2786-2792.

Fan, Q., et al. (2014). "Microstructure and hot corrosion behaviors of two Co modified aluminide coatings on a Ni-based superalloy at 700 C." Applied Surface Science 311: 214-223.

Fattah-Alhosseini, A., et al. (2010). "Effect of solution concentration on semiconducting properties of passive films formed on austenitic stainless steels." Corrosion Science 52(1): 205-209.

Feichtinger, H. and G. Stein (1999). Melting of high nitrogen steels. Materials science forum, Trans Tech Publ.

Feng, K., et al. (2012). "Improved corrosion resistance of stainless steel 316L by Ti ion implantation." Materials Letters 68: 450-452.

FERDINANDOV, N. V., et al. "STRUCTURE AND PITTING CORROSION OF Ti-6Al-4V ALLOY AND Ti-6Al-4V WELDS."

Fernández, A., et al. (2012). "Molten salt corrosion of stainless steels and low-Cr steel in CSP plants." Oxidation of Metals 78(5-6): 329-348.

Fesharaki, M. N., et al. (2019). "Evaluation of the hot corrosion behavior of Inconel 625 coatings on the Inconel 738 substrate by laser and TIG cladding techniques." Optics & Laser Technology 111: 744-753.

Field, R., et al. (1992). "THE DEVELOPMENT OF?‘lr INTERFACIAL DISLOCATION NETWORKS DURING CREEP IN N&BASE SUPERALLOYS."

Fox, J. C., et al. (2016). "Effect of process parameters on the surface roughness of overhanging structures in laser powder bed fusion additive manufacturing." Procedia CIRP 45: 131-134.

Fredriksson, W., et al. (2013). "Corrosion resistances and passivation of powder metallurgical and conventionally cast 316L and 2205 stainless steels." Corrosion Science 67: 268-280.

Freire, L., et al. (2010). "The passive behaviour of AISI 316 in alkaline media and the effect of pH: A combined electrochemical and analytical study." Electrochimica Acta 55(21): 6174-6181.

Frelek-Kozak, M., et al. (2018). "Influence of consolidation process on functional properties of steels." Surface Coatings Technology 355: 234-239.

Fryburg, G., et al. (1984). "Chemical Reactions Involved in the Initiation of Hot Corrosion of IN-738." Journal of the electrochemical society 131(12): 2985.

Fryburg, G. C., et al. (1977). "Mechanism of beneficial effect of tantalum in hot corrosion of nickel-base superalloys."

Fu, N., et al. (2015). "In situ investigation of local corrosion at interphase boundary under an electrochemical-atomic force microscope." Journal of Solid State Electrochemistry 19(2): 337-344.

Gagliano, M. S., et al. (2009). Update on the fireside corrosion resistance of proposed advanced ultrasupercritical superheater and reheater materials: Laboratory and field test results. Clearwater Coal Conference, 34th International Technical Conference on Coal Utilization and Fuel Systems.

Galati, M., et al. (2017). "Modelling energy source and powder properties for the development of a thermal FE model of the EBM additive manufacturing process." Additive Manufacturing 14: 49-59.

Ganesh, P., et al. (2012). "Studies on pitting corrosion and sensitization in laser rapid manufactured specimens of type 316L stainless steel." Materials & Design 39: 509-521.

Gao, W., et al. (2015). "The status, challenges, and future of additive manufacturing in engineering." Computer-Aided Design 69: 65-89.

García, C., et al. (2007). "Pitting corrosion behaviour of PM austenitic stainless steels sintered in nitrogen–hydrogen atmosphere." Corrosion Science 49(4): 1718-1736.

Garip, Y. and O. Ozdemir (2019). "Comparative study of the oxidation and hot corrosion behaviors of TiAl-Cr intermetallic alloy produced by electric current activated sintering." Journal of Alloys and Compounds 780: 364-377.

Gavriljuk, V., et al. (2000). "On the correlation between electron structure and short range atomic order in iron-based alloys." Acta Materialia 48(15): 3879-3893.

GE Additive (2020). "Mlab R." from https://www.ge.com/additive/additive-manufacturing/machines/dmlm-machines/mlab-r.

Geenen, K., et al. (2017). "Corrosion behavior of 316L austenitic steel processed by selective laser melting, hot-isostatic pressing, and casting." Materials and Corrosion 68(7): 764-775.

Ghosal, P., et al. (2018). "Study on direct laser metal deposition." Materials Today: Proceedings 5(5): 12509-12518.

Gibbons, T. and R. Stickler (1982). IN939: Metallurgy, properties and performance. High Temperature Alloys for Gas Turbines 1982, Springer: 369-393.

Gibson, I., et al. (2014). Additive manufacturing technologies, Springer.

Gil, F., et al. (2001). "Formation of α-Widmanstätten structure: effects of grain size and cooling rate on the Widmanstätten morphologies and on the mechanical properties in Ti6Al4V alloy." Journal of Alloys and Compounds 329(1-2): 142-152.

Gil, L., et al. (2006). "Corrosion performance of the plasma nitrided 316L stainless steel." Surface and Coatings Technology 201(7): 4424-4429.

Gockel, J., et al. (2019). "The influence of additive manufacturing processing parameters on surface roughness and fatigue life." International Journal of Fatigue 124: 380-388.

Goebel, J. and F. Pettit (1970). "The influence of sulfides on the oxidation behavior of nickel-base alloys." Metallurgical Transactions 1(12): 3421-3429.

Goebel, J. and F. Pettit (1970). "Na 2 SO 4-induced accelerated oxidation (hot corrosion) of nickel." Metallurgical Transactions 1(7): 1943-1954.

Goebel, J., et al. (1973). "Mechanisms for the hot corrosion of nickel-base alloys." Metallurgical Transactions 4(1): 261-278.

Gollapudi, S. (2012). "Grain size distribution effects on the corrosion behaviour of materials." Corrosion Science 62: 90-94.

Gonzalez-Rodriguez, J., et al. (2006). "Corrosion performance of heat resistant alloys in Na2SO4–V2O5 molten salts." 435: 258-265.

Gorbatov, O. I., et al. (2016). "Effect of composition on antiphase boundary energy in Ni 3 Al based alloys: Ab initio calculations." Physical Review B 93(22): 224106.

Gorsse, S., et al. (2017). "Additive manufacturing of metals: a brief review of the characteristic microstructures and properties of steels, Ti-6Al-4V and high-entropy alloys." Science and Technology of advanced MaTerialS 18(1): 584-610.

Goward, G. (1998). "Progress in coatings for gas turbine airfoils." Surface and Coatings Technology 108: 73-79.

Grünling, H. and R. Bauer (1982). "The role of silicon in corrosion-resistant high temperature coatings." Thin Solid Films 95(1): 3-20.

Gu, D., et al. (2012). "Laser additive manufacturing of metallic components: materials, processes and mechanisms." International materials reviews 57(3): 133-164.

Gu, D. and Y. Shen (2009). "Balling phenomena in direct laser sintering of stainless steel powder: Metallurgical mechanisms and control methods." Materials & Design 30(8): 2903-2910.

Gu, D. D., et al. (2012). "Laser additive manufacturing of metallic components: materials, processes and mechanisms." International materials reviews 57(3): 133-164.

Gubicza, J., et al. (2016). "Microstructure, phase composition and hardness evolution in 316L stainless steel processed by high-pressure torsion." Materials Science and Engineering: A 657: 215-223.

Guo, L., et al. (2010). "Microstructure and mechanical properties of an oxide dispersion strengthened ferritic steel by a new fabrication route." Materials Science Engineering: A 527(20): 5220-5224.

Guo, P., et al. (2017). "Study on microstructure, mechanical properties and machinability of efficiently additive manufactured AISI 316L stainless steel by high-power direct laser deposition." Journal of Materials Processing Technology 240: 12-22.

Gurrappa, I. (1998). "Thermal barrier coatings for hot corrosion resistance of CM 247 LC superalloy." Journal of materials science letters 17(15): 1267-1269.

Gurrappa, I. (1999). "Hot corrosion behavior of CM 247 LC alloy in Na2SO4 and NaCl environments." Oxidation of Metals 51(5-6): 353-382.

Gurrappa, I. (2000). "Hot corrosion of protective coatings." Materials and manufacturing processes 15(5): 761-773.

Gurrappa, I. (2003). "Characterization of titanium alloy Ti-6Al-4V for chemical, marine and industrial applications." Materials Characterization 51(2-3): 131-139.

Gurrappa, I. (2003). "Influence of alloying elements on hot corrosion of superalloys and coatings: necessity of smart coatings for gas turbine engines." Materials Science and Technology 19(2): 178-183.

Gurrappa, I. J. M. s. and technology (2003). "Influence of alloying elements on hot corrosion of superalloys and coatings: necessity of smart coatings for gas turbine engines." 19(2): 178-183.

Habib, K., et al. (2011). "Breakdown and evolution of the protective oxide scales of AISI 304 and AISI 316 stainless steels under high-temperature oxidation." International Journal of Corrosion 2011.

Halada, G. and C. Clayton (1993). "Comparison of Mo–N and W–N synergism during passivation of stainless steel through x-ray photoelectron spectroscopy and electrochemical analysis." Journal of Vacuum Science & Technology A: Vacuum, Surfaces, and Films 11(4): 2342-2347.

Han, F., et al. (2015). "Influence of Ta content on hot corrosion behaviour of a directionally solidified nickel base superalloy." Journal of Alloys and Compounds 619: 102-108.

Han, M., et al. (2015). "The influence of interface morphology on the stress distribution in double-ceramic-layer thermal barrier coatings." Ceramics International 41(3): 4312-4325.

Han, P. (2017). "Additive design and manufacturing of jet engine parts." Engineering 3(5): 648-652.

Han, Y., et al. (2016). "Effect of electropolishing on corrosion of nuclear grade 316L stainless steel in deaerated high temperature water." Corrosion Science 112: 625-634.

Hanbury, R. D. and G. S. Was (2019). "Oxide growth and dissolution on 316L stainless steel during irradiation in high temperature water." Corrosion Science 157: 305-311.

Hancock, P. (1987). "Vanadic and chloride attack of superalloys." Materials Science and Technology 3(7): 536-544.

Hancock, P., et al. (1989). "A review of recent studies of the role of zinc as an inhibitor of hot corrosion from molten sulphates." Materials Science and Engineering: A 120: 313-318.

Hao, Y.-w., et al. (2009). "Effect of surface mechanical attrition treatment on corrosion behavior of 316 stainless steel." Journal of iron and steel research international 16(2): 68-72.

Hari, P., et al. (2020). "Oxidation studies on nickel-base superalloy 617 OCC." Materials Today: Proceedings.

Harun, W., et al. (2018). "A comprehensive review of hydroxyapatite-based coatings adhesion on metallic biomaterials." Ceramics International 44(2): 1250-1268.

Harun, W., et al. (2018). "Surface characterisation and corrosion behaviour of oxide layer for SLMed-316L stainless steel." Journal of Alloys and Compounds 748: 1044-1052.

Hauk, V. (1997). "2-x-ray diffraction." Structural and Residual Stress Analysis by Nondestructive Methods. Amsterdam: Elsevier Science BV: 17.

Haynes, J., et al. (2002). "Influence of sulfur, platinum, and hafnium on the oxidation behavior of CVD NiAl bond coatings." Oxidation of Metals 58(5-6): 513-544.

He, D.-G., et al. (2019). "Influences of solution cooling on microstructures, mechanical properties and hot corrosion resistance of a nickel-based superalloy." Materials Science and Engineering: A 746: 372-383.

He, D., et al. (2000). "Manufacturing, structure and high temperature corrosion of palladium-modified aluminide coatings on nickel-base superalloy M38." Thin Solid Films 376(1-2): 144-151.

He, J., et al. (1997). "Effect of hydrogen on dynamic precipitation of carbide in type 304 stainless steel during creep process." Acta Materialia 45(8): 3377-3388.

He, X., et al. (2003). "Alloying element vaporization during laser spot welding of stainless steel." Journal of Physics D: Applied Physics 36(23): 3079.

Hearley, J., et al. (1999). "The erosion behaviour of NiAl intermetallic coatings produced by high velocity oxy-fuel thermal spraying." Wear 233: 328-333.

Heck, K., et al. (1998). "INCONEL® alloy 783: An oxidation-resistant, low expansion superalloy for gas turbine applications."

Hejwowski, T. (2006). "Investigations of corrosion resistance of Fe-, Ni-and Co-based hardfacings." Vacuum 80(11-12): 1386-1390.

Hemmasian-Ettefagh, A., et al. (2010). "Corrosion inhibition of carbon steel in cooling water." Materials performance 49(3): 60-65.

Henry, P., et al. (2009). "Tribocorrosion of 316L stainless steel and TA6V4 alloy in H2SO4 media." Corrosion Science 51(6): 1308-1314.

Hermawan, H., et al. (2011). "Metals for biomedical applications." Biomedical engineering-from theory to applications: 411-430.

Herzog, D. and V. Seyda (2016). "V.; E. Wycisk, E.; Emmelmann, C." Additive manufacturing of metals, Acta Mater 117: 371-392.

Herzog, D., et al. (2016). "Additive manufacturing of metals." Acta Materialia 117: 371-392.

Hidalgo, V. H., et al. (2001). "High temperature erosion wear of flame and plasma-sprayed nickel–chromium coatings under simulated coal-fired boiler atmospheres." Wear 247(2): 214-222.

Hoelzer, D., et al. (2000). "A microstructural study of the oxide scale formation on ODS Fe–13Cr steel." Journal of Nuclear Materials 283: 1306-1310.

Homaeian, A. and M. Alizadeh (2016). "Interaction of hot corrosion and creep in Alloy 617." Engineering failure analysis 66: 373-384.

Hong, S. L. (2001). "Influence of surface condition on primary water stress corrosion cracking initiation of alloy 600." Corrosion 57(4): 323-333.

Hu, H., et al. (2013). "Corrosion behavior of a 14Cr-ODS steel in supercritical water." Journal of Nuclear Materials 437(1-3): 196-200.

Hu, R., et al. (2012). "Precipitation behavior of grain boundary M23C6 and its effect on tensile properties of Ni–Cr–W based superalloy." Materials Science and Engineering: A 548: 83-88.

Huang, Q., et al. (2016). "Microstructure and inclusion of Ti–6Al–4V fabricated by selective laser melting." Frontiers of Materials Science 10(4): 428-431.

Huang, Y., et al. (2017). "Corrosion performance of high strength low alloy steel AISI 4135 in the marine splash zone." Electrochemistry 85(1): 7-12.

Hunt, J., et al. (2014). "Selection of steels suitable for additive layer manufacturing." Ironmaking & Steelmaking 41(4): 254-256.

Ibrahim, M. Z., et al. (2017). "Biomedical materials and techniques to improve the tribological, mechanical and biomedical properties of orthopedic implants–A review article." Journal of Alloys and Compounds 714: 636-667.

Ingo, G., et al. (2006). "Large scale investigation of chemical composition, structure and corrosion mechanism of bronze archeological artefacts from Mediterranean basin." Applied Physics A 83(4): 513-520.

Isfahany, A. N., et al. (2011). "The effect of heat treatment on mechanical properties and corrosion behavior of AISI420 martensitic stainless steel." Journal of Alloys and Compounds 509(9): 3931-3936.

Itzhak, D. and E. Aghion (1983). "Corrosion behaviour of hot-pressed austenitic stainless steel in H2SO4 solutions at room temperature." Corrosion Science 23(10): 1085-1094.

Jahangiri, M., et al. (2012). "Development of wrought precipitation strengthened IN939 superalloy." 28(12): 1470-1478.

Jamshidinia, M. and R. Kovacevic (2015). "The influence of heat accumulation on the surface roughness in powder-bed additive manufacturing." Surface Topography: Metrology and Properties 3(1): 014003.

Jargelius-Pettersson, R. (1999). "Electrochemical investigation of the influence of nitrogen alloying on pitting corrosion of austenitic stainless steels." Corrosion Science 41(8): 1639-1664.

Jaykumar, T., et al. (2001). "Acoustic Methods for Characterisation of Microstructures and Deformation Processes in Nimonic Alloy PE 16 and Zircaloy-2." Mineral Procesing and Extractive Metallurgy Review 22(1): 249-261.

Jerrard, P., et al. (2009). "Experimental investigation into selective laser melting of austenitic and martensitic stainless steel powder mixtures." Proceedings of the Institution of Mechanical Engineers, Part B: Journal of Engineering Manufacture 223(11): 1409-1416.

Jiang, S., et al. (2010). "High temperature corrosion behaviour of a gradient NiCoCrAlYSi coating II: oxidation and hot corrosion." Corrosion Science 52(7): 2316-2322.

Jin-tao, L., et al. (2018). "Effect of Sulfur and Chlorine on Fireside Corrosion Behavior of Inconel 740 H Superalloy." High Temperature Materials and Processes 37(3): 245-251.

Jinlong, L., et al. (2017). "The effect of surface enriched chromium and grain refinement by ball milling on corrosion resistance of 316L stainless steel." Materials Research Bulletin 91: 91-97.

Jirandehi, A. P. and T. Chakherlou (2019). "A fatigue crack initiation and growth life estimation method in single-bolted connections." The Journal of Strain Analysis for Engineering Design 54(2): 79-94.

Jirandehi, A. P., et al. (2020). "Temperature-induced buckling of ductile metals during cyclic loading and the subsequent early fracture." International Journal of Mechanical Sciences 176: 105525.

Jun, C., et al. (2014). "Corrosion and tribocorrosion behaviors of AISI 316 stainless steel and Ti6Al4V alloys in artificial seawater." Transactions of Nonferrous Metals Society of China 24(4): 1022-1031.

Jun, J., et al. (2014). "Pitting corrosion of very clean type 304 stainless steel." Corrosion 70(2): 146-155.

Kamachimudali, U., et al. (2003). "Corrosion of bio implants." Sadhana 28(3-4): 601-637.

Kamal, S., et al. (2009). "Evaluation of cyclic hot corrosion behaviour of detonation gun sprayed Cr3C2–25% NiCr coatings on nickel-and iron-based superalloys." Surface and Coatings Technology 203(8): 1004-1013.

Kamal, S., et al. (2010). "High temperature cyclic oxidation and hot corrosion behaviours of superalloys at 900 C." Bulletin of Materials Science 33(3): 299-306.

Kamal, S., et al. (2011). "Hot corrosion studies of detonation-gun-sprayed NiCrAlY+ 0.4 wt.% CeO 2 coated superalloys in molten salt environment." Journal of materials engineering and performance 20(6): 1068-1077.

Kamal, S., et al. (2010). "High temperature cyclic oxidation and hot corrosion behaviours of superalloys at 900 C." 33(3): 299-306.

Kamath, C., et al. (2014). "Density of additively-manufactured, 316L SS parts using laser powder-bed fusion at powers up to 400 W." The International Journal of Advanced Manufacturing Technology 74(1-4): 65-78.

Kameswari, S. (1986). "The role of NaCl in the hot-corrosion behavior of nimonic alloy 90." Oxidation of Metals 26(1-2): 33-44.

Kang, B., et al. (2003). "High temperature moiré interferometry investigation of creep crack growth of inconel 783—environment and β-phase effects." Materials Science and Engineering: A 347(1-2): 205-213.

Kargarnejad, S. and F. Djavanroodi (2012). "Failure assessment of Nimonic 80A gas turbine blade." Engineering failure analysis 26: 211-219.

Karimi, S., et al. (2012). "A review of metallic bipolar plates for proton exchange membrane fuel cells: materials and fabrication methods." Advances in Materials Science and Engineering 2012.

Kashaev, N., et al. (2013). "Comparative study of mechanical properties using standard and micro-specimens of base materials Inconel 625, Inconel 718 and Ti-6Al-4 v." Journal of Materials Research and Technology 2(1): 43-47.

Katzarov, I., et al. (2002). "Finite element modeling of the morphology of β to α phase transformation in Ti-6Al-4V alloy." Metallurgical and Materials Transactions A 33(4): 1027-1040.

Kaufman, L. and J. Ågren (2014). "CALPHAD, first and second generation–Birth of the materials genome." Scripta Materialia 70: 3-6.

Kavousi, S., et al. (2020). "Interface kinetics of rapid solidification of binary alloys by atomistic simulations: Application to Ti-Ni alloys." Computational Materials Science 184: 109854.

Kawagishi, K., et al. (2009). "Oxidation resistant Ru containing Ni base single crystal superalloys." Materials Science and Technology 25(2): 271-275.

Ke, R. and R. Alkire (1995). "Initiation of corrosion pits at inclusions on 304 stainless steel." Journal of the electrochemical society 142(12): 4056.

Keicher, D. (2001). "Laser engineered net shapping process." LIA handbook of laser materials processing. Florida: Laser Institute of America: 561-563.

Kellner, T. (2017). "An epiphany of disruption: GE additive chief explains how 3D printing will upend manufacturing." GE Reports 13.

Khajavi, M. and M. Shariat (2004). "Failure of first stage gas turbine blades." Engineering failure analysis 11(4): 589-597.

Khajouei-Nezhad, M., et al. (2017). "Microstructure and mechanical properties of ultrafine-grained aluminum consolidated by high-pressure torsion." Materials Science and Engineering: A 682: 501-508.

Khan, M. A., et al. (2015). "Hot corrosion behaviour of Inconel 617 in Mixed salt environment at 900 and 1000 C for gas turbine applications." High Temperature Materials and Processes 34(3): 221-225.

Khan, M. A., et al. (2014). "Oxidation and hot corrosion behavior of nickel-based superalloy for gas turbine applications." Materials and manufacturing processes 29(7): 832-839.

Khoddami, A., et al. (2007). "Microstructure formation in thermally-sprayed duplex and functionally graded NiCrAlY/Yttria-Stabilized Zirconia coatings." Surface and Coatings Technology 201(12): 6019-6024.

Khorsand, S., et al. (2018). "Hot corrosion behavior of Inconel 625 superalloy in eutectic molten nitrate salts." Oxidation of Metals 90(1-2): 169-186.

Kim, C., et al. (2019). "Cr diffusion coating to improve the corrosion resistance of an ODS steel in super-critical carbon dioxide environment." Surface Coatings Technology 374: 666-673.

Kim, J. J. and Y. M. Young (2013). "Study on the passive film of type 316 stainless steel." Int. J. Electrochem. Sci 8(10): 11847-11859.

Kington, A. and F. Noble (1991). "σ phase embrittlement of a type 310 stainless steel." Materials Science and Engineering: A 138(2): 259-266.

Kluczyński, J., et al. (2018). "The influence of exposure energy density on porosity and microhardness of the SLM additive manufactured elements." Materials 11(11): 2304.

Knutsson, P., et al. (2013). "A method for investigation of hot corrosion by gaseous Na2SO4." Corrosion Science 73: 230-236.

Kocovic, P. (2017). 3D Printing and Its Impact on the Production of Fully Functional Components: Emerging Research and Opportunities: Emerging Research and Opportunities, IGI Global.

Kok, Y., et al. (2018). "Anisotropy and heterogeneity of microstructure and mechanical properties in metal additive manufacturing: A critical review." Materials & Design 139: 565-586.

Kong, D., et al. (2019). "Corrosion of metallic materials fabricated by selective laser melting." Npj Materials Degradation 3(1): 1-14.

Kong, D., et al. (2020). "The passivity of selective laser melted 316L stainless steel." Applied Surface Science 504: 144495.

Kong, D., et al. (2019). "High-throughput fabrication of nickel-based alloys with different Nb contents via a dual-feed additive manufacturing system: Effect of Nb content on microstructural and mechanical properties." Journal of Alloys and Compounds 785: 826-837.

Kong, D., et al. (2019). "Mechanical properties and corrosion behavior of selective laser melted 316L stainless steel after different heat treatment processes." Journal of Materials Science & Technology 35(7): 1499-1507.

Kong, D., et al. (2018). "Surface monitoring for pitting evolution into uniform corrosion on Cu-Ni-Zn ternary alloy in alkaline chloride solution: ex-situ LCM and in-situ SECM." Applied Surface Science 440: 245-257.

Kong, D., et al. (2018). "Bio-functional and anti-corrosive 3D printing 316L stainless steel fabricated by selective laser melting." Materials & Design 152: 88-101.

Kong, D., et al. (2018). "Heat treatment effect on the microstructure and corrosion behavior of 316L stainless steel fabricated by selective laser melting for proton exchange membrane fuel cells." Electrochimica Acta 276: 293-303.

Kosieniak, E., et al. (2012). "Corrosion failures in gas turbine hot components." Journal of failure analysis and prevention 12(3): 330-337.

Krawiec, H., et al. (2005). "Influence of the chemical dissolution of MnS inclusions on the electrochemical behavior of stainless steels." Journal of the electrochemical society 152(7): B213.

Krishnan, S., et al. (2013). "Effect of crystallographic orientation on the pitting corrosion resistance of laser surface melted AISI 304L austenitic stainless steel." International Journal of Mechanical, Aerospace, Industrial and Mechatronics Engineering 7(4): 239-242.

Kruth, J.-P., et al. (2012). "Assessing and comparing influencing factors of residual stresses in selective laser melting using a novel analysis method." Proceedings of the Institution of Mechanical Engineers, Part B: Journal of Engineering Manufacture 226(6): 980-991.

Kruth, J.-P., et al. (2004). "Selective laser melting of iron-based powder." Journal of Materials Processing Technology 149(1-3): 616-622.

Kumar, S., et al. (2009). "Thermal oxidation of CP-Ti: Evaluation of characteristics and corrosion resistance as a function of treatment time." Materials Science and Engineering: C 29(6): 1942-1949.

Kumar, S., et al. (2019). "Effect of surface modification on the hot corrosion resistance of Inconel 718 at 700 C." Materials Research Express 6(8): 086549.

Kurzynowski, T., et al. (2018). "Correlation between process parameters, microstructure and properties of 316 L stainless steel processed by selective laser melting." Materials Science and Engineering: A 718: 64-73.

Lai, G. Y. (2007). High-temperature corrosion and materials applications, ASM international.

Laleh, M., et al. (2020). "Unanticipated drastic decline in pitting corrosion resistance of additively manufactured 316L stainless steel after high-temperature post-processing." Corrosion Science 165: 108412.

Laleh, M., et al. (2019). "Unexpected erosion-corrosion behaviour of 316L stainless steel produced by selective laser melting." Corrosion Science 155: 67-74.

Laleh, M., et al. (2020). "Two and three-dimensional characterisation of localised corrosion affected by lack-of-fusion pores in 316L stainless steel produced by selective laser melting." Corrosion Science 165: 108394.

Lamesle, P. and P. Steinmetz (1995). "Growth mechanisms and hot corrosion resistance of palladium modified aluminide coatings on superalloys." MATERIAL AND MANUFACTURING PROCESS 10(5): 1053-1075.

Langdon, T. G. (2013). "Twenty-five years of ultrafine-grained materials: Achieving exceptional properties through grain refinement." Acta Materialia 61(19): 7035-7059.

Laquai, R., et al. (2018). "X-ray refraction distinguishes unprocessed powder from empty pores in selective laser melting Ti-6Al-4V." Materials Research Letters 6(2): 130-135.

Lee, K., et al. (1995). "In situ scanning electron microscope comparison studies on electromigration of Cu and Cu (Sn) alloys for advanced chip interconnects." Journal of applied physics 78(7): 4428-4437.

Lee, S.-J., et al. (2004). "Corrosion-resistant component for PEM fuel cells." Journal of Power Sources 131(1-2): 162-168.

Lei, J., et al. (2019). "Comparative study on microstructure and corrosion performance of 316 stainless steel prepared by laser melting deposition with ring-shaped beam and Gaussian beam." Optics & Laser Technology 111: 271-283.

Leuders, S., et al. (2013). "On the mechanical behaviour of titanium alloy TiAl6V4 manufactured by selective laser melting: Fatigue resistance and crack growth performance." International Journal of Fatigue 48: 300-307.

Levey, P. and A. Van Bennekom (1995). "A mechanistic study of the effects of nitrogen on the corrosion properties of stainless steels." Corrosion 51(12): 911-921.

Lewandowski, J. J. and M. Seifi (2016). "Metal additive manufacturing: a review of mechanical properties." Annual Review of Materials Research 46: 151-186.

Li, C., et al. (2018). "Residual stress in metal additive manufacturing." Procedia CIRP 71: 348-353.

Li, C., et al. (2017). "Microstructure evolution characteristics of Inconel 625 alloy from selective laser melting to heat treatment." Materials Science and Engineering: A 705: 20-31.

Li, H., et al. (2018). "Effect of process parameters on tribological performance of 316L stainless steel parts fabricated by selective laser melting." Manufacturing letters 16: 36-39.

Li, M., et al. (2014). "Study of biocompatibility of medical grade high nitrogen nickel-free austenitic stainless steel in vitro." Materials Science and Engineering: C 43: 641-648.

Li, M., et al. (2003). "Oxidation behavior of sputter-deposited NiCrAlY coating." Surface and Coatings Technology 165(3): 241-247.

Li, M. C., et al. (2007). "Electrochemical corrosion behavior of nanocrystalline zinc coatings in 3.5% NaCl solutions." Journal of Solid State Electrochemistry 11(9): 1319-1325.

Li, R., et al. (2010). "Densification behavior of gas and water atomized 316L stainless steel powder during selective laser melting." Applied Surface Science 256(13): 4350-4356.

Li, X., et al. (2019). "Microstructure and properties of the laser cladding ODS layers on CLAM steel." Surface and Coatings Technology 357: 172-179.

Li, Y., et al. (2004). "Grain size effect on the electrochemical corrosion behavior of surface nanocrystallized low-carbon steel." Corrosion 60(10): 891-896.

Li, Z., et al. (2016). "Effect of spark plasma sintering temperature on microstructure and mechanical properties of 14Cr-ODS ferritic steels." Materials Science and Engineering: A 660: 52-60.

Li, Z., et al. (2019). "Tensile properties, strain rate sensitivity, and activation volume of additively manufactured 316L stainless steels." International Journal of Plasticity 120: 395-410.

Lillard, R., et al. (2016). "Pit propagation at the boundary between manganese sulfide inclusions and austenitic stainless steel 303 and the role of copper." Journal of the electrochemical society 163(8): C440.

Lin, J., et al. (2017). "Microstructural evolution and mechanical property of Ti-6Al-4V wall deposited by continuous plasma arc additive manufacturing without post heat treatment." Journal of the mechanical behavior of biomedical materials 69: 19-29.

Lin, X., et al. (2012). "Microstructure and mechanical properties of laser forming repaired 17-4PH stainless steel." Materials Science and Engineering: A 553: 80-88.

Lippold, J. and W. Savage (1982). "Solidification of austenitic stainless steel weldments: Part III--the effect of solidification behavior on hot cracking susceptibility." WELDING J. 61(12): 388.

Liu, C., et al. (2010). "Oxidation behavior of a single-crystal Ni-base superalloy between 900 and 1000° C in air." Journal of Alloys and Compounds 491(1-2): 522-526.

Liu, C., et al. (2010). "Oxidation behavior of a single-crystal Ni-base superalloy between 900 and 1000° C in air." 491(1-2): 522-526.

Liu, F., et al. (2006). "Microstructural investigation of protective and non-protective oxides on 11% chromium steel." Oxidation of Metals 66(5-6): 295-319.

Liu, L., et al. (2010). "Electrochemical corrosion behavior of nanocrystalline materials—a review." Journal of Materials Science & Technology 26(1): 1-14.

Liu, R., et al. (2017). "The alumina scale growth and interdiffusion behaviour of Pt modified AlSiY coating during cyclic oxidation." Corrosion Science 120: 121-129.

Liu, T., et al. (2015). "Influence of YH2 nanoparticles addition on the microstructure and mechanical properties of oxide dispersion strengthened ferritic alloys." Advanced Engineering Materials 17(5): 689-696.

Lodhi, M., et al. (2019). "Additively manufactured 316L stainless steel with improved corrosion resistance and biological response for biomedical applications." Additive Manufacturing 27: 8-19.

Lodhi, M., et al. (2018). "Corrosion behavior of additively manufactured 316L stainless steel in acidic media." Materialia 2: 111-121.

Longa-Nava, Y., et al. (1996). "Hot corrosion of nickel-chromium and nickel-chromium-aluminum thermal-spray coatings by sodium sulfate-sodium metavanadate salt." Corrosion 52(9): 680-689.

Lorang, G., et al. (1994). "Chemical composition of passive films on AISI 304 stainless steel." Journal of the electrochemical society 141(12): 3347.

Lou, X., et al. (2018). "Oxide inclusions in laser additive manufactured stainless steel and their effects on impact toughness and stress corrosion cracking behavior." Journal of Nuclear Materials 499: 182-190.

Lou, X., et al. (2017). "Corrosion fatigue crack growth of laser additively-manufactured 316L stainless steel in high temperature water." Corrosion Science 127: 120-130.

Lou, X., et al. (2017). "On the stress corrosion crack growth behaviour in high temperature water of 316L stainless steel made by laser powder bed fusion additive manufacturing." Corrosion Science 128: 140-153.

Lu, B., et al. (2008). "Correlation between repassivation kinetics and corrosion rate over a passive surface in flowing slurry." Electrochimica Acta 53(23): 7022-7031.

Lu, C., et al. (2017). "Effect of Y/Ti atomic ratio on microstructure of oxide dispersion strengthened alloys." Materials Characterization 134: 35-40.

Lu, J., et al. (2018). "Effect of Cobalt Content on the Oxidation and Corrosion Behavior of Ni–Fe-Based Superalloy for Ultra-Supercritical Boiler Applications." Oxidation of Metals 89(1-2): 197-209.

Lu, L. (2011). "OXIDIZING–SULFIDIZING CORROSION OF Ni–xCr–10Al ALLOYS AT 700—800°C." Acta Metall Sin 47(8): 1026-1031.

Luo, Q. and A. Jones (2010). "High-precision determination of residual stress of polycrystalline coatings using optimised XRD-sin2ψ technique." Surface and Coatings Technology 205(5): 1403-1408.

Luo, Y., et al. (2013). Application of biomedical-grade titanium alloys in trabecular bone and artificial joints. Biomaterials and Medical Tribology, Elsevier: 181-216.

Luthra, K. (1982). "Low temperature hot corrosion of cobalt-base alloys: Part II. Reaction mechanism." Metallurgical transactions A 13(10): 1853-1864.

Luthra, K. and H. Spacil (1982). "Impurity deposits in gas turbines from fuels containing sodium and vanadium." Journal of the electrochemical society 129(3): 649.

Ma, C., et al. (2018). "Laser surface modification of Mg-Gd-Ca alloy for corrosion resistance and biocompatibility enhancement." Applied Surface Science 445: 211-216.

Ma, M., et al. (2017). "A comparison on metallurgical behaviors of 316L stainless steel by selective laser melting and laser cladding deposition." Materials Science and Engineering: A 685: 265-273.

Machlin, E. and J. Shao (1977). "Quaternary gamma-prime (Ll2) pseudobinary properties as revealed by the ionicity modified pair potential model." Scripta Metallurgica 11(10): 859-862.

Magdziarz, A. and Z. Kalicka (2007). "Hot corrosion behaviour of Ni3Al in sulphate–chloride mixtures in the atmosphere." Corrosion Science 49(4): 1869-1877.

Mahamood, R. M. and E. T. Akinlabi (2017). Laser additive manufacturing. 3D Printing: Breakthroughs in Research and Practice, IGI Global: 154-171.

Mahesh, R., et al. (2008). "Evaluation of hot corrosion behaviour of HVOF sprayed NiCrAl coating on superalloys at 900 C." Materials Chemistry and Physics 111(2-3): 524-533.

Mahobia, G., et al. (2013). "Hot corrosion behavior of superalloy IN718 at 550 and 650 C." 22(8): 2418-2435.

Majumdar, J. D. and I. Manna (2010). "Mechanical properties of a laser-surface-alloyed magnesium-based alloy (AZ91) with nickel." Scripta Materialia 62(8): 579-581.

Malinov, S., et al. (2001). "Differential scanning calorimetry study and computer modeling of β⇒ α phase transformation in a Ti-6Al-4V alloy." Metallurgical and Materials Transactions A 32(4): 879-887.

Malvern Panalytical Ltd (2019). MASTERSIZER 3000: 2.

Man, C., et al. (2019). "The enhancement of microstructure on the passive and pitting behaviors of selective laser melting 316L SS in simulated body fluid." Applied Surface Science 467: 193-205.

Man, C., et al. (2019). "The effect of sub-grain structure on intergranular corrosion of 316L stainless steel fabricated via selective laser melting." Materials Letters 243: 157-160.

Manam, N., et al. (2017). "Study of corrosion in biocompatible metals for implants: A review." Journal of Alloys and Compounds 701: 698-715.

Manfredi, D., et al. (2014). "Additive manufacturing of Al alloys and aluminium matrix composites (AMCs)." Light metal alloys applications 11: 3-34.

Manivasagam, G., et al. (2010). "Biomedical implants: corrosion and its prevention-a review." Recent patents on corrosion science.

Mannava, V., et al. (2016). "Hot corrosion studies on Ni-base superalloy at 650 C under marine-like environment conditions using three salt mixture (Na2SO4+ NaCl+ NaVO3)." Corrosion Science 105: 109-119.

Mannava, V., et al. (2016). "Hot corrosion studies on Ni-base superalloy at 650° C under marine-like environment conditions using three salt mixture (Na2SO4+ NaCl+ NaVO3)." Corrosion Science 105: 109-119.

Mannava, V., et al. (2019). "An investigation of oxidation/hot corrosion-creep interaction at 800° C in a Ni-base superalloy coated with salt mixture deposits of Na2SO4-NaCl-NaVO3." Corrosion Science 147: 283-298.

Mao, Z., et al. (2018). "Processing optimisation, mechanical properties and microstructural evolution during selective laser melting of Cu-15Sn high-tin bronze." Materials Science and Engineering: A 721: 125-134.

Mao, Z., et al. (2017). "Manufacturing feasibility and forming properties of Cu-4Sn in selective laser melting." Materials 10(4): 333.

Marcus, P., et al. (2008). "Localized corrosion (pitting): A model of passivity breakdown including the role of the oxide layer nanostructure." Corrosion Science 50(9): 2698-2704.

Marino, C. E., et al. (2001). "On the stability of thin-anodic-oxide films of titanium in acid phosphoric media." Corrosion Science 43(8): 1465-1476.

Maskery, I., et al. (2016). "Quantification and characterisation of porosity in selectively laser melted Al–Si10–Mg using X-ray computed tomography." Materials Characterization 111: 193-204.

Massoud, T., et al. (2013). "Nanoscale morphology and atomic structure of passive films on stainless steel." Journal of the electrochemical society 160(6): C232.

Maximenko, A. L. and E. A. Olevsky (2018). "Pore filling during selective laser melting-assisted additive manufacturing of composites." Scripta Materialia 149: 75-78.

Mazumder, J., et al. (1997). "The direct metal deposition of H13 tool steel for 3-D components." Jom 49(5): 55-60.

McCafferty, E. (2001). "Effect of ion implantation on the corrosion behavior of iron, stainless steels, and aluminum—a review." Corrosion 57(12): 1011-1029.

McLean, M. J. P. T. o. t. R. S. o. L. S. A. P. and E. Sciences (1995). "Nickel-base superalloys: current status and potential." 351(1697): 419-433.

Melia, M. A., et al. (2019). "Corrosion properties of 304L stainless steel made by directed energy deposition additive manufacturing." Corrosion Science 152: 20-30.

Meng, Q., et al. (2003). "Stainless-steel corrosion and MnS inclusions." Nature 424(6947): 389-390.

Mercelis, P. and J. P. Kruth (2006). "Residual stresses in selective laser sintering and selective laser melting." Rapid prototyping journal.

Mévrel, R. (1989). "State of the art on high-temperature corrosion-resistant coatings." Materials Science and Engineering: A 120: 13-24.

Mignanelli, P., et al. (2017). "Gamma-gamma prime-gamma double prime dual-superlattice superalloys." Scripta Materialia 136: 136-140.

Miller, J. T., et al. (2018). "Comparison of the effects of a sulfuric acid environment on traditionally manufactured and additive manufactured stainless steel 316L alloy." Additive Manufacturing 23: 272-286.

Milton, S., et al. (2016). "Influence of finish machining on the surface integrity of Ti6Al4V produced by Selective Laser Melting." Procedia CIRP 45: 127-130.

Miranda, G., et al. (2016). "Predictive models for physical and mechanical properties of 316L stainless steel produced by selective laser melting." Materials Science and Engineering: A 657: 43-56.

Mišković, Z., et al. (1992). "Microstructural investigation of IN 939 superalloy." Vacuum 43(5-7): 709-711.

Misra, A. (1986). "Mechanism of Na2 SO 4-Induced Corrosion of Molybdenum Containing Nickel-Base Superalloys at High Temperatures: I. Corrosion in Atmospheres Containing Only." Journal of the electrochemical society 133(5): 1029.

Misra, R., et al. (2013). "Understanding the impact of grain structure in austenitic stainless steel from a nanograined regime to a coarse-grained regime on osteoblast functions using a novel metal deformation–annealing sequence." Acta biomaterialia 9(4): 6245-6258.

Mohan, C. C., et al. (2015). "Nanotextured stainless steel for improved corrosion resistance and biological response in coronary stenting." Nanoscale 7(2): 832-841.

Montero Sistiaga, M., et al. (2016). Effect of heat treatment of 316L stainless steel produced by selective laser melting (SLM). Proceedings of the 27th Annual International Solid Freeform Fabrication Symposium-An Additive Manufacturing Conference.

Montero, X., et al. (2013). "Sulphidation Behavior of a Non Harmful Water-Based Al and Al–Si Slurry Coating on CM247 Superalloy." Oxidation of Metals 80(5-6): 635-649.

Montero, X., et al. (2020). "Effect of surface treatment and crystal orientation on hot corrosion of a Ni-based single-crystal superalloy." Corrosion Science 166: 108472.

Moradi, M., et al. (2019). "Nd: YAG laser hardening of AISI 410 stainless steel: Microstructural evaluation, mechanical properties, and corrosion behavior." Journal of Alloys and Compounds 795: 213-222.

Moradi, M. and M. KaramiMoghadam (2019). "High power diode laser surface hardening of AISI 4130; statistical modelling and optimization." Optics & Laser Technology 111: 554-570.

Mudgal, D., et al. (2014). "Hot corrosion behavior of some superalloys in a simulated incinerator environment at 900 C." Journal of materials engineering and performance 23(1): 238-249.

Mukherjee, T., et al. (2017). "An improved prediction of residual stresses and distortion in additive manufacturing." Computational Materials Science 126: 360-372.

Muley, S. V., et al. (2016). "An assessment of ultra fine grained 316L stainless steel for implant applications." Acta biomaterialia 30: 408-419.

Murata, Y., et al. (2000). Alloying effects on surface stability and creep strength of nickel based single crystal superalloys containing 12 mass% Cr. Ninth International Symposium on Superalloys.

Murr, L. E., et al. (2012). "Microstructures and properties of 17-4 PH stainless steel fabricated by selective laser melting." Journal of Materials Research and Technology 1(3): 167-177.

Muthu, S., et al. (2019). "Investigation of hot corrosion resistance of bare and Ni-20% Cr coated superalloy 825 to Na2SO4-60% V2O5 environment at 900° C." Procedia Structural Integrity 14: 290-303.

Nabavi, B., et al. (2019). "Metallurgical effects of nitrogen on the microstructure and hot corrosion behavior of Alloy 718 weldment." Materials Characterization 157: 109916.

Nakamori, M., et al. (1997). Hot corrosion and its prevention in high temperature heavy oil firing gas turbines. Materials science forum, Trans Tech Publ.

Navai, F. (1995). "Effects of tensile and compressive stresses on the passive layers formed on a type 302 stainless steel in a normal sulphuric acid bath." Journal of materials science 30(5): 1166-1172.

Nazarov, A., et al. (2017). "Effect of mechanical stress on the properties of steel surfaces: scanning Kelvin probe and local electrochemical impedance study." Journal of the electrochemical society 164(2): C66-C74.

Ngo, T. D., et al. (2018). "Additive manufacturing (3D printing): A review of materials, methods, applications and challenges." Composites Part B: Engineering 143: 172-196.

Ni, X.-q., et al. (2019). "Anisotropy in mechanical properties and corrosion resistance of 316L stainless steel fabricated by selective laser melting." International Journal of Minerals, Metallurgy, and Materials 26(3): 319-328.

Ni, X., et al. (2018). "Corrosion behavior of 316L stainless steel fabricated by selective laser melting under different scanning speeds." Journal of materials engineering and performance 27(7): 3667-3677.

Nicholls, J. (2000). "Designing oxidation-resistant coatings." Jom 52(1): 28-35.

Nurminen, J., et al. (2009). "Microstructure and properties of hard and wear resistant MMC coatings deposited by laser cladding." International Journal of Refractory Metals and Hard Materials 27(2): 472-478.

Oblak, J., et al. (1974). "An estimate of the strengthening arising from coherent, tetragonally-distorted particles." Materials Science and Engineering 13(1): 51-56.

Ochial, S., et al. (1984). "Alloying behaviour of Ni3Al, Ni3Ga, Ni3Si and Ni3Ge." Acta Metallurgica 32(2): 289-298.

Ojo, O., et al. (2004). "Contribution of constitutional liquation of gamma prime precipitate to weld HAZ cracking of cast Inconel 738 superalloy." Scripta Materialia 50(5): 641-646.

Okabe, S., et al. (2007). "Succession of sulfur-oxidizing bacteria in the microbial community on corroding concrete in sewer systems." Applied and environmental microbiology 73(3): 971-980.

Oksiuta, Z., et al. (2014). "Microstructure examination of Fe–14Cr ODS ferritic steels produced through different processing routes." Journal of Nuclear Materials 451(1-3): 320-327.

Olsson, C.-O. and D. Landolt (2003). "Passive films on stainless steels—chemistry, structure and growth." Electrochimica Acta 48(9): 1093-1104.

Örnek, C. (2018). "Additive manufacturing–a general corrosion perspective." Corrosion Engineering, Science and Technology 53(7): 531-535.

Örnek, C. and D. Engelberg (2016). "Towards understanding the effect of deformation mode on stress corrosion cracking susceptibility of grade 2205 duplex stainless steel." Materials Science and Engineering: A 666: 269-279.

Örnek, C., et al. (2016). "Atmospheric-induced stress corrosion cracking of grade 2205 duplex stainless steel—effects of 475 C embrittlement and process orientation." Metals 6(7): 167.

Otero, E., et al. (1998). "Corrosion behaviour of AISI 304L and 316L stainless steels prepared by powder metallurgy in the presence of sulphuric and phosphoric acid." Corrosion Science 40(8): 1421-1434.

Otero, E., et al. (1995). "Influence of microstructure on the corrosion resistance of AISI type 304L and type 316L sintered stainless steels exposed to ferric chloride solution." Materials Characterization 35(3): 145-151.

Otsuka, N. and R. A. Rapp (1990). "Hot Corrosion of Preoxidized Ni by a Thin Fused Na2 SO 4 Film at 900° C." Journal of the electrochemical society 137(1): 46.

Padilha, A. F., et al. (2006). Stainless steel heat treatment. Steel Heat Treatment, CRC Press: 706-751.

Pakseresht, A., et al. (2016). "Spark plasma sintering of a multilayer thermal barrier coating on Inconel 738 superalloy: microstructural development and hot corrosion behavior." Ceramics International 42(2): 2770-2779.

Park, C., et al. (2019). "Influence of laser surface engineering of AISI P20-improved mold steel on wear and corrosion behaviors." Surface and Coatings Technology 377: 124852.

Pérez, F., et al. (2001). "Effect of fluidized bed CVD aluminide coatings on the cyclic oxidation of austenitic AISI 304 stainless steel." Surface and Coatings Technology 145(1-3): 1-7.

Peters, K., et al. (1976). "Oxidation and hot corrosion of nickel-based alloys containing molybdenum." Corrosion Science 16(11): 791-804.

Pettit, F. (2011). "Hot corrosion of metals and alloys." Oxidation of Metals 76(1-2): 1-21.

Pettit, F., et al. (1984). "Oxidation and hot corrosion of superalloys." Superalloys 85: 651-687.

Pettit, F., et al. (1984). "Oxidation and hot corrosion of superalloys." 85: 651-687.

Peyre, P., et al. (2007). "Influence of thermal and mechanical surface modifications induced by laser shock processing on the initiation of corrosion pits in 316L stainless steel." Journal of materials science 42(16): 6866-6877.

Peyre, P., et al. (2000). "Surface modifications induced in 316L steel by laser peening and shot-peening. Influence on pitting corrosion resistance." Materials Science and Engineering: A 280(2): 294-302.

Pham, D. and S. Dimov (2001). Rapid prototyping processes. Rapid Manufacturing, Springer: 19-42.

Pieraggi, B. (1987). "Effect of creep or low cycle fatigue on the oxidation or hot corrosion behaviour of nickel-base superalloys." Materials Science and Engineering 88: 199-204.

Pinkerton, A., et al. (2008). "Component repair using laser direct metal deposition." Proceedings of the Institution of Mechanical Engineers, Part B: Journal of Engineering Manufacture 222(7): 827-836.

Pisarek, M., et al. (2007). "The effect of hydrostatic extrusion on resistance of 316 austenitic stainless steel to pit nucleation." Electrochemistry communications 9(10): 2463-2466.

Pistorius, P. and G. Burstein (1992). "Metastable pitting corrosion of stainless steel and the transition to stability." Philosophical Transactions of the Royal Society of London. Series A: Physical and Engineering Sciences 341(1662): 531-559.

Pollock, T. M. and S. Tin (2006). "Nickel-based superalloys for advanced turbine engines: chemistry, microstructure and properties." Journal of propulsion and power 22(2): 361-374.

Popovich, A., et al. (2017). "Anisotropy of mechanical properties of products manufactured using selective laser melting of powdered materials." Russian Journal of Non-Ferrous Metals 58(4): 389-395.

Pottlacher, G., et al. (2002). "Thermophysical properties of solid and liquidInconel 718 Alloy." Scandinavian Journal of Metallurgy 31(3): 161-168.

Poza, P., et al. (2014). "Mechanical properties of Inconel 625 cold-sprayed coatings after laser remelting. Depth sensing indentation analysis." Surface and Coatings Technology 243: 51-57.

Pradhan, D., et al. (2018). "Effect of pre hot corrosion on high cycle fatigue behavior of the superalloy IN718 at 600 C." International Journal of Fatigue 114: 120-129.

Pradhan, D., et al. (2018). "Effect of surface roughness on corrosion behavior of the superalloy IN718 in simulated marine environment." Journal of Alloys and Compounds 740: 250-263.

Pradhan, D., et al. (2018). "Severe Hot Corrosion of the Superalloy IN718 in Mixed Salts of Na 2 SO 4 and V 2 O 5 at 700° C." Journal of materials engineering and performance 27(8): 4235-4243.

Pradhan, S., et al. (2018). "Individual and synergistic influences of microstructural features on intergranular corrosion behavior in extra-low carbon type 304L austenitic stainless steel." Corrosion Science 139: 319-332.

Prashanth, K., et al. (2017). "Friction welding of selective laser melted Ti6Al4V parts." Materials Science and Engineering: A 704: 66-71.

Prashar, G. and H. Vasudev (2020). "Hot corrosion behavior of super alloys." Materials Today: Proceedings.

Prescott, R., et al. (1993). A SIMS study of the effect of Y and Zr on the growth of oxide on p-NiAl. Proc. 2nd Int. Conf. Microscopy of Oxidation.

Pridantsev, M. and F. Levin (1966). "Effect of manganese on the structure and properties of nonmagnetic stainless steels." Metal Science and Heat Treatment 7(12): 786-789.

Prieto, C., et al. (2019). "Investigation of Pitting Corrosion Initiation and Propagation of a Type 316L Stainless Steel Manufactured by the Direct Metal Laser Sintering Process." Corrosion 75(2): 140-143.

Pujadó, M. P. (2012). Carbon nanotubes as platforms for biosensors with electrochemical and electronic transduction, Springer Science & Business Media.

Qiao, M. and C. Zhou (2012). "Hot corrosion behavior of Co modified NiAl coating on nickel base superalloys." Corrosion Science 63: 239-245.

Qiu, C., et al. (2015). "On the role of melt flow into the surface structure and porosity development during selective laser melting." Acta Materialia 96: 72-79.

Rahimi, M., et al. (2012). "Heat treatment of aluminum in preparing porous anodic alumina templates." Micro & Nano Letters 7(2): 125-129.

Rahman, A., et al. (2011). "Study of cyclic hot corrosion of nanostructured Cr/Co–Al coatings on superalloy." Materials Chemistry and Physics 126(1-2): 253-261.

Rahman, M. S., et al. (2009). "Characterization of high temperature deformation behavior of INCONEL 617." Mechanics of Materials 41(3): 261-270.

Raiman, S. S., et al. (2017). "Radiolysis driven changes to oxide stability during irradiation-corrosion of 316L stainless steel in high temperature water." Journal of Nuclear Materials 493: 40-52.

Raj, B., et al. (1995). "Non-destructive testing and evaluation for structural integrity." Sadhana 20(1): 5-38.

Ralston, K., et al. (2010). "Revealing the relationship between grain size and corrosion rate of metals." Scripta Materialia 63(12): 1201-1204.

Ramakrishnan, A. and G. Dinda (2019). "Direct laser metal deposition of Inconel 738." Materials Science and Engineering: A 740: 1-13.

Ramkumar, K. D., et al. (2017). "Investigations on the microstructure, tensile strength and high temperature corrosion behaviour of Inconel 625 and Inconel 718 dissimilar joints." Journal of Manufacturing Processes 25: 306-322.

Ramkumar, K. D., et al. (2017). "Effect of Mo-rich fillers in pulsed current gas tungsten arc welding of Inconel 718 for improved strength and hot corrosion resistance." Journal of materials engineering and performance 26(11): 5620-5640.

Randle, V. (2010). "Grain boundary engineering: an overview after 25 years." Materials Science and Technology 26(3): 253-261.

Rapp, R. A. (1986). "Chemistry and electrochemistry of the hot corrosion of metalls." Corrosion (Houston, Tex.) 42(10): 568-577.

Rapp, R. A. (1987). "Chemistry and electrochemistry of hot corrosion of metals." Materials Science and Engineering 87: 319-327.

Rapp, R. A. (2002). "Hot corrosion of materials: a fluxing mechanism?" Corrosion Science 44(2): 209-221.

Rapp, R. A. and Y.-S. Zhang (1994). "Hot corrosion of materials: fundamental studies." Jom 46(12): 47-55.

Reclaru, L., et al. (2001). "Corrosion behavior of a welded stainless-steel orthopedic implant." Biomaterials 22(3): 269-279.

Reed, R. (1983). "American Society for Metals, Metals Park, Ohio." Materials at low temperatures 154.

Reed, R. C. (2008). The superalloys: fundamentals and applications, Cambridge university press.

Reid, W. T. (1971). "External corrosion and deposits: boilers and gas turbines."

Ren, X., et al. (2005). "High-temperature oxidation and hot corrosion behaviors of the NiCr–CrAl coating on a nickel-based superalloy." Surface and Coatings Technology 198(1-3): 425-431.

Robbiola, L., et al. (2008). "Characterisation of anodic layers on Cu–10Sn bronze (RDE) in aerated NaCl solution." Corrosion Science 50(8): 2205-2215.

Roland, T., et al. (2006). "Fatigue life improvement through surface nanostructuring of stainless steel by means of surface mechanical attrition treatment." Scripta Materialia 54(11): 1949-1954.

Ryan, M. P., et al. (2002). "Why stainless steel corrodes." Nature 415(6873): 770-774.

Saeidi, K., et al. (2015). "Hardened austenite steel with columnar sub-grain structure formed by laser melting." Materials Science and Engineering: A 625: 221-229.

Safdar, A., et al. (2012). "Evaluation of microstructural development in electron beam melted Ti-6Al-4V." Materials Characterization 65: 8-15.

Sailer, I., et al. (2009). "A systematic review of the performance of ceramic and metal implant abutments supporting fixed implant reconstructions." Clinical oral implants research 20: 4-31.

Saladi, S., et al. (2014). "Hot Corrosion Behaviour of Detonation-Gun Sprayed Cr 3 C 2–NiCr Coating on Inconel-718 in Molten Salt Environment at 900° C." Transactions of the Indian Institute of Metals 67(5): 623-627.

Saladi, S., et al. (2015). "Characterization and evaluation of cyclic hot corrosion resistance of detonation-gun sprayed Ni-5Al coatings on Inconel-718." Journal of Thermal Spray Technology 24(5): 778-788.

Salehnasab, B., et al. (2016). "Hot corrosion failure in the first stage nozzle of a gas turbine engine." Engineering failure analysis 60: 316-325.

Salehnasab, B., et al. (2016). "Hot corrosion failure in the first stage nozzle of a gas turbine engine." 60: 316-325.

Sallica-Leva, E., et al. (2016). "Ductility improvement due to martensite α′ decomposition in porous Ti–6Al–4V parts produced by selective laser melting for orthopedic implants." Journal of the mechanical behavior of biomedical materials 54: 149-158.

Salman, O., et al. (2019). "Effect of heat treatment on microstructure and mechanical properties of 316L steel synthesized by selective laser melting." Materials Science and Engineering: A 748: 205-212.

Sames, W. J., et al. (2016). "The metallurgy and processing science of metal additive manufacturing." International materials reviews 61(5): 315-360.

Sander, G., et al. (2018). "Corrosion of additively manufactured alloys: a review." Corrosion 74(12): 1318-1350.

Sander, G., et al. (2017). "On the corrosion and metastable pitting characteristics of 316L stainless steel produced by selective laser melting." Journal of the electrochemical society 164(6): C250.

Sander, G., et al. (2017). "On the corrosion and metastable pitting characteristics of 316L stainless steel produced by selective laser melting." Journal of the electrochemical society 164(6): C250-C257.

Santoro, G., et al. (1984). "Deposition of Na2SO4 from salt-seeded combustion gases of a high velocity burner rig."

Santos, E. C., et al. (2006). "Rapid manufacturing of metal components by laser forming." International Journal of Machine Tools and Manufacture 46(12-13): 1459-1468.

Saroj, S., et al. (2017). "Microstructure and mechanical performance of TiC-Inconel825 composite coating deposited on AISI 304 steel by TIG cladding process." Journal of Materials Processing Technology 249: 490-501.

Šatović, D., et al. (2009). "Corrosion evaluation and surface characterization of the corrosion product layer formed on Cu–6Sn bronze in aqueous Na2SO4 solution." Corrosion Science 51(8): 1596-1603.

Saunders, N. and A. P. Miodownik (1998). CALPHAD (calculation of phase diagrams): a comprehensive guide, Elsevier.

Schajer, G. S. (2013). Practical residual stress measurement methods, John Wiley & Sons.

Schaller, R. F., et al. (2018). "The role of microstructure and surface finish on the corrosion of selective laser melted 304L." Journal of the electrochemical society 165(5): C234.

Schaller, R. F., et al. (2017). "Corrosion properties of powder bed fusion additively manufactured 17-4 PH stainless steel." Corrosion 73(7): 796-807.

Schneibel, J. H. and S. Shim (2008). "Nano-scale oxide dispersoids by internal oxidation of Fe–Ti–Y intermetallics." Materials Science Engineering: A 488(1-2): 134-138.

Scudino, S., et al. (2015). "Additive manufacturing of Cu–10Sn bronze." Materials Letters 156: 202-204.

Sedriks, A. J. (1996). "Corrosion of stainless steel, 2."

Semiatin, S., et al. (2003). "Microstructure evolution during alpha-beta heat treatment of Ti-6Al-4V." Metallurgical and Materials Transactions A 34(10): 2377-2386.

Semiatin, S., et al. (2005). "Prediction of the kinetics of static globularization of Ti-6Al-4V." Metallurgical and Materials Transactions A 36(5): 1372-1376.

Shahryari, A., et al. (2008). "The effect of surface roughness on the efficiency of the cyclic potentiodynamic passivation (CPP) method in the improvement of general and pitting corrosion resistance of 316LVM stainless steel." Materials Letters 62(23): 3906-3909.

Shaikh, A. S. (2018). Development of γ'Precipitation Hardening Ni-Base Superalloy for Additive Manufacturing.

Shao, J., et al. (2019). "Grain size evolution under different cooling rate in laser additive manufacturing of superalloy." Optics & Laser Technology 119: 105662.

Shifeng, W., et al. (2014). "Effect of molten pool boundaries on the mechanical properties of selective laser melting parts." Journal of Materials Processing Technology 214(11): 2660-2667.

Shih, C.-C., et al. (2004). "Effect of surface oxide properties on corrosion resistance of 316L stainless steel for biomedical applications." Corrosion Science 46(2): 427-441.

Shih, S., et al. (1989). "Sub-melting point hot corrosion of alloys and coatings." Materials Science and Engineering: A 120: 277-282.

Shiomi, M., et al. (2004). "Residual stress within metallic model made by selective laser melting process." CIRP Annals 53(1): 195-198.

Sidhu, R., et al. (2007). "Weld cracking in directionally solidified Inconel 738 superalloy." Canadian Metallurgical Quarterly 46(4): 415-424.

Sidhu, T., et al. (2005). "Hot corrosion of some superalloys and role of high-velocity oxy-fuel spray coatings—a review." Surface and Coatings Technology 198(1-3): 441-446.

Sidhu, T., et al. (2006). "Hot corrosion behaviour of HVOF-sprayed NiCrBSi coatings on Ni-and Fe-based superalloys in Na2SO4–60% V2O5 environment at 900° C." Acta Materialia 54(3): 773-784.

Sidhu, T., et al. (2006). "Hot corrosion studies of HVOF NiCrBSi and Stellite-6 coatings on a Ni-based superalloy in an actual industrial environment of a coal fired boiler." Surface and Coatings Technology 201(3-4): 1602-1612.

Sidhu, T., et al. (2006). "Characterizations and hot corrosion resistance of Cr 3 C 2-NiCr coating on Ni-base superalloys in an aggressive environment." 15(4): 811-816.

Sidot, E., et al. (2006). "Study of the corrosion behaviour of Cu–10Sn bronze in aerated Na2SO4 aqueous solution." Corrosion Science 48(8): 2241-2257.

Silverstein, R. and D. Eliezer (2018). "Hydrogen trapping in 3D-printed (additive manufactured) Ti-6Al-4V." Materials Characterization 144: 297-304.

Sims, C. T. and W. C. Hagel (1972). The Superalloys-vital high temperature gas turbine materials for aerospace and industrial power, John Wiley & Sons.

Sims, C. T., et al. (1987). superalloys II, Wiley New York.

Simson, T., et al. (2017). "Residual stress measurements on AISI 316L samples manufactured by selective laser melting." Additive Manufacturing 17: 183-189.

Singh, H., et al. (2005). "Studies of plasma spray coatings on a Fe-base superalloy, their structure and high temperature oxidation behaviour." Anti-Corrosion Methods and Materials.

Singh, H., et al. (2007). "An overview of Na 2 SO 4 and/or V 2 O 5 induced hot corrosion of Fe-and Ni-based superalloys." Rev. Adv. Mater. Sci 16(1-2): 27-50.

Sitek, R., et al. (2016). "Experimental and ab-initio study of the Zr-and Cr-enriched aluminide layer produced on an IN 713C Inconel substrate by CVD; investigations of the layer morphology, structural stability, mechanical properties, and corrosion resistance." Intermetallics 74: 15-24.

Sjöberg, G., et al. (2004). "Evaluation of the in 939 alloy for large aircraft engine structures." Superalloys [Internet]: 441-450.

Sjöberg, G., et al. (2004). "Evaluation of the in 939 alloy for large aircraft engine structures." 441-450.

Slama, C. and M. Abdellaoui (2000). "Structural characterization of the aged Inconel 718." Journal of Alloys and Compounds 306(1-2): 277-284.

Sluiter, M. H. and Y. Kawazoe (1995). "Site preference of ternary additions in Ni 3 Al." Physical Review B 51(7): 4062.

Smith, J. S. and K. A. Heck (1996). Development of low thermal expansion, crack growth resistant superalloy. Proceedings of the Eighth International Symposium on Superalloys, TMS, Seven Springs, PA.

Song, J., et al. (2010). "Simultaneous synthesis by spark plasma sintering of a thermal barrier coating system with a NiCrAlY bond coat." Surface and Coatings Technology 205(5): 1241-1244.

Soro, N., et al. (2019). "Investigation of the structure and mechanical properties of additively manufactured Ti-6Al-4V biomedical scaffolds designed with a Schwartz primitive unit-cell." Materials Science and Engineering: A 745: 195-202.

Souissi, N., et al. (2007). "Corrosion behaviour of Cu–10Sn bronze in aerated NaCl aqueous media–electrochemical investigation." Corrosion Science 49(8): 3333-3347.

SPEX Sampleprep (2010). 8000M MIXER/MILL. Metuchen, NJ: 4.

Sreedhar, G., et al. (2009). "Hot corrosion behaviour of plasma sprayed YSZ/Al2O3 dispersed NiCrAlY coatings on Inconel-718 superalloy." Surface and Coatings Technology 204(3): 291-299.

Stahle, R., et al. (1979). "Stress corrosion cracking and hydrogen embrittlement of iron base alloys." Journal of the electrochemical society 126(5): 215C-215C.

Stefansson, N., et al. (2002). "The kinetics of static globularization of Ti-6Al-4V." Metallurgical and Materials Transactions A 33(11): 3527-3534.

Stellwag, B. (1998). "The mechanism of oxide film formation on austenitic stainless steels in high temperature water." Corrosion Science 40(2-3): 337-370.

Stewart, J. and D. Williams (1992). "The initiation of pitting corrosion on austenitic stainless steel: on the role and importance of sulphide inclusions." Corrosion Science 33(3): 457-474.

Stoloff, N. (1990). "Wrought and P/M superalloys." ASM International, Metals Handbook. Tenth Edition. 1: 950-977.

Stott, F. (1987). "The protective action of oxide scales in gaseous environments at high temperature." Reports on Progress in Physics 50(7): 861.

Strano, G., et al. (2013). "Surface roughness analysis, modelling and prediction in selective laser melting." Journal of Materials Processing Technology 213(4): 589-597.

Stringer, J. (1977). "Hot corrosion of high-temperature alloys." Annual Review of Materials Science 7(1): 477-509.

Stringer, J. (1987). "High-temperature corrosion of superalloys." Materials Science and Technology 3(7): 482-493.

Strondl, A., et al. (2015). "Characterization and control of powder properties for additive manufacturing." Jom 67(3): 549-554.

Suárez, M., et al. (2013). "Challenges and opportunities for spark plasma sintering: a key technology for a new generation of materials." Sintering Applications 13: 319-342.

Sudbrack, C. K., et al. (2015). "Effect of surface preparation on the 815° C oxidation of single-crystal nickel-based superalloys." Jom 67(11): 2589-2598.

Sudhangshu, B. (2007). "High temperature coatings." Publisher: Elsevier Science & Technology Books 301: 301.

SUN, H.-q., et al. (2005). "Cracking Sensitivity on Laser Cladding Inconel 738 on Directionally Solidified Ni-base Superalloy [J]." Journal of Aeronautical Materials 2.

Sun, J., et al. (2018). "Oxidation behaviour of Pt modified aluminized NiCrAlYSi coating on a Ni-based single crystal superalloy." Corrosion Science 139: 172-184.

Sun, M., et al. (2009). "Oxidation of 316 stainless steel in supercritical water." Corrosion Science 51(5): 1069-1072.

Sun, S., et al. (2017). Powder bed fusion processes: An overview. Laser Additive Manufacturing, Elsevier: 55-77.

Sun, Y., et al. (2014). "Sliding wear characteristics and corrosion behaviour of selective laser melted 316L stainless steel." Journal of materials engineering and performance 23(2): 518-526.

Sun, Z., et al. (2016). "Selective laser melting of stainless steel 316L with low porosity and high build rates." Materials & Design 104: 197-204.

Sundararaman, M., et al. (1988). "Precipitation of the δ-Ni 3 Nb phase in two nickel base superalloys." Metallurgical transactions A 19(3): 453-465.

Suresh, G., et al. (2017). "Effect of laser surface melting on the microstructure and pitting corrosion resistance of 304L SS weldment." Metallurgical and Materials Transactions B 48(5): 2516-2525.

Suresh, S. (2001). "Graded materials for resistance to contact deformation and damage." Science 292(5526): 2447-2451.

Suryawanshi, J., et al. (2018). "On the corrosion resistance of some selective laser melted alloys." Materialia 3: 153-161.

Suryawanshi, J., et al. (2017). "Mechanical behavior of selective laser melted 316L stainless steel." Materials Science and Engineering: A 696: 113-121.

Sutton, A. T., et al. (2017). "Powder characterisation techniques and effects of powder characteristics on part properties in powder-bed fusion processes." Virtual and physical prototyping 12(1): 3-29.

Suzuki, M., et al. (2001). "Inclusion particle growth during solidification of stainless steel." ISIJ international 41(3): 247-256.

Swaminathan, J., et al. (1993). "Studies on the Hot Corrosion of Some Nickel-Base Superalloys by Vanadium Pentoxide." Transactions of the Indian Institute of Metals(India) 46(3): 175-181.

Takakuwa, O. and H. Soyama (2014). "Effect of residual stress on the corrosion behavior of austenitic stainless steel." Advances in chemical engineering and science 5(01): 62.

Tamilselvi, S., et al. (2006). "Corrosion behaviour of Ti–6Al–7Nb and Ti–6Al–4V ELI alloys in the simulated body fluid solution by electrochemical impedance spectroscopy." Electrochimica Acta 52(3): 839-846.

Tan, F.-B., et al. (2019). "Titanium clasp fabricated by selective laser melting, CNC milling, and conventional casting: a comparative in vitro study." Journal of prosthodontic research 63(1): 58-65.

Tan, L., et al. (2008). "Corrosion behavior of Ni-base alloys for advanced high temperature water-cooled nuclear plants." Corrosion Science 50(11): 3056-3062.

Tang, F., et al. (2004). "Influence of cryomilling on the morphology and composition of the oxide scales formed on HVOF CoNiCrAlY coatings." Oxidation of Metals 61(3-4): 219-238.

Task, M. N., et al. (2011). "Compositional effects on the Type I hot corrosion of β-NiAl alloys." Surface and Coatings Technology 206(7): 1552-1557.

Tawancy, H., et al. (1992). "Effect of substrate composition on the oxidation behavior of platinum-aluminized nickel-base superalloys." Surface and Coatings Technology 54: 1-7.

Tawancy, H., et al. (1992). "Thermal stability of a platinum aluminide coating on nickel-based superalloys." Journal of materials science 27(23): 6463-6474.

Terachi, T., et al. (2008). "Corrosion behavior of stainless steels in simulated PWR primary water—effect of chromium content in alloys and dissolved hydrogen—." Journal of nuclear science and technology 45(10): 975-984.

Thomsen, P., et al. (2009). "Electron beam-melted, free-form-fabricated titanium alloy implants: Material surface characterization and early bone response in rabbits." Journal of Biomedical Materials Research Part B: Applied Biomaterials 90(1): 35-44.

Tian, Y., et al. (2017). "Influences of processing parameters on surface roughness of Hastelloy X produced by selective laser melting." Additive Manufacturing 13: 103-112.

Tikhonova, M., et al. (2016). Submicrocrystalline austenitic stainless steel processed by cold or warm high pressure torsion. Materials Science Forum, Trans Tech Publ.

Tolosa, I., et al. (2010). "Study of mechanical properties of AISI 316 stainless steel processed by "selective laser melting", following different manufacturing strategies." The International Journal of Advanced Manufacturing Technology 51(5): 639-647.

Tolosa, I., et al. (2010). "Study of mechanical properties of AISI 316 stainless steel processed by "selective laser melting", following different manufacturing strategies." The International Journal of Advanced Manufacturing Technology 51(5-8): 639-647.

Tomeczek, J., et al. (2004). "Modelling of deposits formation on heating tubes in pulverized coal boilers." Fuel 83(2): 213-221.

Tomus, D., et al. (2016). "Influence of post heat treatments on anisotropy of mechanical behaviour and microstructure of Hastelloy-X parts produced by selective laser melting." Materials Science and Engineering: A 667: 42-53.

Touloukian, Y. S., et al. (1970). Thermophysical properties of matter-the tprc data series. volume 1. thermal conductivity-metallic elements and alloys, THERMOPHYSICAL AND ELECTRONIC PROPERTIES INFORMATION ANALYSIS CENTER ….

Toyserkani, E., et al. (2004). Laser cladding, CRC press.

Trelewicz, J. R., et al. (2016). "Microstructure and corrosion resistance of laser additively manufactured 316L stainless steel." Jom 68(3): 850-859.

Triantaphyllou, A., et al. (2015). "Surface texture measurement for additive manufacturing." Surface Topography: Metrology and Properties 3(2): 024002.

Turnbull, A., et al. (2011). "Sensitivity of stress corrosion cracking of stainless steel to surface machining and grinding procedure." Corrosion Science 53(10): 3398-3415.

Ünlü, B. S. and E. Atik (2010). "Evaluation of effect of alloy elements in copper based CuSn10 and CuZn30 bearings on tribological and mechanical properties." Journal of Alloys and Compounds 489(1): 262-268.

Valente, E. H., et al. (2019). The Effect of Heat Treatment and Surface Hardening of 3D Printed Austenitic Stainless Steel AISI316l on Corrosion and Wear Properties. ESSC & DUPLEX 2019.

Valiev, R. Z., et al. (2006). "Producing bulk ultrafine-grained materials by severe plastic deformation." Jom 58(4): 33-39.

Valle, L., et al. (2019). "The influence of heat treatments on the corrosion behaviour of nickel-based alloy 718." Journal of Alloys and Compounds 809: 151781.

Van Boven, G., et al. (2007). "The role of residual stress in neutral pH stress corrosion cracking of pipeline steels. Part I: Pitting and cracking occurrence." Acta Materialia 55(1): 29-42.

Vasquez, E., et al. (2019). "Elaboration of oxide dispersion strengthened Fe-14Cr stainless steel by selective laser melting." Journal of Materials Processing Technology 267: 403-413.

Ventura, A. P., et al. (2017). "Mechanical properties and microstructural characterization of Cu-4.3 Pct Sn fabricated by selective laser melting." Metallurgical and Materials Transactions A 48(1): 178-187.

Verlee, B., et al. (2012). "Density and porosity control of sintered 316L stainless steel parts produced by additive manufacturing." Powder Metallurgy 55(4): 260-267.

Vignal, V., et al. (2013). "Passive properties of lean duplex stainless steels after long-term ageing in air studied using EBSD, AES, XPS and local electrochemical impedance spectroscopy." Corrosion Science 67: 109-117.

Vignal, V., et al. (2007). "The use of local electrochemical probes and surface analysis methods to study the electrochemical behaviour and pitting corrosion of stainless steels." Electrochimica Acta 52(15): 4994-5001.

Vilaro, T., et al. (2011). "As-fabricated and heat-treated microstructures of the Ti-6Al-4V alloy processed by selective laser melting." Metallurgical and Materials Transactions A 42(10): 3190-3199.

Viswanathan, R. (1987). "Corrosion of combustion turbines." Metals handbook 13: 999-1001.

Viswanathan, R., et al. (2005). "US program on materials technology for ultra-supercritical coal power plants." Journal of materials engineering and performance 14(3): 281-292.

Volovitch, P., et al. (2008). "Microstructure and corrosion resistance of magnesium alloy ZE41 with laser surface cladding by Al–Si powder." Surface and Coatings Technology 202(20): 4901-4914.

Vrancken, B., et al. (2012). "Heat treatment of Ti6Al4V produced by Selective Laser Melting: Microstructure and mechanical properties." Journal of Alloys and Compounds 541: 177-185.

Walker, J. C., et al. (2009). "Fabrication of Fe–Cr–Al oxide dispersion strengthened PM2000 alloy using selective laser melting." Advanced Engineering Materials 11(7): 541-546.

Wang, B., et al. (2002). "Oxidation behaviour of NiCrAlY coatings on Ni-based superalloy." Surface and Coatings Technology 149(1): 70-75.

Wang, B., et al. (2000). "Evolution of element distribution in Ni-Cr-Al-Y coating before and after vacuum heat treatment." ACTA METALLURGICA SINICA-CHINESE EDITION- 36(10): 1094-1098.

Wang, C.-J. and S.-M. Chen (2006). "Microstructure and cyclic oxidation behavior of hot dip aluminized coating on Ni-base superalloy Inconel 718." Surface and Coatings Technology 201(7): 3862-3866.

Wang, D., et al. (2016). "Theoretical and experimental study on surface roughness of 316L stainless steel metal parts obtained through selective laser melting." Rapid prototyping journal.

Wang, G., et al. (2020). "Influence of porosity and microstructure on mechanical and corrosion properties of a selectively laser melted stainless steel." Journal of Alloys and Compounds: 154815.

Wang, K., et al. (2011). "High performance environmental barrier coatings, Part II: Active filler loaded SiOC system for superalloys." Journal of the European Ceramic Society 31(15): 3011-3020.

Wang, L., et al. (2008). "Optimization of the LENS® process for steady molten pool size." Materials Science and Engineering: A 474(1-2): 148-156.

Wang, L., et al. (2017). "Effect of sodium chloride on the electrochemical corrosion of Inconel 625 at high temperature and pressure." Journal of Alloys and Compounds 703: 523-529.

Wang, M., et al. (2016). "Fabrication and characterization of selective laser melting printed Ti–6Al–4V alloys subjected to heat treatment for customized implants design." Progress in Natural Science: Materials International 26(6): 671-677.

Wang, Y., et al. (1995). "The cyclic creep behaviour of nickel base superalloy IN738LC." Zeitschrift fur Metallkunde 86(5): 365-370.

Warnes, B. M. and D. C. Punola (1997). "Clean diffusion coatings by chemical vapor deposition." Surface and Coatings Technology 94: 1-6.

Was, G. S., et al. (2011). "Irradiation-assisted stress corrosion cracking." Corrosion Reviews 29(1-2): 7-49.

Washko, S. and G. Aggen (1990). ASM Handbook: Wrought Stainless Steels, Properties and Selection: Irons, Steels, and High-Performance Alloys, Ohio: ASM International.

Wataha, J. C., et al. (2001). "Relating nickel-induced tissue inflammation to nickel release in vivo." Journal of Biomedical Materials Research: An Official Journal of The Society for Biomaterials, The Japanese Society for Biomaterials, and The Australian Society for Biomaterials and the Korean Society for Biomaterials 58(5): 537-544.

Wen, H., et al. (2019). "Laser surface treatment of Ti-10Mo alloy under Ar and N2 environment for biomedical application." Journal of Laser Applications 31(2): 022012.

Wijesinghe, T. S. L. and D. J. Blackwood (2007). "Real time pit initiation studies on stainless steels: the effect of sulphide inclusions." Corrosion Science 49(4): 1755-1764.

Williams, D. E., et al. (2010). "Composition changes around sulphide inclusions in stainless steels, and implications for the initiation of pitting corrosion." Corrosion Science 52(11): 3702-3716.

Wilson, J. M. and Y. C. Shin (2012). "Microstructure and wear properties of laser-deposited functionally graded Inconel 690 reinforced with TiC." Surface and Coatings Technology 207: 517-522.

Wind, J., et al. (2002). "Metallic bipolar plates for PEM fuel cells." Journal of Power Sources 105(2): 256-260.

Withers, P. J. and H. Bhadeshia (2001). "Residual stress. Part 1–measurement techniques." Materials Science and Technology 17(4): 355-365.

Wolff, S., et al. (2016). "Anisotropic properties of directed energy deposition (DED)-processed Ti–6Al–4V." Journal of Manufacturing Processes 24: 397-405.

Wolverton, C. and D. De Fontaine (1994). "Site substitution of ternary additions to Ni 3 Al (γ') from electronic-structure calculations." Physical Review B 49(17): 12351.

Wong, K. V. and A. Hernandez (2012). "A review of additive manufacturing." International scholarly research notices 2012.

Wu, A. S., et al. (2014). "An experimental investigation into additive manufacturing-induced residual stresses in 316L stainless steel." Metallurgical and Materials Transactions A 45(13): 6260-6270.

Wu, J.-H. and C.-K. Lin (2002). "Tensile and fatigue properties of 17-4 PH stainless steel at high temperatures." Metallurgical and Materials Transactions A 33(6): 1715-1724.

Xiang, Z., et al. (2001). "Aluminide coating formation on nickel-base superalloys by pack cementation process." Journal of materials science 36(23): 5673-5682.

Xie, X., et al. (2008). A new improvement of Inconel alloy 740 for USC power plants. Proceedings from the Fifth International Conference on Advance in Materials Technology for Fossil Power Plants.

Xu, C., et al. (2007). "The evolution of homogeneity in processing by high-pressure torsion." Acta Materialia 55(1): 203-212.

Xu, W., et al. (2017). "In situ tailoring microstructure in additively manufactured Ti-6Al-4V for superior mechanical performance." Acta Materialia 125: 390-400.

Yadollahi, A., et al. (2017). "Effects of building orientation and heat treatment on fatigue behavior of selective laser melted 17-4 PH stainless steel." International Journal of Fatigue 94: 218-235.

Yadollahi, A., et al. (2015). "Effects of process time interval and heat treatment on the mechanical and microstructural properties of direct laser deposited 316L stainless steel." Materials Science and Engineering: A 644: 171-183.

Yadroitsev, I., et al. (2007). "Parametric analysis of the selective laser melting process." Applied Surface Science 253(19): 8064-8069.

Yadroitsev, I., et al. (2007). "Strategy of manufacturing components with designed internal structure by selective laser melting of metallic powder." Applied Surface Science 254(4): 980-983.

Yadroitsev, I. and I. Yadroitsava (2015). "Evaluation of residual stress in stainless steel 316L and Ti6Al4V samples produced by selective laser melting." Virtual and physical prototyping 10(2): 67-76.

Yakout, M., et al. (2017). "The selection of process parameters in additive manufacturing for aerospace alloys." The International Journal of Advanced Manufacturing Technology 92(5-8): 2081-2098.

Yakout, M., et al. (2018). "On the characterization of stainless steel 316L parts produced by selective laser melting." The International Journal of Advanced Manufacturing Technology 95(5-8): 1953-1974.

Yang, J., et al. (2016). "Formation and control of martensite in Ti-6Al-4V alloy produced by selective laser melting." Materials & Design 108: 308-318.

Yang, K. and Y. Ren (2010). "Nickel-free austenitic stainless steels for medical applications." Science and Technology of advanced MaTerialS.

Yang, X., et al. (2015). "Effect of high-temperature hot corrosion on the low cycle fatigue behavior of a directionally solidified nickel-base superalloy." International Journal of Fatigue 70: 106-113.

Yanqiu, Y., et al. (2020). "Effect of crystallographic orientation on the corrosion resistance of Ni-based single crystal superalloys." Corrosion Science: 108643.

Yao, H., et al. (2018). Defects Evaluation of Selective Laser Melting Stainless Steel 316 Parts Using Positron Annihilation Lifetime Measurement. ASME International Mechanical Engineering Congress and Exposition, American Society of Mechanical Engineers.

Yap, C. Y., et al. (2015). "Review of selective laser melting: Materials and applications." Applied physics reviews 2(4): 041101.

Yasa, E. and J.-P. Kruth (2011). "Microstructural investigation of Selective Laser Melting 316L stainless steel parts exposed to laser re-melting." Procedia Engineering 19: 389-395.

Yeh, T.-K., et al. (2014). "Corrosion of Alloy 617 in high-temperature gas environments." Nuclear Engineering and Design 271: 257-261.

Yoshiba, M. J. C. S. (1993). "Effect of hot corrosion on the mechanical performances of superalloys and coating systems." 35(5-8): 1115-1124.

Young, D. J., et al. (2014). "Penetration of protective chromia scales by carbon." Scripta Materialia 77: 29-32.

Yu, Z., et al. (2019). "Corrosion behavior of GH4169 alloy under alternating oxidation at 900 C and solution immersion." Materials 12(9): 1503.

Yuan, L. and H. Wang (2010). "Hot corrosion behaviors of a Cr13Ni5Si2-based metal silicide alloy in Na2SO4+ 25 wt.% K2SO4 and Na2SO4+ 25 wt.% NaCl molten salts." Intermetallics 18(3): 324-329.

Yusuf, S. M., et al. (2017). "Investigation on porosity and microhardness of 316L stainless steel fabricated by selective laser melting." Metals 7(2): 64.

Yusuf, S. M., et al. (2020). "Microstructural evolution and strengthening of selective laser melted 316L stainless steel processed by high-pressure torsion." Materials Characterization 159: 110012.

Yusuf, S. M. and N. Gao (2017). "Influence of energy density on metallurgy and properties in metal additive manufacturing." Materials Science and Technology 33(11): 1269-1289.

Yusuf, S. M., et al. (2018). "Microstructure and corrosion performance of 316L stainless steel fabricated by selective laser melting and processed through high-pressure torsion." Journal of Alloys and Compounds 763: 360-375.

Zaeh, M. F. and G. Branner (2010). "Investigations on residual stresses and deformations in selective laser melting." Production Engineering 4(1): 35-45.

Zeng, C., et al. (2020). "Laser nitriding of titanium surfaces for biomedical applications." Surface and Coatings Technology 385: 125397.

Zeng, C., et al. (2020). "Mechanical, thermal, and corrosion properties of Cu-10Sn alloy prepared by laser-powder-bed-fusion additive manufacturing." Additive Manufacturing 35: 101411.

Zeng, C., et al. (2020). "Mechanical, Thermal, and Corrosion Properties of Cu-10Sn Alloy Prepared by Laser-Powder-Bed-Fusion Additive Manufacturing." Additive Manufacturing: 101411.

Zhang, B., et al. (2019). "Grain-size affected mechanical response and deformation behavior in microscale reverse extrusion." Materialia 6: 100272.

Zhang, C., et al. (2017). "Multi-layer functional graded stainless steel fabricated by laser melting deposition." Vacuum 141: 181-187.

Zhang, H., et al. (2018). "Effect of Ni content on stainless steel fabricated by laser melting deposition." Optics & Laser Technology 101: 363-371.

Zhang, J., et al. (1993). "Design and development of hot corrosion-resistant." Metallurgical transactions A 24(11): 2451-2464.

Zhang, J., et al. (2003). "Dependence of creep strength on the interfacial dislocations in a fourth generation SC superalloy TMS-138." Scripta Materialia 48(3): 287-293.

Zhang, J., et al. (2002). "Interfacial dislocation networks strengthening a fourth-generation single-crystal TMS-138 superalloy." Metallurgical and Materials Transactions A 33(12): 3741-3746.

Zhang, K., et al. (2007). "Research on the processing experiments of laser metal deposition shaping." Optics & Laser Technology 39(3): 549-557.

Zhang, K., et al. (2006). "Improved pitting corrosion resistance of AISI 316L stainless steel treated by high current pulsed electron beam." Surface and Coatings Technology 201(3-4): 1393-1400.

Zhang, S., et al. (2018). "Corrosion behavior of oxide films on AISI 316L SS formed in high temperature water with simultaneous injection of zinc and aluminum." Journal of Alloys and Compounds 731: 1230-1237.

Zhang, S., et al. (2014). "Effects of scan line spacing on pore characteristics and mechanical properties of porous Ti6Al4V implants fabricated by selective laser melting." Materials & Design 63: 185-193.

Zhang, T.-b., et al. (2015). "Hot corrosion characteristics of Ni–20Cr–18W superalloy in molten salt." Transactions of Nonferrous Metals Society of China 25(11): 3840-3846.

Zhang, X., et al. (2007). "The influence of grain size on the corrosion resistance of nanocrystalline zirconium metal." Materials Science and Engineering: A 448(1-2): 259-263.

Zhang, Y., et al. (1999). "Synthesis and cyclic oxidation behavior of a (Ni, Pt) Al coating on a desulfurized Ni-base superalloy." Metallurgical and Materials Transactions A 30(10): 2679-2687.

Zhang, Y., et al. (2017). "Effects of surface quality on corrosion resistance of 316L stainless steel parts manufactured via SLM." Journal of Laser Applications 29(2): 022306.

Zhang, Y. and R. Rapp (1987). "Solubilities of CeO2, HfO2 and Y2O3 in fused Na2SO4-30 mol% NaVO3 and CeO2 in Pure Na2SO4 at 900° C." Corrosion 43(6): 348-352.

Zhao, S., et al. (2004). "The oxidation behavior of the new nickel-based superalloy Inconel 740 with and without Na2SO4 deposit." Surface and Coatings Technology 185(2-3): 178-183.

Zhao, S., et al. (2005). "The corrosion of INCONEL alloy 740 in simulated environments for pulverized coal-fired boiler." Materials Chemistry and Physics 90(2-3): 275-281.

Zhao, S., et al. (2006). "Research and improvement on structure stability and corrosion resistance of nickel-base superalloy INCONEL alloy 740." Materials & Design 27(10): 1120-1127.

Zhao, S., et al. (2005). "The corrosion of INCONEL alloy 740 in simulated environments for pulverized coal-fired boiler." Materials chemistry 90(2-3): 275-281.

Zhao, X., et al. (2017). "Numerical modeling of the thermal behavior and residual stress in the direct metal laser sintering process of titanium alloy products." Additive Manufacturing 14: 126-136.

Zheng, B., et al. (2008). "Thermal behavior and microstructure evolution during laser deposition with laser-engineered net shaping: part II. Experimental investigation and discussion." Metallurgical and Materials Transactions A 39(9): 2237-2245.

Zheng, L., et al. (2011). "Hot corrosion behavior of powder metallurgy Rene95 nickel-based superalloy in molten NaCl–Na2SO4 salts." Materials & Design 32(4): 1981-1989.

Zheng, L., et al. (2012). "Mechanism of intermediate temperature embrittlement of Ni and Ni-based superalloys." Critical Reviews in Solid State and Materials Sciences 37(3): 181-214.

Zheng, L., et al. (2012). "Mechanism of intermediate temperature embrittlement of Ni and Ni-based superalloys." 37(3): 181-214.

Zheng, S., et al. (2013). "Mechanism of (Mg, Al, Ca)-oxide inclusion-induced pitting corrosion in 316L stainless steel exposed to sulphur environments containing chloride ion." Corrosion Science 67: 20-31.

Zheng, Z., et al. (2012). "Corrosion behaviour of nanocrystalline 304 stainless steel prepared by equal channel angular pressing." Corrosion Science 54: 60-67.

Zhilyaev, A., et al. (2003). "Experimental parameters influencing grain refinement and microstructural evolution during high-pressure torsion." Acta Materialia 51(3): 753-765.

Zhong, Y., et al. (2016). "Intragranular cellular segregation network structure strengthening 316L stainless steel prepared by selective laser melting." Journal of Nuclear Materials 470: 170-178.

Zhou, C., et al. (2020). "Improvement of corrosion resistance of SS316L manufactured by selective laser melting through subcritical annealing." Corrosion Science 164: 108353.

Zhou, H., et al. (2004). "Deformation microstructures after low-cycle fatigue in a fourth-generation Ni-base SC superalloy TMS-138." Materials Science and Engineering: A 381(1-2): 20-27.

Zhou, Y., et al. (2014). "Atomic-scale decoration for improving the pitting corrosion resistance of austenitic stainless steels." Scientific reports 4: 3604.

Zhu, J., et al. (2013). "High-temperature-oxidation-induced ordered structure in Inconel 939 superalloy exposed to oxy-combustion environments." Materials Science and Engineering: A 566: 134-142.

Zhu, J., et al. (2013). "High-temperature-oxidation-induced ordered structure in Inconel 939 superalloy exposed to oxy-combustion environments." 566: 134-142.

Zhu, Y. T. and T. G. Langdon (2004). "The fundamentals of nanostructured materials processed by severe plastic deformation." Jom 56(10): 58-63.

Ziętala, M., et al. (2016). "The microstructure, mechanical properties and corrosion resistance of 316 L stainless steel fabricated using laser engineered net shaping." Materials Science and Engineering: A 677: 1-10.

Zohdy, K., et al. (2014). "Corrosion behavior of leaded-bronze alloys in sea water." Materials Chemistry and Physics 147(3): 878-883.

Zuo, Y., et al. (2002). "The aspect ratio of surface grooves and metastable pitting of stainless steel." Corrosion Science 44(1): 25-35.

Vita

Ali Hemmasian Ettefagh was born in Esfahan, Iran in 1983. In spring 2006, he graduated from Amirkabir University of Technology and received his Bachelor of Science in Metallurgical and Materials Engineering. He received his Master's degree in Corrosion Engineering in fall of 2009 from University of Tehran. He enrolled in the Graduate School at Louisiana State University under the supervision of Dr. Shengmin Guo to pursue his PhD of Mechanical Engineering (Materials Science and Engineering) in spring 2017.